Piezoelectric-based Multi-Scale Multi-Environment Energy Harvesting

Hyun-Cheol Song

Dissertation submitted to the faculty of the Virginia Polytechnic Institute and State University in partial fulfillment of the requirements for the degree of

Doctor of Philosophy
in
Materials Science and Engineering

Shashank Priya, Chair
William B. Reynolds Jr., Co-chair
Alex O. Aning
Kathy Lu
Jean J. Heremans

June 22nd, 2017
Blacksburg, Virginia

Keywords: energy harvesting, piezoelectric material, MEMS, nanowire, nanostructure, magneto-thermoelectric generator

Piezoelectric-based Multi-Scale Multi-Environment Energy Harvesting

Hyun-Cheol Song

ABSTRACT

Energy harvesting is a technology for generating electrical power from ambient or wasted energy. It has been investigated extensively as a means of powering small electronic devices. The recent proliferation of devices with ultra-low power consumption – devices such as RF transmitters, sensors, and integrated chipsets – has created new opportunities for energy harvesters. There is a variety of ambient energies such as vibration, thermal, solar, stray current, etc. Depending on energy sources, different kinds of energy conversion mechanism should be employed. For energy harvesters to become practical, their energy conversion efficiency must improve. This efficiency depends upon advances in two areas: the system or structural design of the energy harvester, and the properties of the materials employed in energy conversion. This dissertation explores developments in both areas. In the first area, the role of nano-, micro-, and bulk structure of the energy conversion materials were investigated. In the second area, piezoelectric energy harvesters and a magneto-thermoelectric generator are treated from the perspective of system design.

In the area of materials development, $PbTiO_3$ (PTO) nanostructures consisting of nanofibers and three-dimensional (3-D) nanostructure arrays were hydrothermally synthesized. The growth mechanism of the PTO nanofibers and 3-D nanostructures were investigated experimentally and theoretically. The PTO nanostructures were composed of oriented PTO crystals with high tetragonality; these arrays could be promising candidates for nanogenerators.

Different designs for energy harvesters were explored as a means of improving energy conversion efficiency. Piezoelectric energy harvesters were designed and constructed for applications with a low frequency vibrational energy and for applications with a broadband energy spectrum. A spiral MEMS piezoelectric energy harvester design was fabricated using a silicon MEMS process and demonstrated to extract high power density at ultra-low resonance frequencies and low acceleration conditions. For a broadband energy harvester, a magnetically-coupled array of oscillators was designed and built that broadened the harvester's effective resonance frequency with considerably improved output power.

A new design concept for thermal energy harvesting that employs a magneto-thermoelectric generator (MTG) design was proposed. The MTG exploits a thermally-induced second order phase transition in a soft magnetic material near the Curie temperature. The MTG harvested electric power from oscillations of the soft magnet between hot and cold sources. For the MTG design, suitable soft magnetic materials were selected and developed using $La_{0.85}Sr_{0.15}MnO_3$-$Ni_{0.6}Cu_{0.2}Zn_{0.2}Fe_2O_4$ magnetic composites. The MTG was fabricated from a PVDF cantilever and a gadolinium (Gd) soft magnetic material. The feasibility of the design for harvesting energy from the waste heat was demonstrated by attaching an MTG array to a computer CPU.

Piezoelectric-based Multi-Scale Multi-Environment Energy Harvesting

Hyun-Cheol Song

GENERAL AUDIENCE ABSTRACT

Energy harvesting is a technology for generating electrical power from ambient or wasted energy. It has been investigated extensively as a means of powering small electronic devices. The recent proliferation of devices with ultra-low power consumption – devices such as RF transmitters, sensors, and integrated chipsets – has created new opportunities for energy harvesters. There is a variety of ambient energies such as vibration, thermal, solar, stray current, etc. Depending on energy sources, different kinds of energy conversion mechanism should be employed. For energy harvesters to become practical, their energy conversion efficiency must improve. This efficiency depends upon advances in two areas: the system or structural design of the energy harvester and the properties of the materials employed in energy conversion. This dissertation explores developments in both areas. In the first area, the role of nano-, micro-, and bulk structure of the energy conversion materials were investigated. In the second area, vibration energy harvesters using piezoelectric materials (mechanical to electrical energy conversion) and thermoelectric generator employing magnetic phase transition are treated from the perspective of system design.

Dedication

To my lovely wife Juyun and sweetheart daughter Jian for their endless love and dedication

Table of Contents

List of Figures

the interface. For better visibility, the TEM image is artificially colored. (d) Scanning TEM (STEM) elemental mapping of Pb and Sr in the $PbTiO_3/SrTiO_3$ interface region.

Figure 3.10. (a) Schematic description of PFM analysis. 0.5 wt% Nb-doped $SrTiO_3$ substrate with (001) orientation was used for measurement of piezoresponse. (b) Amplitude and (c) phase from piezoelectric response taken from the cross-hatched $PbTiO_3$ 3-D nanostructures on (001) oriented Nb-doped $SrTiO_3$ substrates. (d) Combined signal of amplitude and phase of $PbTiO_3$ 3-D nanostructures, which confirms the ferroelectric behavior of $PbTiO_3$ nanostructure.

Figure 4.1. Schematic design of spiral MEMS energy harvester.

Figure 4.2. Schematic fabrication procedure for piezoelectric MEMS energy harvester with spiral structure. (i) Multilayer deposition, (ii) Top electrode patterning, (iii) PZT etching, (iv) Bottom electrode patterning, (v) Front side DRIE etching and (vi) Back side DRIE etching and releasing structure.

Figure 4.3. (a) Cross-sectional and (b) surface SEM images of PZT thin films used in the fabrication of spiral MEMS energy harvester. The surface SEM image was taken after etching top electrodes.

Figure 4.4. Surface topographic image of the PZT film used in the MEMS energy harvester.

Figure 4.5. (a) X-ray diffraction patterns (b) Polarization vs. electric field (P-E) hysteresis curve of the PZT thin film.

Figure 4.6. Out-of-plane PFM images of the PZT film: (a) Amplitude and (b) Phase.

Figure 4.7. Out The clamped longitudinal effective piezoelectric coefficient ($d_{33,f}$) and calculated real longitudinal piezoelectric coefficient (d_{33}) with variation of applied dc field for the PZT thin film grown on the spiral cantilever.

Figure 4.8. SEM images of (a) front side, (b) etched edge, (c) cross-section of membrane and (d) back side of the spiral cantilever energy harvester. Simulated stress distribution of (e) sharp junction and (f) round shape junction in the spiral energy harvester.

Figure 4.9. Experimental test set-up for the spiral MEMS energy harvesters

Figure 4.10. (a) Frequency dependence of output peak voltages with the variation of number of turns of the spiral energy harvester. The harvesters were excited by 2.45 m/s^2 (0.25 g) acceleration. (Inset) Optical pictures of the fabricated spiral energy harvester with number of turns; (i) 2 turns, (ii) 3 turns, (iii) 4 turns, (iv) 5 turns, (v) 6 turns and (vi) 7 turns.

Figure 4.11. 2D live scan images obtained by laser vibrometer of the (a) first and (b) second vibration modes and FEM simulated images of (c) first and (d) second vibration modes for the 3 turns of spiral MEMS energy harvester. (Inset) Simulated stress distributions in the first and second modes.

Figure 4.12. (a) Natural frequencies of the spiral energy harvesters with variation of number of turns. (b) Output power and voltage of the 5 turns spiral energy harvester with variation of external electrical load.

Figure 5.1. (a) Schematic description of vibration and stray magnetic field dual phase energy harvester. (b) Schematic layout of the MaCoPEHA. The picture shows fabricated cantilever energy harvester array. (c) Expected output voltage of the MaCoPEHA with respect to cantilever beam positions. (d) Schematic diagram of the cantilever energy harvester consisting of 2-2 composite structure of metal shims and piezoelectric ceramic layers in order to improve the strength and output power. (e) Configuration of coupled magnetic proof masses that have same polarity and repulsive force.

Figure 5.2. Testing setup for vibration characteristics of energy harvesters with two-dimensional laser vibrometer.

Figure 5.3. Frequency spectrums of open-circuit output voltage of individual harvesters in the MaCoPEHA at (a) 0.01 V, (b) 0.02 V, and (c) 0,03 V burst chirp signals applied to shaker. The output voltages were normalized by applied acceleration (g). The MaCoPEHA has multiple-resonance frequencies and a broadband frequency spectrum. With increase of the applied voltage to the shaker (acceleration, g), the bandwidths increase, and the resonance frequencies of each harvester slightly shift due to the augmented magnetic interaction between adjacent beams.

Figure 5.4. Generated open-circuit output voltages of the MaCoPEHA with 1 g acceleration at (a) 52.5 Hz, (b) 60.5 Hz, (c) 70 Hz and (d) 78 Hz. Pictures show coupled vibration mode shapes measured by the two-dimensional laser vibrometer at each frequency. The phase deviation of the generated voltage signal and the coupled mode shape of the MaCoPEHA vary depending upon the interaction of beams at different frequencies.

Figure 5.5. Frequency dependent rectified DC voltages of the MaCoPEHA through a full-bridge rectifier under (a) 1 g sinusoidal vibration and (b) 500 μT magnetic field. 0.5 Hz interval of the frequencies were stepped. Inset pictures are the vibration and the magnetic field testing setups, respectively. Helmholtz coils was used to generate the H_{ac} magnetic field. The summation of the generated total output voltage of each beam energy harvester under (c) 1 g vibration and (d) 500 μT magnetic field. The MaCoPEHA exhibited multi-resonance peaks and broadband characteristics under both vibrations and magnetic fields conditions.

Figure 5.6. (a) Experimental setup for energy harvesting from pump vibrations. (b) Frequency analysis of pump vibration using an accelerometer. The fundamental vibration frequency is 29.5 Hz and the second and the third harmonic frequencies are 59 Hz and 118 Hz, respectively. (c) Generated open-circuit voltage measured via a full-bridge rectifier. The MaCoPEA responds to the second harmonic frequency of 59 Hz. (d) Measured internal impedance of the beam #2 in the MaCoPEHA. (e) Output voltage and power of the beam #2 in MaCoPEHA with various load resistors under 1 g acceleration at 60Hz. The impedance matching resistance is 290 kΩ at 59 Hz and identical to the measured impedance in (c). (f) Rectified output voltages of the MaCoPEHA connected with optimum load resistances under the pump vibration.

Figure 5.7. (a) Experimental setup for the stray magnetic field energy harvesting from the power cable of an electric kettle. (b) Generated open-circuit voltage of the MaCoPEHA from

a power cable of an electric kettle. (c) Rectified output voltage of individual energy harvesters in the MaCoPEHA across the optimum load resistance of each beam.

Figure 5.8. (a) Experimental setup for the vibration energy harvesting from an automobile engine. The MaCoPEHA with 4 beams was mounted on the top of the engine room. (b) Generated open-circuit voltages of the MaCoPEHA with variation of the engine acceleration. As alternating the engine acceleration, the responding beam in resonance is immediately shifted according to the frequency. The MaCoPEHA shows the broadband characteristics and is able to generate the sufficient power regardless of alternating vibration frequency.

Figure 6.1. Schematic structure of Magneto-electric Thermal Generator (MTG).

Figure 6.2. Field-cooled (FC) temperature-dependent magnetization of $La_{(1-x)}Sr_xMnO_3$ in the $0.15 \leq x \leq 0.30$ strontium content range with applied field of 100 Oe. The inset shows magnetization vs. applied magnetic field (M-H hysteresis curves) data of $La_{0.85}Sr_{0.15}MnO_3$ at various temperatures.

Figure 6.3. M-H hysteresis curves of $La_{(1-x)}Sr_xMnO_3$ with variation of Sr content at 250 K. The inset shows zoomed view of hysteresis curves.

Figure 6.4. SEM and EDS mapping images of 70 wt.% LSMO – 30 wt.% NCZF magnetic Composites sintered by conventional firing schedule (1200 °C for 2hours).

Figure 6.5. SEM Field-cooled (FC) temperature-dependent magnetization of (100-x) wt.% LSMO – x wt.% NCZF magnetic composites sintered by conventional firing schedule (1200 °C for 2hours) in the $0 \leq x \leq 30$ NCZF content range.

Figure 6.6. XRD patterns of (a) $Ni_{0.6}Cu_{0.2}Zn_{0.2}Fe_2O_4$, (b) $La_{0.85}Sr_{0.15}MnO_3$, (c) 90 *wt.*%LSMO-10*wt.*%NCZF, (d) 80*wt.*%LSMO-20*wt.*NCZF, and (e) 70*wt.*%LSMO-30*wt.*%NCZF magnetic composites sintered by two-step schedule (1075 °C => 1025 °C for 8 hours).

Figure 6.7. Two-step sintered LSMO-NCZF (70:30 *wt.*%) magnetic composite (a) SEM image, (b) EBSD image, (c) EDS mapping image for Fe and Mn elements, (d) EDS mapping image for Mn element and (e) EDS mapping image for Fe element.

Figure 6.8. (a) Topographic and (b) MFM magnetic phase images of two-step sintered LSMO-NCZF (70:30 *wt.*%) magnetic composite

Figure 6.9. The M-T curves of mixed powder and two-step sintered magnetic composite with LSMO-NCZF (70:30 *wt.*%) composition.

Figure 6.10. (a) The M-H hysteresis curves of two-step sintered LSMO-NCZF (70:30 *wt.*%) magnetic composites with variation of temperature. Inset is zoomed view of hysteresis curves. (b) The M-H hysteresis curve of gadolinium (Gd) foil. Inset is the M-T curves of Gd foil with variation of temperature.

Figure 6.11 (a) MTG operation test set-up for the soft magnetic material. (b) Bimorph piezoelectric cantilever beam with LSMO–NCZF (70:30 *wt.*%) soft magnetic material developed in this study.

List of Tables

List of symbols and acronyms

Symbols

A	Acceleration
C_0	Capacitance of material
c_{ij}	Elastic stiffness coefficient
d_{33}	Longitudinal piezoelectric strain constant
$d_{33,f}$	Effective longitudinal piezoelectric strain constant
d_{31}	Transverse piezoelectric strain constant
D_i	Electrical displacement
D_g	Grain boundary diffusivity
E_i	Electric Field
E	Elastic modulus
e_{ij}	Piezoelectric stress constant
e_{33}	Longitudinal piezoelectric stress constant
g_{ij}	Piezoelectric voltage constant
g_{31}	Transverse piezoelectric voltage constant
$g_{31,f}$	Effective transverse piezoelectric voltage constant
H_c	Coercive magnetic field
I	Moment of inertia
I_{out}	Output current
K	Transverse stiffness
k_B	Boltzmann constant
k_p	Planar electromechanical coupling factor
k_{33}	Longitudinal electromechanical coupling coefficient
L	Length of beam
L_g	Mean grain size
M	Effective mass
M_s	Saturated magnetization
$M_{s,\,Tc}$	Saturated magnetization at T_C
$M_{s,\,T1}$	Saturated magnetization at T_1
M_r	Remnant magnetization

m	Proof mass
P_s	Saturated polarization
P_r	Remanent polarization
P_{out}	Output power
Q_m	Electro-mechanical quality factor
S_j	Mechanical strain
s	Surface energy
s_{ij}	Elastic stiffness coefficient
T_C	Curie Temperature
T	Absolute Temperature
t	Time
V_{out}	Output voltage
V_{piezo}	Volume of the piezo material
V_a	Atomic volum
ω_n	Natural frequency
ω_r	Resonance frequency
ω_{short}	Short circuit resonance frequency
ω_{open}	Open circuit resonance frequency
Z	Impedance
α	Thermal diffusivity
σ_{ij}	Mechanical stress
σ	Poisson's ratio
ζ_m	Mechanical damping ratio
ζ_e	Electrical damping ratio
δ	Grain boundary width
ε_{ij}	Dielectric permittivity
η	Energy conversion efficiency

Acronyms

AD	Aerosol Deposition
AFM	Atomic Force Microscopy
CIP	Cold Isostatic Press
CNO	$Ca_2Nb_3O_{10}$
CMOS	Complementary Metal Oxide Semiconductor
CPU	Central Processing Unit
CVD	Chemical Vapor Deposition
DC-DC	Direct Current to Direct Current
DI water	Deionized Water
DFOM	Dimensionless Figure of Merit
DRIE	Deep Reactive Ion Etching
EBSD	Electron Backscattered Diffraction
EDS	Energy Dispersive Spectroscopy
FDM	Finite Difference Method
FEM	Finite Element Method
FeRAM	Ferroelectric Random Access Memory
FESEM	Field-emission Scanning Electron Microscope
FIB	Focused Ion Beam
FOM	Figure of Merit
GEMC	Generalized Electromechanical Coupling
GSV	Granule Spray in Vacuum
HR-TEM	High resolution transmission electron microscopy
IDE	Interdigitated Electrodes
IoT	Internet of Things
JCPDS	Joint Committee on Powder Diffraction Standards
KNN	$(K_{0.5}Na_{0.5})NbO_3$
LNO	$LaNiO_3$
MaCoPEHA	Magnetically Coupled Piezoelectric Energy Harvester Array
ME	Magnetoelectric
MEMS	Micro Electromechanical System

MFM	Magnetic Force Microscopy
MLCC	Multilayer Ceramics Capacitor
MOCVD	Metalorganic Vapour Phase Epitaxy
MPB	Morphotropic Phase Boundary
MTG	Magneto-Thermoelectric Generator
NAPD	Normalized Areal Power Density
NCZF	$(Ni_{0.6}Cu_{0.2}Zn_{0.2})Fe_2O_4$
NVPD	Normalized Volumetric Power Density
P-E	Polarization–Electric field
PFM	Piezoresponse Force Microscopy
PI	Performance Index
PPMS	Physical Property Measurement System
PZT	$Pb(Zr_{0.52}Ti_{0.48})TiO_3$
PAA	Poly(acrylic acid)
PVA	Poly(vinyl alcohol)
PVDF	Polyvinylidene Fluoride
ME	Magnetoelectric
PDMS	Polydimethylsiloxane
PLD	Pulsed Laser Deposition
PMN-PT	$(PbMg_{1/3}Nb_{2/3})O_3$-$PbTiO_3$
PST	$(PbSc_{0.5}Ta_{0.5}O_3)$
PTO	$PbTiO_3$
PYN–PT	$Pb(Y_{1/2}Nb_{1/2})O_3$-$PbTiO_3$
PZN-PT	$Pb(Zn_{1/3}Nb_{2/3})O_3$–$PbTiO_3$
RIE	Reactive Ion Etching
RF	Radio Frequency
SAED	Selected Area Electron Diffraction
SAW	Surface Acoustic Wave
SOI	Silicon on Insulator
SRO	$SrRuO_3$
STEM	Scanning Transmission Electron Microscopy
STO	$SrTiO_3$,
TAC	Thermal Accommodation Coefficient

TEM	Transmission Electron Microscopy
TTT	Temperature-Time-Transformation
UAVs	Unmanned Aerial Vehicles
VCP	Voided Charged Polymers
VLSI	Very Large Scale Integration
VSM	Vibrating Sample Magnetometer
XRD	X-ray Diffraction
YSZ	Yttria Stabilized Zirconia
2D	Two-dimensional
3D	Three-dimensional

1. Chapter 1: Introduction to Energy Harvesting

1.1. Introduction

Recent advanced technologies in low power consumption sensors, RF transmitters and CMOS circuitry have led to focused research effort on a self-sustain power system. In particular, the energy harvesting technology can generate the useful electrical energy from the dumped ambient energy i.e. engine vibration, human activity, boiler pipe heat, indoor light, stray current surrounding power cord etc. has been extensively investigated as a means of powering small electronic devices such as wireless sensor nodes as described in Figure 1.1.

The standalone wireless sensor by the energy harvesting is attractive due to cost-effective as removing the cost of batteries and the labor required to install complex wiring as well as time-effective as saving time to replace and maintain the batteries. Sometimes, the replacement of battery or power wiring are almost impossible in hazardous, harsh and large terrain environments when we consider that a large number of sensors are typically installed in ubiquitous sensor networks (USN). Therefore, in such cases, developing on-site generators that can convert any available environmental energy at that location into electrical energy is more reasonable.[1] Moreover, the energy harvesting can provide a breakthrough for implantable sensors and artificial electronic organs such as pace maker, glucose sensor for diabetes, artificial retina, cochlea, etc. as avoiding repeat surgery for changing batteries.

Energy harvesting technology can provide a battery-less solution by power generating from unused environmental energy sources such as machines, human body, vehicles, and structures, all of which could be an excellent source of capturing small power without affecting the source itself. Furthermore, energy harvesting can offer alternative solution for severe environmental conditions hard to use battery such as very high or low temperature environment of dessert, deep in the sea, and polar regions. The energy harvesting can be simply classified according to

size in two categories: (i) energy harvesting for small electronic devices using bulk size devices, and (ii) energy harvesting for USN using Microelectromechanical systems (MEMS). The bulk energy harvester can provide a main or additional electric power to operate small electronic devices. The MEMS energy harvester can give a new opportunity for system-on-chip integration with low power consumption sensors and microprocessor, which can provide capability to interact with vast range of platform leading to new and enhanced functionality.

Figure 1.1. Schematic illustration of energy harvesting.

In past decades, several energy harvesting approaches have been proposed using solar, thermoelectric, electromagnetic, capacitive, piezoelectric, and magneto-electric schemes.[1-3] Depending on energy sources, different type of energy conversion mechanism should be utilized. Typically, the direction energy conversion mechanism from ambient energy source into electrical energy is employed because it is more efficient than the multi-step energy conversion. For examples, thermal gradient for thermoelectric (Seebeck) effect, mechanical stress for piezoelectric effect, light for photovoltaic effect, and stray electromagnetic wave for

electromagnetic induction generally are exploited for the electric energy conversion. However, in some cases, the multi-step energy transformation could be more attractive option due to the limitation of environmental conditions such that the figure of merits, *ZT* values, of the thermoelectric materials at low temperature are very poor for thermal energy harvesting.[4]

Mechanical energy can be converted into electrical energy using piezoelectric, electromagnetic and electrostatic transducers. Among them, the piezoelectric transducers are the most attractive due to their high energy density and conversion efficiency. Furthermore, the piezoelectric energy conversion offers more following advantages: (1) scaling of devices for miniaturization because the energy density of piezoelectric materials remains high with reducing size, (2) temperature stability at low and high temperatures, (3) easy implementation by simple structure, and (4) easy application to high frequency. In this work, to overcome limitations of the direction energy conversion of thermoelectric and electromagnetic induction effects, different forms of energies of vibration, thermal gradient, and stray magnetic field were transformed to the mechanical energy and then the electrical energy were obtained from the mechanical energy through the piezoelectric materials as shown in Figure 1.2. For the mechanical energy conversion from the thermal gradient and the stray magnetic field, the thermally induced second order phase transition of soft magnetic material and the coupling of magnets and magnetic fields were exploited, respectively. Based on the piezoelectric energy harvester, different types of vibration, thermal, and stray magnetic field energy harvesters were developed and investigated at different scales of bulk, micro and nano.

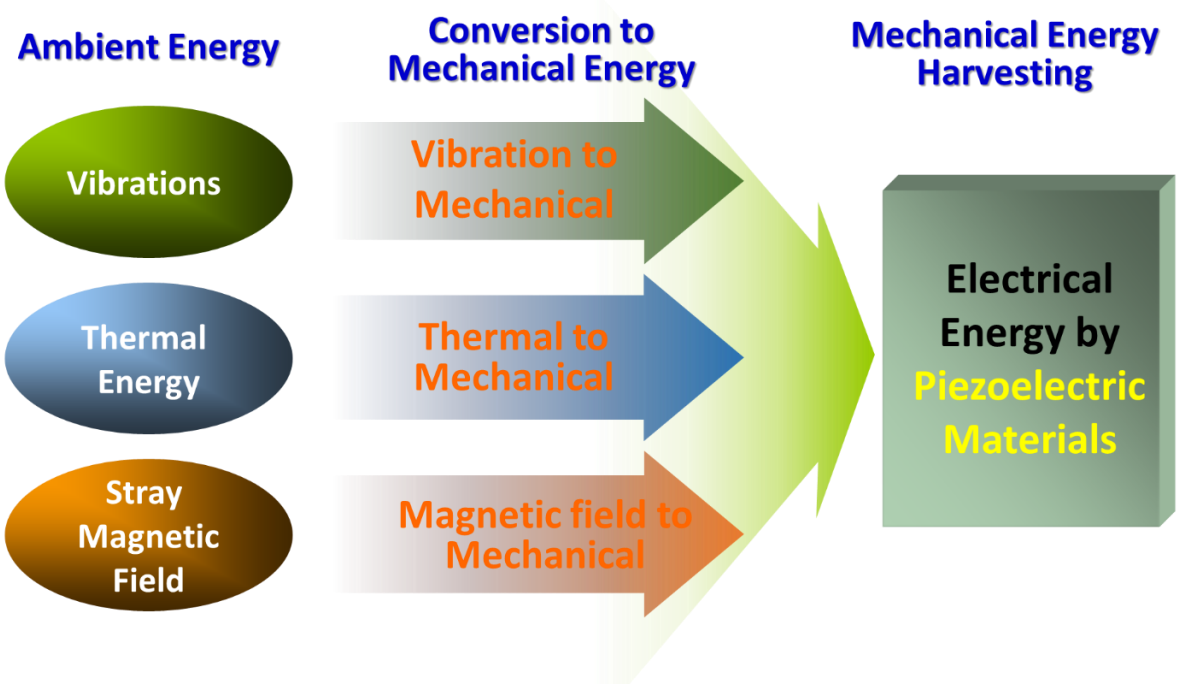

Figure 1.2. Energy conversion steps for the multi-source energy harvesting: vibrations, thermal energy, and stray magnetic field convert into mechanical energy which is transformed to electrical energy by piezoelectric materials

The ultimate goal of the energy harvesting research is improving the total energy conversion efficiency from the ambient energy to the electrical power in order to generate the maximum power from limited energy. Energy transition flow in the typical piezoelectric energy harvesting is shown schematically in Figure 1.2. There are three primary energy couplings or energy transition steps in the piezoelectric energy harvesting as outlined in this schematic: (a) Mechanical-to-mechanical energy coupling in trapping the mechanical AC stress from ambient mechanical source, (b) mechanical-to-electrical energy coupling in converting the mechanical into the electrical energy by direct piezoelectric conversion, and (c) electrical-to-electrical energy coupling in processing and storing the generated electrical energy. To increase the total energy conversion efficiency, each steps of energy couplings should be improved and the losses occurring at each step should be reduced. First step of the energy coupling is closely influenced by the harvester structure how efficiently extract the external mechanical stress. Depending

upon the frequency and amplitude of the mechanical stress, one can design the required transducer, its dimensions, and vibration mode. In particular, the natural frequency of the energy harvester is the most important factor on designing the transducer since the vibration amplitude of a system at resonance is significantly larger than that at off-resonance. Thus, the natural frequency of the energy harvester should be tuned in accordance with the ambient vibration frequency to become a resonance and maximize output power. The mechanical-to-electrical coupling is solely related to the energy conversion media from mechanical to electrical energy (piezoelectric material). The magnitude of the electromechanical coupling factor (k_p) of the piezoelectric material can directly affect to the energy conversion efficiency of this step [5-8]. For improving the mechanical-to-electrical coupling, the proper piezoelectric material selection is necessary. The final step of energy conversion is the electrical-to-electrical coupling. The generated electrical energy from the piezoelectric material have AC form as presented in Figure 1.3 need to be rectified for powering electronic devices or storing batteries. The diodes consumes a certain amount of electrical energy during the rectifying process. In addition, the electrical loss can occur due to the impedance mismatch between the energy harvesting system and the load. To improve the electrical-to-electrical coupling, therefore, the electrical loss consumed in the electrical circuit should be reduced through developing the low loss rectifying circuit and impedance matching to avoid the current reflection from the load.

This dissertation mainly focuses on improving the mechanical-to-mechanical and the mechanical-to-electrical energy couplings as devising the novel structure of piezoelectric transducers and developing the piezoelectric materials. The impedance matching between the piezoelectric energy harvester and the load was also employed in all energy harvesting studies for enhancing the electrical-to-electrical coupling.

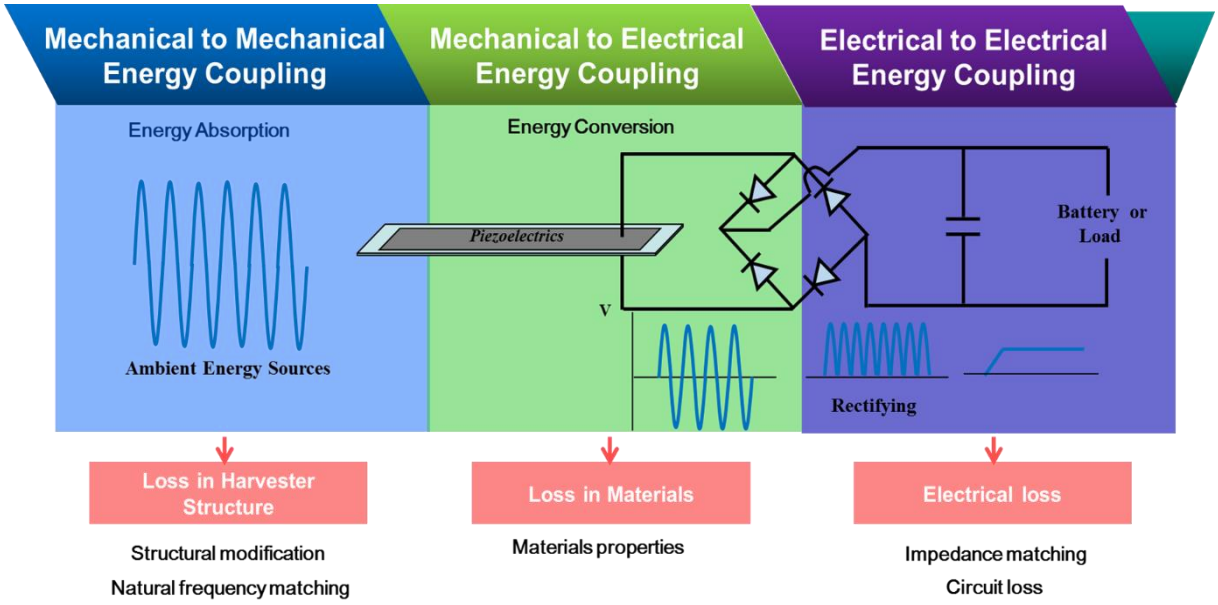

Figure 1.3. Energy transition flow in piezoelectric energy harvesting.

1.2. Fundamentals of Piezoelectric Energy Harvesting

1.2.1. Fundamentals of Piezoelectricity

Piezoelectricity is the property of certain crystals to generate an electric potential in response to applied mechanical stress. There are two different kinds of phenomena commonly observed which are termed as direct and the converse piezoelectric effects. When the mechanical stress is applied to a piezoelectric material, an electric charge proportional to the applied stress is produced. This refers to the direct piezoelectric effect. Conversely, when electric field is applied to the same material, strain or displacement is produced proportional to the magnitude of electric field. This is called as converse piezoelectric effect. The following two constitutive equations are used to describe the piezoelectric effect:

$$D_i = d_{ij}\,\sigma_j + \varepsilon_{ii}^{T} E_i \quad \text{or} \quad D_i = e_{ij}\,S_j + \varepsilon_{ii}^{S} E_i \tag{1.1}$$

$$S_j = s_{ij}^{E}\,\sigma_j + d_{ij} E_i \quad \text{or} \quad T_j = c_{ij}^{E}\,S_j - e_{ij} E_i \tag{1.2}$$

Here in these two constitutive equations D_i is the electrical displacement, S_j is mechanical strain, σ_j is mechanical stress, E_i is the electric field, c_{ij} is the elastic stiffness coefficient, s_{ij} is the elastic compliance coefficient, and ε_{ij} is the permittivity. The superscript used in the equation shows the constant parameter used. d_{ij} and e_{ij} are piezoelectric coefficients which are third rank tensors.

Piezoelectric ceramics are anisotropic in nature implying that the electromechanical properties exhibit maximum along specific crystallographic direction. The properties are commonly described using two subscripts (reduced order tensor notation) which indicate the direction of the electrical and mechanical parameters. Figure 1.4 shows the direction indexes of constants in rectangular crystallographic system. The principal properties along X, Y and Z axes are described using 1, 2 and 3 notations, respectively. The shear constants are represented by 4, 5 and 6 respectively. For example, in case of piezoelectric charge constant d_{31}, the first index "*3*" indicates that electrodes are perpendicular to axis 3 and the second index "*1*" indicates that the applied stress or induced strain is along direction 1. A superscript index on the electromechanical constant is used to represent the constant condition under which measurements were conducted. For example, in case of compliance, s_{36}^{E}, "E" indicates that the compliance was measured under constant electric field or with electrodes connected together.

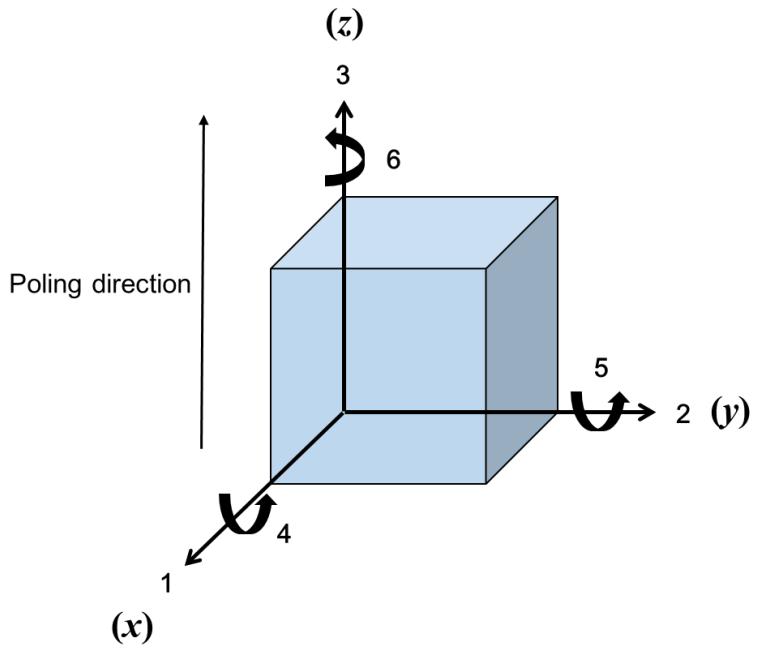

Figure 1.4. Direction index of electromechanical constants in poled piezoelectric ceramics.

Non-centrosymmetricity is requirement for observing the piezoelectric effect and most of the high performance piezoelectric materials are ferroelectric perovskites as shown in Figure 1.5. The leading representative of the perovskite piezoelectric ceramics, $Pb(Zr,Ti)O_3$ (PZT), has many possible variations depending upon the doping and solid solution. As shown in Figure 4 (a), PZT unit cell has a symmetric cubic structure above the Curie temperature (paraelectric), however, below that it transforms into asymmetric tetragonal structure (approximately Zr/Ti ratio < 1, where Zr+Ti=1) as schematically depicted in Figure 1.5 (b). Thus, PZT unit cell shows spontaneous polarization because of the shift in the position of B-site atom.

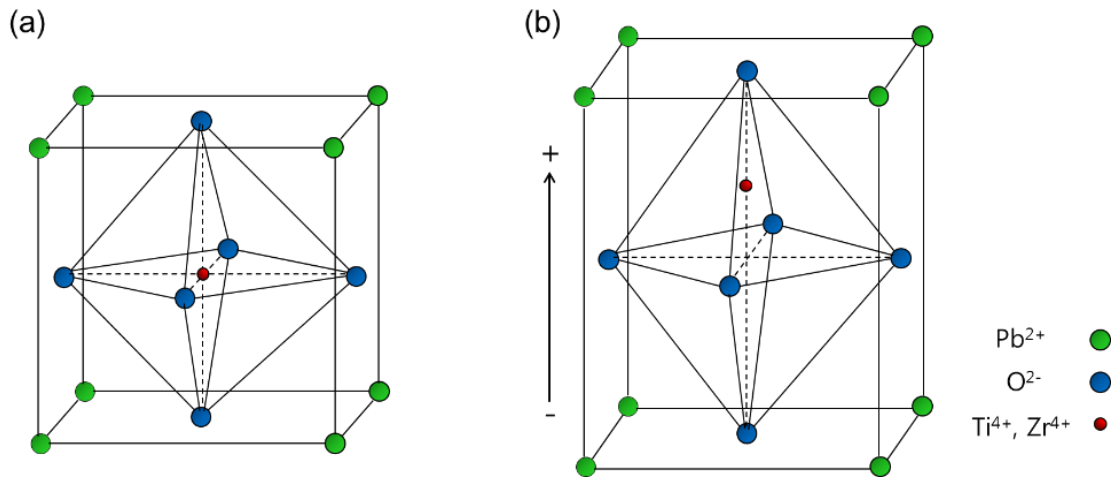

Figure 1.5. Perovskite PZT unit cell. (a) PZT unit cell in the symmetric cubic state above the Curie temperature. (b) Tetragonally distorted unit cell below the Curie temperature.

Neighboring dipoles formed in the distorted perovskite unit cell align together to form domains. Typically, polycrystalline piezoelectric ceramics have randomly oriented domain distribution as shown in Figure 1.6 (a), thus, overall net polarization of material is negligible. Because of the ferroelectric nature of the material, domains can be permanently aligned by applying strong electric field. This process is called poling (see Figure. 1.6 (b)) and is normally performed at an elevated temperature slightly below Curie point to facilitate the domain wall motion. During poling process, most of the domains are aligned along applied electric field direction and neighboring domains exhibit new dimensions through nucleation and growth. After poling process, most of the dipoles retain their alignment imparting the piezoelectric material a remanent polarization (see Figure. 1.6 (c)).

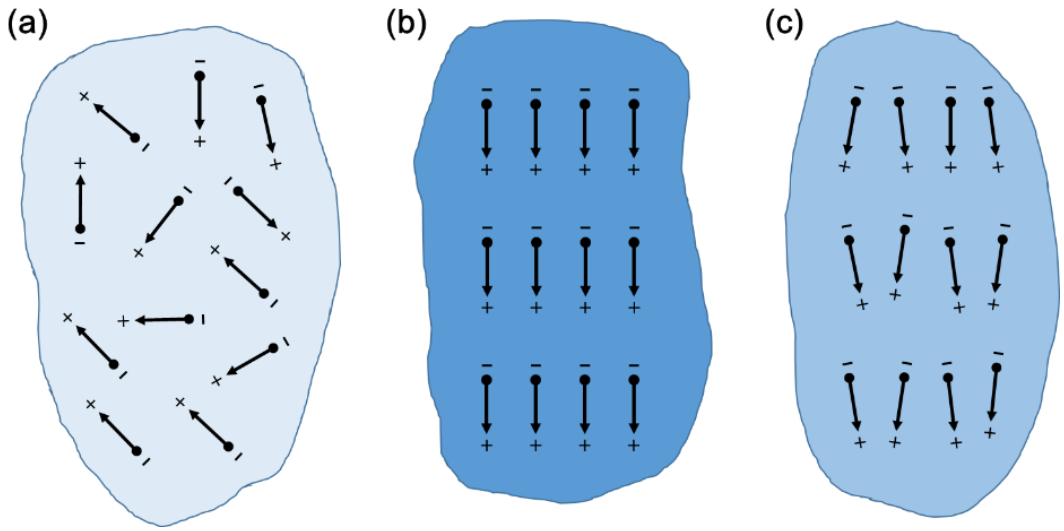

Figure 1.6. Piezoelectric domains in piezoelectric materials. (a) Randomly oriented domains, (b) domains during and (c) after poling process.

Besides piezoelectric ceramics, there are piezoelectric polymer materials which have semi-crystalline structure for examples polyvinylidene fluoride (PVDF), polyamides, ParyleneC, liquid crystal polymers, PVDF-TrFE block copolymer and etc. The operation principle of these piezoelectric polymers are similar to piezoelectric ceramic materials. The semi-crystalline polymers have microscopic crystals inside matrix which are also polarized and function as dipoles as described Figure 1.6. The microcrystals are distributed within an amorphous matrix. To obtain effective piezoelectricity of such materials, there should be reoriented these small crystals and keep them in one orientation through electrical poling or mechanical stretch process. There is another type of piezoelectric materials known as voided charged polymers (VCP, sometimes called ferroelectret or piezoelectret) that contain internal gas voids. When the polymer surfaces surrounding the void are charged by electrical poling or X-ray, the space charges are created inside matrix and the VCP behaves like piezoelectric material. These polymers have very high d_{33} values of several tens of thousands pC/N in some cases. However, these piezoelectric polymers have serious life time and ageing problems. The VCP is easily

neutralized in extremely moist environment and the surface charge can be rapidly decayed in high temperature.

1.2.2. Transfer Function for Energy Harvester

The simple vibration energy harvester can be modeled as a second-order, spring-mass system. The characteristics of the energy harvester can be described by damping constant and natural frequency of the system. A cantilever beam structure with piezoelectric plate and proof mass is equivalent to a lumped spring mass system of a vibrating rigid body. Thus, the governing equation of motion of a lumped spring mass system can be written as:

$$m \cdot \frac{d^2z(t)}{dt^2} + b \cdot \frac{dz(t)}{dt} + k \cdot z(t) = -m \cdot \frac{d^2y(t)}{dt^2} \tag{1.3}$$

which can be transformed using Laplace transform as following:

$$m \cdot s^2 z(s) + b \cdot s \cdot z(s) + k \cdot s \cdot z(s) = -m \cdot a(s) \tag{1.4}$$

where $a(s)$is the Laplace transform of the acceleration, $a(t)$, given as:

$$a(t) = \frac{d^2y(t)}{dt^2} \tag{1.5}$$

Therefore, the transfer function of the energy harvester can be expressed as:

$$\frac{z(s)}{a(s)} = {1}\Big/{(s^2 + \frac{b}{m}s + \frac{k}{m})} = {1}\Big/{(s^2 + \frac{\omega_r}{Q}s + \omega_r^2)} \tag{1.6}$$

where Q $= \sqrt{km}/b$ is quality factor of system and ω_r is resonance frequency of the energy harvester. The natural frequency of the spring mass system and energy harvester can be given as:

$$\omega_n = \sqrt{\frac{K}{M}} \tag{1.7}$$

where *K* and *M* are the transverse stiffness and effective mass, respectively. The stiffness *K* can be calculated from loading condition. In case of simple cantilever beam structure, the stiffness can be expressed as:

$$K = 3EI/L^3 \tag{1.8}$$

where *E* is modulus of elasticity, *I* is the moment of inertia, and L is the length of beam. The moment of inertia for a rectangular cross-section is $I = \left(\frac{1}{12}\right) bh^3$, where *b* and *h* are the width and thickness of the beam in transverse direction, respectively.

1.2.3. Frequency Dependence of Output Power

The vibration displacement of energy harvester can be maximized in resonance. The harvester will convert mechanical to electric energy most effectively when the applied vibration frequency is closer to the fixed natural frequency of the device. As shown in Figure 1.7, a few percent of mismatched frequency with resonance results in a dramatic decrease of output power. Therefore, tuning or adjusting frequency to an external vibration source is essential in order to improve energy conversion efficiency. From Equation 1.7, the natural frequency of the energy harvester is closely related to dimension and effective mass. The natural frequency of the energy harvester is usually adjusted by changing the weight of proof mass. However, the bandwidth at resonance frequency is usually narrow and thus needs some additional mechanism to effectively capture ambient vibrations which usually represent a wide spectrum of frequencies or time varying vibration spectra.

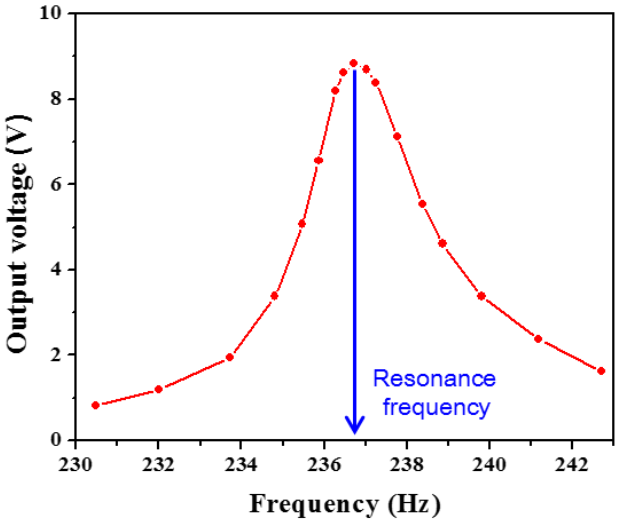

Figure 1.7. Frequency dependent output power of typical vibration energy harvester. The maximum output power can be achieved at resonance frequency.

1.2.4. Vibration Kinematics

Vibration is common ambient energy source that can be found in household appliances (refrigerators, microwave ovens, washing machines etc.), large civil structures (buildings, bridges etc.), industrial plant (refineries), automobiles and many other common locations. Table 1 shows some of the common sources of mechanical energy that can be harnessed through piezoelectrics. Table 2 quantifies the vibration energy available in some of these environments.[9, 10]

Table 1. Sources of energy available in the surrounding which are/can be tapped for generating electricity.

Human body	Vehicles	Structures	Industrial	Environment
Breathing, blood pressure, exhalation, body heat	Aircraft, uav, helicopter, automobiles, trains	Bridges, roads, tunnels, farm house structures	Motors, compressors, chillers, pumps, fans	Wind, solar, temperature gradient, daily temperature
Walking, arm motion, finger motion, jogging, swimming, eating, talking	Tires, tracks, peddles, brakes, shock absorbers, turbines	Control-switch, hvac systems, ducts, cleaners, etc.	Conveyors, cutting g and dicing, vibrating mach.	Ocean currents, acoustic waves, em waves, rf signal

Table 2. Peak acceleration and frequency of common structures. [11, 12]

Vibration Source	Peak acceleration (m/s^2)	Frequency (Hz)
Base of a 5 HP 3-axis machine tool	10	70
Notebook computer while CD is being read	0.6	75
Clothes dryer	3.5	120
Second story floor of a wood frame office building	0.2	100
Railway	1.078 – 1.568	12 - 16
Truck	1.96 - 3.43	8 - 15
Ship	0.98 – 2.45	12 - 13

The general model of a vibration energy harvester is a typical mass-spring-damper system. Maximum power is achieved when the excitation frequency ω is equal to the natural frequency ω_n. Maximum extractable electrical power in terms of mechanical damping ratio ζ_m, electrical damping ratio ζ_e, proof mass m and acceleration A becomes,

$$P = \frac{\zeta_e}{4\omega_n(\zeta_e + \zeta_m)^2} mA^2 \tag{1.9}$$

Several conclusions can be drawn from the observation of Equation 1.9.[13] The extractable power from the beam is inversely proportional to resonance frequency at a fixed acceleration, A; therefore the energy harvester should be designed at lowest possible frequency to achieve highest power if we do not consider that frequencies of external vibration sources are normally fixed in real applications. The extractable power is also proportional to the square of acceleration [14], which limits the energy available for conversion with low-g vibrations whatever the specific design is chosen. It can also be seen that power is proportional to the proof mass, so a large proof mass is always desirable for energy harvesting. Finally, the term

composed of the mechanical and electrical damping ratio implies that the maximum power is achieved when the electrical damping matches the mechanical damping.[15] When the electrical damping is equal to mechanical damping ($\zeta_e = \zeta_m$), the maximum electrical power is given as:

$$P_{e,\max}(w_n) = \frac{mA^2}{16 w_n z_m} = \frac{mY^2 w_n^3}{16 z_m} \tag{1.10}$$

where the acceleration amplitude *A* and proof mass deflection *Y* are related by the relationship given as:

$$A = w_n^2 Y \tag{1.11}$$

Equation (1.10) represents the theoretical maximum of extractable power, which can be dissipated in the electrical load. This is actually a limiting factor for all linear resonator based energy harvesters if the piezoelectric layer's transformation capacity is not a limiting factor. It has been reported that a nonlinear resonator based energy harvester can circumvent this limit and is able to generate much higher power than the mechanical damping, which will be discussed in the later section. Another parameter of interest in design of thin film harvesters is given by the generalized electromechanical coupling (GEMC) factor, k_G^2.[8] The GEMC factor is obtained from the equation:

$$k_G^2 = \frac{\omega_{short}^2 - \omega_{open}^2}{\omega_{short}^2} \tag{1.12}$$

where ω_{short} and ω_{open} are the angular resonance frequencies of the associated short and open circuits, respectively. The GEMC represents the power generation performance of the vibration

harvesters, and this value can be theoretically derived from the mechanical properties, thickness ratio, and electromechanical coupling factors of piezoelectric thin films.[16]

1.2.5. Impedance Matching

Likewise the natural frequency matching with an external vibration source, the impedance of the piezoelectric generator should be matched to that of an external circuit in order to maximize the power extraction. Usually, an electrical impedance matching circuit is placed between the piezoelectric generator and external loads such as a rechargeable battery and supercapacitor. Thus, the matching network should be lossless and requires that the input impedance should be matched to the output impedance. Equation 1.13 shows the mechanical input impedance of the energy source generated by the piezoelectric harvester.

$$\boldsymbol{Z = \frac{1}{2\pi\omega \cdot C_0}} \tag{1.13}$$

where $\boldsymbol{\omega}$ is vibration frequency of energy harvester, C_0 is capacitance of piezoelectric materials. The impedance matching circuit can be consisted of load resistors in accordance with the impedance of the piezoelectric generator calculated by Equation 1.13.

References

[1] S. Priya, and D. J. Inman, *Energy harvesting technologies*: Springer, 2009.

[2] S. P. Beeby, M. J. Tudor, and N. White, "Energy harvesting vibration sources for microsystems applications," *Measurement science and technology,* vol. 17, no. 12, pp. R175, 2006.

[3] Z. L. Wang, and J. Song, "Piezoelectric nanogenerators based on zinc oxide nanowire arrays," *Science,* vol. 312, no. 5771, pp. 242-246, 2006.

[4] A. Minnich, M. Dresselhaus, Z. Ren, and G. Chen, "Bulk nanostructured thermoelectric materials: current research and future prospects," *Energy & Environmental Science,* vol. 2, no. 5, pp. 466-479, 2009.

[5] D. Findeisen, *System dynamics and mechanical vibrations: an introduction*: Springer Science & Business Media, 2013.

[6] J. H. Ginsberg, and J. H. Ginsberg, *Mechanical and structural vibrations: theory and applications*, 2001.

[7] L. Jiang, and R. Miles, "A passive damper for the vibration modes of the head actuator in hard disk drives," *Journal of sound and vibration,* vol. 220, no. 4, pp. 683-694, 1999.

[8] K. Uchino, *Ferroelectric Devices 2nd Edition*: CRC press, 2009.

[9] A. Marin, and S. Priya, "Multi-mechanism vibration harvester combining inductive and piezoelectric mechanisms." pp. 83411L-83411L-11.

[10] S. Priya, "Advances in energy harvesting using low profile piezoelectric transducers," *Journal of electroceramics,* vol. 19, no. 1, pp. 167-184, 2007.

[11] E. E. Aktakka, "Integration of bulk piezoelectric materials into microsystems," The University of Michigan, 2012.

[12] B. Lee, S. Lin, W. Wu, X. Wang, P. Chang, and C. Lee, "Piezoelectric MEMS generators fabricated with an aerosol deposition PZT thin film," *Journal of Micromechanics and Microengineering,* vol. 19, no. 6, pp. 065014, 2009.

[13] R. Xu, "The design of low-frequency, low-g piezoelectric micro energy harvesters," Massachusetts Institute of Technology, 2012.

[14] A. Chandrakasan, R. Amirtharajah, J. Goodman, and W. Rabiner, "Trends in low power digital signal processing." pp. 604-607.

[15] N. E. Dutoit, B. L. Wardle, and S.-G. Kim, "Design considerations for MEMS-scale piezoelectric mechanical vibration energy harvesters," *Integrated Ferroelectrics,* vol. 71, no. 1, pp. 121-160, 2005.

[16] Q.-M. Wang, X.-H. Du, B. Xu, and L. E. Cross, "Electromechanical coupling and output efficiency of piezoelectric bending actuators," *Ultrasonics, Ferroelectrics, and Frequency Control, IEEE Transactions on,* vol. 46, no. 3, pp.

2. Chapter 2: Growth of Piezoelectric $PbTiO_3$ Nanofiber Arrays on Rutile Seed Crystals

2.1. Introduction

Over the past few decades, one-dimensional (1-D) piezoelectric nanomaterials including nanorods[1-3], nanotubes[4], nanobelts[5] and nanofibers[6] have been studied extensively because of their unique physical and chemical properties such as a large surface area[7], excellent charge transport[8, 9], high electro-mechanical coupling[10] and superior ferroelectric properties[11]. One-dimensional nanostructures have high aspect ratio and anisotropic geometry that can provide higher sensitivity as compared to planar configurations.[12] Further, one-dimensional piezoelectric nanostructures are promising candidates for nonvolatile memory[13, 14], pressure sensors[12, 15-18], actuators[19], bio-interfaced mechanical probes[20] and nanogenerators.[21-27] In this paper, we report one-dimensional epitaxial piezoelectric nanofiber arrays grown through a rutile template and provide their growth mechanism.

Among the piezoelectric nanomaterials, semiconducting ZnO nanowire is the most extensively studied material over the past decade. Single crystal vertically aligned ZnO nanowire can be grown with preferred direction and without any seed layer owing to its hexagonal Wurtzite structure. However, the piezoelectric constant (d) of ZnO (d_{33} = ~26.7 pm/V) is low compared to typical piezoelectric materials with perovskite structure.[28] Thus, there is desire to fabricate the piezoelectric nanostructures having perovskite crystal structure and exhibiting high piezoelectric properties from compositions such as $PbTiO_3$, $Pb(Zr,Ti)O_3$, $Pb(Mg,Nb)O_3$–$PbTiO_3$, $BaTiO_3$, $KNbO_3$ etc. Among these different perovskite piezoelectric materials, $PbTiO_3$ (PTO) has some appealing characteristics such as a low aging rate of the

dielectric constant, a high voltage constant (g), and a high Curie temperature of 490 ^{o}C.[29, 30] Also, PTO has high tetragonality (c:a ratio of 1.063) which can provide a low ratio for the planar-to-thickness coupling factor.[31] However, the high tetragonality also makes PTO ceramics difficult to synthesize via conventional high temperature synthesis. As PTO undergoes the ferroelectric phase transition at the Curie temperature, it experiences a large expansion in crystal c-direction and contractions in the two orthogonal crystal directions during cooling from high temperature and these strains generate internal stress and cause micro cracks.[32] It has been suggested that these problems can be avoided by fabricating PTO phase below the phase transition, under 490 ^{o}C, through low temperature synthesis routes.[33]

A number of studies on $PbTiO_3$ nanostructures have been reported, however, in most cases the material was randomly oriented polycrystalline phase[34-36], or in powder form if synthesized as single crystalline phase.[37-41] Only limited number of studies have been conducted on vertically aligned crystals grown on semiconducting or metallic substrates.[42, 43] A vertically aligned piezoelectric nanostructure array can offer many advantages such as enhanced mechanical to electrical energy conversion efficiency and facilitate the fabrication of devices such as nanogenerators and sensors. Moreover, the growth mechanism in terms of single crystal PTO nanostructures through TiO_2 seed crystals has not been cleary verified yet.

Here, we report the epitaxial growth of vertically aligned PTO nanofibers array on a Ti metal substrate coated with a rutile TiO_2 seed layer. High quality single crystal $PbTiO_3$ nanofibers oriented along the [100] PTO direction were obtained on an (110) oriented TiO_2 seed layer using a low temperature hydrothermal synthesis technique. The seed layer was established by electrolytic polishing Ti foil, spin coating sol-gel TiO_2 seed crystals, and annealing under controlled conditions. The vertically aligned PTO nanofiber arrays were densely packed and grown over a large area of the TiO_2/Ti foil substrate. The crystalline phase, orientation, and morphology of the PTO nanofibers were confirmed with high resolution transmission electron

microscopy (HRTEM) and scanning electron microscopy (SEM). Furthermore, a systematic study of the growth mechanism of PTO nanofiber through rutile TiO_2 seed layer is provided by crystallographic matching between PTO and TiO_2 atomic surfaces by computational simulation.

2.2. Experimental

2.2.1. Electrolytic Polishing Ti Foil

Titanium foils (99.99% pure, Sigma-Aldrich) were mechanically polished to a mirror finish and ultrasonically cleaned in Micro-90 clean solution, sequentially rinsed with acetone, isopropanol, and methanol prior to electrolytic polishing. Titanium anode and platinum cathode sheets 1 cm × 1 cm in size were electropolished at ~1 °C in an agitated solution of glacial acetic acid /perchloric acid (9/1 volume ratio) at 55 V for roughly 2 min.[44] The polished Ti surface was examined with SEM to assess the topography of the electropolished foil surface.

2.2.2. TiO_2 Seed Layer Growth

The TiO_2 sol-gel solution for the seed layer was prepared using a previously reported process.[44] About 369 μL of titanium isopropoxide (99.99% pure, Sigma-Aldrich) was mixed with 2.53 mL of ethanol. In a separate vial, 35 μL of 2 M HCl solution (99% pure, Sigma-Aldrich) was added to 2.53 mL of ethanol. This HCl solution was then added dropwise to the titanium isopropoxide solution under 500 rpm stirring for 1 h and then the mixture was filtered by using a PTFE 0.2 μm filter. The prepared TiO_2 sol-gel solution was spin coated on the mechanically polished Ti plates at 6000 rpm for 60 s. After drying at 120 °C for 10 min, the TiO_2 films were annealed at 450 °C, 650 °C and 800 °C for 10 min, respectively. The annealing was carried in air at atmospheric pressure in the tube furnace. The morphology and structure of the annealed films were examined with FESEM (LEO 1550) and XRD (Bruker D8 advance).

2.2.3. $PbTiO_3$ Nanofiber Growth by Hydrothermal Synthesis

Chemical grade tetrabutyl titanate $(C_4H_9O)_4Ti$ and lead nitrate $Pb(NO_3)_2$ were used as reactants and potassium hydroxide (KOH) was employed as a mineralizer. Poly(vinyl alcohol)(PVA) and Poly(acrylic acid) (PAA) were added as a polymer surfactant to facilitate one dimensional growth. Firstly, $(C_4H_9O)_4Ti$ was distilled with a high purity ethanol under 200 rpm stirring for 10 min. Next this solution was precipitated in a 0.1 M ammonia solution. The precipitate was filtered and washed with distilled D.I. water for 10 min in order to remove ammonium ions and ethanol. The $TiO(OH)_2$ precipitate was re-dispersed with 50 ml D.I. water to a 0.1M concentration and a stoichiometric amount of $Pb(NO_3)_2$ was added to this aqueous solution with vigorous stirring. Pellets of KOH were slowly introduced to a 2M concentration. Finally, the polymer components, 0.02g PVA and 0.4g PAA, were added to the solution and stirred for more than 12 hours. Hydrothermal synthesis was performed in a stainless autoclave with a 23 ml volume Teflon vessel (Parr Instrument Company). Titanium foil with the TiO_2 seed layer was vertically suspended in the solution from a Teflon holder. The Teflon vessel was filled with 20 ml of hydrothermal solution, sealed in a stainless steel autoclave and placed in a low temperature furnace at 225 °C for 12 hours. After cooling to room temperature, the synthesized specimens were washed several times with D.I. water and high purity ethanol (99.9%) and dried in the air. The fabricated piezoelectric nanostructures were characterized by XRD (Bruker D8 advance), FESEM (LEO 1550), HRTEM (FEI Titan 300), and PFM (Bruker).

2.3. Results and Discussion

2.3.1. $PbTiO_3$ Nanostructure on Rutile TiO_2 Seeds

A schematic of the sequence of the fabrication process of PTO fibers array is depicted in Figure 2.1 (a). We started with a titanium foil with mirror like flat surface prepared by

mechanical and electrolytic polishing for the vertical alignment of PTO nanofibers on the Ti foil. Prior to the electrolytic polishing, the mechanically polished Ti foil was cleaned by ultrasonication. The electrolytic polishing was conducted at low temperature (below 1^{o}C) in consideration of the polishing plateau to broaden with decreasing temperature.[45] Figure 2.1 (b) shows SEM image of the electrolytic polished surface of the Ti foil and a quite flat surface with very small plateaus was obtained. The TiO_2 thin film was deposited on the polished Ti foil via sol-gel process for seeding epitaxial PTO growth and annealed at 700^{o}C for a short time (5 min) to obtain desired rutile TiO_2 thin film without excessive oxidation of Ti substrate. The surface SEM image of the deposited TiO_2 is depicted in Figure 1c and it shows a quite flat and clean surface. It is interesting to note that grain like section was observed as indicated by white dash line in Figure 2.1 (c). There are also boundaries between each sections which have different TiO_2 grain sizes. The formation of these sections could be related to grains of Ti substrate under TiO_2 seed layer. The different grain size of TiO_2 depending on sections could be attributed to orientation dependent grain growth rate governed by the surface of Ti foil. The actual grain size of TiO_2 seeds was approximately from 20 nm to 50 nm with respect to different grain sections as indicated by white arrows in Figure 2.1 (c). Using this TiO_2/Ti substrate, PTO nanofibers were synthesized hydrothermally at 225^{o}C for 12 hours. The vertically well aligned $PbTiO_3$ dense nanofiber array were obtained as shown Figure 2.1 (d) by small size grain seeding. The mean diameter and length of $PbTiO_3$ nanowire were measured from a magnified SEM image and was found to be approximately 200 nm and 10 μm, respectively. The aspect ratio (c/a) of the $PbTiO_3$ nanowires was mostly larger than 50 which can be controlled by adjusting PVA/PAA surfactant ratio and quantity.[46] Furthermore, we can fabricate vertically aligned $PbTiO_3$ nanofiber arrays on the considerably large dimension through formation of homogenous TiO_2 seed layer on Ti foil as shown in Figure 2.2 (a) and (b).

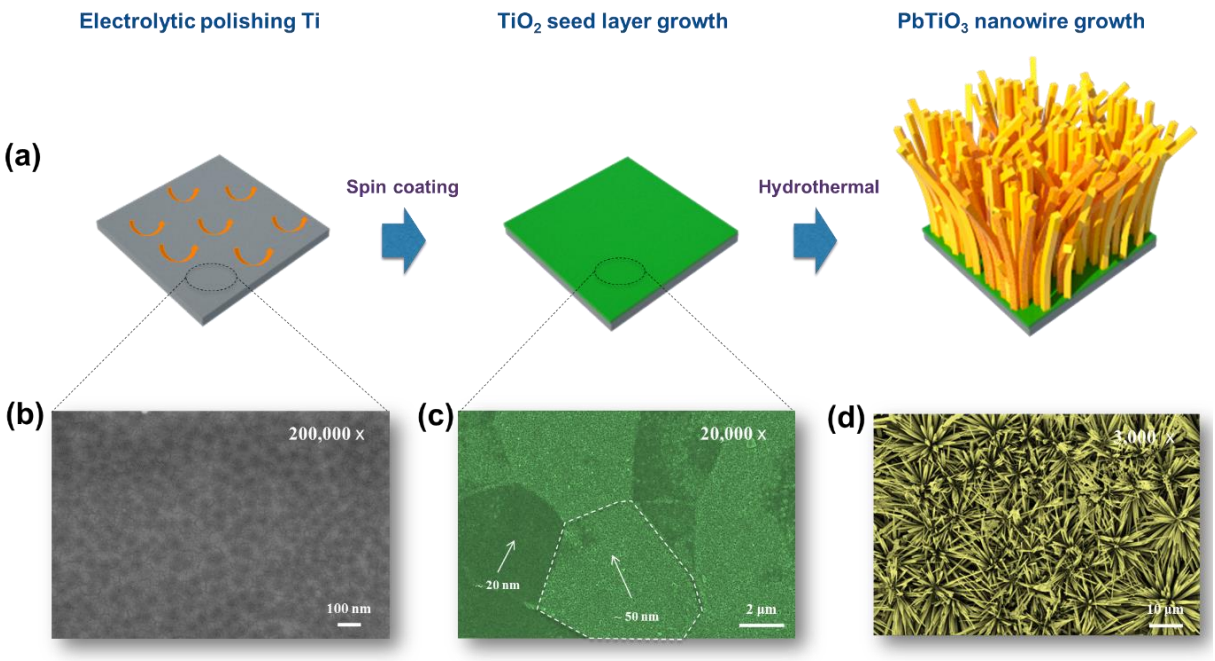

Figure 2.1. (a) Schematic illustration of fabrication process of $PbTiO_3$ nanofibers on Ti substration with rutile TiO_2 seed layer. (b) Surface SEM image of electrolytic polished Ti foil. (c) Surface SEM image of TiO_2 seed layer on Ti foil annealed at 700 ºC for 5 minutes. (d) Vertically grown $PbTiO_3$ nanofiber arrays on TiO_2(Rutile)/Ti substrate by hydrothermal synthesis.

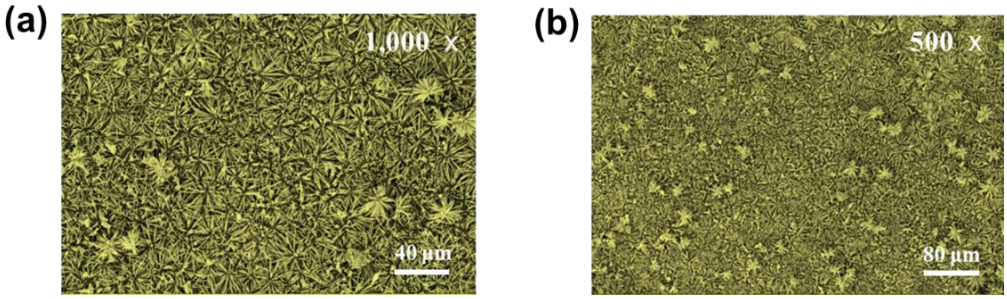

Figure 2.2. Vertically grown $PbTiO_3$ nanofiber arrays on the considerably large area of TiO_2/Ti substrate in (a) 1,000 and (b) 500 times magnification.

From our experimental results, the seed layer of TiO_2 plays important role in growth of single crystal PTO nanofibers in case of solution-based synthesis. Generally, the template has very similar crystal structure as the phase being targeted. In case of TiO_2, however, the atomic structure is quite different from the PTO perovskite, and thus we need to understand why the

TiO_2 template layer can provide an epitaxial growth for PTO nanofiber. Firstly, in order to investigate the growth mechanism, we carried out 3-dimensional crystal structure matching between interface of PTO and TiO_2 atomic surfaces using computational simulation. In case of TiO_2 crystal structure, a rutile phase was selected owing to the most similarity with PTO perovskite structure among several polymorphic TiO_2 phases. Through simulation of random orientation relationships between PTO and rutile TiO_2 stucrues, the best matching orienation were found to be: $(0\ 0\ 1)_{Rrutile}$ // $(0\ -1\ 0)_{PTO}$ and $(1\ 0\ -1)_{Rutile}$ // $(1\ 1\ 0)_{PTO}$. However, (110) orientation is mostly prefered growth direction in typical condtions because the surface entropy of the (110) surface is known to be much smaller than those of the (001) and (101) surfaces ((10-1) and (101) have same surface entropy). The calculated surface energy values of (110), (100) and (101) are 2.61 J/m^2, 3.69 J/m^2 and 4.33 J/m^2, respectively.[47] Taking into account the consideration that (110) facet is the most stable surface, we fixed rutile TiO_2 orientation as (110) facets. The atomic structures of O-terminated rutile TiO_2 (110) and Ti-terminated PTO (001) surfaces which are the most plausible interface in a lattice match are presented in Figure 2.3 (a). The top-view of interface between rutile TiO_2 (110) and Ti-terminated PTO (001) surfaces are depicted in Figure 2.3 (b). The blue and red balls are titanium and oxygen atoms in the rutile TiO_2 and the light blue and pink balls are titanium and oxygen atoms in the PTO, respectively. Along the horizontal direction, six Ti atoms in $(0\ -1\ 0)_{PTO}$-type planes approximately matched seven Ti atoms in $(-1\ 1\ 0)_{Rutile}$-type planes. Similarly, along the vertical direction, four Ti atoms in $(0\ -1\ 0)_{PTO}$-type planes correspond to five Ti atoms in $(-1\ 1\ 0)_{Rutile}$-type planes. While a PTO thin film on ruitle TiO_2 is constrained laterally due to the lattice misfits during growth, a nanofiber can relieve the strain energy through lateral relaxation.[48] Thus, we can expect that one dimensional PTO nanofibers can be grown dislocation-free single crystals more readily than two dimenstional PTO thin films. The lattice matched O-terminated

Ti sites in rutile TiO_2 can play important role in nucleation that drives the epitaxial growth of the [001] orientation of PTO nanofibers.

At elevated temperature and pressure of hydrothermal conditions, the nuclei of crystalline PTO can be formed at the lattice matched site on the rutile TiO_2 by precipitation of the solute ions according to following reaction:

$$HPbO_2^-(\text{aqueous}) + Ti(OH)_y^{4-y}(\text{aqueous}) \rightarrow PbTiO_3 + 2H_2O$$

The PTO crystalline nuclei grow and gradually evolve to a facet nanocrystal with cube shape. The dissolved ions re-precipitate on surfaces of the nanocrystal grown in all direction except a conjoined facet. When the nanocrystal reaches a certain diameter and thickness, the growth of PTO crystal is temporarily hindered by adsorption of surfactants (PVA/PAA) on the surface by hydrogen boding. The surfactant encapsulation of exposed (001) facet which has the lowest surface energy can be broken in order to create chemical bonding with growth components, while the other facets are hindered by steric surfactant due to surface energy differences. Because of big difference of growth rate with respect to orientations, the nanocrystals on nucleation sites can be elongated and lead to nanofiber growth. Additionally, the presence of dipole in the growth components is able to facilitate one dimensional growth in [001] dipole direction by dipole induced attractions.[49] The nanofiber growth is accomplished by reduction of the concentration of the growth components until equilibrium is reached.

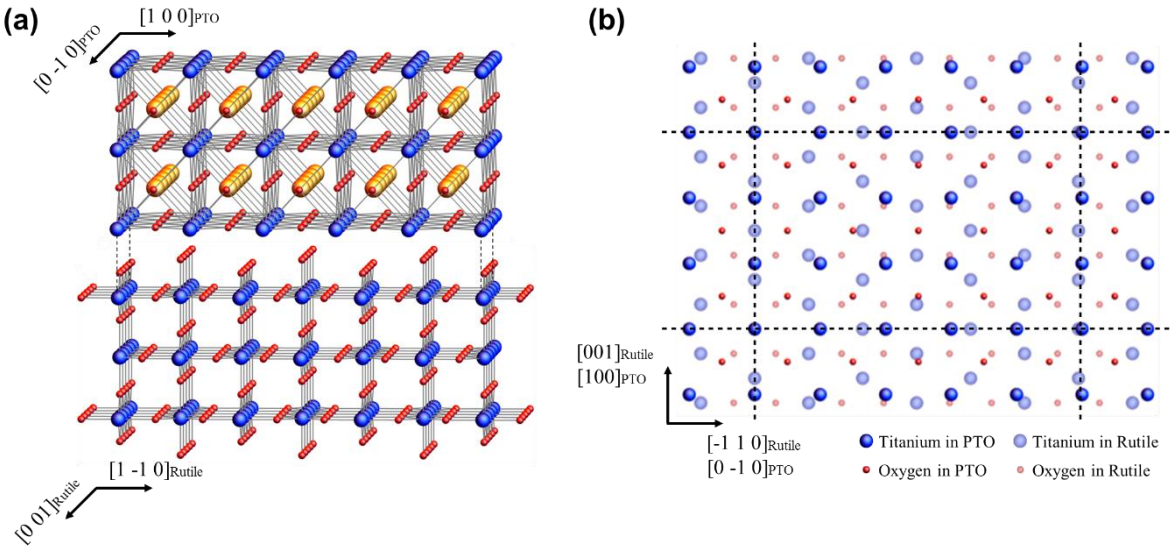

Figure 2.3. (a) 3-D atomic structures of interface of TiO_2 (110) Rutile and $PbTiO_3$ (001) surfaces. (b) Schematic illustration of in-plane atomic structure between $(110)_{Rutile}$ and $(001)_{PTO}$ surfaces which are in parallel. Along the horizontal direction, six Ti atoms in $(0\ -1\ 0)_{PTO}$ -type planes match seven Ti atoms, $(-1\ 1\ 0)_{Rutile}$ -type planes. Similarly, along the vertical direction, four Ti atoms, $(0\ -1\ 0)_{PTO}$-type planes correspond to five Ti atoms in $(-1\ 1\ 0)_{Rutile}$-type planes. Blue or light blue ball: Ti; red of pink ball: O; yellow ball: Pb.

To validate the simulation results for lattice matching of the rutile (110) TiO_2 and (001) PTO, we fabricated PTO nanofibers with varying TiO_2 phases by changing annealing temperature. Figure 6.4 (a) shows the X-ray diffraction (XRD) patterns of TiO_2 seed layers on Ti foil after annealing at different temperature. The TiO_2 films were fabricated via sol-gel chemical solution technique and annealed at 450 ^oC, 650 ^oC and 800 ^oC for 10 min, respectively. To prevent excess oxidation of the Ti foil substrate under TiO_2 seed layer, the specimens were also quickly cooled to room temperature in air atmosphere by taking them out of the furnace as soon as the annealing process was over. Rutile TiO_2 phase was formed above 650 ^oC annealing temperature as shown in XRD pattern in Figure 2.4 (a). With increasing annealing temperature from 650 ^oC to 800 ^oC, the intensity of the XRD peak was considerably increased which is related to the crystallinity of rutile TiO_2 film. As shown in Figure 2.4 (a). the (110) orientation peak is the

most dominant which indicates that the TiO_2 film on Ti foil annealed at 800 ^oC has a (110) preferred orientation and 96% texturing along this orientation (calculated by peak instensity comparison). This corresonds to previously reported results that (110) facet is the most stable for a rutile TiO_2.[50, 51] The TiO_2 film annealed at 450 ^oC for 10 min did not show any other perceptible XRD peaks except the Ti substrate peaks. This might be because annealing time is too short to form the anatase phase at low temperature. The XRD results well correspond with the known TiO_2 phase diagram with respect to temperature and pressure as shown in Figure 2.4 (b).

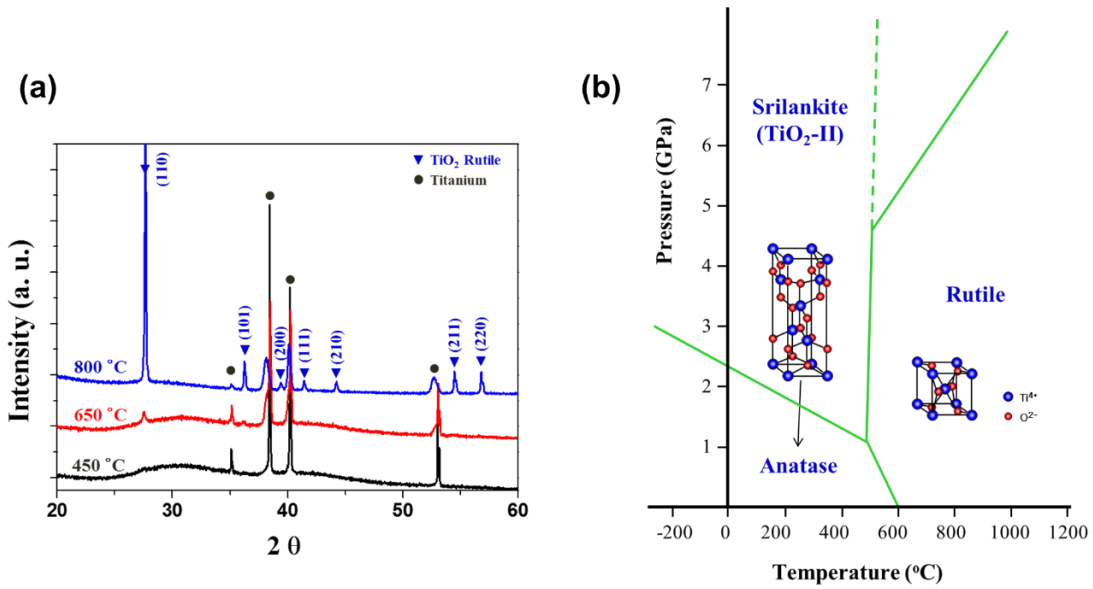

Figure 2.4. (a) XRD patterns of TiO_2/Ti substrate annealed at 450 ^oC, 650 ^oC and 800 ^oC. (b) TiO_2 phase diagram with temperature and pressure (Reproduced with permission.[52] 2000, Springer).

Surface scanning electron microscopy images of Figure 2.5 (a), (b) and (c) show the TiO_2 seed layer deposited on the mechanically polished Ti foils annealed at 450 ^oC, 650 ^oC and 800 ^oC for 10 min, respectively. The TiO_2 film annealed at 450 ^oC shows no tangible grains which is consistent with the XRD data of Figure 2.5 (a). The average grain size of the TiO_2 films was determined from a magnified SEM images (Figure 2.6 (a), (b) and (c)) and found to be 50 ~ 200 nm at 650 ^oC and 200 ~ 500 nm at 800 ^oC, respectively. Despite same material and

annealing condition, the different mean grain size was observed according to the sections indicated by white arrows in Figure 4b. With increasing annealing temperature to 800 ^{o}C, the grain size of TiO_2 was significantly increased and abnormal grain growth was also observed as indicated by white circles in Figure 2.6 (c). Figure 2.5 (d), (e) and (f) show surface SEM images of PTO nanofibers grown on Figure 2.5 (a), (b) and (c) TiO_2 templates by hydrothermal reaction at 225 ^{o}C for 12 hours. As expected, TiO_2 phase formed at low temperature did not achieve one dimensional PTO nanostructure. On the other hand, the hydrothermal growth using the rutile TiO_2 seed layers formed above 650 ^{o}C resulted in a bush-like $PbTiO_3$ nanostructures as shown in Figure 2.5 (e) and (f). A relatively rough surface and abnormal grain growth of the TiO_2 layer without electrolytic polishing resulted in the formation of the bush-like nanostructures instead of vertically aligned. Inset figures of Figure 2.5 (e) and (f) show magnified SEM images of the bush-like $PbTiO_3$ nanostructures with the rutile TiO_2 seed layers annealed at 650 ^{o}C and 800 ^{o}C, respectively. The length and density of the bushes further increased with increasing annealing temperature of TiO_2 seed. Each nanofiber has rectangular cross-sectional shape. The nanofiber at 650 ^{o}C of TiO_2 seeding showed a larger mean diameter of ~ 400nm than that of 800 ^{o}C TiO_2 seeding of ~ 250 nm. The close packed nucleation sites obstruct the planar direction growth of nanofiber and have smaller diameter. Thus, dense $PbTiO_3$ nano bushes would have smaller diameter of nanofiber. From the XRD patterns for TiO_2 seed layer and SEM image for $PbTiO_3$ nanofibers, we can clearly confirm that only rutile TiO_2 seed layer would serve as suitable seed to guide the growth of the $PbTiO_3$ nanorods.

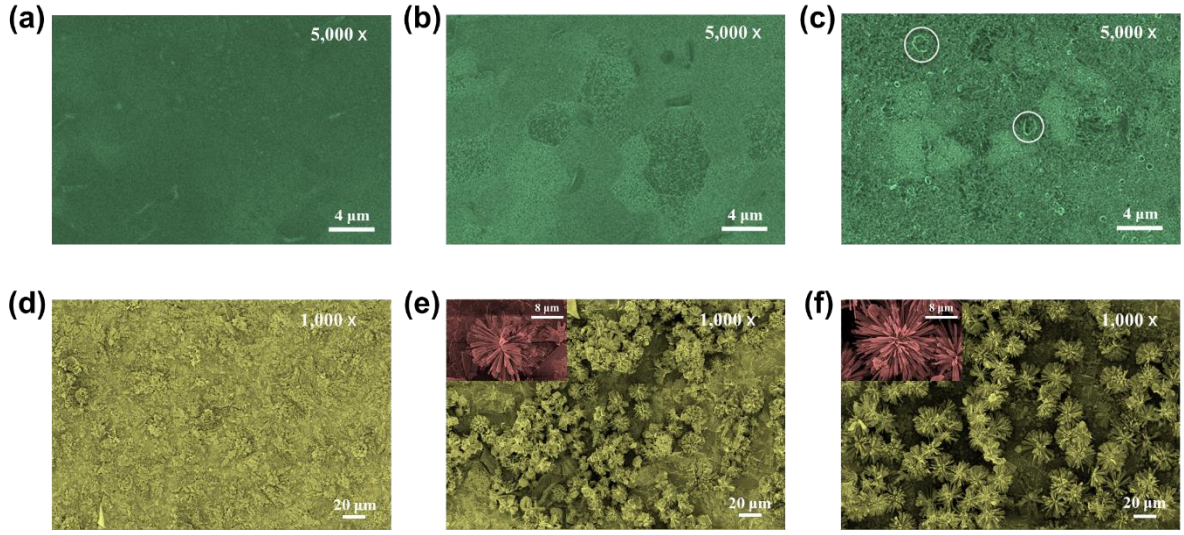

Figure 2.5. Surface SEM images of TiO_2 seed layers on Ti plate annealed at (a) 450 ºC, (b) 650 ºC and (c) 800 ºC for 10 minutes. SEM images of $PbTiO_3$ nano rods grown on TiO_2/Ti substrates annealed at (d) 450 ºC , (e) 650 ºC and (f) 800 ºC for 10 minutes by hydrothermal synthesis at 225 ºC for 12 hours. Insets are magnified images of $PbTiO_3$ nano rods.

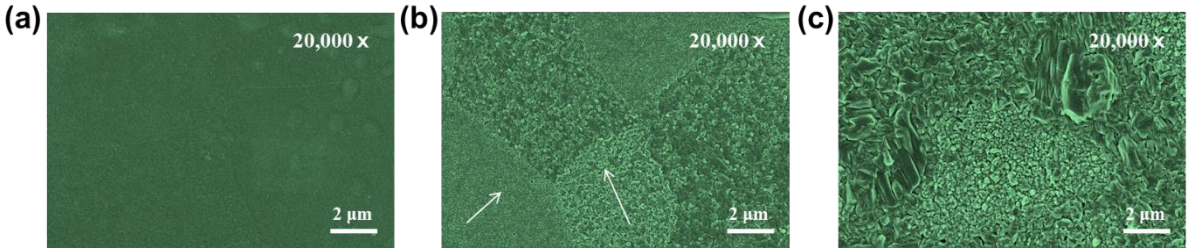

Figure 2.6. Surface SEM images of TiO_2 seed layers on Ti foils annealed at (a) 450 ºC, (b) 650 ºC and (c) 800 ºC for 10 minutes.

Further morphological and structural characterizations of the PTO nanofiber arrays were performed using transmission electron microscopy (TEM). Figure 2.8 (a) and (b) shows the typical TEM images of PTO nanofibers with 200 nm in diameter which coincide with the SEM observation. As shown in Figure 2.8 (a) ~ (c), individual PTO nanofibers have same lattice fringes along growing direction and no grain boundaries, defects, and dislocations. Interestingly, the dark line was observed in the middle of nanowire along longitudinal direction.

This contrast line could be a ferroelectric domain similar to that observed in PZT nanowire.[53] This ferroelectric domain is the strong evidence that the PTO nanofibers have ferroelectric characteristics. The TEM results confirmed that the PTO nanofiber is single crystalline across its entire length and grows along the [100] direction. This result also closely agrees with XRD pattern of the PTO nanofiber arrays on TiO_2/Ti foil as depicted in Figure 2.8 (d). The XRD patterns in Figure 2.8 (d) exhibit very sharp diffraction peaks indicating that the samples are well crystallized. All of the diffraction peaks can be indexed as the tetragonal perovskite structure of PTO which was in exactly agreement with that of JCPDS Card No. 77-2002. This confirmed that the fabricated PTO nanowire arrays have a single perovskite structure without the trace of any second phases. In addition, as shown EDS analysis of Figure 2.8, we can verify that the nanofibers are stoichiometrically equivalent to $PbTiO_3$ phase. The high resolution TEM image in Figure 2.8 (c) shows the clear lattice fringes, which indicates that the $PbTiO_3$ nanowires are structurally uniform and well crystallized. The observed lattice-fringe distances of 3.87 Å is in agreement with the d-spacing of the tetragonal (101) plane. The selected area electron diffraction (SAED) pattern (Figure 2.8 (c) inset) shows clear diffraction spots of PTO crysalline obtained from nanowire region in Figure 2.8 (c), which unambiguously confirms the single crystalline nature of the nanowires.

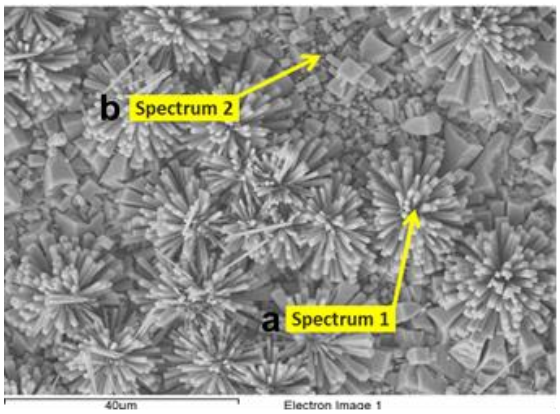

a. Spectrum 1 (Nanorods)

Element	Atomic %
O	55.3
Ti	22.76
Pb	22.21

b. Spectrum 2 (Bottom)

Element	Atomic %
O	59.48
K	2.23
Ti	19.76
Pb	18.53

Figure 2.7. EDS analisys taken at (a) $PbTiO_3$ nanorods and (b) bottom region

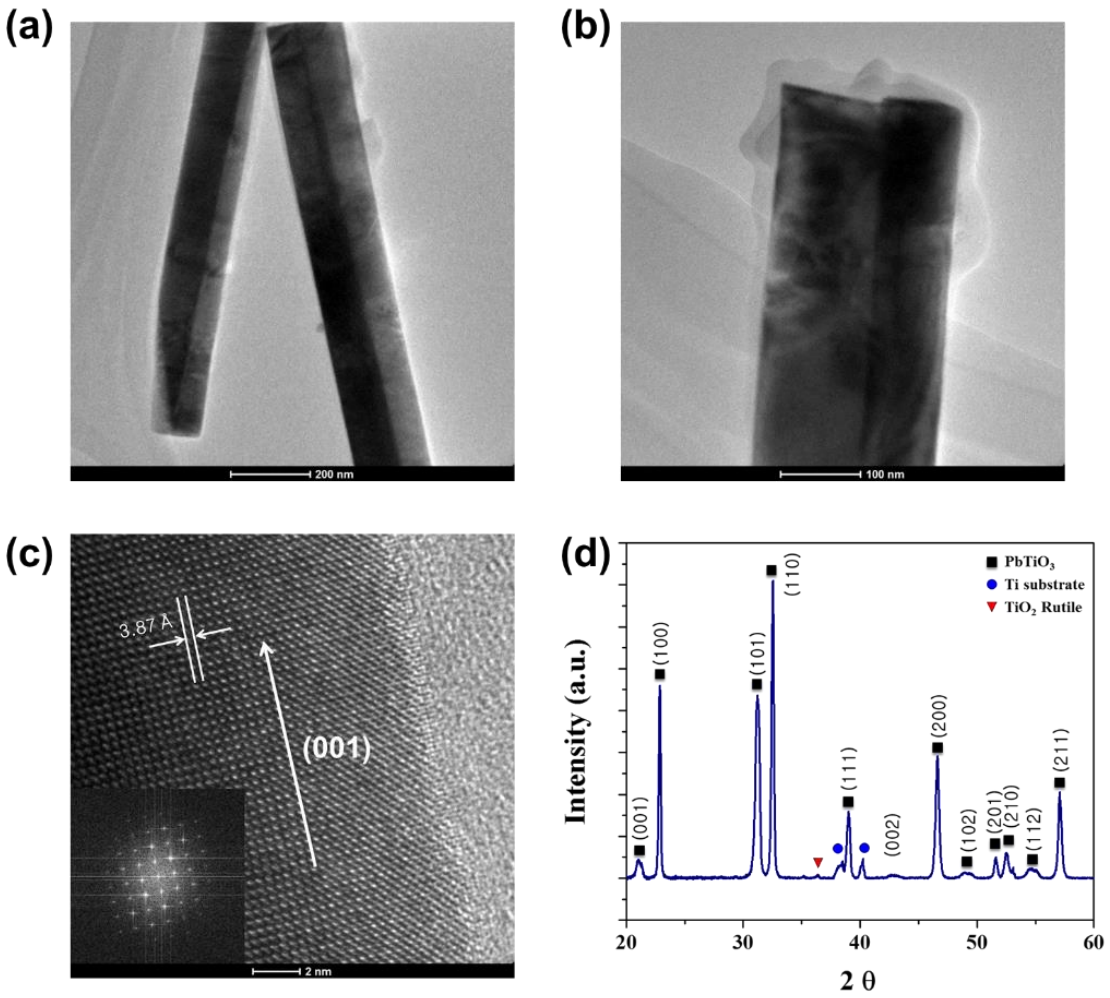

Figure 2.8. TEM images and XRD patterns of $PbTiO_3$ nanofibers hydrothermally grown on TiO_2/Ti substrate at 225 ^oC for 12 hours. (a) and (b) TEM images of individual $PbTiO_3$ nanofiber. (c) HRTEM image and SAED pattern (inset) of outside edge of $PbTiO_3$ fiber. (d) XRD patterns of $PbTiO_3$ nanofibers grown on Ti substrate with Rutile TiO_2 seeding.

For further survey of vibrational modes in PTO nanofibers, a Raman scattering investigation was performed at various temperature. The Raman scattering spectrum of PTO nanofibers recorded at room temperature (20 ^oC) is shown in Figure 2.9. All Raman modes of the PTO nanofibers were indexed based on the earlier study of Burns and Scott.[54] The frequency of Raman lines in the nanofiber agrees well with the previously reported typical spectra of the tetragonal PTO phase.[55, 56] At room temperature, PTO have tetragonal unit cells of P4mm point group symmetry and the zone-center optical phonons are grouped as: five A_1, six E, and

one B_1 symmetry, all of which are Raman active. One of soft phonon modes, E(1LO) was observed in 124.4 cm^{-1} which indicates the nanofibers are polar at room temperature. The Raman spectra of PTO nanofibers with variation of temperature from 400 ^oC to 500 ^oC are shown in inset of Figure 2.9. As increasing temperature, the Raman lines downshift and significanly broadened comparing of the room temperature spectrum. At 450 ^oC, the intensity of the Raman lines dramatically reduced and almost vanished at 500 ^oC. The result indicates the tetragonal-to-cubic phase transition (Ferroelectric-to-paraelectric) was occured between 450 ^oC ~ 500 ^oC which is in accordance with previous Raman study and typical Curie temperature of PTO.[57] It is concluded that this ferroelectric transition is clearly evidence of ferroelectric behavior of the PTO nanofiber.

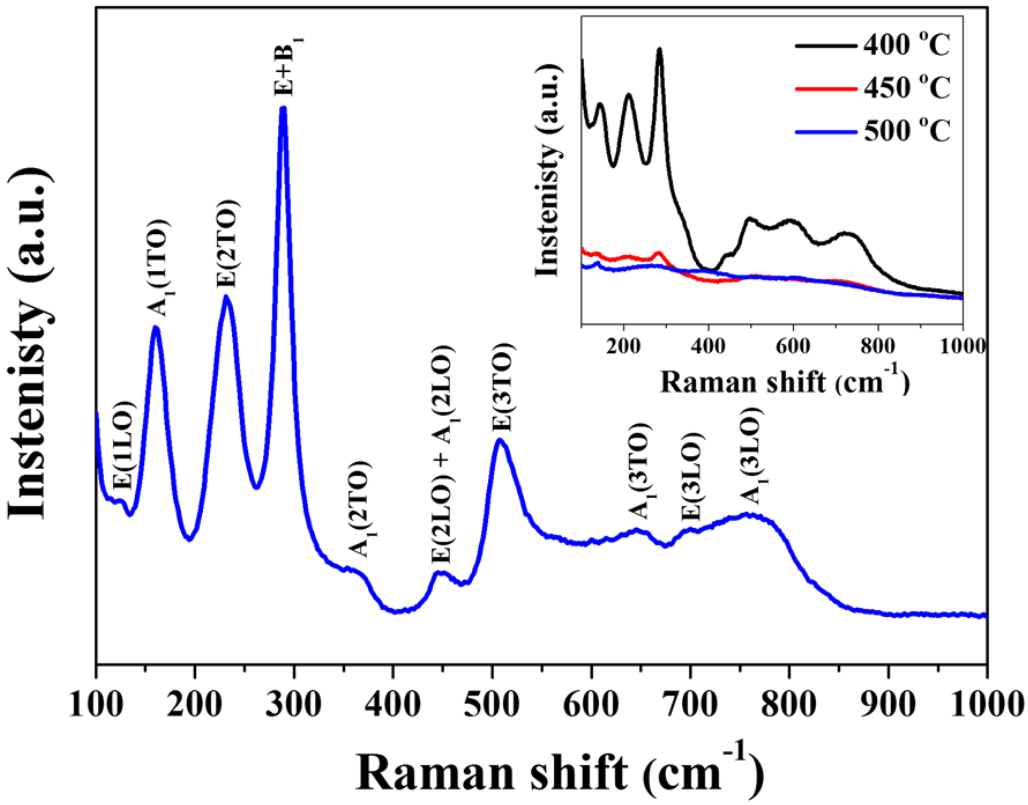

Figure 2.9. Raman spectra of $PbTiO_3$ nanofibers at room temperature. Inset is Raman spectra of $PbTiO_3$ nanofibers in the vicinity of Curie temperature (400 ^oC, 450 ^oC and 500 ^oC).

2.4. Summary

In summary, vertically aligned single crystal PTO nanofiber arrays have been demonstrated on metal Ti substrate via rutile TiO_2 seeding. From crystal surface matching simulation, rutile TiO_2 (110) and PTO (001) surfaces are the best fitting interface. The six Ti atoms in $(0\ -1\ 0)_{PTO}$ and four Ti atoms in $(0\ -1\ 0)_{PTO}$ planes are matched with seven Ti atoms in $(-1\ 1\ 0)_{Rutile}$ and five Ti atoms in $(-1\ 1\ 0)_{Rutile}$-type planes, respectively. The lattice matched plane could be a nucleation site to induce an epitaxial nanofiber growth. Furthermore, the experimental results confirm that only rutile phase TiO_2 template can give rise to the PTO nanofiber epitaxial growth and the (110) orientation of rutile TiO_2 of the most stable facet can provide (100) direction growth of PTO nanofibers. We have investigated the growth mechanism of $PbTiO_3$ nanowires experimentally and theoretically, which has a broader appeal, as it can be readily extended to real application of piezoelectric nanofibers.

References

[1] S. Xu, Y.-w. Yeh, G. Poirier, M. C. McAlpine, R. A. Register, and N. Yao, "Flexible piezoelectric PMN–PT nanowire-based nanocomposite and device," *Nano letters,* vol. 13, no. 6, pp. 2393-2398, 2013.

[2] S. J. Limmer, S. Seraji, Y. Wu, T. P. Chou, C. Nguyen, and G. Z. Cao, "Template-based growth of various oxide nanorods by sol-gel electrophoresis," *Advanced Functional Materials,* vol. 12, no. 1, pp. 59-64, 2002.

[3] M. Y. Choi, D. Choi, M. J. Jin, I. Kim, S. H. Kim, J. Y. Choi, S. Y. Lee, J. M. Kim, and S. W. Kim, "Mechanically powered transparent flexible charge-generating nanodevices with piezoelectric ZnO nanorods," *Advanced Materials,* vol. 21, no. 21, pp. 2185-2189, 2009.

[4] A. Bernal, A. Tselev, S. Kalinin, and N. Bassiri-Gharb, "Free-Standing Ferroelectric Nanotubes Processed via Soft-Template Infiltration," *Advanced Materials,* vol. 24, no. 9, pp. 1160-1165, 2012.

[5] F. Wu, W. Cai, Y.-W. Yeh, S. Xu, and N. Yao, "Energy scavenging based on a single-crystal PMN-PT nanobelt," *Scientific reports,* vol. 6, 2016.

[6] J. Chang, M. Dommer, C. Chang, and L. Lin, "Piezoelectric nanofibers for energy scavenging applications," *Nano Energy,* vol. 1, no. 3, pp. 356-371, 2012.

[7] Z. L. Wang, "Piezoelectric nanostructures: From growth phenomena to electric nanogenerators," *MRS bulletin,* vol. 32, no. 02, pp. 109-116, 2007.

[8] Z. L. Wang, X. Y. Kong, Y. Ding, P. Gao, W. L. Hughes, R. Yang, and Y. Zhang, "Semiconducting and piezoelectric oxide nanostructures induced by polar surfaces," *Advanced Functional Materials,* vol. 14, no. 10, pp. 943-956, 2004.

[9] Y. Xia, P. Yang, Y. Sun, Y. Wu, B. Mayers, B. Gates, Y. Yin, F. Kim, and H. Yan, "One-dimensional nanostructures: synthesis, characterization, and applications," *Advanced materials,* vol. 15, no. 5, pp. 353-389, 2003.

[10] Z. Yan, and L. Jiang, "Surface effects on the electromechanical coupling and bending behaviours of piezoelectric nanowires," *Journal of Physics D: Applied Physics,* vol. 44, no. 7, pp. 075404, 2011.

[11] L. Liang, X. Kang, Y. Sang, and H. Liu, "One-Dimensional Ferroelectric Nanostructures: Synthesis, Properties, and Applications," *Advanced Science*, 2016.

[12] X. Chen, J. Shao, N. An, X. Li, H. Tian, C. Xu, and Y. Ding, "Self-powered flexible

pressure sensors with vertically well-aligned piezoelectric nanowire arrays for monitoring vital signs," *Journal of Materials Chemistry C,* vol. 3, no. 45, pp. 11806-11814, 2015.

[13] L. Liao, H. Fan, B. Yan, Z. Zhang, L. Chen, B. Li, G. Xing, Z. Shen, T. Wu, and X. Sun, "Ferroelectric transistors with nanowire channel: toward nonvolatile memory applications," *Acs Nano,* vol. 3, no. 3, pp. 700-706, 2009.

[14] J. I. Sohn, S. S. Choi, S. M. Morris, J. S. Bendall, H. J. Coles, W.-K. Hong, G. Jo, T. Lee, and M. E. Welland, "Novel nonvolatile memory with multibit storage based on a ZnO nanowire transistor," *Nano letters,* vol. 10, no. 11, pp. 4316-4320, 2010.

[15] X. Wang, J. Zhou, J. Song, J. Liu, N. Xu, and Z. L. Wang, "Piezoelectric field effect transistor and nanoforce sensor based on a single ZnO nanowire," *Nano letters,* vol. 6, no. 12, pp. 2768-2772, 2006.

[16] Y. Hu, C. Xu, Y. Zhang, L. Lin, R. L. Snyder, and Z. L. Wang, "A Nanogenerator for Energy Harvesting from a Rotating Tire and its Application as a Self-Powered Pressure/Speed Sensor," *Advanced Materials,* vol. 23, no. 35, pp. 4068-4071, 2011.

[17] C. Pan, L. Dong, G. Zhu, S. Niu, R. Yu, Q. Yang, Y. Liu, and Z. L. Wang, "High-resolution electroluminescent imaging of pressure distribution using a piezoelectric nanowire LED array," *Nature Photonics,* vol. 7, no. 9, pp. 752-758, 2013.

[18] C. Lang, J. Fang, H. Shao, X. Ding, and T. Lin, "High-sensitivity acoustic sensors from nanofibre webs," *Nature communications,* vol. 7, 2016.

[19] H. A. Sodano, A. Koka, C. R. Guskey, T. M. Seigler, and S. C. Bailey, "Introducing Perturbations into Turbulent Wall-Bounded Flow With Arrays of Long TiO_2 Nanowires," *Journal of Fluids Engineering,* vol. 137, no. 2, pp. 024501, 2015.

[20] T. D. Nguyen, N. Deshmukh, J. M. Nagarah, T. Kramer, P. K. Purohit, M. J. Berry, and M. C. McAlpine, "Piezoelectric nanoribbons for monitoring cellular deformations," *Nat Nanotechnol,* vol. 7, no. 9, pp. 587-93, Sep, 2012.

[21] X. Chen, S. Y. Xu, N. Yao, and Y. Shi, "1.6 V Nanogenerator for Mechanical Energy Harvesting Using PZT Nanofibers," *Nano Letters,* vol. 10, no. 6, pp. 2133-2137, Jun, 2010.

[22] Z. L. Wang, and J. H. Song, "Piezoelectric nanogenerators based on zinc oxide nanowire arrays," *Science,* vol. 312, no. 5771, pp. 242-246, Apr 14, 2006.

[23] S. N. Cha, J. S. Seo, S. M. Kim, H. J. Kim, Y. J. Park, S. W. Kim, and J. M. Kim, "Sound-Driven Piezoelectric Nanowire-Based Nanogenerators," *Advanced materials,*

vol. 22, no. 42, pp. 4726-4730, 2010.

[24] Y. Hu, L. Lin, Y. Zhang, and Z. L. Wang, "Replacing a Battery by a Nanogenerator with 20 V Output," *Advanced Materials,* vol. 24, no. 1, pp. 110-114, 2012.

[25] J. H. Jung, M. Lee, J.-I. Hong, Y. Ding, C.-Y. Chen, L.-J. Chou, and Z. L. Wang, "Lead-free $NaNbO_3$ nanowires for a high output piezoelectric nanogenerator," *ACS nano,* vol. 5, no. 12, pp. 10041-10046, 2011.

[26] P. X. Gao, J. Song, J. Liu, and Z. L. Wang, "Nanowire piezoelectric nanogenerators on plastic substrates as flexible power sources for nanodevices," *Advanced Materials,* vol. 19, no. 1, pp. 67-72, 2007.

[27] R. Yang, Y. Qin, L. Dai, and Z. L. Wang, "Power generation with laterally packaged piezoelectric fine wires," *Nature Nanotechnology,* vol. 4, no. 1, pp. 34-39, 2009.

[28] M.-H. Zhao, Z.-L. Wang, and S. X. Mao, "Piezoelectric characterization of individual zinc oxide nanobelt probed by piezoresponse force microscope," *Nano Letters,* vol. 4, no. 4, pp. 587-590, 2004.

[29] I. Ueda, and S. Ikegami, "Piezoelectric properties of modified $PbTiO_3$ ceramics," *Japanese Journal of Applied Physics,* vol. 7, no. 3, pp. 236, 1968.

[30] N. Ichinose, and M. Kimura, "Microstructure and piezoelectric properties of modified PbTiO3 ceramics," *Japanese journal of applied physics,* vol. 31, no. 9S, pp. 3033, 1992.

[31] Z. Jiwei, Y. Xi, W. Mingzhong, and Z. Liangying, "Preparation and microwave characterization of $PbTiO_3$ ceramic and powder," *Journal of Physics D: Applied Physics,* vol. 34, no. 9, pp. 1413, 2001.

[32] J. Ryu, G. Han, T. K. Song, A. Welsh, S. Trolier-McKinstry, H. Choi, J.-P. Lee, J.-W. Kim, W.-H. Yoon, and J.-J. Choi, "Upshift of phase transition temperature in nanostructured $PbTiO_3$ thick film for high temperature applications," *ACS applied materials & interfaces,* vol. 6, no. 15, pp. 11980-11987, 2014.

[33] J. B. Blum, and S. Gurkovich, "Sol-gel-derived $PbTiO_3$," *Journal of materials science,* vol. 20, no. 12, pp. 4479-4483, 1985.

[34] B. A. Hernandez, K.-S. Chang, E. R. Fisher, and P. K. Dorhout, "Sol-gel template synthesis and characterization of BaTiO3 and $PbTiO_3$ nanotubes," *Chemistry of Materials,* vol. 14, no. 2, pp. 480-482, 2002.

[35] J. Yoon, S. Kim, D. Kim, I. D. Kim, S. Hong, and K. No, "Fabrication of Highly Ordered and Well-Aligned PbTiO3/TiN Core–Shell Nanotube Arrays," *Small,* vol. 11, no. 31, pp. 3750-3754, 2015.

[36] M. Hsu, I.-C. Leu, Y. Sun, and M.-H. Hon, "Template synthesis and characterization of $PbTiO_3$ nanowire arrays from aqueous solution," *Journal of Solid State Chemistry,* vol. 179, no. 5, pp. 1421-1425, 2006.

[37] Y. Wang, G. Xu, L. Yang, Z. Ren, X. Wei, W. Weng, P. Du, G. Shen, and G. Han, "Preparation of single-crystal $PbTiO_3$ nanorods by phase transformation from $Pb_2Ti_2O_6$ nanorods," *Journal of Alloys and Compounds,* vol. 481, no. 1, pp. L27-L30, 2009.

[38] Z. Liu, Z. Ren, Z. Xiao, C. Chao, X. Wei, Y. Liu, X. Li, G. Xu, G. Shen, and G. Han, "Size-Controlled Single-Crystal Perovskite $PbTiO_3$ Nanofibers from Edge-Shared TiO_6 Octahedron Columns," *Small,* vol. 8, no. 19, pp. 2959-2963, 2012.

[39] H. Gu, Y. Hu, J. You, Z. Hu, Y. Yuan, and T. Zhang, "Characterization of single-crystalline $PbTiO_3$ nanowire growth via surfactant-free hydrothermal method," *Journal of applied physics,* vol. 101, no. 2, pp. 024319, 2007.

[40] B. Im, H. Jun, K. H. Lee, S.-H. Lee, I. K. Yang, Y. H. Jeong, and J. S. Lee, "Fabrication of a vertically aligned ferroelectric perovskite nanowire array on conducting substrate," *Chemistry of Materials,* vol. 22, no. 16, pp. 4806-4813, 2010.

[41] G. Wang, R. Sæterli, P. M. Rørvik, A. T. van Helvoort, R. Holmestad, T. Grande, and M.-A. Einarsrud, "Self-assembled growth of $PbTiO_3$ nanoparticles into microspheres and bur-like structures," *Chemistry of materials,* vol. 19, no. 9, pp. 2213-2221, 2007.

[42] P. M. Rørvik, T. Grande, and M.-A. Einarsrud, "Hierarchical $PbTiO_3$ nanostructures grown on $SrTiO_3$ substrates," *Crystal Growth and Design,* vol. 9, no. 4, pp. 1979-1984, 2009.

[43] A. Nafari, C. C. Bowland, and H. A. Sodano, "Vertically Aligned Lead Titanate Nanowire Arrays for High Temperature Energy Harvesting." pp. V002T07A018-V002T07A018.

[44] B. Chen, X. Zheng, M. Yang, Y. Zhou, S. Kundu, J. Shi, K. Zhu, and S. Priya, "Interface band structure engineering by ferroelectric polarization in perovskite solar cells," *Nano Energy,* vol. 13, pp. 582-591, 2015.

[45] R. Räty, V. Lindroos, A. Saarinen, J. Forsten, and H. Miekk-Oja, "The preparation of thin foils for electron microscopy using a controlled low temperature technique," *Journal of Scientific Instruments,* vol. 43, no. 6, pp. 367, 1966.

[46] G. Xu, Z. Ren, P. Du, W. Weng, G. Shen, and G. Han, "Polymer-Assisted Hydrothermal Synthesis of Single-Crystalline Tetragonal Perovskite $PbZr_{0.52}Ti_{0.48}O_3$ Nanowires," *Advanced Materials,* vol. 17, no. 7, pp. 907-910, 2005.

[47] J. Ziółkowski, "New method of calculation of the surface enthalpy of solids," *Surface Science,* vol. 209, no. 3, pp. 536-561, 1989.

[48] E. Ertekin, P. A. Greaney, D. Chrzan, and T. D. Sands, "Equilibrium limits of coherency in strained nanowire heterostructures," *Journal of Applied Physics,* vol. 97, no. 11, pp. 114325, 2005.

[49] X. Zhang, Z. Zhang, and S. C. Glotzer, "Simulation study of dipole-induced self-assembly of nanocubes," *The Journal of Physical Chemistry C,* vol. 111, no. 11, pp. 4132-4137, 2007.

[50] M. Li, W. Hebenstreit, U. Diebold, A. M. Tyryshkin, M. K. Bowman, G. G. Dunham, and M. A. Henderson, "The influence of the bulk reduction state on the surface structure and morphology of rutile TiO_2 (110) single crystals," *The Journal of Physical Chemistry B,* vol. 104, no. 20, pp. 4944-4950, 2000.

[51] Z. Jiang, W. Zhang, L. Jin, X. Yang, F. Xu, J. Zhu, and W. Huang, "Direct XPS evidence for charge transfer from a reduced rutile TiO_2 (110) surface to Au clusters," *The Journal of Physical Chemistry C,* vol. 111, no. 33, pp. 12434-12439, 2007.

[52] R. Ren, Z. Yang, and L. Shaw, "Polymorphic transformation and powder characteristics of TiO_2 during high energy milling," *Journal of materials science,* vol. 35, no. 23, pp. 6015-6026, 2000.

[53] J. Wang, C. Sandu, E. Colla, Y. Wang, W. Ma, R. Gysel, H. Trodahl, N. Setter, and M. Kuball, "Ferroelectric domains and piezoelectricity in monocrystalline Pb(Zr, Ti)O_3 nanowires," *Applied physics letters,* vol. 90, no. 13, pp. 133107, 2007.

[54] G. Burns, and B. A. Scott, "Lattice Modes in Ferroelectric Perovskites: $PbTiO_3$," *Physical Review B,* vol. 7, no. 7, pp. 3088, 1973.

[55] E. R. Camargo, and M. Kakihana, "Peroxide-based route free from halides for the synthesis of lead titanate powder," *Chemistry of materials,* vol. 13, no. 4, pp. 1181-1184, 2001.

[56] E. R. Camargo, E. Longo, E. R. Leite, and V. R. Mastelaro, "Phase evolution of lead titanate from its amorphous precursor synthesized by the OPM wet-chemical route," *Journal of Solid State Chemistry,* vol. 177, no. 6, pp. 1994-2001, 2004.

[57] Y. I. Yuzyuk, R. Farhi, V. Lorman, L. Rabkin, L. Sapozhnikov, E. Sviridov, and I. Zakharchenko, "A comparative Raman study of ferroelectric $PbTiO_3$ single crystal and thin film prepared on MgO substrate," *Journal of applied physics,* vol. 84, no. 1, pp. 452-457, 1998.

3. Chapter 3: Interface-Controlled Self-assembly of 3-D Piezoelectric Single Crystalline Nanostructures

3.1. Introduction

The past few decades have seen rising interest in the three-dimensional (3-D) nanostructures because of their unique characteristics, such as large surface area[1], novel coupled behavior [2] and better physical/chemical properties resulting from nano scale effects.[3-6] The 3-D nanostructures are attracting interest for applications in sensors, nano templates, electronic materials, transistors, catalysts and battery electrodes. There are two main methodologies for fabricating 3-D nanostructures, namely, soft-template assisted growth and self-assembly. The soft-template assisted fabrication process for 3-D nanostructures has advantages of scalability and precise microstructure control.[7-9] However, it is difficult to fabricate high quality 3-D nanostructures, especially single crystal structures, using soft-template assisted methods because of limitations in developing recipes and in separating the fabricated structures from the template.[10-13] Self-assembly provides a practical pathway towards overcoming these limitations and realizing 3-D single crystalline nanostructures while enabling the control of growth orientation.[1, 13-17] Here, we provide a breakthrough in this direction by exploiting interface driven growth that assists in relaxing the interfacial strain through shape modulation resulting piezoelectric 3-D nanostructures.

Piezoelectric 3-D nanostructures provide additional advantages that arise from their anisotropic functional properties, that makes them promising for applications in nanogenerators, sensors and nonvolatile memory.[18-21] Among various known piezoelectric materials, $PbTiO_3$ (PTO) has some appealing characteristics such as a low aging rate of the dielectric constant, a high voltage constant (g), and a high Curie temperature of 490 ^{o}C.[22, 23]

Also, PTO has high tetragonality (c:a ratio of 1.063) which can provide a low ratio for the planar-to-thickness coupling factor.[24] Photocatalytic characteristics of PTO for the production of O_2 and H_2 by splitting water have been explored recently.[25] However, synthesis of PTO 3-D nanostructures has been challenging and few successes have been reported. PTO exhibits high intrinsic strain during cooling from high temperature to room temperature, which normally fractures the ceramic material. Overcoming this issue, in the synthesis of the PTO nanostructures, without compromising the electromechanical properties, is highly desired but has been fundamentally difficult. In this paper, we report a novel interface controlled growth to achieve functional 3-D nanostructures and provide the fundamental understanding of the growth process. The (001) oriented PTO single crystal arrays with well-defined geometrical shapes were grown on (001) $SrTiO_3$ (STO) substrates through a hydrothermal synthesis process. The growth mechanism of the 3-D PTO nanostructures was found to be governed by the atomic interface between the PTO and underlying STO substrate. The crystallinity, orientation, and morphology of 3-D PTO nanostructures were investigated using high resolution transmission electron microscopy (HRTEM), Raman spectroscopy and energy-dispersive X-ray spectroscopy (EDX). The piezoelectric behavior of the 3-D PTO nanostructure was demonstrated using piezo response force microscopy (PFM).

3.2. Experimental

3.2.1. Fabrication of Three-dimensional $PbTiO_3$ Nanostructure

Reagent grade Tetrabutyl Titanate $(C_4H_9O)_4Ti$ (97%, Sigma-Aldrich) and Lead Nitrate $Pb(NO_3)_2$ (99.5%, Sigma-Aldrich) were used as reactants and potassium hydroxide (KOH) was employed as a mineralizer. Poly(vinyl alcohol) (PVA) and Poly(acrylic acid) (PAA) were added as a polymer surfactant to facilitate two-dimensional growth. First, $(C_4H_9O)_4Ti$ was

distilled with a high purity ethanol under 200 rpm stirring for 10 min. Next, this solution was precipitated in a 0.1 M ammonia solution. The precipitate was filtered and washed with distilled D.I. water 10 times in order to remove ammonium ions and ethanol. The $TiO(OH)_2$ precipitate was re-dispersed with 50 ml D.I. water to 0.1M concentration and a stoichiometric amount of $Pb(NO_3)_2$ was added to this aqueous solution with vigorous stirring. Pellets of KOH were slowly introduced to a 2M concentration. Finally, the polymer components, 0.02g PVA and 0.4g PAA, were added to the solution and stirred for more than 12 hours. Hydrothermal synthesis was performed in a stainless steel autoclave with a 23 ml volume Teflon vessel (Parr Instrument Company, Model 4746) as shown in Figure 3.1 (b). $SrTiO_3$ substrates with orientations corresponding to (001), (110) and (111) surface planes were prepared and cleaned ultrasonically in high purity acetone (99.9%) and ethanol (99.9%) in sequence. A $SrTiO_3$ substrate coated with a TiO_2 film through a sol-gel process was prepared for comparison with the bare, oriented STO substrates. The TiO_2 sol-gel solution was prepared using a previously reported process.[26] The TiO_2 sol-gel solution was spin coated on a (001) $SrTiO_3$ substrate at 6000 rpm for 30 s. After drying at 120 °C for 10 min, the TiO_2 films were annealed at 700 °C for 5 min. The as-prepared $SrTiO_3$ substrates ((001), (110), (111) and TiO_2 coated (001) $SrTiO_3$)) were vertically suspended in the solution from a homemade Teflon holder as described Figure S*3a*. The Teflon vessel was filled with 20 ml of hydrothermal solution, sealed in a stainless steel autoclave and placed in a low temperature furnace at 200 °C for 12 hours. After cooling to room temperature, the synthesized specimens were washed several times with D.I. water and high purity ethanol (99.9%) and dried in air. The fabricated 2-D piezoelectric $PbTiO_3$ nanostructures were characterized by XRD (Bruker D8 advance), FESEM (LEO 1550), HRTEM (FEI Titan 300), Raman spectroscopy (JY Horiba LabRam HR800-U) and PFM (Bruker).

(a) (b)

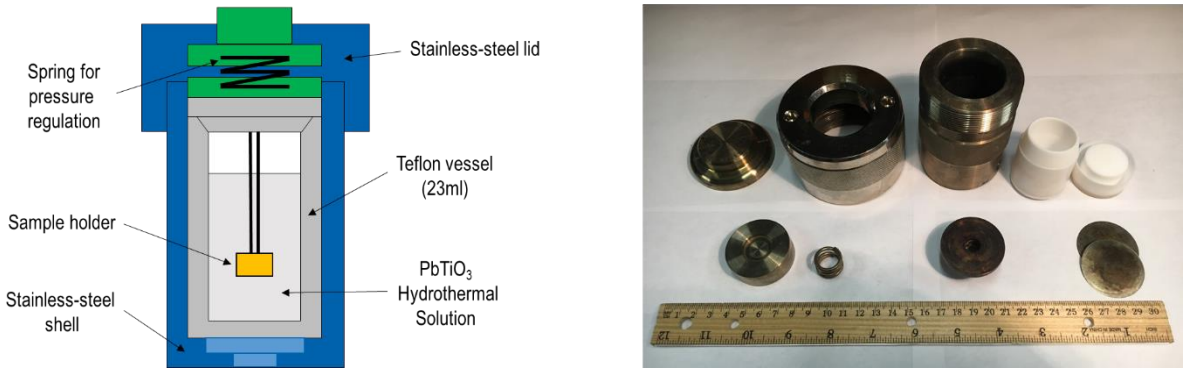

Figure 3.1. (a) Schematic description of hydrothermal synthesis. (b) Picture for autoclave used in hydrothermal synthesis.

3.3. Results and Discussion

3.3.1. $PbTiO_3$ Nanostructure on $SrTiO_3$ substrates

STO has the same crystal structure as PTO and a comparable a- and b- axis lattice parameter, which makes it a suitable substrate with least lattice mismatch. The a- and b-axis lattice constants of PTO (3.904 Å) have almost no mismatch with the corresponding axes of STO (3.905 Å), which favors epitaxial PTO growth in the [001] direction on (001) STO substrates. Representative SEM images of 3-D nanostructured PTO crystals grown using a hydrothermal synthesis process on (001) STO substrate are shown in Figure 1e. The growth procedure is schematically illustrated in Figure 3.2 (a) ~ (d). The inset in Figure 3.2 (e) is the magnified image of 3-D PTO nanostructures. The PTO nano-crystals are arranged in a three-dimensional array with a cross-hatched pattern that suggests 4-fold rotational symmetry. The individual PTO grains correspond to two-dimensional (2-D) PTO nanosheets that are periodically aligned in a cross-hatched pattern. The 2-D nanosheets have a rectangular plate-morphology with 1μm length and width and 50nm thickness and the plate are aligned along the [100] and [010] directions of the (001) STO substrate. As shown in Figure 3.2 (e), the average spacing of the

PTO grains is approximately 1μm, and is roughly the same in both alignment directions. In some cases, the large intersecting plates enclose a group of smaller plates, which are caused by the geometric constraint imposed by large plates on the subsequent growth of smaller plates. A fraction of the 2-D nanosheets grew at a 45^{o} angle to the dominant alignment direction and intersected each other at right angles as shown in the magnified image in Figure 3.2 (e) inset. Figure 3.3 (a) demonstrates the 3-D PTO nanostructure has a uniform distribution over a relatively large area of the STO substrate.

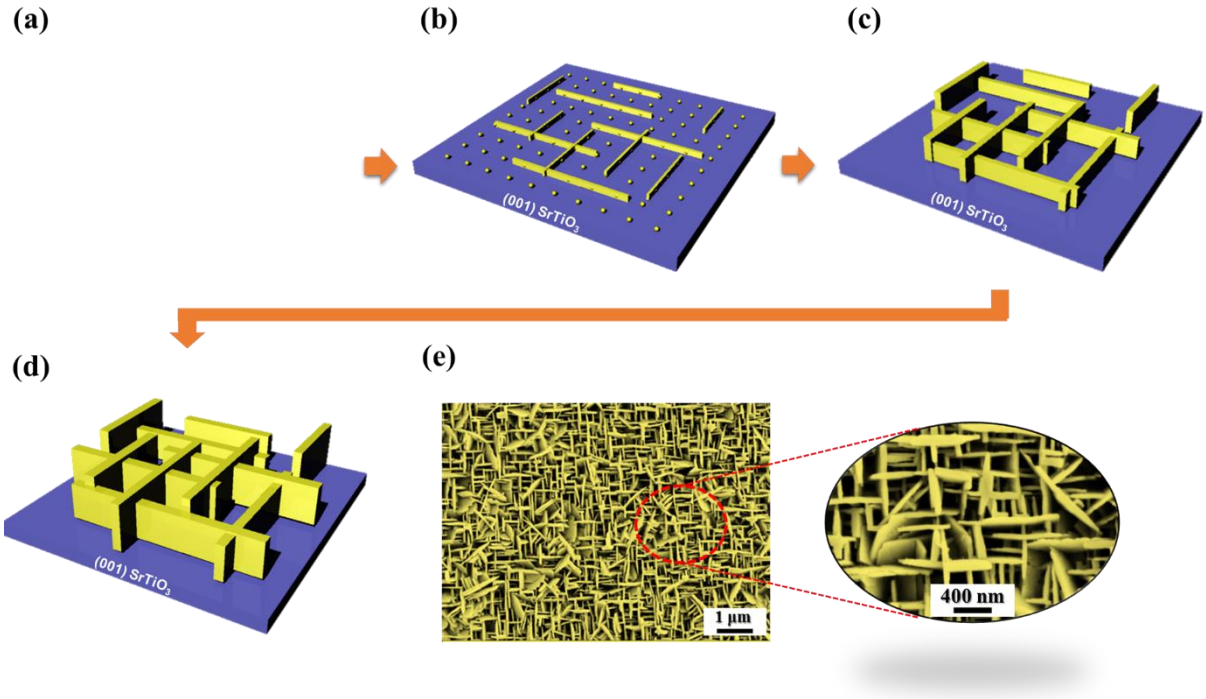

Figure 3.2. Schematic illustration of the growth mechanism of 3-dimensional $PbTiO_3$ nanostructures. (a) Ti-terminated (001) $SrTiO_3$ substrate. (b) Nucleation dominated along the Ti-atom sites in [100] and [010] direction of (001) $SrTiO_3$ substrate. (c) 2-dimensional nanosheet growth along c-axis of $PbTiO_3$. (d) Growth of 2-dimensional nanosheets to reach equilibrium. (e) SEM image of 3-dimensional $PbTiO_3$ nanostructures with aligned cross-links. Inset shows a magnified SEM image.

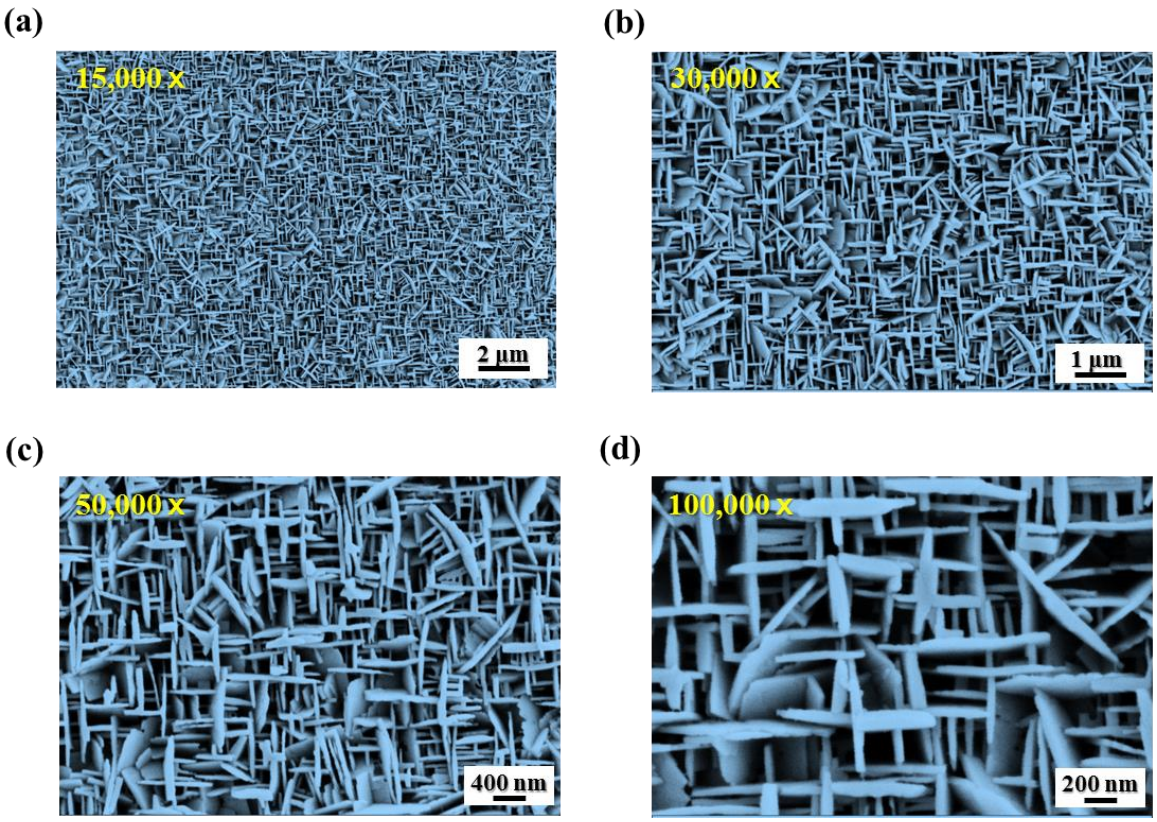

Figure 3.3. 3-dimensional $PbTiO_3$ nanostructure with cross-hatched patterns synthesized on (001) $SrTiO_3$ substrate. (a) 15,000, (b) 30,000, (c) 50,000 and (d) 100,000 magnifications.

In order to investigate the growth mechanism of the 3-D PTO nanostructure, different orientations of STO substrates were used under the same hydrothermal synthesis conditions. Figure 3.4 (a), (b) and (c) show the PTO nanostructures fabricated on (001), (110) and (111) oriented STO substrates, respectively. Remarkably, the orientation of the STO substrate clearly modulates the PTO morphology (Figure 3.4 (a), (b) and (c)), as 3-D nanostructures with cross-hatched patterns were formed on (001) STO substrate, while linearly aligned nanostructures were formed on (110) and triangular pattern (indicated by red lines in Figure 3.4 (c)) was produced on (111) oriented STO substrates. The PTO nanostructures on (001) STO were fabricated along the [100] and [010] directions, while in the case of (110) STO and (111) STO substrates, the nanostructures formed along the [100] direction of (110) STO and at 30^o angle

from [100] and [010] of (111) STO, respectively. An explanation for the growth tendency of PTO grains is shown through schematic surface atomic structure of STO substrates (Figure 3.4 (d), (e) and (f)) obtained via a rotation of the fundamental STO crystal structure (Figure 3.4 (g)). If we assume that the STO (001), (110) and (111) surfaces are Ti-O terminated, the alignment direction of the PTO nanostructure is closely related to the Ti atom configurations in the substrate surface (See Figure 3.4 (d), (e) and (f)). The atomic structure of (001), (110) and (111) surfaces of the STO substrate has symmetry similar to the nanostructured arrangement of PTO crystals: square (4-fold rotational symmetry), linear (2-fold), and triangular (3-fold), respectively. Ti cations and O anions occupy corresponding sites in the STO and PTO lattices and they have similar symmetry and bonding environments. For this reason, Ti and O–terminated surfaces of an STO substrate are likely to be effective nucleation sites for PTO nanostructure growth. The similarity in the symmetry of the nanostructures in Figure 3.4 (a), (b), and (c) with the symmetry of the arrangement of Ti and O in the STO substrate surfaces in Figure 3.2 (d), (e) and (f) suggest this explanation is plausible, and Ti and/or O atoms in the STO surface greatly influence the shape and direction of growing PTO crystals. Thus, we suggest the shape evolution and distribution of 3-D PTO nanostructures are directly related to the Ti and O arrangements in the surface of the STO substrate.

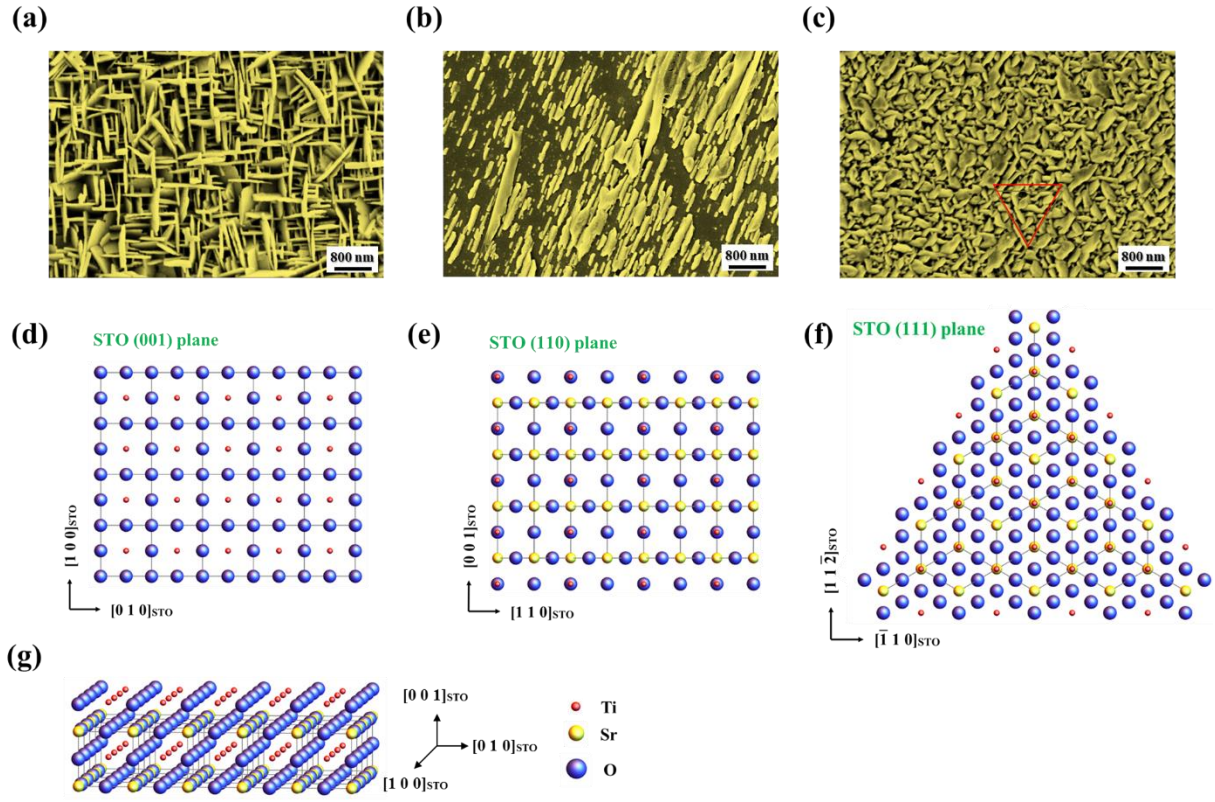

Figure 3.4. $PbTiO_3$ nanostructures hydrothermally synthesized on (a) (001), (b) (110) and (c) (111) oriented $SrTiO_3$ substrates. Surface atomic structures of (d) (001), (e) (110) and (f) (111) oriented $SrTiO_3$ substrates. 1 unit cell thickness of surface atoms were projected. (e) Schematic atomic crystal structure of Ti- and O- terminated $SrTiO_3$

To further test the role of arrangement of Ti atoms on the initial growth of 3-D PTO nanostructures, we deposited TiO_2 thin films on (001) oriented STO substrate using the sol-gel process. This film includes both Ti and O cations, but in completely different geometric arrangements from that of the underlying STO substrate. Figure 3.5 (a) and (b) shows SEM images of the TiO_2 sol-gel thin film spin-coated and annealed at 700 ^oC for 5 min. As shown in Figure 3.5 (a) and (b), the TiO_2 thin film has a smooth surface with an average grain size of ca. 20 nm. Using this TiO_2/STO substrate, the PTO nanostructure was hydrothermally synthesized under the same experimental condition used previously for the sample shown in Figure 3.4. The PTO nanostructures grown on the TiO_2 seed layer are depicted in Figure 3.5 (c)

and (d). The presence of the TiO_2 layer induces randomly-aligned nanosheets of PTO rather than the highly organized 3-D nanosheets of PTO formed on bare STO (Figure 3.4). This result confirms that the geometric arrangement of Ti atoms on the substrate surface plays an important role in the directional growth of PTO nanostructures.

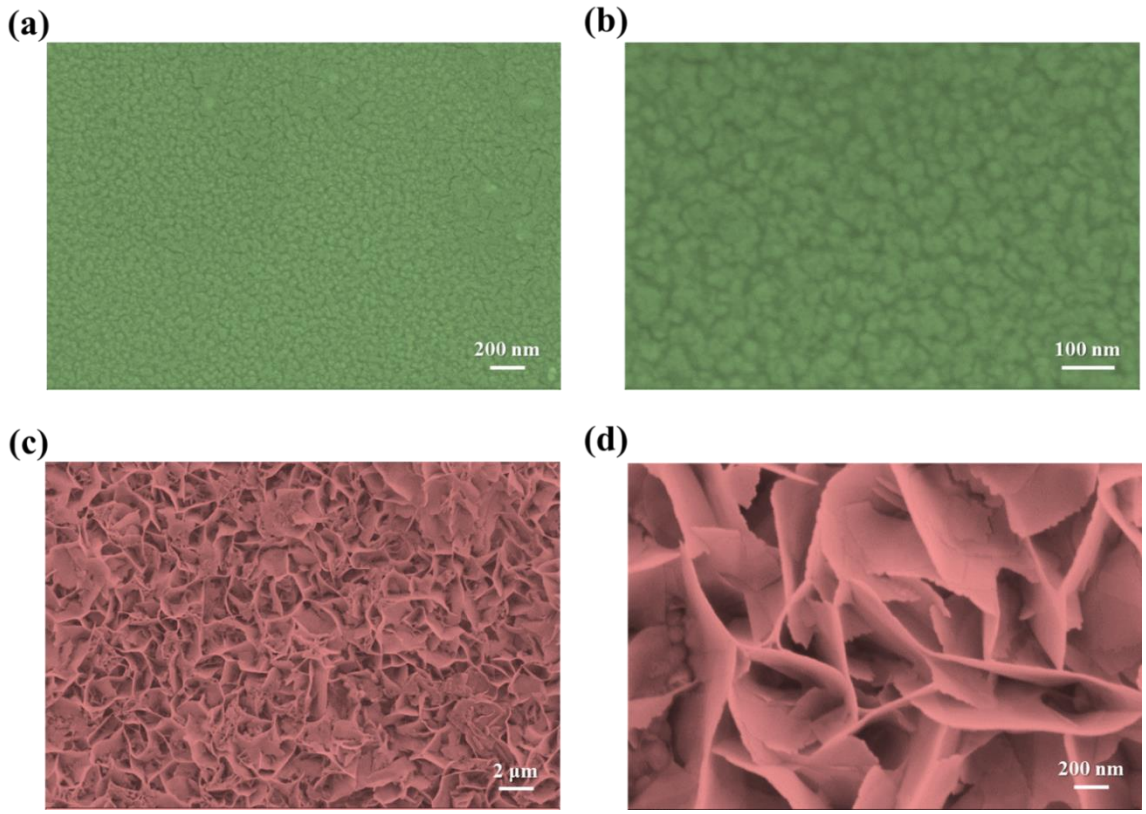

Figure 3.5. (a), (b) Polycrystalline TiO_2 thin films on (001) $SrTiO_3$ substrate annealed at 700 ^oC for 5 min. (c), (d) Hierarchical two-dimensional $PbTiO_3$ nanosheet network on TiO_2 / (001) $SrTiO_3$ Substrate.

The X-ray diffraction (XRD) pattern of 3-D PTO nanostructures on (001) oriented STO is shown in Figure 3.6. Except for the peaks of STO substrate, all the diffraction peaks can be indexed as tetragonal perovskite structured PTO (in agreement with positions given in JCPDS Card No. 77-2002). The XRD pattern also indicated the nanosheets are highly textured and have 99.5% texturing degree, as obtained from the peak intensity comparison. The composition

of the 3-D PTO nanostructures with cross-hatched pattern was analyzed using energy dispersive X-ray spectroscopy (EDS) mapping and is presented in Figure 3.7. These results clearly show the Pb and Ti atomic distribution in 2D nanosheets. Given the approximately 1.0 μm depth of the EDS probe, the dark inter-crystal regions between individual PTO nanosheets can arise from the STO substrate or thin PTO film. The atomic ratio in Figure 3.7 was obtained from a large area of the image and is consistent with $PbTiO_3$ and $SrTiO_3$ stoichiometry.

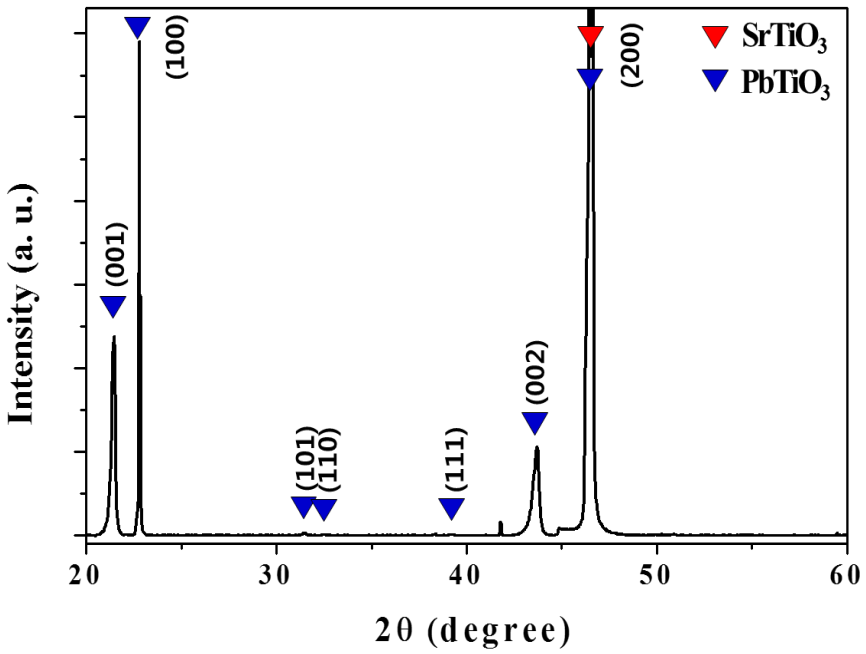

Figure 3.6. XRD patterns for the two-dimensional $PbTiO_3$ nanosheets on (100) oriented $SrTiO_3$ substrates

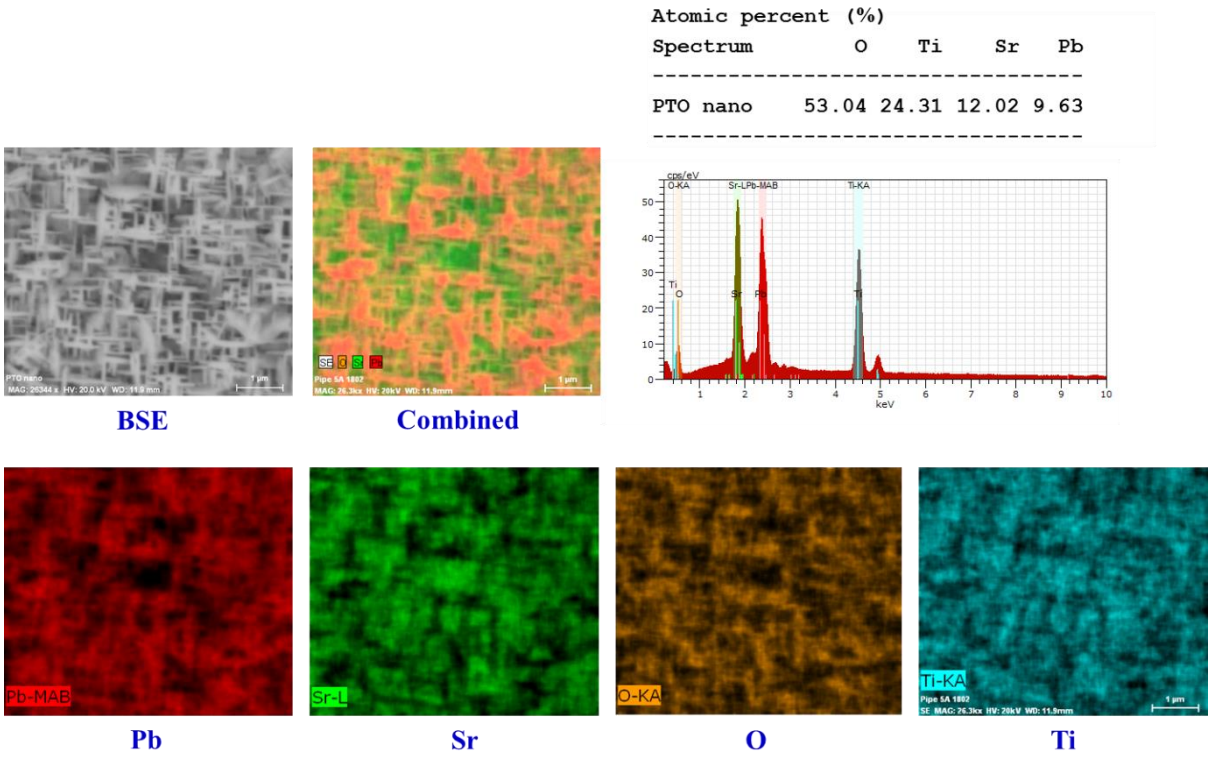

Figure 3.7. EDX analysis of two-dimensional $PbTiO_3$ nanosheets on (001) oriented $SrTiO_3$ substrates confirming the stoichiometry of plates. No inter-diffusion was observed in this analysis.

Figure 3.8 (a) shows the Raman scattering spectrum of the 3-D PTO nanostructures recorded at room temperature (20 ºC). All Raman modes of the 3-D nanostructure were indexed using based on the earlier study of Burns and Scott.[27] Most of the principal-axes modes were observed and are shown in Figure 3.8 (a). The frequency of Raman lines in the 3-D PTO nanostructure agrees well with the previously reported results for single crystal [28] and textured thin film PTO [29] (See Table 3). The lowest frequency soft phonon mode (Polar phonon mode), E(1TO), was below the detection limit of the equipment, but some signal was detected from another low-frequency soft phonon mode, E(1LO). It is found that Raman modes E(1LO), A1(1TO), E(2TO) and E(3TO) are notably shifted to higher frequencies (relative to single crystal PTO), whereas the mode A1(2TO) is downshifted and the silent mode B1+E is upshifted slightly. This blue shift of Raman lines, which is unusual in nanostructured crystals,

can be explained by assuming the presence of tensile stress in the specimen [30] due to increased tetragonality of the 3-D PTO nanostructures. Figure 3.8 (b) shows the temperature dependence of Raman spectra obtained from the 3-D PTO nanostructures near the Curie temperature. In the vicinity of the Curie point, the short- and long-range interactions compete with each other in such a way that the frequency of the transverse optical (TO) phonon approaches zero.[31] With increasing temperature, Figure 3.8 (b), the Raman lines shift to lower frequency and the peak width broadens significantly compared to the room temperature spectrum in Figure 3.8 (a). At 500 ^{o}C, one can still observe some prominent low-frequency peaks in the Raman spectra indicating the polar nature of the PTO nanostructures at this temperature.[32] These results suggest that the 3-D PTO nanostructures have a higher tetragonal-to-cubic phase transition temperature (Curie temperature) than that of bulk PTO (490^{o}C).

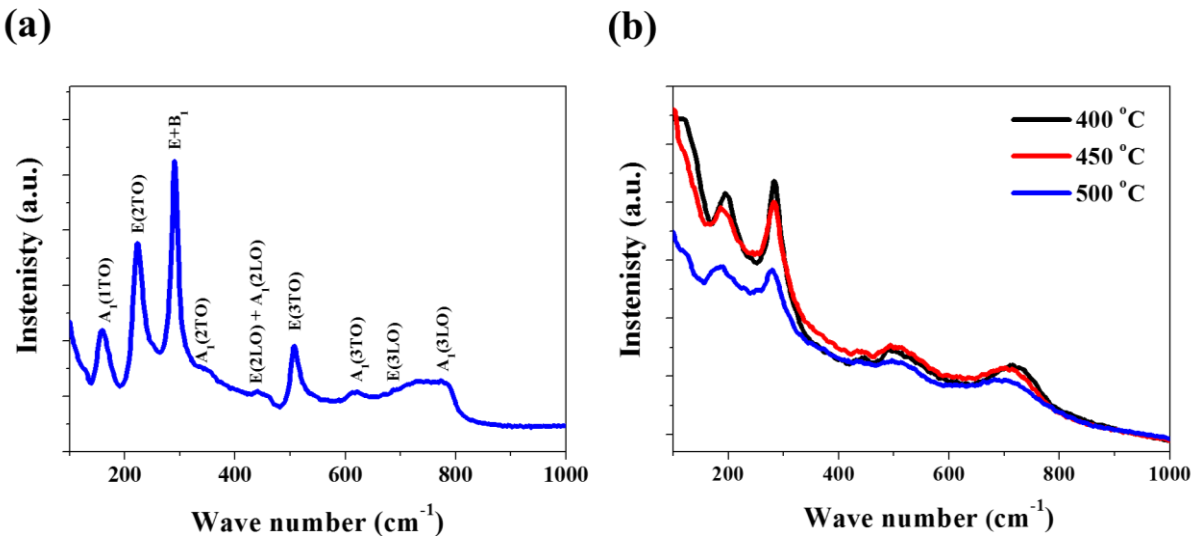

Figure 3.8. (a) Raman scattering spectrum of 3-dimenstional $PbTiO_3$ nanostructure at room temperature and (b) variation of Raman spectrum with temperature near the Curie temperature.

Table 3. Frequencies of Raman modes observed in the 3-D $PbTiO_3$ nanostructures at room temperature.

Mode	This work	Single crystal (Ref.1)[28]	Textured film (Ref.2)[29]
E(1LO)	130	128	
A_1(1TO)	158	148.5	147
A_1(1LO)		194	
E(2TO)	224	218.5	212
E+B1	289.5	289	288
A_1(2TO)	340	359.5	340
E(2LO)+A1(2LO)	440	440.5, 465	442
E(3TO)	507.5	505	503
A_1(3TO)	622	647	621
E(3LO)	686	687	728
A_1(3LO)	772.5	795	

To further confirm the crystal structure of the PTO nanostructures on a (001) oriented STO substrate, we conducted microstructure analysis using transmission electron microscopy (TEM) and scanning transmission electron microscopy (STEM). Figure 3.9 (a) shows TEM images of a cross-section through the PTO nanostructure grown on the (001) oriented STO substrate. The short PTO crystal in Figure 3.9 (a) is approximately 130 nm high and 240 nm wide. The PTO nanostructures are not continuous on the STO substrate, rather there are gaps individual PTO crystals and the crystals have different thicknesses (See Figure 3.9 (a) and inset). The growth shape of individual crystals was found to vary as evident from the regular rectangular shape depicted in Figure 3.9 (a) and a more random shape in the inset of Figure 3.9 (a). The two white arrows in the upper left of the figure indicate the location of 45^o ferroelectric domains. Figure 3.9 (b) and (c) show high-resolution TEM (HRTEM) images of the interface between STO substrate and PTO nanostructure. The lattice fringes of PTO nanostructure and the underlying STO substrate are in a cube-cube epitaxial relationship with the [001] PTO growth direction oriented perpendicular to the (001) substrate surface. The TEM results confirm that the individual PTO nanosheets are single crystal that grow along the [001] direction with respect to STO substrate. This result is also in well agreement with the (001) textured XRD pattern of

the PTO nanostructures depicted in Figure 3.6. The selected area electron diffraction (SAED) pattern was taken from the area indicated by the red square in Figure 3.9 (b). The fundamental diffraction spots split into pairs; one half for PTO and the other for STO phase because of the slightly different lattice parameters of the two phases (See the inset of Figure 3.9 (b)). The brighter diffraction spots match well with the lattice spacing of PTO and the weaker spots are consistent with the lattice spacing of STO substrate. Figure 3.9 (c) shows the magnified HRTEM image of the interface of the PTO nanostructure and the STO substrate. The spacing of the PTO plane, 3.917 Å, almost coincides with the 3.905Å lattice spacing of (110) plane in STO, with only 0.3 % lattice mismatch. Based on the *d*-spacing values measured from the diffraction pattern, the PTO nanostructure has higher tetragonality (c:a ratio of 1.070) than typical bulk crystals of (c:a = 1.063); which is expected to result in higher polarization and Curie temperature.[24, 33] The result of the increased tetragonality is in line with the Raman blue shift and increased phase transition temperature of 3-D PTO nanostructures. As shown in Figure 3.9 (d), the line scan concentration profile across the interface obtained from STEM shows that Pb and Sr are strictly confined to the PTO and STO crystals, respectively.

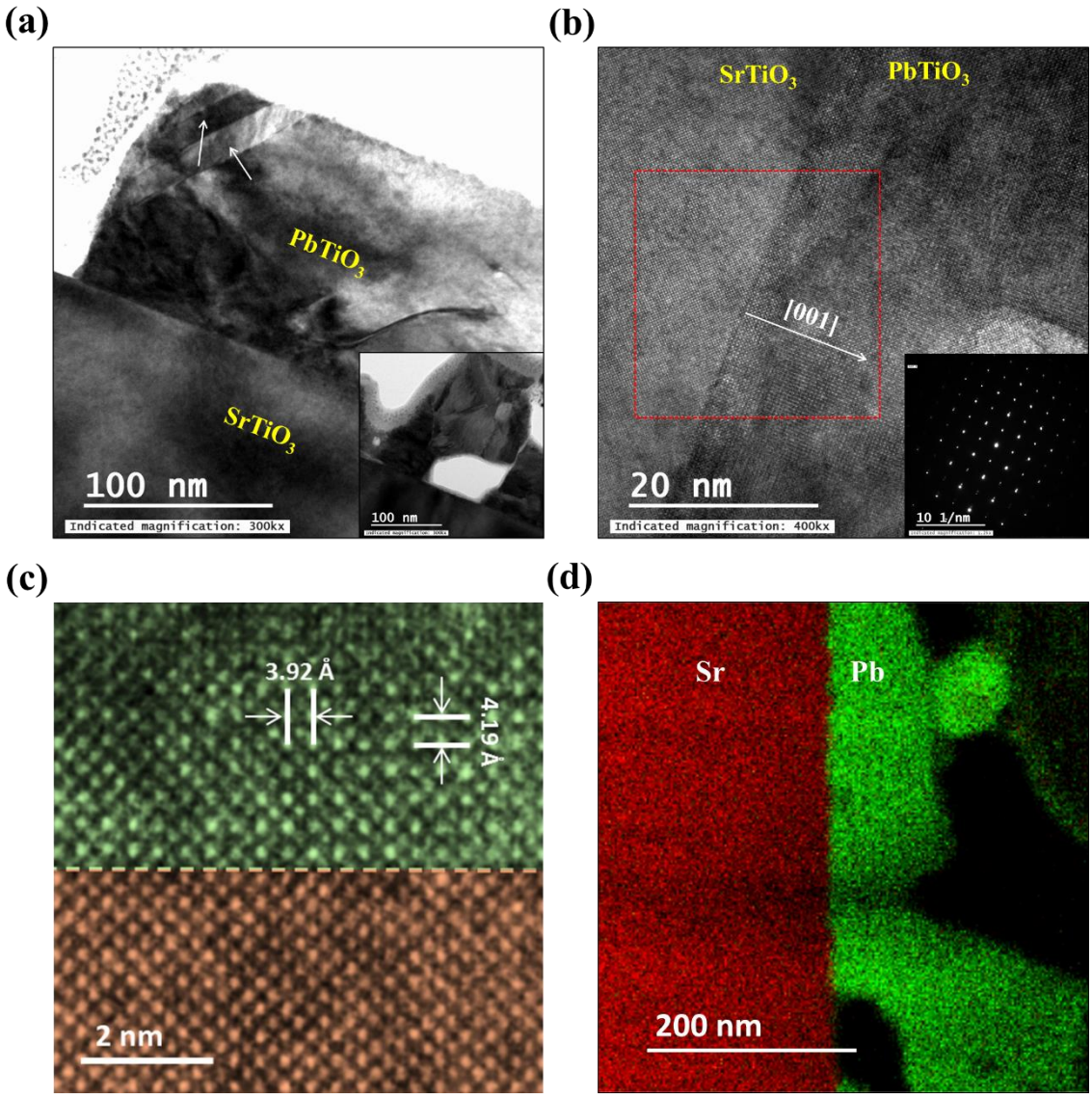

Figure 3.9. (a) Cross-sectional TEM image for 2-dimensional $PbTiO_3$ nanosheets on (001) oriented $SrTiO_3$ substrates. Inset is TEM image of another region. (b) A high-resolution TEM (HRTEM) image of the interface between $SrTiO_3$ substrate and $PbTiO_3$ nanosheet. Inset is the SAED pattern taken from the area indicated by red square. (c) Magnified HRTEM image of the interface. For better visibility, the TEM image is artificially colored. (d) Scanning TEM (STEM) elemental mapping of Pb and Sr in the $PbTiO_3/SrTiO_3$ interface region.

In order to measure the piezoelectric property of PTO nanostructures, an electrically conducting (001) oriented, 0.5 wt.% Nb-doped STO substrate was used in the hydrothermal synthesis as illustrated in Figure 3.10 (a). The local piezoelectric response of the PTO

nanostructure was collected using piezoelectric response microscopy (PFM) under DC bias sweep from -12 to 12 V. The phase signal indicates that the PTO nanostructure exhibits unambiguous 180° ferroelectric domain switching behavior (Figure 3.10 (b)). From the amplitude and piezoelectric response signals, it was found that the PTO nanostructure has a strong piezoelectric response (Figure 3.10 (c) and (d)), which is evidence of an outstanding longitudinal piezoelectric coefficient.

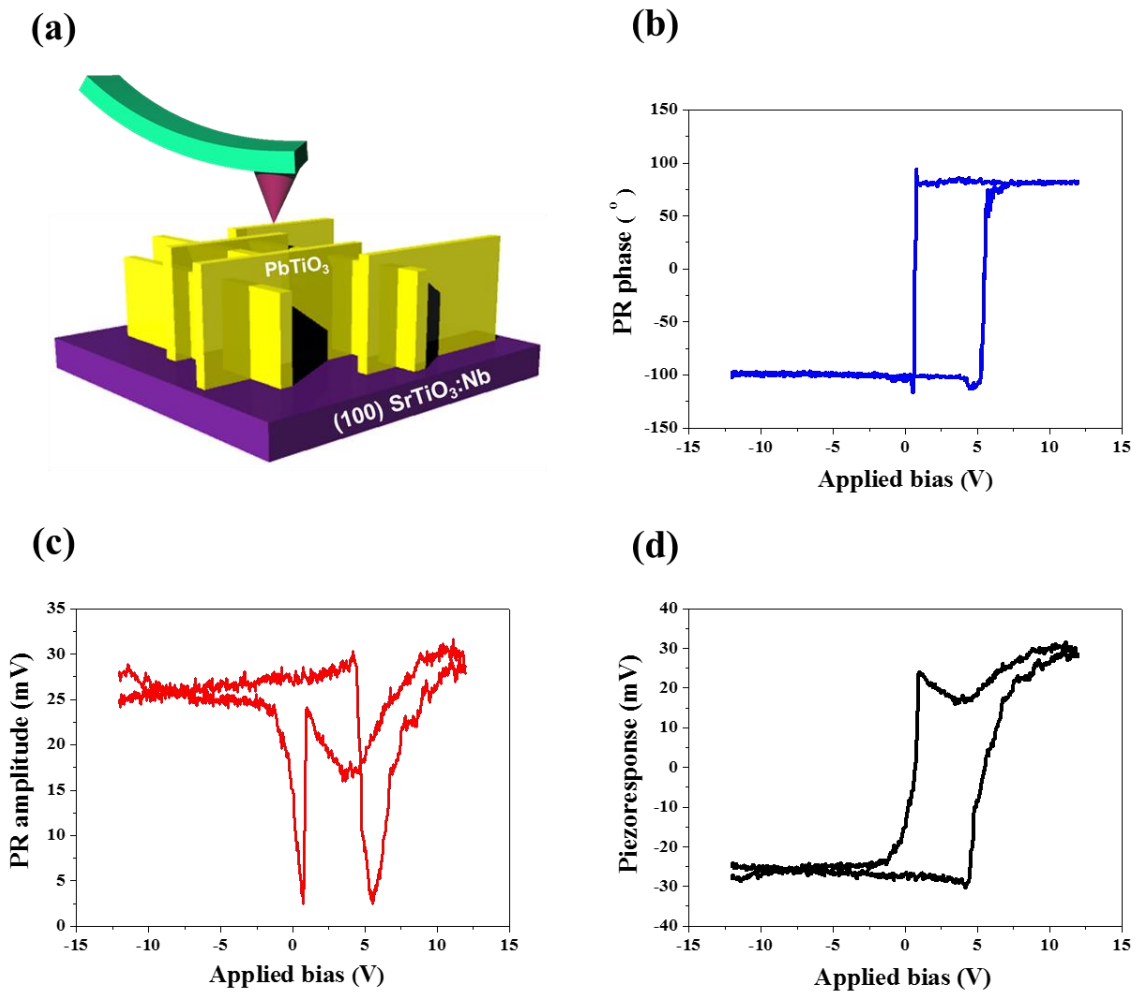

Figure 3.10. (a) Schematic description of PFM analysis. 0.5 wt% Nb-doped $SrTiO_3$ substrate with (001) orientation was used for measurement of piezoresponse. (b) Amplitude and (c) phase from piezoelectric response taken from the cross-hatched $PbTiO_3$ 3-D nanostructures on (001) oriented Nb-doped $SrTiO_3$ substrates. (d) Combined signal of amplitude and phase of $PbTiO_3$ 3-D nanostructures, which confirms the ferroelectric behavior of $PbTiO_3$ nanostructure.

3.4. Summary

Novel 3-D PTO nanostructures with aligned patterns were formed on STO substrates using a hydrothermal synthesis process. Different crystalline patterns were obtained depending upon the STO substrate orientation; (001), (110), or (111) substrates produced cross-hatch, linear, and triangular patterns, respectively. The PTO nanostructures were aligned with symmetry consistent with that of Ti atomic configuration on the surface of STO substrate. When the STO substrate was coated with a thin film of polycrystalline TiO_2 prior to hydrothermal synthesis, the resulting PTO nanostructures were random with no preferential alignment. 3-D PTO nanostructures were single crystal plates of PTO grown along the (001) crystal direction. The Raman shift as a function of temperature near the phase transition temperature indicates that the 3-D PTO nanostructure has a Curie temperature above 500^{o}C. Using electrically conducting (001) oriented 0.5 wt.% Nb-doped STO substrate, the piezoelectric response of the 3-D PTO nanostructure was confirmed. These 3-D PTO nanostructures with large surface area, high ferroelectric and piezoelectric properties could be promising candidates for water splitting, nanogenerators, and high sensitivity strain sensors.

References

[1] Z. L. Wang, "Nanostructures of zinc oxide," *Materials today,* vol. 7, no. 6, pp. 26-33, 2004.

[2] B. Duan, M. Wang, W. Y. Zhou, W. L. Cheung, Z. Y. Li, and W. W. Lu, "Three-dimensional nanocomposite scaffolds fabricated via selective laser sintering for bone tissue engineering," *Acta Biomaterialia,* vol. 6, no. 12, pp. 4495-4505, 2010.

[3] X. S. Fang, C. H. Ye, L. D. Zhang, J. X. Zhang, J. W. Zhao, and P. Yan, "Direct observation of the growth process of MgO nanoflowers by a simple chemical route," *Small,* vol. 1, no. 4, pp. 422-428, 2005.

[4] Y. j. Zhang, Y. Zhang, Z. h. Wang, D. Li, T. y. Cui, W. Liu, and Z. d. Zhang, "Controlled synthesis of cobalt flowerlike architectures by a facile hydrothermal route," *European Journal of Inorganic Chemistry,* vol. 2008, no. 17, pp. 2733-2738, 2008.

[5] Y. Luo, S. Li, Q. Ren, J. Liu, L. Xing, Y. Wang, Y. Yu, Z. Jia, and J. Li, "Facile synthesis of flowerlike Cu_2O nanoarchitectures by a solution phase route," *Crystal growth & design,* vol. 7, no. 1, pp. 87-92, 2007.

[6] Y.-S. Luo, W.-D. Zhang, X.-J. Dai, Y. Yang, and S.-Y. Fu, "Facile synthesis and luminescent properties of novel flowerlike $BaMoO_4$ nanostructures by a simple hydrothermal route," *The Journal of Physical Chemistry C,* vol. 113, no. 12, pp. 4856-4861, 2009.

[7] X. Zheng, H. Lee, T. H. Weisgraber, M. Shusteff, J. DeOtte, E. B. Duoss, J. D. Kuntz, M. M. Biener, Q. Ge, and J. A. Jackson, "Ultralight, ultrastiff mechanical metamaterials," *Science,* vol. 344, no. 6190, pp. 1373-1377, 2014.

[8] X. Zheng, W. Smith, J. Jackson, B. Moran, H. Cui, D. Chen, J. Ye, N. Fang, N. Rodriguez, and T. Weisgraber, "Multiscale metallic metamaterials," *Nature Materials*, 2016.

[9] H. Yan, C. F. Blanford, W. H. Smyrl, and A. Stein, "Preparation and structure of 3D ordered macroporous alloys by PMMA colloidal crystal templating," *Chemical Communications*, no. 16, pp. 1477-1478, 2000.

[10] H. G. Moon, Y.-S. Shim, H. W. Jang, J.-S. Kim, K. J. Choi, C.-Y. Kang, J.-W. Choi, H.-H. Park, and S.-J. Yoon, "Highly sensitive CO sensors based on cross-linked TiO_2 hollow hemispheres," *Sensors and Actuators B: Chemical,* vol. 149, no. 1, pp. 116-121, 2010.

[11] D. V. Bavykin, J. M. Friedrich, and F. C. Walsh, "Protonated titanates and TiO_2 nanostructured materials: synthesis, properties, and applications," *Advanced Materials,* vol. 18, no. 21, pp. 2807-2824, 2006.

[12] A. Bernal, A. Tselev, S. Kalinin, and N. Bassiri-Gharb, "Free-Standing Ferroelectric Nanotubes Processed via Soft-Template Infiltration," *Advanced Materials,* vol. 24, no. 9, pp. 1160-1165, 2012.

[13] G. Von Freymann, A. Ledermann, M. Thiel, I. Staude, S. Essig, K. Busch, and M. Wegener, "Three-Dimensional Nanostructures for Photonics," *Advanced Functional Materials,* vol. 20, no. 7, pp. 1038-1052, 2010.

[14] V. Polshettiwar, B. Baruwati, and R. S. Varma, "Self-assembly of metal oxides into three-dimensional nanostructures: synthesis and application in catalysis," *Acs Nano,* vol. 3, no. 3, pp. 728-736, 2009.

[15] L. S. Zhong, J. S. Hu, H. P. Liang, A. M. Cao, W. G. Song, and L. J. Wan, "Self-Assembled 3D flowerlike iron oxide nanostructures and their application in water treatment," *Advanced Materials,* vol. 18, no. 18, pp. 2426-2431, 2006.

[16] S. M. Stratulat, X. Lu, A. Morelli, D. Hesse, W. Erfurth, and M. Alexe, "Nucleation-induced self-assembly of multiferroic $BiFeO_3$–$CoFe_2O_4$ nanocomposites," *Nano letters,* vol. 13, no. 8, pp. 3884-3889, 2013.

[17] H.-F. Zhang, A. C. Dohnalkova, C.-M. Wang, J. S. Young, E. C. Buck, and L.-S. Wang, "Lithium-assisted self-assembly of aluminum carbide nanowires and nanoribbons," *Nano Letters,* vol. 2, no. 2, pp. 105-108, 2002.

[18] Z. L. Wang, X. Y. Kong, Y. Ding, P. Gao, W. L. Hughes, R. Yang, and Y. Zhang, "Semiconducting and piezoelectric oxide nanostructures induced by polar surfaces," *Advanced Functional Materials,* vol. 14, no. 10, pp. 943-956, 2004.

[19] H. Zheng, J. Wang, S. Lofland, Z. Ma, L. Mohaddes-Ardabili, T. Zhao, L. Salamanca-Riba, S. Shinde, S. Ogale, and F. Bai, "Multiferroic $BaTiO_3$-$CoFe_2O_4$ nanostructures," *Science,* vol. 303, no. 5658, pp. 661-663, 2004.

[20] F. Morrison, Y. Luo, I. Szafraniak, V. Nagarajan, R. Wehrspohn, M. Steinhart, J. Wendroff, N. Zakharov, E. Mishina, and K. Vorotilov, "Ferroelectric nanotubes," *arXiv preprint cond-mat/0303609*, 2003.

[21] Y. Qi, J. Kim, T. D. Nguyen, B. Lisko, P. K. Purohit, and M. C. McAlpine, "Enhanced piezoelectricity and stretchability in energy harvesting devices fabricated from buckled PZT ribbons," *Nano letters,* vol. 11, no. 3, pp. 1331-1336, 2011.

[22] I. Ueda, and S. Ikegami, "Piezoelectric properties of modified $PbTiO_3$ ceramics," *Japanese Journal of Applied Physics,* vol. 7, no. 3, pp. 236, 1968.

[23] N. Ichinose, and M. Kimura, "Microstructure and piezoelectric properties of modified $PbTiO_3$ ceramics," *Japanese journal of applied physics,* vol. 31, no. 9S, pp. 3033, 1992.

[24] Z. Jiwei, Y. Xi, W. Mingzhong, and Z. Liangying, "Preparation and microwave characterization of $PbTiO_3$ ceramic and powder," *Journal of Physics D: Applied Physics,* vol. 34, no. 9, pp. 1413, 2001.

[25] D. Arney, T. Watkins, and P. A. Maggard, "Effects of particle surface areas and microstructures on photocatalytic H_2 and O_2 production over $PbTiO_3$," *Journal of the American Ceramic Society,* vol. 94, no. 5, pp. 1483-1489, 2011.

[26] B. Chen, X. Zheng, M. Yang, Y. Zhou, S. Kundu, J. Shi, K. Zhu, and S. Priya, "Interface band structure engineering by ferroelectric polarization in perovskite solar cells," *Nano Energy,* vol. 13, pp. 582-591, 2015.

[27] G. Burns, and B. A. Scott, "Lattice Modes in Ferroelectric Perovskites: $PbTiO_3$," *Physical Review B,* vol. 7, no. 7, pp. 3088, 1973.

[28] C. Foster, Z. Li, M. Grimsditch, S.-K. Chan, and D. Lam, "Anharmonicity of the lowest-frequency A 1 (TO) phonon in $PbTiO_3$," *Physical Review B,* vol. 48, no. 14, pp. 10160, 1993.

[29] Y. I. Yuzyuk, R. Farhi, V. Lorman, L. Rabkin, L. Sapozhnikov, E. Sviridov, and I. Zakharchenko, "A comparative Raman study of ferroelectric $PbTiO_3$ single crystal and thin film prepared on MgO substrate," *Journal of applied physics,* vol. 84, no. 1, pp. 452-457, 1998.

[30] M. Chen, Z. Shen, S. Tang, W. Shi, D. Cui, and Z. Chen, "Stress effect on Raman spectra of Ce-doped BaTiO3 films," *Journal of Physics: Condensed Matter,* vol. 12, no. 31, pp. 7013, 2000.

[31] B. Mani, C.-M. Chang, and I. Ponomareva, "Atomistic study of soft-mode dynamics in $PbTiO_3$," *Physical Review B,* vol. 88, no. 6, pp. 064306, 2013.

[32] I. Taguchi, A. Pignolet, L. Wang, M. Proctor, F. Levy, and P. Schmid, "Raman scattering from $PbTiO_3$ thin films prepared on silicon substrates by radio frequency sputtering and thermal treatment," *Journal of Applied Physics,* vol. 73, no. 1, pp. 394-399, 1993.

[33] J. Ryu, G. Han, T. K. Song, A. Welsh, S. Trolier-McKinstry, H. Choi, J.-P. Lee, J.-W. Kim, W.-H. Yoon, and J.-J. Choi, "Upshift of phase transition temperature in nanostructured $PbTiO_3$ thick film for high temperature applications," *ACS applied*

materials & interfaces, vol. 6, no. 15, pp. 11980-

4. Chapter 4: Low Frequency MEMS Energy Harvester

4.1. Introduction

Recent advances in RF transmitters, sensors (e.g. temperature sensor ~ 71 nW, pressure sensor ~ 5.3nW)[1, 2] and integrated chipsets (e.g. microprocessor ~500 pW)[3] have enabled the possibility of developing ambient powered microdevices [4-10]. Considerable attention has been paid to mature this possibility by demonstrating microscale solar[11], thermal[12], electromagnetic[13, 14] and mechanical energy harvesters[15-18]. Especially, energy harvesting from mechanical vibrations is attractive due to it ubiquitous nature on platforms such as machines, transportation and humans. There are four typical mechanical-to-electrical energy conversion mechanisms: piezoelectric, electromagnetic, triboelectric and electrostatic. Among these mechanisms, at micro-scale, piezoelectric energy harvesting has been extensively investigated because of high electromechanical conversion efficiency, energy density, and simplicity in integration with silicon [19-23].

In order to achieve direct integration with system-on-a-chip, the energy harvester should have microscale dimension and the fabrication process should be compatible with integrated circuits based on silicon. To maximize the generated electrical power from vibrations, the energy harvester should be operated at resonance frequency because displacement of piezoelectrics is significantly reduced in off-resonance and thereby most of the input vibrational energy is lost [16]. The natural frequency of the cantilever beam for the first bending mode can be expressed as [20]:

$$\omega_n = \sqrt{\frac{k_{eq}}{m_{eq}}} = \sqrt{\frac{3EI}{L^3(M_l+0.24M_p)}} \qquad (4.1)$$

where m_{eq} is the equivalent mass, k_{eq} is the equivalent spring constant, L is the length of the

beam, EI is the bending stiffness of the beam, M_l is the mass per unit beam length, and M_p is weight of proof mass. From this expression it can be seen that the natural frequency of cantilever beam is inversely proportional to length of beam and directly proportional to stiffness of the beam. Typical silicon-based MEMS energy harvesters have high natural frequency, typically in the range 500 Hz ~ 10 kHz, owing to their small dimensions (L) and stiff silicon substrate [16, 24, 25]. However, natural frequencies of most of the ambient vibration sources are normally less than 200 Hz [26]. To tune the natural frequency of the energy harvester to lower frequencies, the silicon beam needs to be designed to have higher effective length but smaller dimension along other directions.

The generated output power is dependent on the area of the effective electrode area of piezoelectric materials. The generated output power from a piezoelectric material based unimorph cantilever can be determined from the expression [27]:

$$P_{output} = V_{piezo} E_{piezo} S f k_{xy}^2 \tag{4.2}$$

and

$$k_{xy}^2 = \frac{Stored\ energy}{Input\ mechanical\ energy} = \frac{d_{xy}^2 E}{\varepsilon} \tag{4.3}$$

where V_{piezo} , E_{piezo} , S , f , k_{xy} , and ε are the volume of the piezo material, Young's modulus, strain, excitation frequency (Hz), electromechanical coupling coefficient with x- poling and y- applied stress direction, and dielectric permittivity, respectively. From Equation (4.2) and (4.3), we can see that the generated electric power is proportional to piezoelectric constant (d_{xy}) which is entirely related to characteristics of piezoelectric materials. In addition, according to the poling and applied stress direction of the piezoelectric material, the d_{xy} value can be changed in the same material. For example, a unimorph cantilever structure uses a transversal 31 mode because applied stress direction is perpendicular to poling direction in piezoelectric material.

By using interdigitated electrodes (IDE) instead of parallel electrodes, we can exploit longitudinal 33 mode. Generally, the d_{33} value is about two times larger than the d_{31} value in the same piezoelectric material. However, it is difficult to confirm if the generated power in a device with IDE is larger than that of parallel electrode because of large capacitance which results in small electric current. In this paper, we present solutions to these challenges in the design of low natural frequency and high power density MEMS piezoelectric energy harvester. The structure was fabricated by silicon MEMS process and exhibited an ultra-low natural frequency in few millimeter square dimension. The design is based upon a novel circular spiral cantilever structure as shown in Figure 4.1. In order to control the natural frequency of the energy harvester we provide relationship of the frequency with number of turns in spiral.

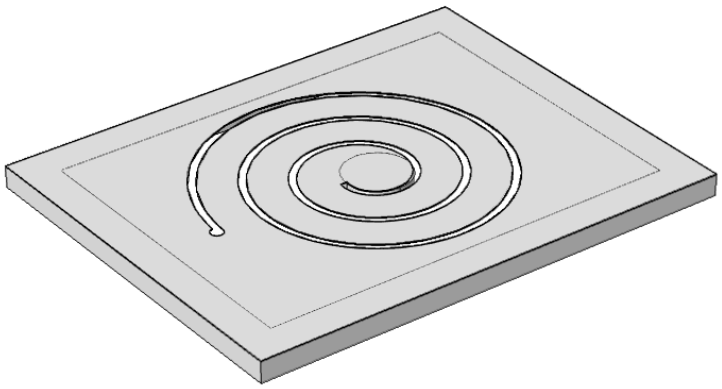

Figure 4.1. Schematic design of spiral MEMS energy harvester.

4.2. Experimental

4.2.1. Multilayer Deposition of Films

The spiral-shape MEMS cantilevers were fabricated using a silicon-on-insulator (SOI) wafer with 10 μm silicon device layer, 1 μm buried oxide layer, and 300 μm silicon handle layer. The process started with deposition of Pt/Ti/PZT/Ti/Pt/SiO_2 films on the SOI wafer as shown in

Figure 4.2. After thermally growing the oxide layer of 500 nm on the front and back side of the wafer, a Pt(150 nm) /Ti(50 nm) bottom electrode was in-situ deposited by thermal evaporator. The Ti was used as a buffer layer for better adhesion between the oxide substrate and the bottom electrode Pt. $Pb(Zr_{0.52},Ti_{0.48})O_3$ (PZT) sol-gel solution was prepared following a previous experiment without Poly(N-vinylpyrrolidone) addition [28]. The PZT sol was spin-coated multiple times on the platinized SOI wafer at a rate of 4,000 rpm for 40 seconds to reach the thickness of 1.8 μm. The film was pyrolized by a two-step heat treatment at 150 ^{o}C and 350 ^{o}C for 10 minutes per-process on a hot plate in order to remove solvents and organics. Every third layer was annealed at 600 ^{o}C for 10 minutes by rapid thermal annealing. Lastly, Pt(150 nm) / Ti(50 nm) thin films were sequentially deposited by DC magnetron sputtering without breaking vacuum to form the top electrode. The microstructure and crystal orientation of the PZT films were determined by using a field-emission scanning electron microscope (FESEM) and an X-ray diffractometer (XRD). The polarization and piezoelectric properties of the PZT thin films were measured using the Radiant Technology RT-66A and piezo response force microscopy (PFM), respectively.

4.2.2. MEMS Fabrication Process

Following the multilayer deposition, the cantilever structure with spiral shape was produced using typical surface and bulk micromachining process. The detailed micromachining process is illustrated in Figure 4.2 (b). First, the SOI wafer with the multilayer films was rinsed in D.I water and then dehydrated at 110 ^{o}C. The wafer was coated on both front and back sides by thick photoresist (AZ 9260, Microchemicals GmbH) and patterned. The Pt/Ti top electrode was etched by reactive ion etching (RIE) as shown in Figure 4.2 (b) (ii). The wet-etching solution for PZT film was prepared as mixing HF and HCl aqueous solutions (HF: HCl : D.I. water =

1 : 2 : 8) at room temperature [29]. The etching process was performed by immersing the PZT films into as-prepared etchant at room temperature with gentle agitation as illustrated in Figure 4.2 (b) (iii). The etch rate was approximately 50 nm/sec. The bottom electrode and surface oxide layer were also patterned using RIE as shown in Figure 4.2 (b) (iv). In Figure 4.2 (b) (v), the 10 μm silicon device layer and buried oxide layer were etched by deep reactive ion etching (DRIE) and RIE to define the thickness of the cantilever substrate, respectively. Finally, in Figure 4.2 (b) (vi), the surface oxide window and the silicon handle layer were etched from the backside using DRIE to release the PZT cantilever structure and to form a silicon proof mass at the center of the spiral cantilever. When etching was completed, the photoresist masks were removed by acetone. Fabricated devices were diced by laser cutting machine. To avoid electrical short and to achieve complete poling of the piezoelectric layers under a high electric field, a corona poling system was exploited [30]. Electric field of 8 kV was applied at the center of the spiral energy harvester at 1 cm distance from top electrodes. After poling, the energy generation was characterized by a vibration shaker (type 4809, Brüel & Kjær) and digital oscilloscope (Tektronix TDS754). The output voltage and generated power of the energy harvesters were measured by varying resistive loads while considering an inner resistance of the oscilloscope (1MΩ). The vibration characteristics of the spiral energy harvesters were analyzed using a scanning laser vibrometer (Polytec, PSV-400).

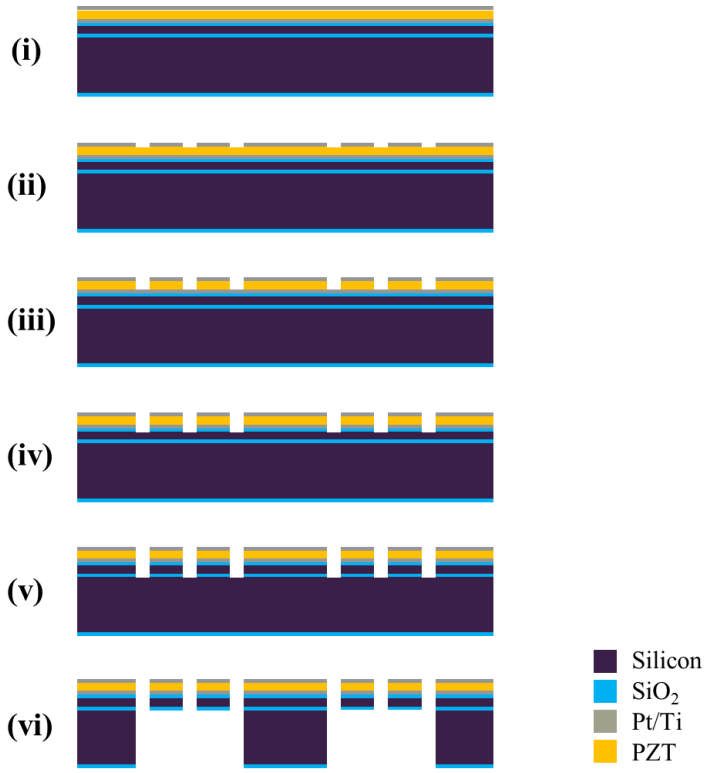

Figure 4.2. Schematic fabrication procedure for piezoelectric MEMS energy harvester with spiral structure. (i) Multilayer deposition, (ii) Top electrode patterning, (iii) PZT etching, (iv) Bottom electrode patterning, (v) Front side DRIE etching and (vi) Back side DRIE etching and releasing structure.

4.3. Results and Discussion

4.3.1. Characterization of PZT Thin Film

For the MEMS piezoelectric energy harvester, one of the most important issues is growth of a quality piezoelectric film on a silicon substrate. We have fabricated the PZT film on a 4-inch platinized silicon SOI wafer by sol-gel method. The overall deposition and annealing process were conducted inside clean room in order to form homogenous perovskite PZT film without cracks and defects. Figure 4.3 (a) and (b) shows the cross-section and top surface SEM images of 1.8 μm PZT (52/48) thin films. As shown in Figure 4.3 (a), the PZT film has the columnar structure as a result of the nucleation on the bottom electrode and vertical grain growth. The

surface SEM image, as shown in Figure 4.3 (b), was taken after Pt/Ti top electrode etching to check the reactive ion etch-induced damages on the PZT film and it shows a dense and crack-free morphology. The grain boundaries are not clear in this image because of RIE etching however the grain size can be estimated to be approximately 150 nm from the topographic atomic force microscopy (APM) image shown in Figure 4.4.

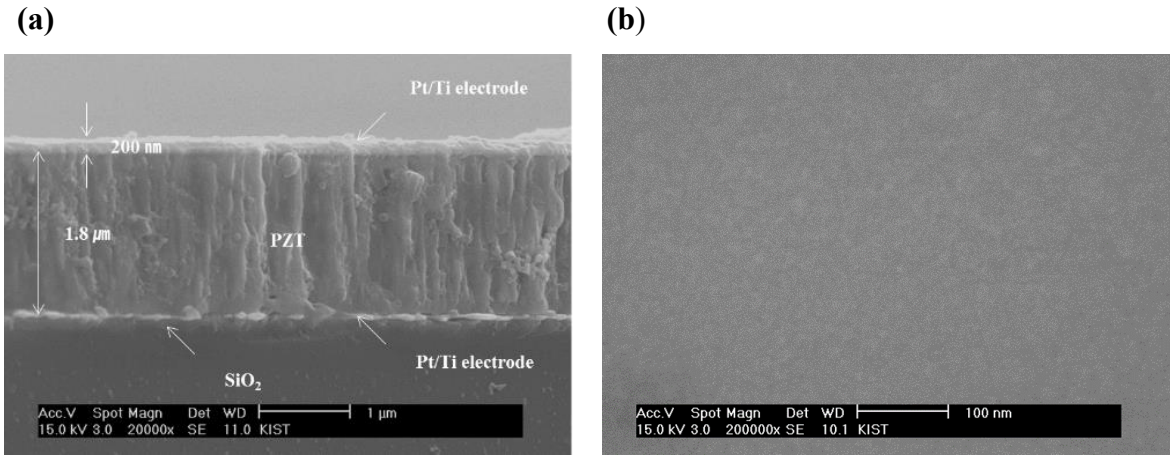

Figure 4.3. (a) Cross-sectional and (b) surface SEM images of PZT thin films used in the fabrication of spiral MEMS energy harvester. The surface SEM image was taken after etching top electrodes.

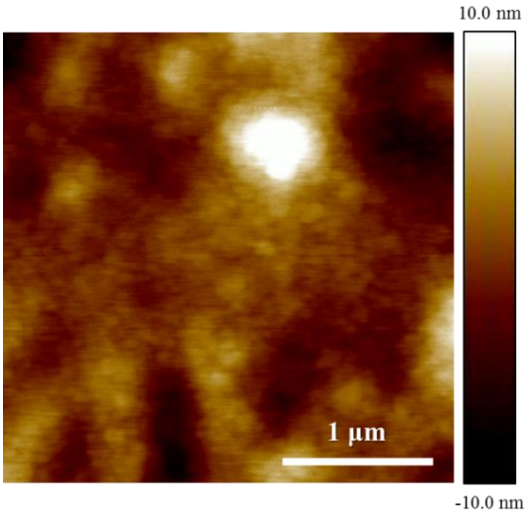

Figure 4.4. Surface topographic image of the PZT film used in the MEMS energy harvester.

Figure 4.5 (a) shows the X-ray diffraction (XRD) spectra of the PZT thin film. A single-phase PZT with perovskite crystal structure was formed with randomly oriented grain morphology. Figure 4.5 (b) shows the polarization-electric filed (P-E) hysteresis loops of the PZT thin film on the spiral MEMS energy harvester. The remnant polarization (P_r) and spontaneous polarization (P_s) of the PZT thin film are 36.2 μC/cm^2 and 59.8 μC/cm^2, respectively. The coercive electric field is 141 kV/cm. For energy harvesting applications, the deposited PZT films will show higher electric power through transverse piezoelectric properties [31].

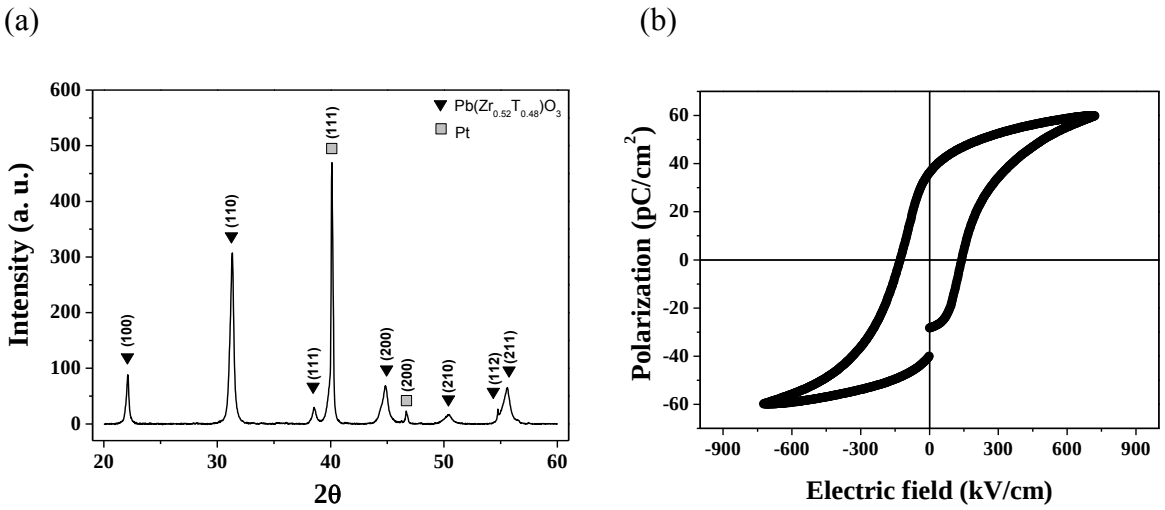

Figure 4.5. (a) X-ray diffraction patterns (b) Polarization vs. electric field (P-E) hysteresis curve of the PZT thin film.

To understand the ferroelectric behavior and domain structure of the PZT thin film, piezoresponse force microscopy (PFM) was employed. Figure 4.6 (a) and (b) shows the out-of-plane PFM phase and amplitude images acquired from the PZT film used in the spiral MEMS energy harvester, respectively. In the phase image (Figure 4.6 (a)), different color contrast corresponds to different polarization [32]. The film exhibits strong longitudinal amplitude as shown in Figure 4.6 (b), which suggests the predominantly out-of-plane

orientation of the polarization vector and high piezoelectric response along this direction. To verify this, the effective longitudinal piezoelectric constant, $d_{33,f}$ of the PZT film was measured using piezoresponse force microscope (PFM) [33]. The typical hysteresis loop obtained by measuring the piezo response by small ac signal as a function of a superimposed dc field is given in Figure 4.7. The value of $d_{33,f}$ was found to be higher ~97 pm/V under negative bias. It is well known that thin film piezoelectric constants are reduced with respect to bulk ceramic values because of the clamping effect on the substrate. The real d_{33} value of piezoelectric thin films can be calculated by following equation (4.4) [34]:

$$d_{33,f} = d_{33} - 2d_{31}\frac{(s_{13}^{E}+\sigma/Y)}{(s_{11}^{E}+s_{12}^{E})} \tag{4.4}$$

where s_{11}, s_{12}, and s_{11} are the mechanical compliances of the piezoelectric film and d_{31} is the transverse piezoelectric coefficient, and Y and σ are the Young's modulus and the Poisson's ratio of the substrate, respectively. The real d_{33} value of this PZT thin film has been calculated from ceramics data in previous studies [35, 36]. The calculated d_{33} vales were depicted in Figure 4.7 and exhibited the maximum value at 155 pm/V.

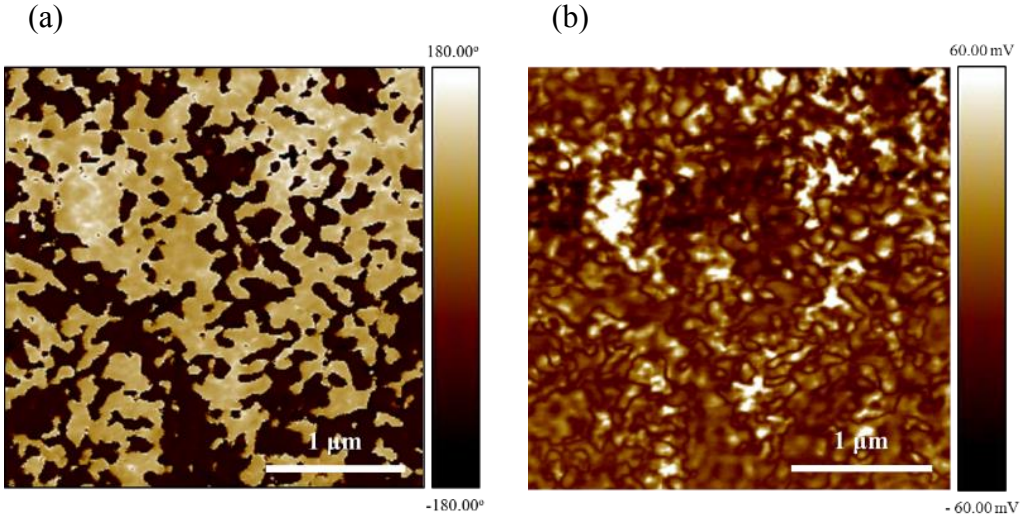

Figure 4.6. Out-of-plane PFM images of the PZT film: (a) Amplitude and (b) Phase.

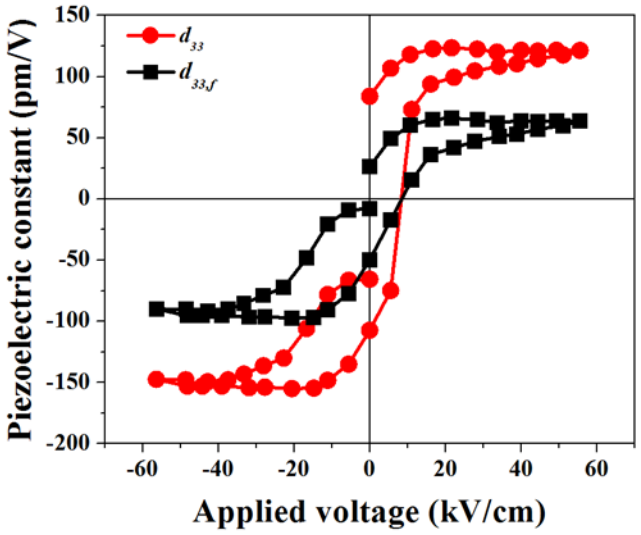

Figure 4.7. Out The clamped longitudinal effective piezoelectric coefficient ($d_{33,f}$) and calculated real longitudinal piezoelectric coefficient (d_{33}) with variation of applied dc field for the PZT thin film grown on the spiral cantilever.

4.3.2. Evaluation of MEMS Energy Harvester

Figure 4.8 shows SEM images of fabricated spiral MEMS energy harvester. From Figure 4.8 (a) and (d), we can see a clearly defined cantilever structure with spiral shape. Figure 4.8 (a) shows the front view of the fabricated two turns of the spiral MEMS harvester. In case of spiral cantilever structure, the bending stress will be concentrated on only one end of the connection region with clamping substrate. Therefore, we included in our harvester design a round-shaped notch in order to release the stress and prevent crack propagation as indicated by red dot in Figure 4.8 (a). This was verified by FEM simulation. Figure 4.8 (e) and (f) show the simulated stress distributions of sharp and round-shaped junction in the spiral MEMS energy harvester, respectively. As indicated in red dot circles in Figure 4.8 (e) and (f), the stress was much more relaxed in round-shaped junctions than sharp ones. The etched surface of the sidewalls of the spiral MEMS energy harvester was magnified in Figure 4.8 (b). An accurately defined vertical sidewall of the silicon substrate was achieved without ripples by etching and passivating cycles in the Bosch process. However, a relatively rough surface with planar direction was observed

due to the uneven recession of the soft masking of photoresist that transfers vertical striations onto the sidewalls. The use of hard masking materials, like silicon dioxide, helps alleviate this kind of surface roughness problem with planar direction [37]. We can observe that the 1~2 μm gap between the PZT layer and Pt/Si substrate was formed by a slight over etching of PZT layer during isotropic wet-etching. However, it did not affect the electrical isolation between the top and bottom electrodes.

Figure 4.8 (c) shows the cross-sectional view of the diaphragm of the spiral MEMS energy harvester. The crack-free and homogeneous interface of PZT film and silicon diaphragm can be seen in this figure which ensures excellent transfer of input mechanical energy to the piezoelectric layer. The 10 μm thickness silicon substrate of spiral cantilever was uniformly achieved throughout the diaphragm due to the SiO_2 etch stop in SOI wafer during backside DRIE etching process. Figure 4.8 (d) shows the back side image of the fabricated four turns of spiral MEMS harvester with a silicon proof mass which was formed by backside anisotropic dry etching of silicon substrate. The figure demonstrates the clearly defined and released silicon proof mass. The diameter and thickness of the proof mass are 945 μm and 300 μm, respectively. The weight of the silicon proof mass can be determined to be approximately 4.90×10^{-4} g using density of single crystal silicon substrate to be 2330 kg/m^3. The same size and weight of proof masses were fabricated and applied to all different spiral MEMS energy harvesters fabricated in this study.

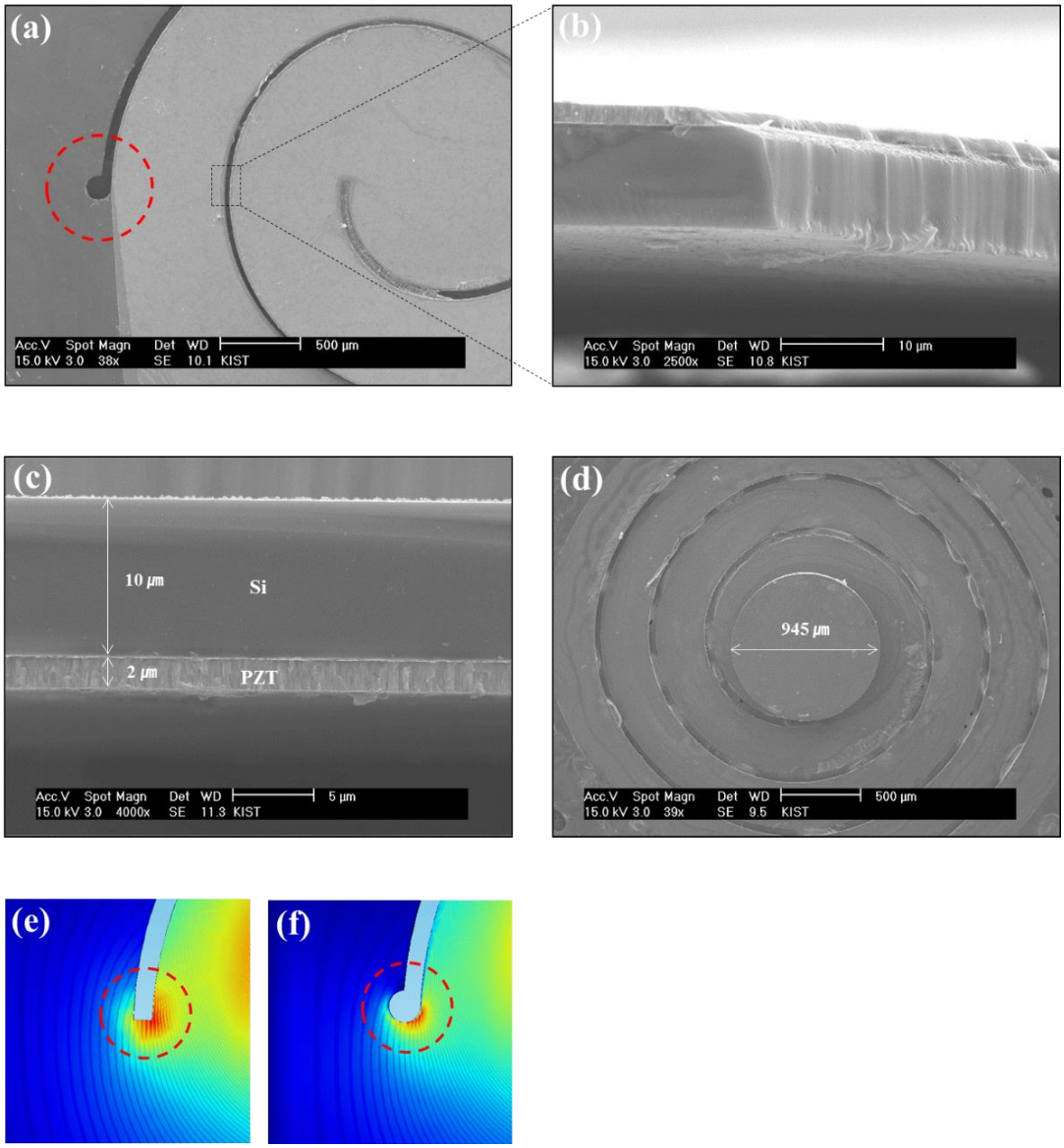

Figure 4.8. SEM images of (a) front side, (b) etched edge, (c) cross-section of membrane and (d) back side of the spiral cantilever energy harvester. Simulated stress distribution of (e) sharp junction and (f) round shape junction in the spiral energy harvester.

The dynamic behavior of the fabricated spiral MEMS energy harvester was characterized by using the vibration testing system (Figure 4.9) including a shaker, power amplifier, function generator and oscilloscope. The harvester was assembled in a mounting holder by superglue and then attached on top of the shaker whose vibration conditions were monitored by an accelerometer. The devices were excited by 2.45 m/s^2 (0.25 g) acceleration and maintained

same acceleration under changing vibration frequency. The generated output voltages of the harvesters were measured by digital oscilloscope.

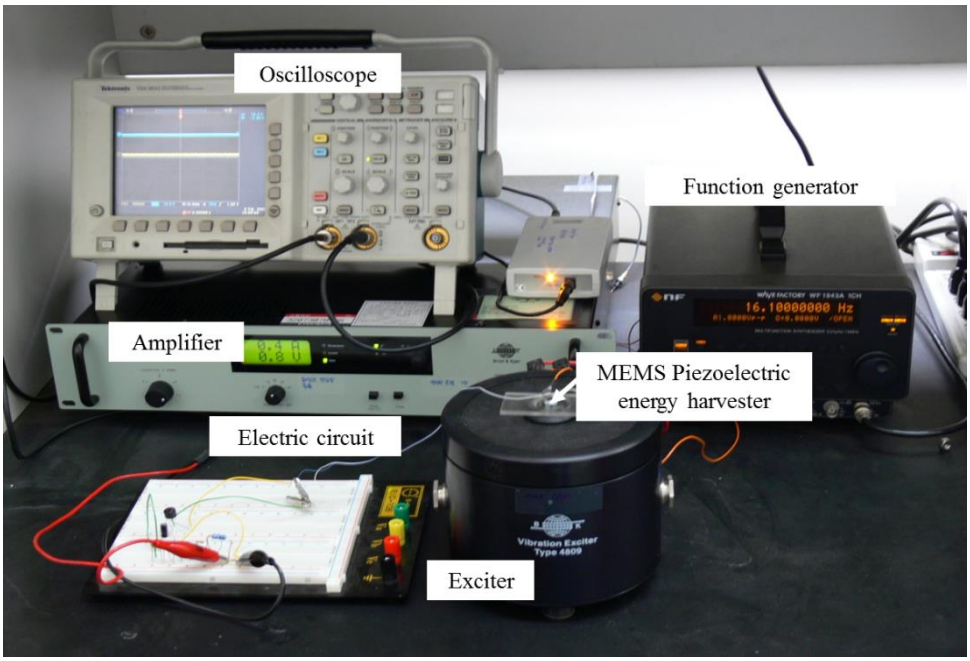

Figure 4.9. Experimental test set-up for the spiral MEMS energy harvesters

Figure 4.10 shows the frequency dependence of output voltage with varying number of turns of the spiral energy harvester. The open circuit output voltages of each harvester was measured by oscilloscope and the RMS value ($V_{Peak\text{-}Peak}/\sqrt{2}$) was recorded for further analysis. The generated output voltage gradually increased up to five turns and then started to slightly decrease with increasing number of turns. This might be because the dimension of active region in the energy harvesters was slightly increased with increasing number of turns as shown in Figure 4.10 (i) ~ (vi) images, however at higher number of turn the vibration mode became mixed. With increasing number of turns in spiral structure, it is more likely to have higher vibration modes such that torsion starts to influence the bending mode. Figure 4.10 (i) ~ (vi) shows the optical images of the fabricated spiral MEMS energy harvesters from two to seven turns, respectively. The access pads of top and bottom electrodes were wire-bonded onto the

mounting holder and connected to an electric circuit board as indicated in Figure 4.10 (i). The overall dimensions of devices are approximately 19.25 (7 × 5.5 × 0.5) mm^3. The active area and volume of the piezoelectric energy harvesters are less than 10.75 mm^2 and 0.11 mm^3, respectively.

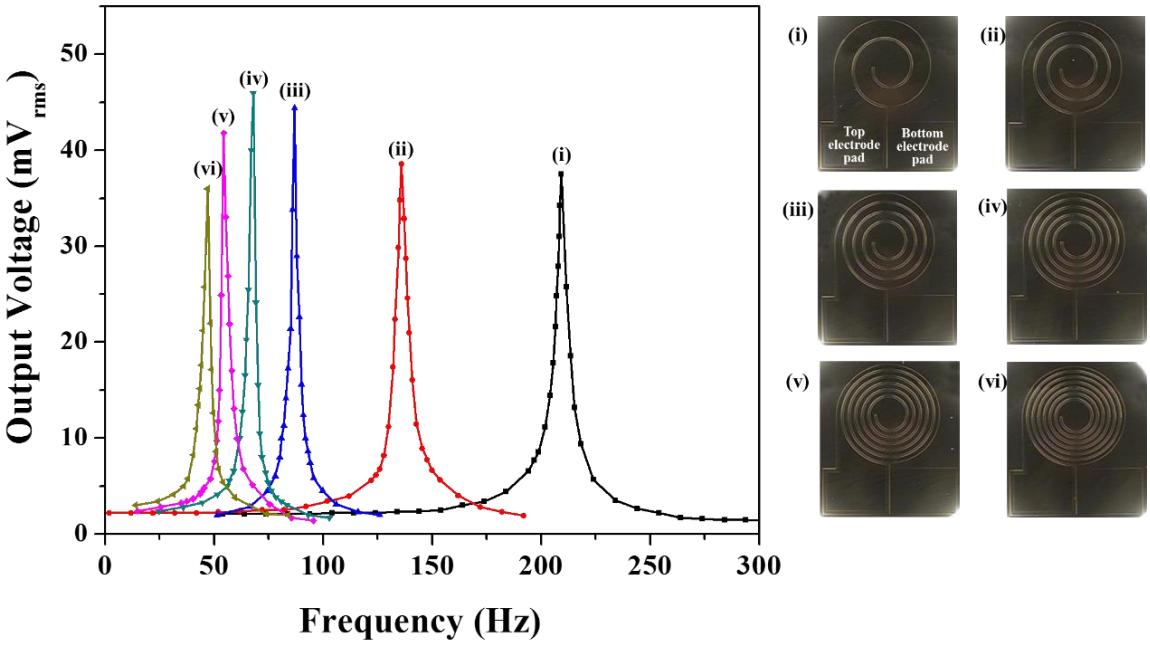

Figure 4.10. (a) Frequency dependence of output peak voltages with the variation of number of turns of the spiral energy harvester. The harvesters were excited by 2.45 m/s^2 (0.25 g) acceleration. (Inset) Optical pictures of the fabricated spiral energy harvester with number of turns; (i) 2 turns, (ii) 3 turns, (iii) 4 turns, (iv) 5 turns, (v) 6 turns and (vi) 7 turns.

Figure 4.11 (a) ~ (d) shows the measured and simulated vibration mode shapes of three turns of spiral MEMS energy harvesters. Figure 4.11 (a) and (c) are the measured first and second vibration mode shapes of the spiral MEMS harvester obtained by scanning laser vibrometer respectively. The first resonance vibration mode at 136 Hz shows a distinct up and down displacement. The center of the spiral harvester on which the proof mass was placed reached the maximum displacement amplitude. This clearly guarantees that there will be no voltage cancellation by polarity difference in the piezoelectric element. However, the second resonance

mode observed at 348Hz shows a flapping shape with the edges of spiral exhibiting maximum displacement amplitude instead of center. This vibration motion could reduce the overall output power by the voltage cancellation from the left and right side regions of piezoelectric element having different polarity during bending motion as shown in Figure 4.11 (b). Thus, the second vibration mode should be avoided or the electrodes of left and right side parts should be separated to prevent the voltage cancellation. In order to further analyze the vibration characteristics of the MEMS harvester, the finite element modeling (FEM) was conducted using COMSOL Multiphysics simulation tool. Figure 4.11 (c) and (d) shows the simulated mode shapes of the first and second vibration modes corresponding to resonance frequencies of 139Hz and 356Hz, respectively. Both simulated shapes of the first and second modes exactly matched to the experimental result shown in Figure 4.11 (a) and (b). The inset image in Figure 4.11 (c) shows simulated stress distributions of the first resonance mode. Most of the stress is concentrated at the emerging curvature rather than the center of spiral and the stress distribution in an inside edge is much larger than that on outside edge. The stress distribution of the second resonance mode are also shown in Figure 4.11 (d) inset. Most of stress in second vibration mode is concentrated on the flapping bending regions and the bending region closed to clamping point has a lager stress than the other end. The generated output power is proportional to the applied stress to piezoelectric element.

(a) **(b)**

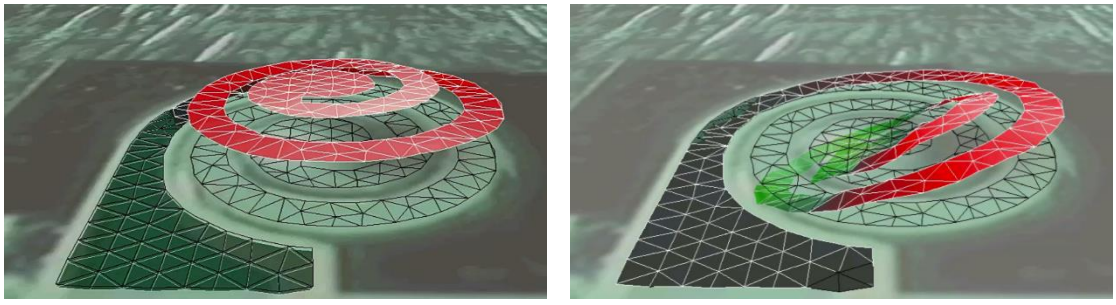

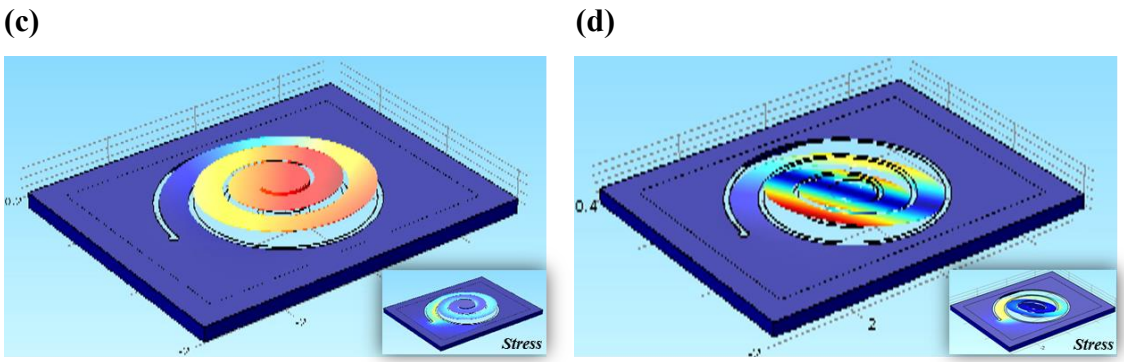

Figure 4.11. 2D live scan images obtained by laser vibrometer of the (a) first and (b) second vibration modes and FEM simulated images of (c) first and (d) second vibration modes for the 3 turns of spiral MEMS energy harvester. (Inset) Simulated stress distributions in the first and second modes.

Figure 4.12 (a) shows the change in natural frequency with variation of number of turns in the spiral MEMS energy harvester. The FEM simulation results for natural frequencies are almost matched to the experimental results. The slightly different values between simulation and experiment could be attributed to the fabrication deviation from the expected dimensions. As can be seen from Figure 4.12 (a), the resonance frequencies of the spiral MEMS energy harvesters were gradually decreased with increasing number of turns. The lowest resonance frequency of 48 Hz was achieved in the 7 turns spiral MEMS energy harvester, which is one of the lowest natural frequency reported in literature for silicon MEMS energy harvesters at millimeter square dimension. One can further reduce the natural frequency of the MEMS harvester by increasing the weight of the proof mass. The natural frequency of the spiral harvester can be expressed in terms of the number of spiral N by the empirical fit:

$$f = 555.3N^{-1.273} \tag{4.5}$$

where N is number of turns in MEMS energy harvester and f is natural frequency. The equation (4.5) was obtained from a parabolic fitting of FEM simulation results in Figure 4.12 (a). The

natural frequency of spiral energy harvester exponentially decreased with increasing number of turns. Following equation (4.5), the natural frequency of the MEMS harvester can be adjusted through variation in number of turns and weight of proof mass.

Figure 4.12 (b) shows the output power and voltage with variation of load resistances at resonance frequency of 68 Hz when the five turn spiral MEMS energy harvester was excited at acceleration of 0.25 g. The maximum output power of 23.3 nW was obtained at an optimum load resistance of about 40 kΩ. This value was matched to the measured impedance value of the piezoelectric materials in the MEMS harvester at same frequency. The energy density of MEMS harvester was normalized by acceleration, resonance frequency and dimension. The normalized area and volumetric energy density of five turn spiral MEMS energy harvester were 5.04×10^{-4} μW/mm^2·g^2·Hz and 4.92×10^{-2} μW/mm^3·g^2·Hz, respectively. The comparison of the resonance frequency and normalized energy density of recent piezoelectric MEMS energy harvesters are shown in Table 4. The energy densities of the harvesters were normalized by active area, volume, square of acceleration and resonance frequency in order to fairly compare experimental conditions. The spiral MEMS energy harvester in this work showed the lowest resonance frequency which is within useable ambient frequency region and a high volumetric power density as shown in Table 4. The spiral MEMS energy harvester was excited at low acceleration of 0.25g and generated enough power to operate the ultralow power sensors and microprocessors [2, 3].

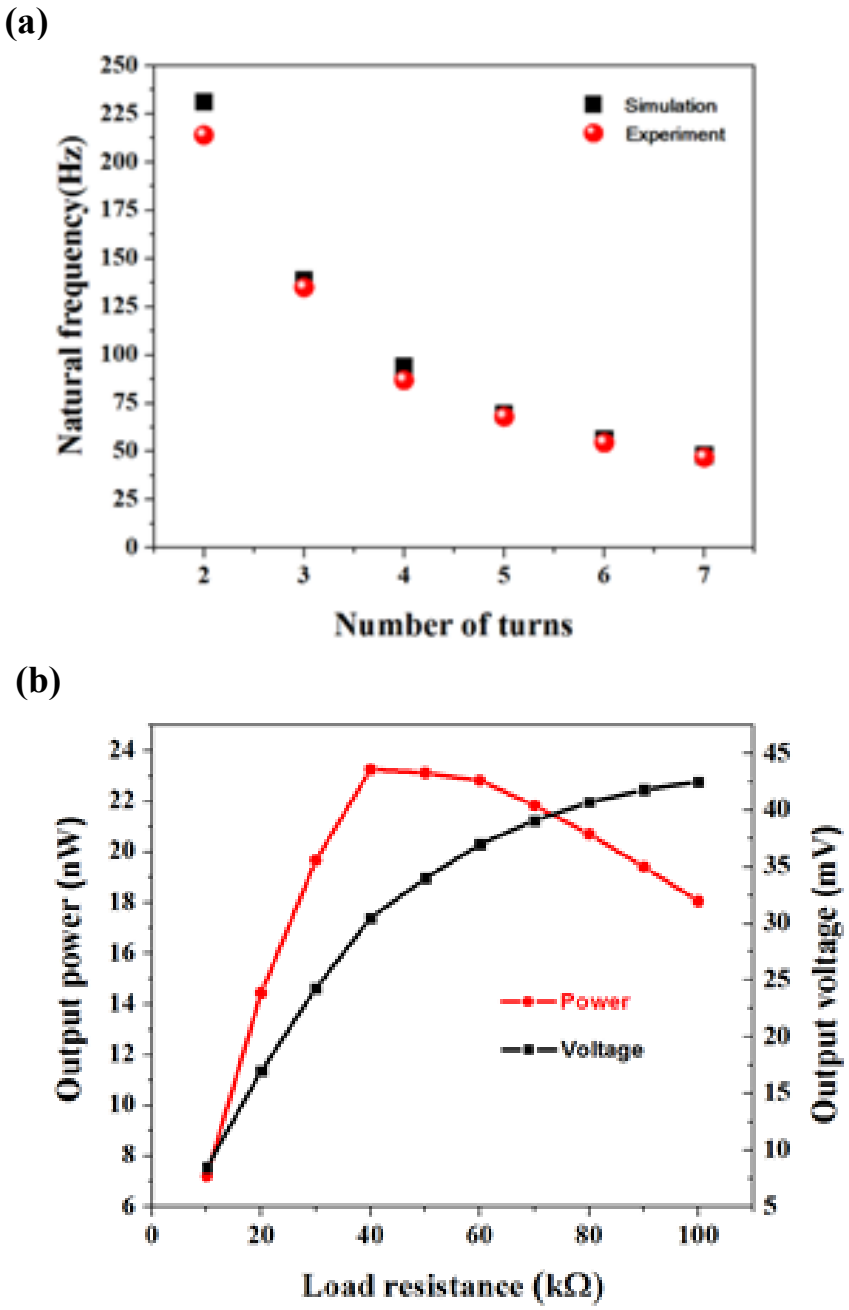

Figure 4.12. (a) Natural frequencies of the spiral energy harvesters with variation of number of turns. (b) Output power and voltage of the 5 turns spiral energy harvester with variation of external electrical load.

Table 4. Comparison of normalized power density and resonance frequency of recent MEMS energy harvesters [38-50]

	Active Area (mm^2)	Active Volume (mm^3)	Acceleration (g)	Resonance Frequency (Hz)	Power (μW)	Normalized Areal Power Density, ($\mu W/(mm^2.g^2.Hz)$)	Normalized Volumetric Power Density, ($\mu W/(mm^3.g^2.Hz)$)
This work	10.75	0.11	0.25	68	0.023	5.04×10^{-4}	0.0492
Durou et al. (2010)		464	0.2	76	13.9		0.01
Morimoto et al. (2010)	76.5	4.05	0.5	126	5.3	2.2×10^{-3}	0.042
Aktakka (2012)	49	27	1.5	154	205	0.0121	0.0219
Defosseux et al. (2012)	3.573 (est.)	2.8	0.275	214	0.63	0.0109	0.0138
Lei et al. (2011)		18.6	1.0	235	14		0.0032
Xu et al. (2012)	35.75	11.53	1.0	247	37.1	4.2×10^{-3}	0.013
Park et al. (2010)	1.8	1.05	0.39	528	1.1	7.69×10^{-3}	0.0131
Elfrink et al. (2010)		15	0.2	599	69		0.192
Fang et al. (2006)	2.65	0.78	1.0	608	2.16	1.34×10^{-3}	0.0046
Hirasawa et al. (2010)		1.63	1.0	857	0.18		1.29×10^{-4}
Muralt et al. (2009)	0.96	0.48	2.0	870	1.4	4.19×10^{-4}	8.8×10^{-4}
Kanno et al. (2012)	56.1	11.4	1.0	1036	1.1	1.89×10^{-5}	9.31×10^{-5}
Hajati and Kim (2011)	120	0.02	4.0	1300	22	8.83×10^{-5}	0.053

4.4. Summary

In summary, we have demonstrated the fabrication of spiral MEMS energy harvester with an ultra-low resonance frequency and high power density. The PZT thin film with 1.8 um thickness was deposited on a platinized SOI wafer exhibiting high crystalline quality and good piezoelectric properties. The spiral cantilever structure with different number of turns was fabricated by the industry compatible microfabrication process. In order to analyze dynamic behavior of the energy harvester, the vibration mode shape and stress distribution in the first and second resonance were characterized by scanning laser vibrometer and FEM simulation. The natural frequency of the spiral MEMS harvester gradually decreased with increasing number of turns and the lowest resonance frequency of 48 Hz was achieved in harvester with seven turns. Depending on the number of turns and weight of proof mass, the natural frequency of the spiral MEMS harvester was tunable to low frequency ambient vibrations. The maximum output power of 23.3 nW was obtained in the 5 turns spiral MEMS harvester excited at 0.25g and at its resonance frequency of 68 Hz. The results show that spiral piezoelectric MEMS energy harvester could provide solution for realizing standalone MEMS devices.

References

[1] S. Jeong, Z. Foo, Y. Lee, J.-Y. Sim, D. Blaauw, and D. Sylvester, “A fully-integrated 71 nW CMOS temperature sensor for low power wireless sensor nodes,” *Solid-State Circuits, IEEE Journal of,* vol. 49, no. 8, pp. 1682-1693, 2014.

[2] G. Chen, H. Ghaed, R. Haque, M. Wieckowski, Y. Kim, G. Kim, D. Fick, D. Kim, M. Seok, and K. Wise, "A cubic-millimeter energy-autonomous wireless intraocular pressure monitor." pp. 310-312.

[3] H. Okada, T. Itoh, and T. Masuda, "Development of custom CMOS LSI for ultra-low power wireless sensor node in health monitoring systems." pp. 1197-1200.

[4] B. Dang, and T. Kaya, “A Low Power Wireless Signal Transmitter for Biomedical Micro-Sensors,” 2012.

[5] S. Hanson, M. Seok, Y.-S. Lin, Z. Foo, D. Kim, Y. Lee, N. Liu, D. Sylvester, and D. Blaauw, “A low-voltage processor for sensing applications with picowatt standby mode,” *Solid-State Circuits, IEEE Journal of,* vol. 44, no. 4, pp. 1145-1155, 2009.

[6] Y. Lee, S. Bang, I. Lee, Y. Kim, G. Kim, M. H. Ghaed, P. Pannuto, P. Dutta, D. Sylvester, and D. Blaauw, “A Modular 1 mm Die-Stacked Sensing Platform With Low Power I C Inter-Die Communication and Multi-Modal Energy Harvesting,” *Solid-State Circuits, IEEE Journal of,* vol. 48, no. 1, pp. 229-243, 2013.

[7] G. Kim, Y. Lee, Z. Foo, P. Pannuto, Y.-S. Kuo, B. Kempke, M. H. Ghaed, S. Bang, I. Lee, and Y. Kim, "A millimeter-scale wireless imaging system with continuous motion detection and energy harvesting." pp. 1-2.

[8] Y.-s. Kuo, P. Pannuto, G. Kim, Z. Foo, I. Lee, B. Kempke, P. Dutta, D. Blaauw, and Y. Lee, "MBus: A 17.5 pJ/bit/chip portable interconnect bus for millimeter-scale sensor systems with 8 nW standby power." pp. 1-4.

[9] Q. Zhou, A. Sussman, J. Chang, J. Dong, A. Zettl, and W. Mickelson, “Fast response integrated MEMS microheaters for ultra low power gas detection,” *Sensors and Actuators A: Physical,* vol. 223, pp. 67-75, 2015.

[10] M. Balouchestani, and S. Krishnan, “Effective low-power wearable wireless surface EMG sensor design based on analog-compressed sensing,” *Sensors,* vol. 14, no. 12, pp. 24305-24328, 2014.

[11] X. Sheng, C. A. Bower, S. Bonafede, J. W. Wilson, B. Fisher, M. Meitl, H. Yuen, S. Wang, L. Shen, and A. R. Banks, “Printing-based assembly of quadruple-junction four-

terminal microscale solar cells and their use in high-efficiency modules," *Nature materials,* vol. 13, no. 6, pp. 593-598, 2014.

[12] N. Wojtas, L. Rüthemann, W. Glatz, and C. Hierold, "Optimized thermal coupling of micro thermoelectric generators for improved output performance," *Renewable energy,* vol. 60, pp. 746-753, 2013.

[13] S. P. Beeby, R. Torah, M. Tudor, P. Glynne-Jones, T. O'Donnell, C. Saha, and S. Roy, "A micro electromagnetic generator for vibration energy harvesting," *Journal of Micromechanics and microengineering,* vol. 17, no. 7, pp. 1257, 2007.

[14] B. Yang, C. Lee, W. Xiang, J. Xie, J. H. He, R. K. Kotlanka, S. P. Low, and H. Feng, "Electromagnetic energy harvesting from vibrations of multiple frequencies," *Journal of Micromechanics and Microengineering,* vol. 19, no. 3, pp. 035001, 2009.

[15] N. E. Dutoit, B. L. Wardle, and S.-G. Kim, "Design considerations for MEMS-scale piezoelectric mechanical vibration energy harvesters," *Integrated Ferroelectrics,* vol. 71, no. 1, pp. 121-160, 2005.

[16] J.-Q. Liu, H.-B. Fang, Z.-Y. Xu, X.-H. Mao, X.-C. Shen, D. Chen, H. Liao, and B.-C. Cai, "A MEMS-based piezoelectric power generator array for vibration energy harvesting," *Microelectronics Journal,* vol. 39, no. 5, pp. 802-806, 2008.

[17] M. Renaud, K. Karakaya, T. Sterken, P. Fiorini, C. Van Hoof, and R. Puers, "Fabrication, modelling and characterization of MEMS piezoelectric vibration harvesters," *Sensors and Actuators A: Physical,* vol. 145, pp. 380-386, 2008.

[18] S. Saadon, and O. Sidek, "A review of vibration-based MEMS piezoelectric energy harvesters," *energy conversion and management,* vol. 52, no. 1, pp. 500-504, 2011.

[19] S. Roundy, and P. K. Wright, "A piezoelectric vibration based generator for wireless electronics," *Smart Materials and structures,* vol. 13, no. 5, pp. 1131, 2004.

[20] S. Priya, and D. J. Inman, *Energy harvesting technologies*: Springer, 2009.

[21] A. Erturk, and D. J. Inman, *Piezoelectric energy harvesting*: John Wiley & Sons, 2011.

[22] X. Wang, "Piezoelectric nanogenerators—harvesting ambient mechanical energy at the nanometer scale," *Nano Energy,* vol. 1, no. 1, pp. 13-24, 2012.

[23] B. Kumar, and S.-W. Kim, "Energy harvesting based on semiconducting piezoelectric ZnO nanostructures," *Nano Energy,* vol. 1, no. 3, pp. 342-355, 2012.

[24] Y. Jeon, R. Sood, J.-H. Jeong, and S.-G. Kim, "MEMS power generator with transverse mode thin film PZT," *Sensors and Actuators A: Physical,* vol. 122, no. 1, pp. 16-22, 2005.

[25] D. Shen, J.-H. Park, J. Ajitsaria, S.-Y. Choe, H. C. Wikle III, and D.-J. Kim, "The design, fabrication and evaluation of a MEMS PZT cantilever with an integrated Si proof mass for vibration energy harvesting," *Journal of Micromechanics and Microengineering,* vol. 18, no. 5, pp. 055017, 2008.

[26] S. Roundy, P. K. Wright, and J. Rabaey, "A study of low level vibrations as a power source for wireless sensor nodes," *Computer communications,* vol. 26, no. 11, pp. 1131-1144, 2003.

[27] S.-G. Kim, S. Priya, and I. Kanno, "Piezoelectric MEMS for energy harvesting," *MRS bulletin,* vol. 37, no. 11, pp. 1039-1050, 2012.

[28] S. M. Oh, M.-G. Kang, H. Do Young, C. Y. Kang, S. J. Yoon, and S. Nahm, "Fabrication of 1 μm thickness lead zirconium titanate films using poly (N-vinylpyrrolidone) added sol-gel method," *Transactions on Electrical and Electronic Materials,* vol. 12, no. 5, pp. 222-225, 2011.

[29] S. Mancha, "Chemical etching of thin film PLZT," *Ferroelectrics,* vol. 135, no. 1, pp. 131-137, 1992.

[30] J. Marshall, Q. Zhang, and R. Whatmore, "Corona poling of highly (001)/(100)-oriented lead zirconate titanate thin films," *Thin Solid Films,* vol. 516, no. 15, pp. 4679-4684, 2008.

[31] I. Kanno, H. Kotera, and K. Wasa, "Measurement of transverse piezoelectric properties of PZT thin films," *Sensors and Actuators A: Physical,* vol. 107, no. 1, pp. 68-74, 2003.

[32] J. Ricote, G. Leclerc, D. Chateigner, P. Ramos, R. Bouregba, and G. Poullain, "Local piezoelectric properties of oriented PZT based ferroelectric thin films," *Ferroelectrics,* vol. 335, no. 1, pp. 191-199, 2006.

[33] V. Nagarajan, A. Stanishevsky, L. Chen, T. Zhao, B.-T. Liu, J. Melngailis, A. Roytburd, R. Ramesh, J. Finder, and Z. Yu, "Realizing intrinsic piezoresponse in epitaxial submicron lead zirconate titanate capacitors on Si," *Applied physics letters,* vol. 81, no. 22, pp. 4215-4217, 2002.

[34] K. Lefki, and G. Dormans, "Measurement of piezoelectric coefficients of ferroelectric thin films," *Journal of applied physics,* vol. 76, no. 3, pp. 1764-1767, 1994.

[35] B. Jaffe, W. R. Cook, and H. Jaffe, "Piezoelectric ceramics," 1971.

[36] G.-T. Park, J.-J. Choi, J. Ryu, H. Fan, and H.-E. Kim, "Measurement of piezoelectric coefficients of lead zirconate titanate thin films by strain-monitoring pneumatic loading method," *Applied physics letters,* vol. 80, no. 24, pp. 4606-4608, 2002.

[37] H. Jansen, H. Gardeniers, M. de Boer, M. Elwenspoek, and J. Fluitman, "A survey on the reactive ion etching of silicon in microtechnology," *Journal of micromechanics and microengineering,* vol. 6, no. 1, pp. 14, 1996.

[38] E. E. Aktakka, "Integration of bulk piezoelectric materials into microsystems," The University of Michigan, 2012.

[39] M. Defosseux, M. Allain, E. Defay, and S. Basrour, "Highly efficient piezoelectric micro harvester for low level of acceleration fabricated with a CMOS compatible process," *Sensors and Actuators A: Physical,* vol. 188, pp. 489-494, 2012.

[40] H. Durou, G. A. Ardila-Rodriguez, A. Ramond, X. Dollat, C. Rossi, and D. Esteve, "Micromachined bulk pzt piezoelectric vibration harvester to improve effectiveness over low amplitude and low frequency vibrations," *Proceedings Power MEMS*, pp. 19-22, 2010.

[41] R. Elfrink, M. Renaud, T. Kamel, C. De Nooijer, M. Jambunathan, M. Goedbloed, D. Hohlfeld, S. Matova, V. Pop, and L. Caballero, "Vacuum-packaged piezoelectric vibration energy harvesters: damping contributions and autonomy for a wireless sensor system," *Journal of Micromechanics and Microengineering,* vol. 20, no. 10, pp. 104001, 2010.

[42] H.-B. Fang, J.-Q. Liu, Z.-Y. Xu, L. Dong, L. Wang, D. Chen, B.-C. Cai, and Y. Liu, "Fabrication and performance of MEMS-based piezoelectric power generator for vibration energy harvesting," *Microelectronics Journal,* vol. 37, no. 11, pp. 1280-1284, 2006.

[43] A. Hajati, and S.-G. Kim, "Ultra-wide bandwidth piezoelectric energy harvesting," *Applied Physics Letters,* vol. 99, no. 8, pp. 083105, 2011.

[44] T. H. Hirasawa, Y. T.-T. Yen, P. K. Wright, A. P. Pisano, and L. Lin, "Design and fabrication of piezoelectric aluminum nitride corrugated beam energy harvester," *Proceedings PowerMEMS*, pp. 211-214, 2010.

[45] A. Lei, R. Xu, A. Thyssen, A. C. Stoot, T. L. Christiansen, K. Hansen, R. Lou-Moller, E. V. Thomsen, and K. Birkelund, "MEMS-based thick film PZT vibrational energy harvester." pp. 125-128.

[46] K. Morimoto, I. Kanno, K. Wasa, and H. Kotera, "High-efficiency piezoelectric energy harvesters of c-axis-oriented epitaxial PZT films transferred onto stainless steel cantilevers," *Sensors and Actuators A: Physical,* vol. 163, no. 1, pp. 428-432, 2010.

[47] P. Muralt, M. Marzencki, B. Belgacem, F. Calame, and S. Basrour, "Vibration energy

harvesting with PZT micro device," *Procedia Chemistry,* vol. 1, no. 1, pp. 1191-1194, 2009.

[48] J. C. Park, J. Y. Park, and Y.-P. Lee, "Modeling and Characterization of Piezoelectric-Mode MEMS Energy Harvester," *Microelectromechanical Systems, Journal of,* vol. 19, no. 5, pp. 1215-1222, 2010.

[49] R. Xu, A. Lei, C. Dahl-Petersen, K. Hansen, M. Guizzetti, K. Birkelund, E. V. Thomsen, and O. Hansen, "Fabrication and characterization of MEMS-based PZT/PZT bimorph thick film vibration energy harvesters," *Journal of Micromechanics and Microengineering,* vol. 22, no. 9, pp. 094007, 2012.

[50] I. Kanno, T. Ichida, K. Adachi, H. Kotera, K. Shibata, and T. Mishima, "Power-generation performance of lead-free (K, Na)NbO_3 piezoelectric thin-film energy harvesters," *Sensors and Actuators A: Physical,* vol. 179, pp. 132-136, 2012.

5. Chapter 5: Broadband Dual Phase Energy Harvester: Vibration and Magnetic field

5.1. Introduction

In the past decade, energy harvesting technology has been extensively investigated to realize self-powered low power consuming devices such as transceivers, sensors and MEMS components.[1-4] There are several mechanisms for converting ambient energy into electricity including photovoltaics[5], thermoelectrics[6], magneto-thermoelectric[7, 8], electromagnetics[9, 10], magneto-mechano-electric (MME) conversion, and various types of mechanical energy harvesters.[11-15] Mechanical energy harvesters utilize many different energy conversion phenomena and materials including piezoelectric, magnetic, electrostatic, electrets, triboelectric, dielectric elastomer, ionic polymer, etc. Among this large number of candidates, piezoelectric energy harvesting has been extensively studied as it can provide high electromechanical energy conversion efficiency, energy density, and high voltage.[4, 16-19] Mechanical energy is attractive due to its availability in a variety of scenarios such as vehicles, aircrafts, industrial machines, household appliances, and human motion. In some scenarios, mechanical energy is parasitically supplemented by the stray magnetic field generated from surrounding power cord in electronic devices and transmission cables. Simultaneous dual phase energy harvesting of mechanical and magnetic energy provides an attractive opportunity to amplify the power density and thereby strengthen the argument for self-powered devices.[20-22]

Traditionally, electromagnetic generators have been utilized for harvesting magnetic energy, but they are bulky in size and difficult to be integrated with low force – low frequency oscillations.[9, 20, 23, 24] An example of constant oscillation frequency source would be stray

magnetic field generated from A/C power cords on electronic devices. The electric power transmission cables can generate low magnetic fields (<1 mT = 10 G at a distance of 10 mm from 50 A cable) at fixed frequency of 50/60 Hz (depending upon the geographical region). The available stray magnetic fields can be higher in the vicinity of electric equipment/machines. Recently, a magneto-mechano-electric (MME) energy conversion mechanism has been proposed that allows the combination of piezoelectric energy harvester and magnets to simultaneously harvest this magnetic energy and mechanical energy.[25-28] In contrast to magnetic fields, vibration frequency is seldom constant rather it varies over a band depending upon the mass and operating environment. Thus, the challenge lies in capturing this wide range of vibrations while also optimizing the power production at specific frequencies.

In order to maximize the generated electrical power from mechanical vibrations, the piezoelectric energy harvester should be operated at resonance frequency.[12, 26] However, piezoelectric structures exhibit narrowband resonance frequency and thus it is difficult to couple with broadband vibrations. In particular, it is more difficult to harvest a sufficient power from continuously varying frequency conditions such as automobile and airplane engine vibrations. In order to fully capture the energy from vibrations, ideally piezoelectric harvesters should have a broadband response or ability to automatically tune the resonance frequency in accordance with an ambient vibration source.[29-33] One of the simpler methods introduced in prior literature for achieving the broadband response is arraying piezoelectric bimorph/unimorph type energy harvesters with different lengths. However, in this case, the energy density dramatically decreases because only one of the energy harvester generate electric power at a specific resonance frequency. In addressing this problem of low power density in broadband energy harvester arrays, we demonstrate a magnetically coupled piezoelectric energy harvester array (MaCoPEHA) that couples each harvester in the array through the interaction of magnetic proof masses. If one of the harvesters in the MaCoPEHA

is vibrating at resonance, the next neighbor harvester will be excited to a quasi-resonance state through the magnetic interaction. Thus, in varying vibration conditions, the generated power and bandwidth will increase significantly in comparison with a normal (non-magnetically coupled) harvester array. The MaCoPEHA shown in Figure. 5.1 (a) uses the MME mechanism, whereby piezoelectric bimorph cantilevers are mounted with magnetic proof masses such that they can also function as a magnetic field energy harvester while maintaining the broadband nature. The MaCoPEHA can respond to both mechanical vibrations and magnetic fields through the oscillation of the cantilever directly through bending stresses or indirectly through the coupling of magnetic proof mass displacements in neighboring beams. Vibrations from rotary pump, automobile engine and stray magnetic field surrounding the power cord of an electric kettle were successfully harvested using the MaCoPEHA and output power densities corresponding to the vibration and the magnetic field input were found to be 243 $\mu W/cm^3 \cdot g^2$ at 78 Hz and 36.5 $\mu W/cm^3 \cdot Oe^2$ at 79.5 Hz, respectively.

5.2. Experimental

5.2.1. Fabrication of MaCoPEHA

The cantilever type energy harvester was fabricated with 2-2 composite structure comprising of stainless steel (STS) shims (SUS304H, JINEI Corp.) and piezoelectric ceramics. The STS shims and piezoelectric ceramic plates with 5 mm × 50 mm dimension were fabricated by dicing larger size plates. Three layers of STS shims and two layers of piezoelectric ceramics were stacked alternately and bonded using high strain epoxy (DP-460, 3M) as shown in Figure 5.1 (b) and cured at 80^{o}C for 6 hours under pressure. Different lengths (30 mm, 27.5 mm, 25 mm, 22.5 mm, and 20 mm) of cantilever beam were arrayed with 5mm interval using a 3D printed jig. The NdFeB magnetic proof masses with 144.18 mm^3 (6.35mm x 3.18 mm x 7.14

mm, density $\rho = 7.4$ g/cm^3) volume were attached at the free end of each beam. All attached magnetic proof masses on the cantilever beam arrays had the same polarity and applied repulsive force on each other.

5.2.2. Measurement of vibration and magnetic field characteristics

The vibration characteristics of the MaCoPEHA was investigated using a vibration shaker (K2007E01, The modal shop, Inc.) and scanning laser Doppler vibrometer (Polytec, PSV 500). The cantilever beam arrays were clamped using a home-made jig. The energy harvester was excited by 1 g acceleration which was constantly monitored using an accelerometer. The resonance frequency and transfer function of the energy harvester were measured by laser vibrometer and Polytec data management system (DMS) by applying burst chirp vibrations and discrete sine sweep (manually stepping through frequencies). The generated output voltage of the energy harvester arrays was measured using a 4-channel digital oscilloscope (DSO1014A, Keysight). The actuation mode shapes of each cantilever beam were also measured simultaneously using the two-dimensional scanning laser vibrometer (Polytec, PSV 500). The magnetic field response of the MaCoPEHA was tested using a homemade Helmholtz coil. The Helmholtz coil was driven by a bipolar amplifier and function generator to generate 500μT magnetic field. The generated magnetic field was monitored using a Teslameter/gaussmeter (Model 6010, Laboratorio Electtofisico / Walker LDJ Scientific), and maintained a constant value with variation of frequency.

For characterization of generated power from the MaCoPEHA, the generated voltage was measured across connected load resistance using a variable resistor (IET Labs, OS-260 RTD simulator). Internal impedance (1MΩ) of the oscilloscope was considered for calculation of the total connected load resistance. The generated average power from the MaCoPEHA was calculated using the formula $P = V^2/R$, where V is the rectified RMS voltage. The impedance

matching point was determined to be the impedance value where maximum in output power is obtained. The internal impedance of the energy harvester was also directly measured using an impedance analyzer (Agilent, 4990 A), and compared with the experimentally found impedance matching point.

5.3. Results and Discussion

5.3.1. MaCoPEHA Device Design and Operation

The design of the MaCoPEHA is depicted in Figure 5.1 (a) and (b), where the use of magnetic poof masses on arrayed energy harvesters allows coupling between them and a subsequent broadband response. Figure 5.1 (c) illustrates of the expected output voltage generated from an individual energy harvester in the MaCoPEHA shown in Figure 5.1 (d), with an assumtion that the arrayed harvesters are coupled via magnetic force of attraction/repulsion. As shown in Figure 5.1 (c), each harvester in the array can have multiple resonance frequencies because the harvester is not only responds at its own fundamental frequency but also at the coupled frequencies corresponding to the response of other harvesters in the array. The maximum output voltage is obtained at the fundamental resonance frequency and decreases as the frequency varies, while still maintaining a significant magnitude over the wide range corresponding to $f_{long} - f_{short}$, where f_{long} and f_{short} are the fundamental resonance frequencies of the longest beam and the shortest beam in the array, respectively.

Figure 5.1 (d) shows the schematic configuration of each piezoelectric energy harvester in the MaCoPEHA comprised of a bimorph structure with the piezoelectric ceramic (PSI-5A4E, Piezo System, Inc.) and stainless steel (STS) shim (SUS304H, JINEI Corp.) layers. The piezoelectric ceramics layers were combined with an opposite poling direction in order to avoid the output power cancelation due to phase mismatch. In order to maximize the output power

from the bimorph cantilever, the configuration of each layer should be decided to maximize the value of the stiffness coupling parameter (κ) expressed as [34]:

$$\kappa = \frac{\left(1+\frac{t_s}{t_p}\right)^2}{\frac{1}{6}\left(\frac{c_s}{c_p}\right)\left(\frac{t_s}{t_p}\right)^3+\frac{1}{3}+\left(1+\frac{t_s}{t_p}\right)^2} \tag{5.1}$$

where c_s, and c_p are elastic moduli of the STS shim layer and the piezoelectric ceramic layer, respectively, and t_s, and t_p are the thicknesses of the STS shim layer and the piezoelectric layer, respectively. The optimum t_s/t_p value can be calculated as:

$$\left(\frac{t_s}{t_p}\right)_{opt} = \left\{\left[\left(\frac{2}{c_s/c_p}-1\right)^2-1\right]^{\frac{1}{2}}+\frac{2}{c_s/c_p}-1\right\}^{-\frac{1}{3}} + \left\{\left[\left(\frac{2}{c_s/c_p}-1\right)^2-1\right]^{\frac{1}{2}}+\frac{2}{c_s/c_p}-1\right\}^{\frac{1}{3}}-1 \tag{5.2}$$

The optimum t_s/t_p value was found to be 0.6 using elastic moduli of the STS and the piezoelectric ceramic.[35] Using this value, the thicknesses of the STS shim and the piezoelectric layer were determined to be 80 μm and 125 μm, respectively. The piezoelectric ceramics and the STS shims were precisely sliced by a dicing saw and combined together using epoxy adhesive (DP-460, 3M) with a high strain rate according to configuration shown in Figure 5.1 (b). The total thickness of each cantilever beam was approximately 530 μm after bonding. 5 cantilever energy harvesters of the same size were fabricated and clamped at different length.

For broadband operation, the energy harvesters possessing different resonance frequencies were arrayed to respond to varying ambient vibrations. The first natural frequency of the cantilever beam structure can be expressed as [4]:

$$\omega_n = \sqrt{\frac{k_{eq}}{m_{eq}}} = \sqrt{\frac{3EI}{L^3(M_l+0.24M_p)}} \tag{5.3}$$

$$I = \frac{bd^3}{12} \tag{5.4}$$

where m_{eq} is the equivalent mass, k_{eq} is the equivalent spring constant, L is the length of beam, E is elastic modulus of the beam, I is moment of inertia of the beam cross-section, M_l is the mass per unit beam length, M_p is the weight of a proof mass, and b and d are the breadth and depth of the beam cross-section. From equation (5.3), the natural frequency of a cantilever energy harvester is proportional to the elastic modulus (E) and the moment of inertia (I), while inversely proportional to the length of beam (L) and weight of a proof mass (M_p). To engineer the natural frequency, we can control the length of beam and weight of a proof mass.[12] In this work, we gradually modulated the length of beam (L) to adjust the natural frequency of each harvester in the array instead of changing the weight of the proof mass so that all energy harvesters have a similar magnetic force of the interaction with each other. The lengths of the beams were varied from 20 mm to 30 mm at an increment of 2.5 mm as shown in Figure 5.1 (b). The fabricated harvester beams were fixed at 5 mm equidistant intervals in the 3-D printed plastic jig which was tightly clamped by a metal clamp as shown in picture of Figure 5.1 (e). For coupling of arrayed energy harvesters, permanent NdFeB magnet proof masses with the same polarity were attached at the end of each beam. The same weight magnets were placed on each beam equally spaced with respect to each other for homogeneous interaction between the harvesters. As shown in the front view of harvester in Figure 5.1 (e), the magnetic masses

were alternately shifted up and down in order to provide a magnetic force equilibrium. The longer beams deflected more than the shorter beams because of their lower stiffness.

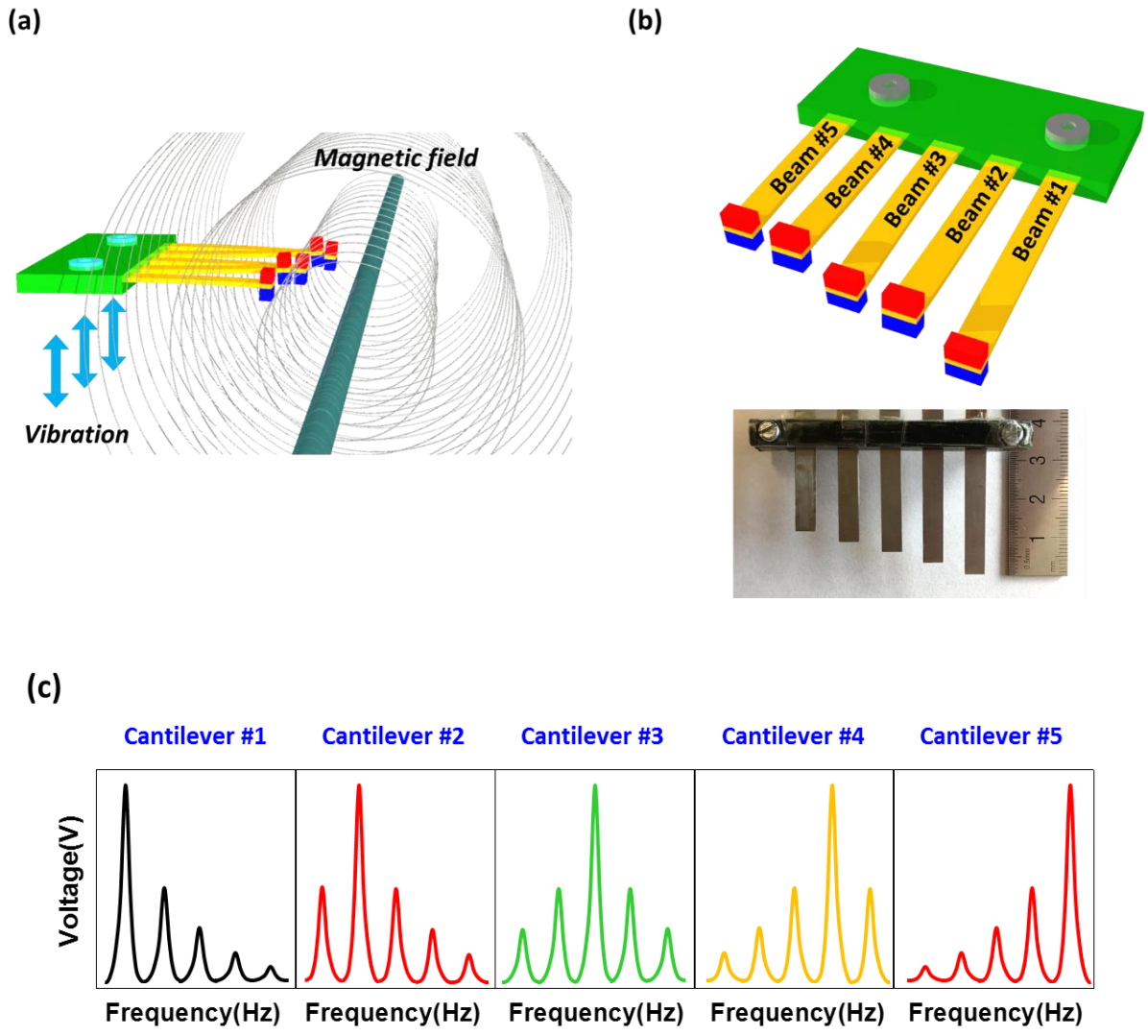

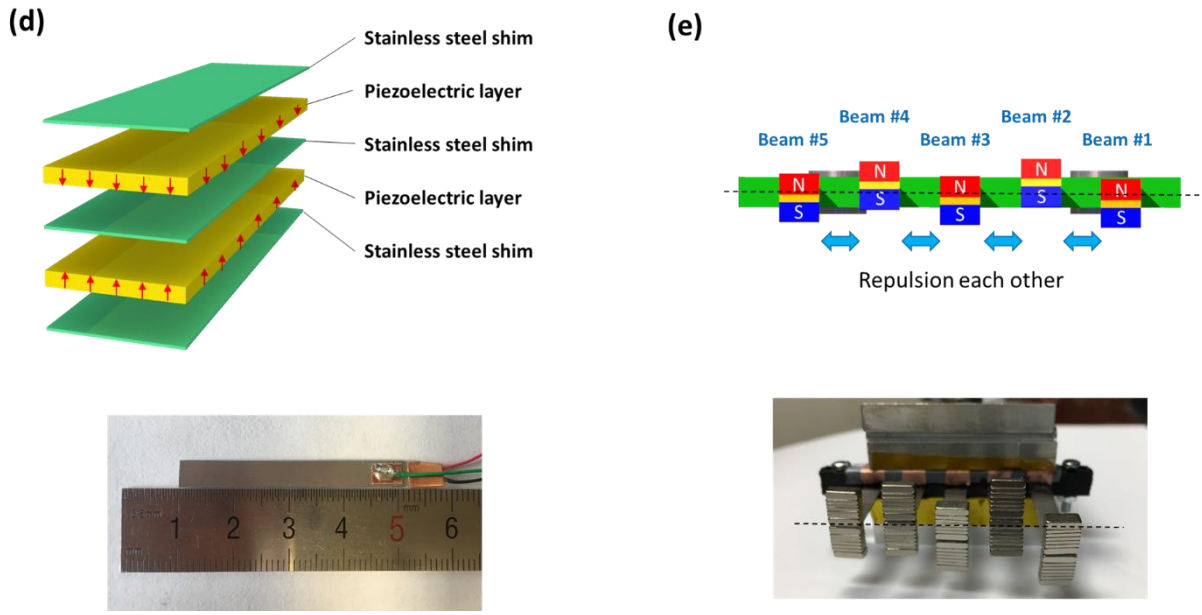

Figure 5.1. (a) Schematic description of vibration and stray magnetic field dual phase energy harvester. (b) Schematic layout of the MaCoPEHA. The picture shows fabricated cantilever energy harvester array. (c) Expected output voltage of the MaCoPEHA with respect to cantilever beam positions. (d) Schematic diagram of the cantilever energy harvester consisting of 2-2 composite structure of metal shims and piezoelectric ceramic layers in order to improve the strength and output power. (e) Configuration of coupled magnetic proof masses that have same polarity and repulsive force.

5.3.2. Vibration and Magnetic Energy Harvesting Performance

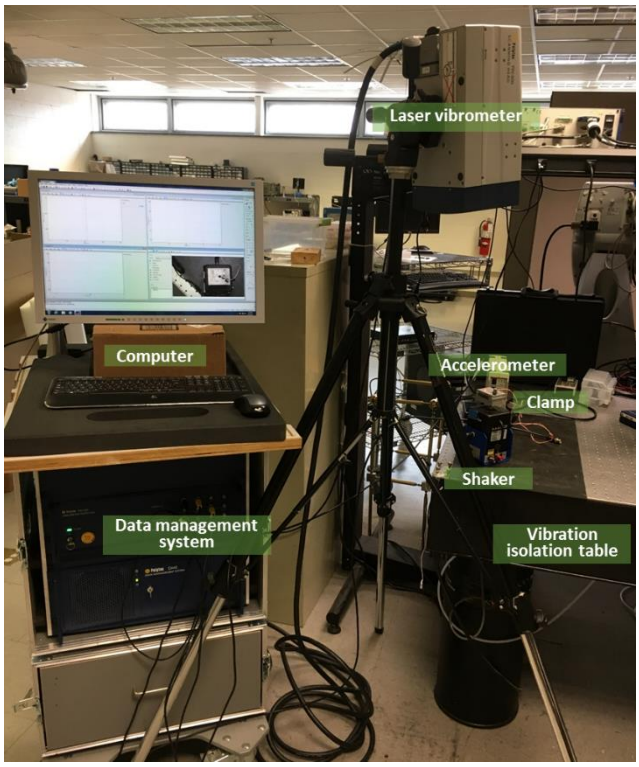

Figure 5.2. Testing setup for vibration characteristics of energy harvesters with two-dimensional laser vibrometer.

Using the vibration testing setup shown in Figure 5.2, frequency response spectrum for the MaCoPEHA was measured by applying a burst chirp frequency sweep (50%) from 35 to 100 Hz at different acceleration conditions from a shaker. Open-circuit output voltage signal of each beam in the MaCoPEHA was recorded simultaneously using a multi-channel digital signal processor. Figure 5.3 (a), (b) and (c) show the burst chirp frequency spectrums for the MaCoPEHA output voltage at 0.01 V, 0.02 V, and 0.03 V excitation voltage applied to the shaker (to yield different acceleration conditions), respectively. For comparison, the output voltage was normalized by acceleration (g). It is apparent from the frequency spectrums that the MaCoPEHA provides broadband operation characteristics. Transfer function for the

individual beam is provided in Figure 5.3 (a), (b) and (c), which indicates that there are five resonance peaks in the MaCoPEHA which originate from the respective natural frequency of each beam without magnetic interference. Besides the mechanical resonance, each beam has coupled modes generated by the magnetic field interaction from neighboring beams. As shown in Figure 5.3, the higher order modes for each beam comply with the fundamental resonance frequency of the adjacent beams, which confirms that the magnetic interaction results in elastic coupling. With decrease of beam length (from beam #1 to beam #5), bandwidth of individual beam tends to broaden of low acceleration conditions, as presented in Figure 5.3 (a). This could be attributed to the fact that the longer beams lead higher bending deflection caused by the magnetic repulsion and lower non-linear interaction (magnetic force varies non-linearly with distance) with neighboring harvester beams as shown in the front view of the MaCoPEHA in Figure 5.1 (e). Additionally, as shown in Figure 5.3 (a), (b) and (c), beam #5 has the widest bandwidth which is due to two adjacent resonant modes merging with each other. With increase of acceleration, the frequency of fundamental modes was slightly shifted and those of higher order modes increased due to augmented interaction between adjacent beams as shown in Figure 5.3 (a), (b), and (c). This resulted in an increase of total bandwidth of the MaCoPEHA with increasing acceleration. Even though the broadband behavior of the MaCoPEHA was achieved at low acceleration, the non-linear stiffening effect by the magnetic field interaction was not sufficient. From the above results, it is worth noting that in order to improve the bandwidth and output power of our MaCoPEHA, the magnetic interaction between energy harvesters needs to be increased and bending deflection of the cantilever beam needs to be reduced.

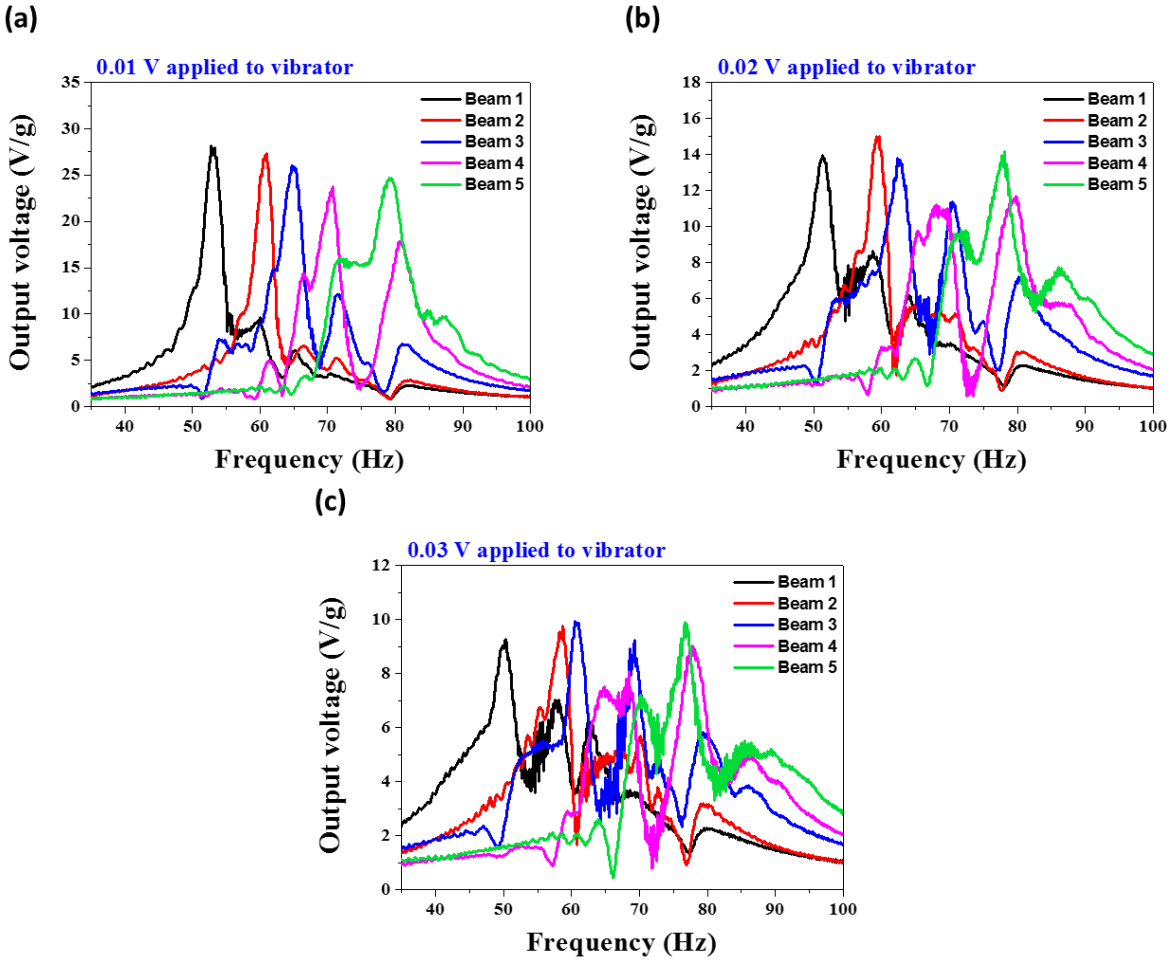

Figure 5.3. Frequency spectrums of open-circuit output voltage of individual harvesters in the MaCoPEHA at (a) 0.01 V, (b) 0.02 V, and (c) 0,03 V burst chirp signals applied to shaker. The output voltages were normalized by applied acceleration (g). The MaCoPEHA has multiple-resonance frequencies and a broadband frequency spectrum. With increase of the applied voltage to the shaker (acceleration, g), the bandwidths increase, and the resonance frequencies of each harvester slightly shift due to the augmented magnetic interaction between adjacent beams.

To quantify the magnetic coupling between beams, the phase deviation of generated voltage signal and the coupled mode shape of each beam at different frequencies were investigated. The phase deviation in generated power is a very critical factor when combining electrical energy from various beams as any difference could lead to cancellation of electric potential. Figure 5.4 shows the generated output voltages and coupled mode shape of the MaCoPEHA

under 1 g acceleration. In order to examine the mode shape of the first bending mode of each beam, all beams in the MaCoPEHA were scanned using a scanning laser vibrometer (Polytec, PSV 500) under a constant acceleration and frequency. Figure 5.4 (a) shows the output voltage and mode shape of the beam #1 at 52.5 Hz which generated the highest output voltage but has 90^{o} phase deviation with respect to the other beams. Figure 5.4 (b) and (c) display the time domain output voltages and phase characteristics of the MaCoPEHA at the fundamental resonance frequencies of beam #2 and beam #3, respectively. Due to complex magnetic interaction of all beams, the generated output voltages have different phases as shown in Figure 5.4 (b) and (c). On the other hand, it is interesting to note that all beams have almost synchronized phase at the frequency of 78 Hz as shown in Figure 5.4 (d). At 78 Hz, all beams are near resonance and the actuation of each beam does not affect the movement of neighboring beams due to strong coupling. When we consider the amplitude of generated output voltage and the actuation mode shape of adjacent beams, the coupling among beams #3, #4, and #5 seems to be stronger than the coupling between beam #1 and #2.

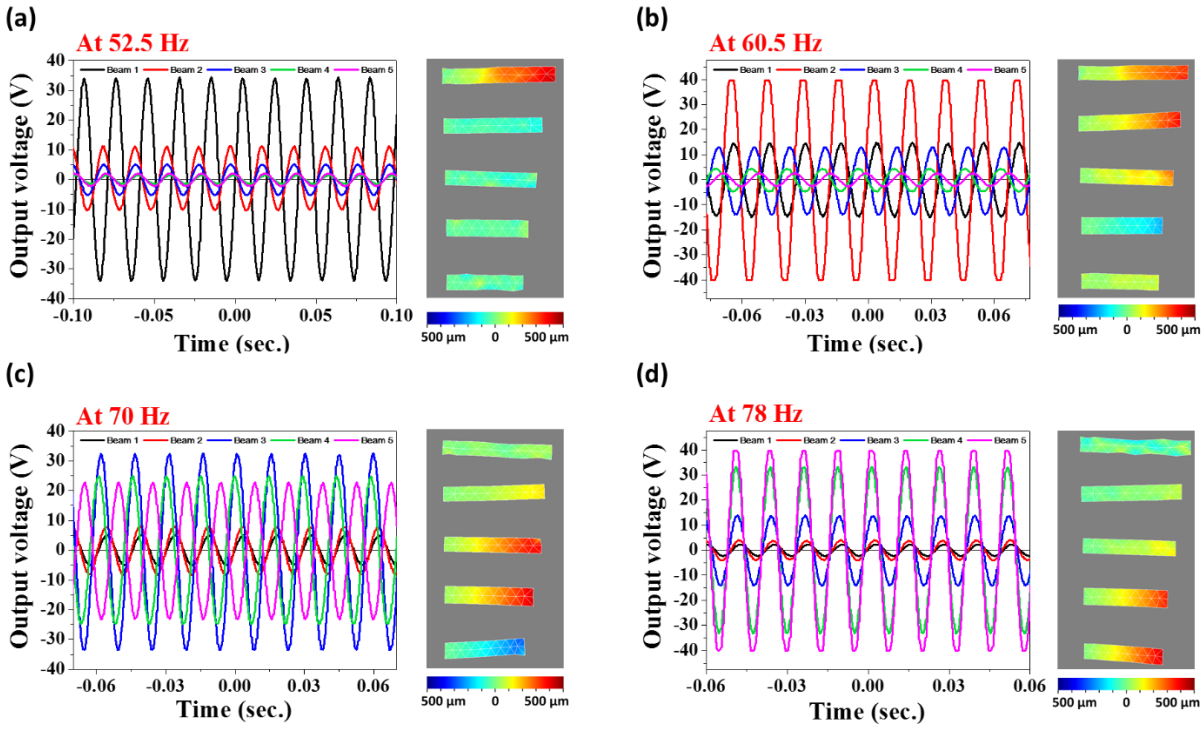

Figure 5.4. Generated open-circuit output voltages of the MaCoPEHA with 1 g acceleration at (a) 52.5 Hz, (b) 60.5 Hz, (c) 70 Hz and (d) 78 Hz. Pictures show coupled vibration mode shapes measured by the two-dimensional laser vibrometer at each frequency. The phase deviation of the generated voltage signal and the coupled mode shape of the MaCoPEHA vary depending upon the interaction of beams at different frequencies.

To investigate the generated output power, the output voltage under sinusoidal vibration condition was investigated in the frequency range of 30 ~ 100 Hz at 1g acceleration. Figure 5.5 (a) and (c) show the open-circuit output DC voltage through a full-bridge rectifier from each beam and the summed voltage from individual beams with the variation of the applied vibration frequency, respectively. The inset picture shows the measurement set-up for vibration testing. Applied acceleration on the device was monitored by the accelerometer, and maintained at a constant value with the variation of the vibration frequency. As shown in Figure 5.5 (a), the frequency spectrum for the output voltage under a constant acceleration was similar to the frequency spectrum in burst chirp frequency sweep shown in Figure 5.3 (a), and the system exhibited multi-resonance peaks and broadband characteristics. The maximum total output power of 430.7 μW (beam #1: 0.9 μW, beam #2: 2.4 μW beam #3: 30.8 μW, beam #4: 110.5 μW, and beam #5: 286.2 μW) was obtained at 78 Hz across the optimum load resistance of each beam (beam #1: 245 kΩ, beam #2: 230 kΩ, beam #3: 230 kΩ, beam #4: 200 kΩ and beam5: 130 kΩ). The power density of our MaCoPEHA including proof masses was 243 $\mu W/cm^3 \cdot g^2$ at 78 Hz under 1 g acceleration. Beam #5 showed the highest output power of 286.2 μW with the power density of 838.4 $\mu W/cm^3 \cdot g^2$ under the same vibration condition.

The output performance of the MaCoPEHA under the magnetic field was measured using a homemade Helmholtz coil without any external vibrations. As shown in the inset of testing set-up in Figure 5.5 (b), the MaCoPEHA was placed at the center of the Helmholtz coil and exposed to a constant amplitude AC magnetic field of varying frequency. The magnetic force

moment of the magnet (M_m) generated along the longitudinal direction of the cantilever beam can be expressed as [36]

$$M_m = 2V_m J_r B_{ac} \tag{5.5}$$

where V_m is the volume of magnetic proof mass, B_{ac} is the applied magnetic field on the energy harvester, and J_r is the remanent magnetic polarization of magnet. The measured remanent magnetic polarization of NdFeB magnet used in the MaCoPEHA was 1.2 T. It should be pointed out that from equation (5.5), in order to increase magnetic force moment on the energy harvester, a larger size magnet with high remanent magnetic polarization should be employed. Figure 5.5 (b) shows the rectified output voltage through the full-bridge rectifier across a load resistance of 1MΩ (internal resistance of oscilloscope) under 500 μT magnetic field with varying magnetic field frequency. Figure 5.5 (d) shows the total generated output voltage from the individually arrayed beams with varying frequency. As presented in Figure 5.5 (b), the frequency spectrum under applied magnetic field also showed broadband nature with multiple-peaks, similar to that of the vibration excitation as shown in Figure 5.5 (a). However, the observation that the output voltage at resonance peak of ~79.5 Hz is superior to the voltages at other resonance peaks draw our attention. This implies that generated output voltage from beam #1, #2, and #3 reduced relatively compared with the output under vibration condition. This could be due to the fact that driving force for the output under the applied magnetic field arises from the displacement of magnetic proof masses at the free end of the cantilever beam, while the driving force under the vibration condition is from the shaker movement at the clamped end of the beam. Moreover, the interaction between applied magnetic field and the magnet might be more effective depending upon the placement of beam #4 and beam #5 within a coil. The maximum power of 1,619.7 μW (beam #1: 2.7 μW, beam #2: 8.5 μW beam #3: 139.1 μW,

beam #4: 409.6μW, and beam #5: 1,059.8 μW) was measured across the optimum load resistances (beam #1: 245 kΩ, beam #2: 230 kΩ, beam #3: 230 kΩ, beam #4: 200 kΩ and beam #5: 130 kΩ) at 79.5 Hz. The power density was calculated to 36.5 μW/cm^3·Oe^2 at 79.5 Hz. The result indicates that in order to improve the performance of the MaCoPEHA under the stray magnetic field conditions, the magnetic coupling between the individual beams should be enhanced.

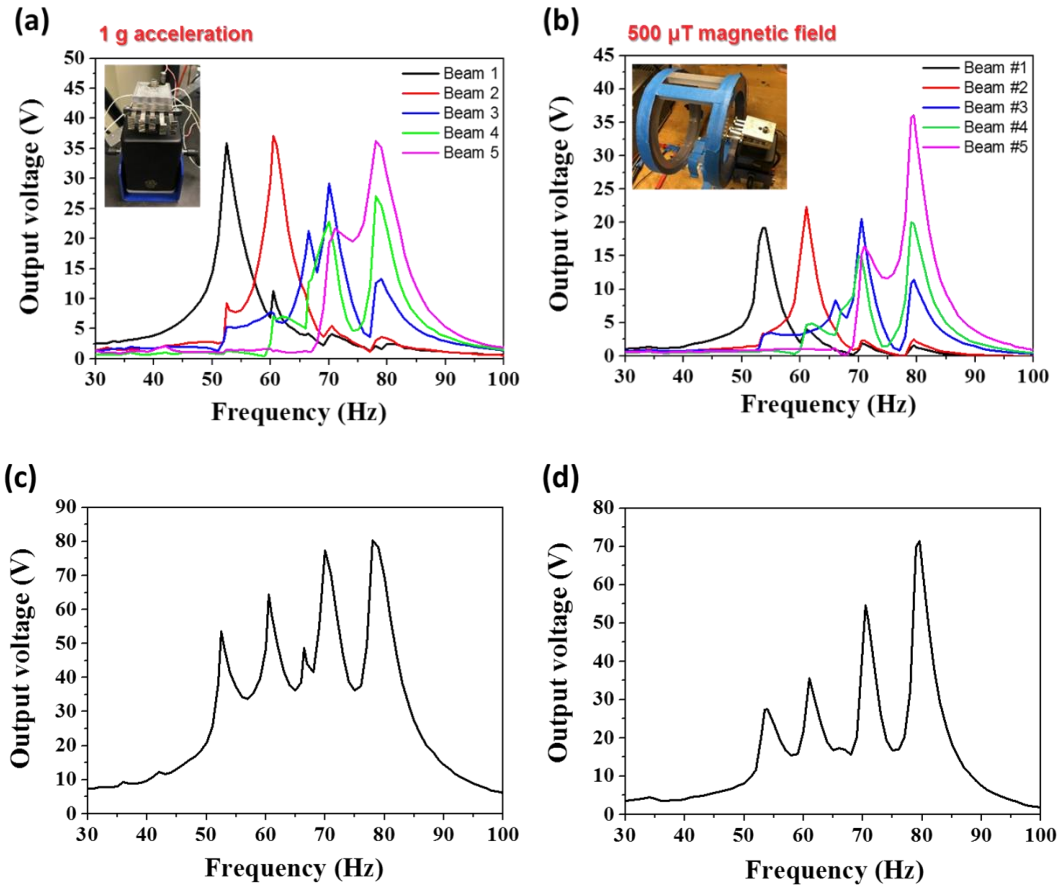

Figure 5.5. Frequency dependent rectified DC voltages of the MaCoPEHA through a full-bridge rectifier under (a) 1 g sinusoidal vibration and (b) 500 μT magnetic field. 0.5 Hz interval of the frequencies were stepped. Inset pictures are the vibration and the magnetic field testing setups, respectively. Helmholtz coils was used to generate the H_{ac} magnetic field. The summation of the generated total output voltage of each beam energy harvester under (c) 1 g vibration and (d) 500 μT magnetic field. The MaCoPEHA exhibited multi-resonance peaks and broadband characteristics under both vibrations and magnetic fields conditions.

5.3.3. Harvesting Performance under Realistic Environments

To validate the feasibility of the MaCoPEHA for practical applications, it is necessary to evaluate the energy harvesting characteristics under realistic operating conditions. First, we tested the power generation on a small rotary vacuum pump (115V, 6.5A, 1770 rpm) which is used in pneumatic machines. Figure 5.6 (a) displays the photograph of the vibration energy harvesting testing set-up on the rotary pump. The MaCoPEHA module was fixed on top of the rotary pump using a super glue and the generated output voltage was recorded using the multi-channel oscilloscope. To analyze the vibration characteristics of the rotary pump, the accelerometer was attached on top surface of the rotary pump. As represented in Figure 5.6 (b), the spectral content of the rotary pump vibration was obtained via discrete Fourier transformation of the accelerometer signal. The measured acceleration was approximately ~0.35g. It can be seen that the fundamental vibration frequency of pump was 29.5 Hz, and the second and the third harmonic frequencies were observed at 59 Hz and 118 Hz, respectively. Figure 5.6 (b) shows the open-circuit output voltage of the MaCoPEHA generated from the pump vibration.

In order to find impedance matching at the operation frequency of 59 Hz, the internal impedance of each harvester in the MaCoPEHA was investigated by an impedance analyzer (Agilent, 4990 A). Figure 5.6 (d) shows the measured impedance curve of beam #2 as a function of frequency. At 59 Hz, the measured impedance was 290 kΩ. To confirm the optimum impedance, the output voltage and power were measured as a function of external load resistance. The internal load resistance of oscilloscope (1MΩ) was also considered for the calculation of the total resistance. Figure 5.6 (e) shows the output voltage and power from the beam # 2 energy harvester with variation of the external load resistance when the harvester was excited under 1 g acceleration at 59 Hz. The maximum output power was obtained across 290 kΩ which is identical to the measured impedance value in Figure 5.6 (d). Using optimum

resistance for all beams in the energy harvester mounted on the rotary pump, the maximum output power of the MaCoPEHA was measured. Figure 5.6 (f) shows the rectified output voltage of the MaCoPEHA under the pump vibration across the optimum load resistances. Combining output voltage signals of each beam in the MaCoPEHA across optimum load resistance, the total generated power was 51.7 μW, which indicates that there is enough power to operate wireless sensor nodes or recharge battery under realistic environmental conditions.[37]

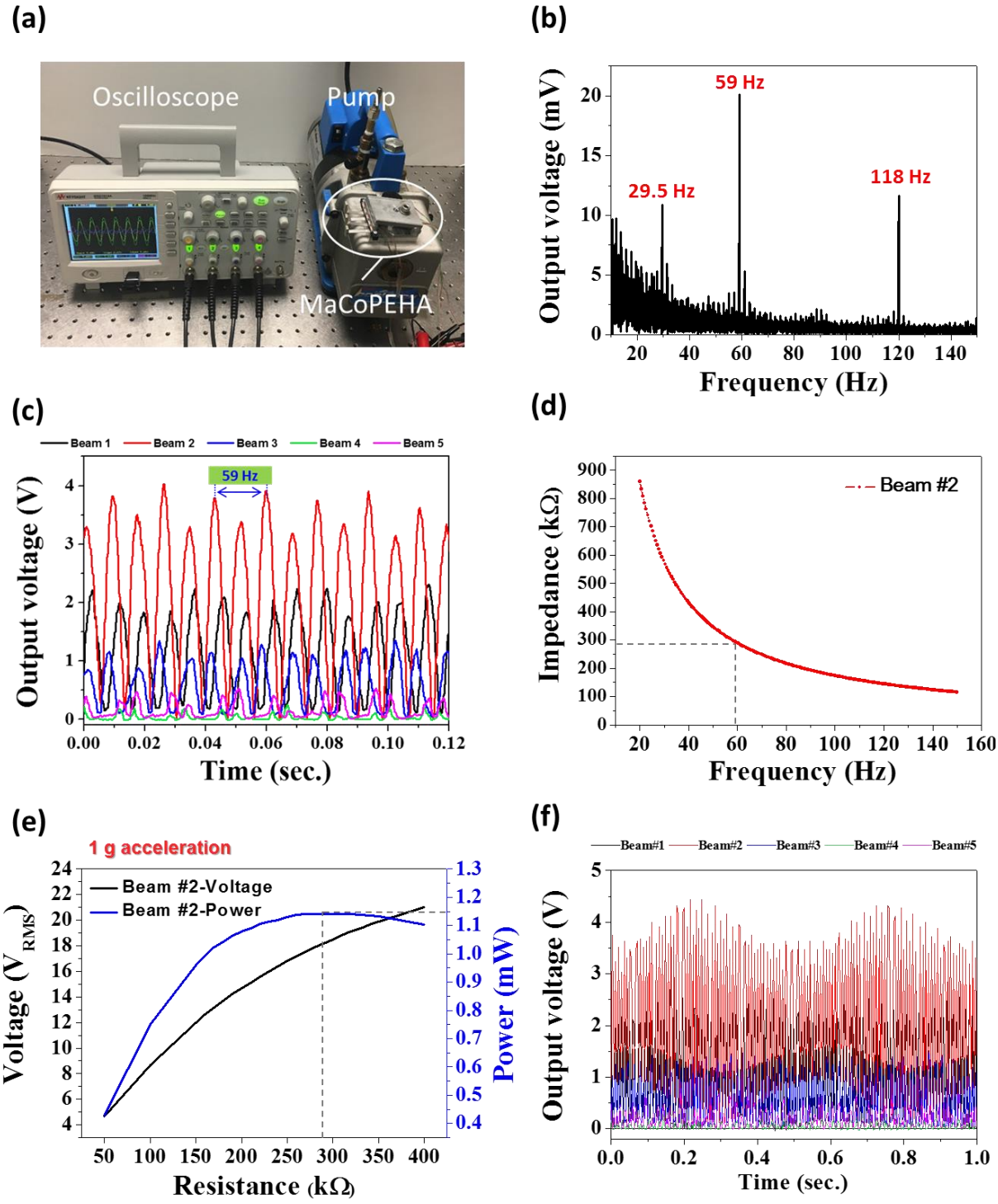

Figure 5.6. (a) Experimental setup for energy harvesting from pump vibrations. (b) Frequency analysis of pump vibration using an accelerometer. The fundamental vibration frequency is 29.5 Hz and the second and the third harmonic frequencies are 59 Hz and 118 Hz, respectively. (c) Generated open-circuit voltage measured via a full-bridge rectifier. The MaCoPEA responds to the second harmonic frequency of 59 Hz. (d) Measured internal impedance of the beam #2 in the MaCoPEHA. (e) Output voltage and power of the beam #2 in MaCoPEHA with

various load resistors under 1 g acceleration at 60Hz. The impedance matching resistance is 290 kΩ at 59 Hz and identical to the measured impedance in (c). (f) Rectified output voltages of the MaCoPEHA connected with optimum load resistances under the pump vibration.

Next, in order to identify the energy generation under stray magnetic field environment, the MaCoPEHA was mounted on a power cord of an electric kettle (120V, 60Hz, 1500W). As shown in the test setup in Figure 5.7 (a), the MaCoPEHA was located at 2mm distance from the power cable in order to generate high power because the magnetic field strength is inversely proportional to distance from the power line. The beams were mounted perpendicular to the direction of the current flow in order to match the magnetic flux direction of the power cable and the movement of the permanent magnets as described in Figure 5.1 (a). Figure 5.7 (b) shows the rectified DC output voltage of the MaCoPEHA from the stray magnetic field of the power cable in the open-circuit condition (across oscilloscope internal impedance). Beam #2 generated the maximum output voltage because its resonance frequency is almost same as the driving frequency of 60 Hz. To clarify that the generated power was caused only by the stray magnetic field, we conducted the power line on/off test and the clamped boundary test to evaluate the source of output voltage. The generated voltage on the oscilloscope appeared and disappeared in exact accordance with turning on and off the electric kettle. The results from the clamped boundary test showed that by fixing the free end of the cantilever beam to hinder vibration, the generated output voltage reduced proportionally. It verifies that the electric power was generated from the mechanical vibration of the energy harvester, with no other effects such as magnetic field induction from conducting lines. Figure 5.7 (c) shows that the rectified output voltage from individual beams under the stray magnetic field arises from the power cable of the electric kettle. The output power of beam #1, #2, #3, #4 and #5 were found to be 46.3 μW, 172.5 μW, 17 μW, 5.3 μW and 5.5 μW across optimum load resistances (320kΩ, 290kΩ, 200 kΩ, 170 kΩ and 270 kΩ), respectively. The total generated output power of the

system was 246.5 μW from the magnetic field generated from the power cable of the electronic kettle which is sufficient power to operate wireless sensor node (WSN).[37]

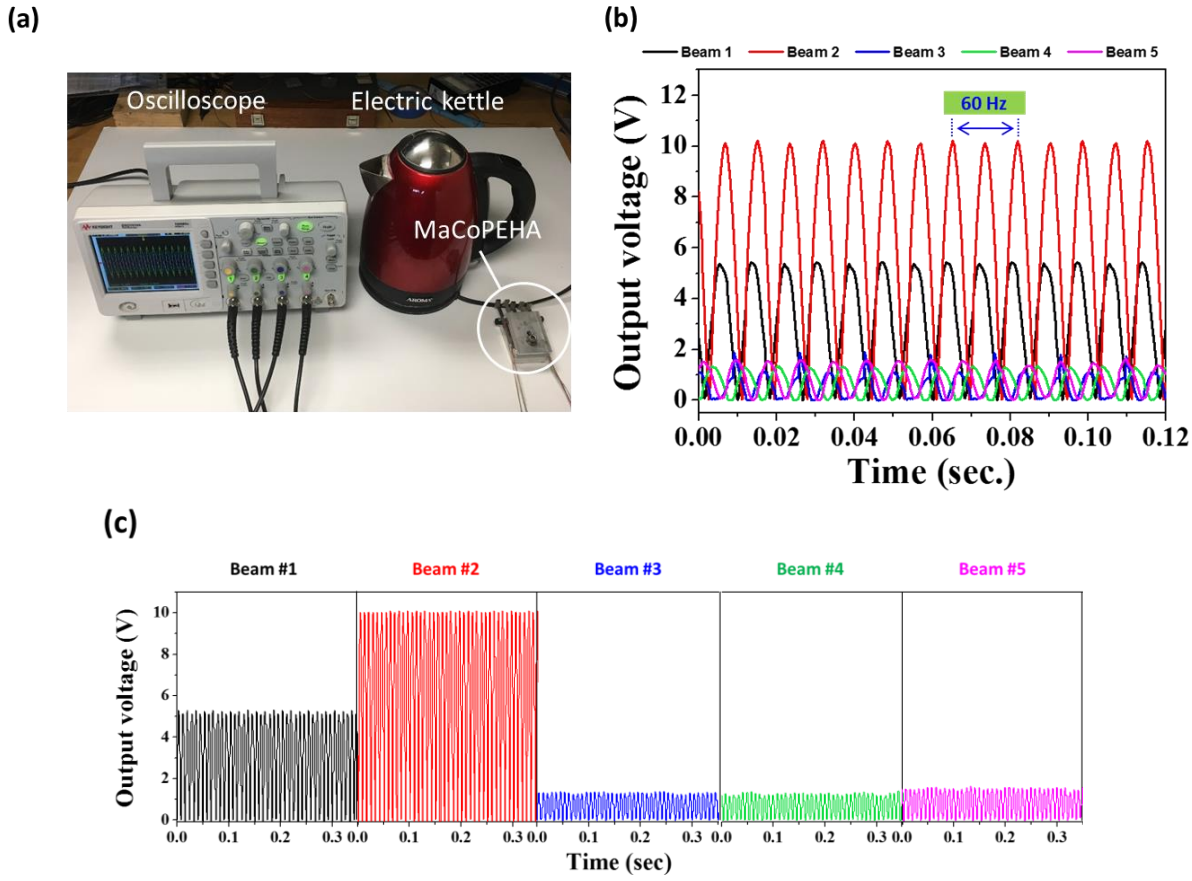

Figure 5.7. (a) Experimental setup for the stray magnetic field energy harvesting from the power cable of an electric kettle. (b) Generated open-circuit voltage of the MaCoPEHA from a power cable of an electric kettle. (c) Rectified output voltage of individual energy harvesters in the MaCoPEHA across the optimum load resistance of each beam.

Lastly, we implemented the MaCoPEHA on an automobile engine that naturally exhibits the continuously varying frequency in accordance to engine speed. Figure 3.8 (a) shows the experimental testing set-up on the automobile engine (Honda Accord 2014, 4 cycle 2.4L, 185 hp). The MaCoPEHA constituting four beams was mounted on top of the engine using superglue. Generated output voltage was recorded via 4-channel oscilloscope. The acceleration

and frequency of the engine vibration were monitored by accelerometer. Engine acceleration was varied in the range of 0.2 g ~ 0.55 g depending upon the throttle condition. Figure 3.8 (b) shows the generated voltages of the MaCoPEHA (internal load resistance of oscilloscope (1MΩ)) by varying the speed of the engine. The beam generating the maximum voltage in resonance was switched according to the vibration frequency. As shown in Fig. 3.8 (b), the dominant energy harvester in response to the engine vibration gradually changed from beam #4 to beam #1 with decrease of acceleration frequency. The results indicate that the MaCoPEHA has broadband characteristics and is able to generate sufficient power regardless of alternating vibration frequency. The generated power was measured through the rectifying circuit at the fixed load resistance of 250 kΩ; the maximum power of 67 μW was obtain at 70 Hz.

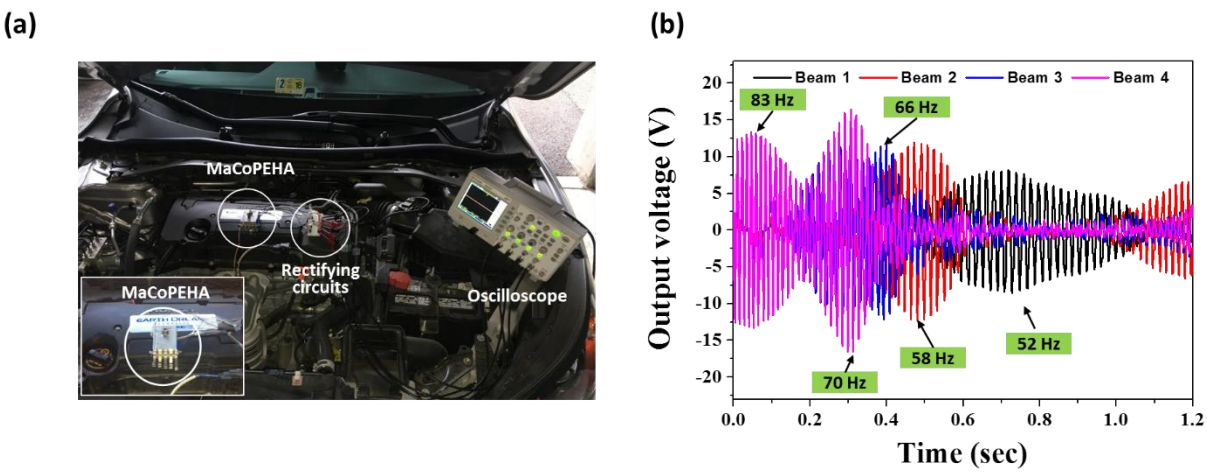

Figure 5.8. (a) Experimental setup for the vibration energy harvesting from an automobile engine. The MaCoPEHA with 4 beams was mounted on the top of the engine room. (b) Generated open-circuit voltages of the MaCoPEHA with variation of the engine acceleration. As alternating the engine acceleration, the responding beam in resonance is immediately shifted according to the frequency. The MaCoPEHA shows the broadband characteristics and is able to generate the sufficient power regardless of alternating vibration frequency.

5.4. Summary

We have demonstrated the magnetically coupled piezoelectric energy harvester array with broadband characteristics for harvesting the vibration and stray magnetic field. The broadband energy harvester was designed by arraying piezoelectric bimorph beams with gradually changing resonance frequencies and employing coupling between the magnetic proof masses. The harvester array showed significantly broad resonance frequency and improved output power density due to the magnetically induced coupling under both vibration and magnetic field conditions. The power densities under the vibration and the magnetic field were found to 243 $\mu W/cm^3 \cdot g^2$ at 78 Hz and 36.5 $\mu W/cm^3 \cdot Oe^2$ at 79.5 Hz, respectively. The magnetic coupling of arrayed energy harvesters is a promising strategy towards achieving broad bandwidth with high power density. For demonstrating the relevance in practical applications, our harvester was mounted on a rotary pump, and an automobile engine to quantify the vibration harvesting capability, as well as, on the power cord of an electric kettle to quantify the stray magnetic field harvesting capability. The array generated 51.7 μW, 67 μW and 246.5 μW from the pump vibration, the engine vibration and the magnetic field of power cord, respectively. This power is sufficient to run wireless sensor nodes for health monitoring of machines.

References

[1] S. P. Beeby, M. J. Tudor, and N. White, "Energy harvesting vibration sources for microsystems applications," *Measurement science and technology,* vol. 17, no. 12, pp. R175, 2006.

[2] H. S. Kim, J.-H. Kim, and J. Kim, "A review of piezoelectric energy harvesting based on vibration," *International Journal of precision engineering and manufacturing,* vol. 12, no. 6, pp. 1129-1141, 2011.

[3] P. D. Mitcheson, E. M. Yeatman, G. K. Rao, A. S. Holmes, and T. C. Green, "Energy harvesting from human and machine motion for wireless electronic devices," *Proceedings of the IEEE,* vol. 96, no. 9, pp. 1457-1486, 2008.

[4] S. Priya, and D. J. Inman, *Energy harvesting technologies*: Springer, 2009.

[5] X. Sheng, C. A. Bower, S. Bonafede, J. W. Wilson, B. Fisher, M. Meitl, H. Yuen, S. Wang, L. Shen, and A. R. Banks, "Printing-based assembly of quadruple-junction four-terminal microscale solar cells and their use in high-efficiency modules," *Nature materials,* vol. 13, no. 6, pp. 593-598, 2014.

[6] N. Wojtas, L. Rüthemann, W. Glatz, and C. Hierold, "Optimized thermal coupling of micro thermoelectric generators for improved output performance," *Renewable energy,* vol. 60, pp. 746-753, 2013.

[7] H.-C. Song, D. Maurya, J. Chun, Y. Zhou, M.-E. Song, D. Gray, N. K. Yamoah, D. Kumar, A. McDannald, and M. Jain, "Modulated Magneto-Thermal Response of $La_{0.85}Sr_{0.15}MnO_3$ and $(Ni_{0.6}Cu_{0.2}Zn_{0.2})Fe_2O_4$ Composites for Thermal Energy Harvesters," *Energy Harvesting and Systems*.

[8] J. Chun, H.-C. Song, M.-G. Kang, H. B. Kang, R. A. Kishore, and S. Priya, "Thermo-Magneto-Electric Generator Arrays for Active Heat Recovery System," *Scientific Reports,* vol. 7, 2017.

[9] S. P. Beeby, R. Torah, M. Tudor, P. Glynne-Jones, T. O'Donnell, C. Saha, and S. Roy, "A micro electromagnetic generator for vibration energy harvesting," *Journal of Micromechanics and microengineering,* vol. 17, no. 7, pp. 1257, 2007.

[10] B. Yang, C. Lee, W. Xiang, J. Xie, J. H. He, R. K. Kotlanka, S. P. Low, and H. Feng, "Electromagnetic energy harvesting from vibrations of multiple frequencies," *Journal of Micromechanics and Microengineering,* vol. 19, no. 3, pp. 035001, 2009.

[11] N. E. Dutoit, B. L. Wardle, and S.-G. Kim, "Design considerations for MEMS-scale piezoelectric mechanical vibration energy harvesters," *Integrated Ferroelectrics,* vol. 71, no. 1, pp. 121-160, 2005.

[12] J.-Q. Liu, H.-B. Fang, Z.-Y. Xu, X.-H. Mao, X.-C. Shen, D. Chen, H. Liao, and B.-C. Cai, "A MEMS-based piezoelectric power generator array for vibration energy harvesting," *Microelectronics Journal,* vol. 39, no. 5, pp. 802-806, 2008.

[13] M. Renaud, K. Karakaya, T. Sterken, P. Fiorini, C. Van Hoof, and R. Puers, "Fabrication, modelling and characterization of MEMS piezoelectric vibration harvesters," *Sensors and Actuators A: Physical,* vol. 145, pp. 380-386, 2008.

[14] S. Saadon, and O. Sidek, "A review of vibration-based MEMS piezoelectric energy harvesters," *energy conversion and management,* vol. 52, no. 1, pp. 500-504, 2011.

[15] S. Priya, H.-C. Song, Y. Zhou, R. Varghese, A. Chopra, S.-G. Kim, I. Kanno, L. Wu, D. S. Ha, and J. Ryu, "A Review on Piezoelectric Energy Harvesting: Materials, Methods, and Circuits," *Energy Harvesting and Systems,* vol. 4, no. 1, pp. 3-39, 2017.

[16] S. Roundy, and P. K. Wright, "A piezoelectric vibration based generator for wireless electronics," *Smart Materials and structures,* vol. 13, no. 5, pp. 1131, 2004.

[17] A. Erturk, and D. J. Inman, *Piezoelectric energy harvesting*: John Wiley & Sons, 2011.

[18] X. Wang, "Piezoelectric nanogenerators—harvesting ambient mechanical energy at the nanometer scale," *Nano Energy,* vol. 1, no. 1, pp. 13-24, 2012.

[19] B. Kumar, and S.-W. Kim, "Energy harvesting based on semiconducting piezoelectric ZnO nanostructures," *Nano Energy,* vol. 1, no. 3, pp. 342-355, 2012.

[20] G. Liu, P. Ci, and S. Dong, "Energy harvesting from ambient low-frequency magnetic field using magneto-mechano-electric composite cantilever," *Applied Physics Letters,* vol. 104, no. 3, pp. 032908, 2014.

[21] Y. Zhou, D. J. Apo, and S. Priya, "Dual-phase self-biased magnetoelectric energy harvester," *Applied Physics Letters,* vol. 103, no. 19, pp. 192909, 2013.

[22] D. R. Patil, Y. Zhou, J.-E. Kang, N. Sharpes, D.-Y. Jeong, Y.-D. Kim, K. H. Kim, S. Priya, and J. Ryu, "Anisotropic self-biased dual-phase low frequency magneto-mechano-electric energy harvesters with giant power densities," *APL Materials,* vol. 2, no. 4, pp. 046102, 2014.

[23] K. Tashiro, H. Wakiwaka, S.-i. Inoue, and Y. Uchiyama, "Energy harvesting of magnetic power-line noise," *IEEE Transactions on Magnetics,* vol. 47, no. 10, pp. 4441-4444, 2011.

[24] R. Vullers, R. van Schaijk, I. Doms, C. Van Hoof, and R. Mertens, "Micropower energy harvesting," *Solid-State Electronics,* vol. 53, no. 7, pp. 684-693, 2009.

[25] J. Ryu, J.-E. Kang, Y. Zhou, S.-Y. Choi, W.-H. Yoon, D.-S. Park, J.-J. Choi, B.-D. Hahn, C.-W. Ahn, and J.-W. Kim, "Ubiquitous magneto-mechano-electric generator," *Energy & Environmental Science,* vol. 8, no. 8, pp. 2402-2408, 2015.

[26] R. C. Kambale, J.-E. Kang, W.-H. Yoon, D.-S. Park, J.-J. Choi, C.-W. Ahn, J.-W. Kim, B.-D. Hahn, D.-Y. Jeong, and Y.-D. Kim, "Magneto-Mechano-Electric (MME) Energy Harvesting Properties of Piezoelectric Macro-fiber Composite/Ni Magnetoelectric Generator," *Energy Harvesting and Systems,* vol. 1, no. 1-2, pp. 3-11, 2014.

[27] V. Annapureddy, H. Y. Lee, W.-H. Yoon, H.-J. Woo, J.-H. Lee, H. Palneedi, H.-J. Kim, J.-J. Choi, D.-Y. Jeong, and S. N. Yi, "Enhanced magnetic energy harvesting properties of magneto-mechano-electric generator by tailored geometry," *Applied Physics Letters,* vol. 109, no. 9, pp. 093901, 2016.

[28] V. Annapureddy, M. Kim, H. Palneedi, H. Y. Lee, S. Y. Choi, W. H. Yoon, D. S. Park, J. J. Choi, B. D. Hahn, and C. W. Ahn, "Low-Loss Piezoelectric Single-Crystal Fibers for Enhanced Magnetic Energy Harvesting with Magnetoelectric Composite," *Advanced Energy Materials,* vol. 6, no. 24, 2016.

[29] F. Cottone, H. Vocca, and L. Gammaitoni, "Nonlinear energy harvesting," *Physical Review Letters,* vol. 102, no. 8, pp. 080601, 2009.

[30] S. C. Stanton, C. C. McGehee, and B. P. Mann, "Nonlinear dynamics for broadband energy harvesting: Investigation of a bistable piezoelectric inertial generator," *Physica D: Nonlinear Phenomena,* vol. 239, no. 10, pp. 640-653, 2010.

[31] A. Hajati, and S.-G. Kim, "Ultra-wide bandwidth piezoelectric energy harvesting," *Applied Physics Letters,* vol. 99, no. 8, pp. 083105, 2011.

[32] S.-E. Jo, M.-S. Kim, and Y.-J. Kim, "A resonant frequency switching scheme of a cantilever based on polyvinylidene fluoride for vibration energy harvesting," *Smart Materials and Structures,* vol. 21, no. 1, pp. 015007, 2011.

[33] D. Zhu, S. Roberts, J. Tudor, and S. Beeby, "Closed loop frequency tuning of a vibration-based micro-generator," *Proceedings of PowerMEMS 2008,* pp. 229–232, 2008.

[34] A. M. Wickenheiser, "Design optimization of linear and non-linear cantilevered energy harvesters for broadband vibrations," *Journal of Intelligent Material Systems and Structures,* vol. 22, no. 11, pp. 1213-1225, 2011.

[35] K.-H. Cho, H.-Y. Park, J. S. Heo, and S. Priya, “Structure–performance relationships for cantilever-type piezoelectric energy harvesters,” *Journal of Applied Physics*, vol. 115, no. 20, pp. 204108, 2014.

[36] S. Dong, J. Zhai, J. Li, D. Viehland, and S. Priya, “Multimodal system for harvesting magnetic and mechanical energy,” *Applied Physics Letters*, vol. 93, no. 10, pp. 103511, 2008.

[37] C. Ó. Mathúna, T. O’Donnell, R. V. Martinez-Catala, J. Rohan, and B. O’Flynn, “Energy scavenging for long-term deployable wireless sensor networks,” *Talanta*, vol. 75, no. 3, pp. 613-623, 2008

6. Chapter 6: Modulated magneto-thermal response of $La_{0.85}Sr_{0.15}MnO_3$ and $(Ni_{0.6}Cu_{0.2}Zn_{0.2})Fe_2O_4$ composites

6.1. Introduction

In last few decades, thermoelectric generators have been the focus for converting thermal energy into electrical energy.[1-8] The performance of thermoelectric device depends upon the figure of merit of the material, *ZT*, where *Z* is a measure of a material's electrical and thermal properties and *T* is the absolute temperature. Most of bulk thermoelectric materials show *ZT* values lower than 1 at room temperature, although there has been report of *ZT* = ~ 2.4 at 300 K in thermoelectric thin film with superlattice structure.[9, 10] However, thermoelectric devices even with these high *ZT* values require large temperature gradient (Carnot's efficiency is related to difference in hot and cold side temperature) in the material to achieve high output power. It is challenging to preserve the large temperature differential within thermoelectric devices because of the lack of thermal dissipation and radiative losses. It is even more challenging to find sustainable large temperature gradient in the surrounding environment conducive for energy harvesting. Therefore, practical implementation of thermoelectric devices near room temperature has been limited.

To overcome these problems of thermoelectric devices, magneto-thermoelectric generator (MTG) concept has been proposed which exploits the thermally induced second order phase transition of soft magnetic material at their Curie temperature (T_C).[11-13] The MTG is composed of two main parts; an actuating part and heat exchanger. The actuating part consists of a bimorph piezoelectric cantilever structure (piezoelectric layers applied on both side of metal shim) and a soft magnet which is placed at the end of the cantilever as shown in Figure 6.1. The actuating part is kept between the heat exchanger comprising of cold sink and hot

source as described in Figure 6.1. The hard magnet is attached to the hot source and it attracts the soft magnet mounted on the cantilever. At the beginning of operation, soft magnet is attracted to the hard magnet attached to the hot source. When the soft magnet is heated above its T_C, it transitions into the paramagnetic state and loses the attraction force. At that instant, the elastic forces from the cantilever detaches it from the hard magnet surface and returns it back towards the cold sink. Upon contacting the cold surface, the soft magnet again cools below T_C and transforms into ferromagnetic state. Thus, it once again gets attracted towards the hard magnet surface due to magnetic force of attraction. This continuous heat exchanging cycle repeats until the hot source temperature is maintained above certain threshold with respect to T_C of the soft magnet. During this continuous cycle, the soft magnet periodically oscillates at a fixed frequency and the mechanical energy is converted into electric energy through piezoelectric elements attached/deposited on the cantilever.

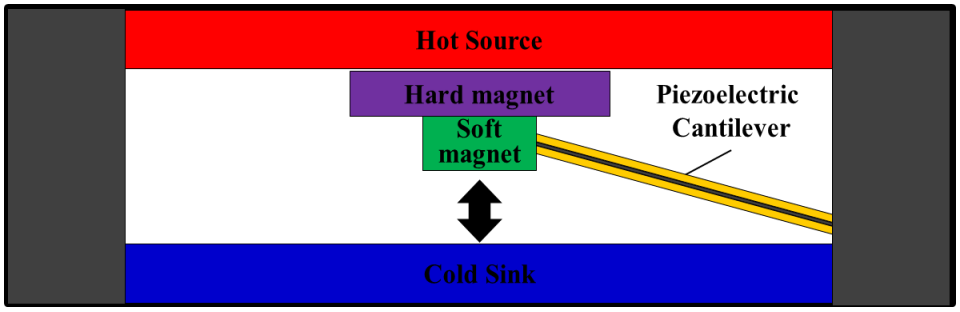

Figure 6.1. Schematic structure of Magneto-electric Thermal Generator (MTG).

To efficiently operate the MTG, the fundamental challenge lies in synthesizing suitable soft magnetic materials that exhibit high magnetization change at T_C. Further, the soft magnetic material can be easily magnetized by the external magnetic field. To operate MTG near room temperature, the T_C of soft magnetic material should be close to the room temperature while maximizing the saturated (M_s) and remnant (M_r) magnetization with small coercive field (H_c). The magnetic force between the hard and soft magnet (Figure 6.1) can be expressed as:[11]

$$F_{mag} = \int_V M \nabla B_{mag} dV = -\int_V (\nabla . \mathrm{M}) B_{mag} dV + \int_S \mathrm{M} B_{mag} dS$$
$$= \int_V \rho_{mag} B_{mag} dV + \int_S \sigma_{mag} B_{mag} dS \quad (6.1)$$

Here, $\rho_{mag} = -\nabla . M =$ volume (magnetic) charge density, $\sigma_{mag} = M =$ surface (magnetic) charge density. Thus, magnetic force is function of magnetization M and gradient of magnetization $\nabla . M$ that in turn are function of temperature and temperature gradient respectively. The force in z-direction, assuming temperature is uniform throughout cross-section, can be determined as:

$$F_{mag}(z) = -A_{Gd} \int_{w_m}^{w_m+th} \frac{dM}{dz} B_{mag}(z) dz$$
$$+ A_{Gd} \left(M(w_m + th) B_{mag}(w_m + th) - M(w_m) B_{mag}(w_m) \right) \quad (6.2)$$

Equation (6.1) and (6.2) show that the gradient in magnetization of the soft magnet along with the B-magnetic field of hard magnet as function of distance z from the surface are critical parameters. In this study, we engineered the composite material architecture based upon $La_{0.85}Sr_{0.15}MnO_3$ (LSMO) and $Ni_{0.6}Cu_{0.2}Zn_{0.2}Fe_2O_4$ (NCZF) that is able to meet the above mentioned requirements for continuous operation of MTG near room temperature.

6.2. Experimental

6.2.1. Synthesis LSMO and NCZF Magnetic Composites

$La_{(1-x)}Sr_xMnO_3$ ceramics with composition $0.15 \leq x \leq 0.30$ were prepared using high purity (> 99%) oxide precursors through conventional solid-state reaction. These oxide compounds

La_2O_3, $SrCO_3$ and MnO_2 (Sigma-Aldrich, St. Louis, USA, > 99 %) were ball milled under high purity ethanol for 24 h in a nylon jar with zirconia balls as milling media. After ball-milling, the slurry was dried and calcined at 850 °C for 3 hours. After calcination, the resulting powders were further ball milled for 24 hours followed by drying in an oven. The dried powders were sieved and pressed uniaxially into cylindrical pellets followed by sintering at 1300 °C for 2 hours. We synthesized Ni–Cu–Zn ferrite having composition of $Ni_{0.6}Cu_{0.2}Zn_{0.2}Fe_2O_4$ (NCZF) using conventional solid-state reaction with NiO, CuO, ZnO and Fe_2O_3 (Sigma-Aldrich, > 99 %) as precursors. The calcination and sintering temperatures for NCZF were selected to be 750 °C (5h) and 900 °C (2h), respectively. The sintered NCZF powder was crushed and ball-milled for 48 hours to achieve fine powder. In order to make LSMO-NCZF magnetic composite system, different amounts of NCZF powder were mechanically mixed with the LSMO powder. These mixed powders were uniaxially pressed into cylindrical pellets followed by isostatic pressing under 200 MPa. The composite green pellets were sintered using two-step heating method in order to prevent the inter diffusion of LSMO and NCZF phases (Chen and Wang 2000; Wang et al. 2006a). The LSMO-NCZF composite samples were first heated at the rate of 10 °C/min up to 1075 °C followed by rapid cooling to a lower temperature of 1025 °C at the rate of 200 °C/min for isothermal sintering with a dwell time of 8 h. The phase formation and microstructure of specimens was examined by X-ray diffraction (XRD, Brucker, D8 Advance) and field-emission scanning electron microscopy (FESEM, LEO (Zeiss) 1550), respectively. The composition of various specimens was investigated through energy-dispersive spectroscopy (EDS). The magnetic domain configuration was observed using magnetic force microscopy (MFM, Brucker, Dimension FastScan). For quantifying magnetic properties, vibrating sample magnetometer (VSM) attached to the evercool physical property measurement system (PPMS, Quantum Design) was used.

6.2.2. Fabrication of Magneto-thermoelectric Generator using Magnetic Composite

The two-step sintered soft magnetic material was machined to rectangular shape of 8.7 × 5.4 × 0.4 mm^3 dimension. To reduce surface thermal contact resistance, a silver electrode was coated on both side of the soft magnetic material. The fabricated soft magnetic material was attached on a bimorph piezoelectric cantilever beam using super glue as shown in Figure 6.1 (b). The bimorph piezoelectric cantilever consisted of 200 μm thickness platinized PVDF films (Kureha Inc.) assembled on 30 μm steel shim by double sided tape. In order to prevent voltage cancelation, poling direction of PVDF films were opposite to each other. The testing set up for the hot source and cold sink was designed using thermoelectric modules as heater and cooler. Cooling fan was added on cold-side to maintain the temperature steady. Neodymium (Nd) based permanent magnet was attached on the hot-side using conductive silver epoxy for efficient heat transfer. The moving part of the piezoelectric cantilever beam was fixed between thermoelectric heater and cooler. The gap distance between cold-side and the hard magnet was fixed at 6 mm. The operation test of MTG using the LSMO-NCZF composite was conducted using experimental set-up shown in Figure 6.11 (a).

6.3. Results and Discussion

6.3.1. LSMO and NCZF Magnetic Composite

Figure 6.2 (a) shows the temperature-dependent magnetization of $La_{(1-x)}Sr_xMnO_3$ ceramics in terms of strontium content (x) variation from 0.15 to 0.30. The magnetization curves were measured after field cooling at 100 Oe. The T_C was derived from the M-T curves by determining the intersection on the T-axis by the tangent at the inflexion point. The T_C of $La_{(1-x)}Sr_xMnO_3$ ceramics gradually increased from 310 K to 370 K with increase of strontium content (x). The variation of the T_C in perovskite lanthanum manganite is directly related to

concentration of tetravalent manganese ion (Mn^{4+}) in the lattice.[14] This can be attributed to the fact that Mn^{4+} ions can improve the double-exchange (DE) interaction [15-17] between heterovalent ion (Mn^{3+}, Mn^{4+}) neighbors in the manganite lattice.[18] The increased exchange interaction could elevate binding force between the magnetic ions and consequently the T_C. According to *Jonker et al. (1950)*, the amount of Mn^{4+} in $La_{(1-x)}Sr_xMnO_3$ ceramics can be increased by increasing the La^{3+} substitution on Sr^{2+} site up to about 35% Sr when fired in air atmosphere. In case of more than 35% Sr content, it is possible to obtain higher concentration of Mn^{4+} by firing in pure oxygen atmosphere. Thus, the T_C of $La_{(1-x)}Sr_xMnO_3$ system can be engineered through control of Sr content and sintering atmosphere as shown by our results which is consistent with the previous studies.

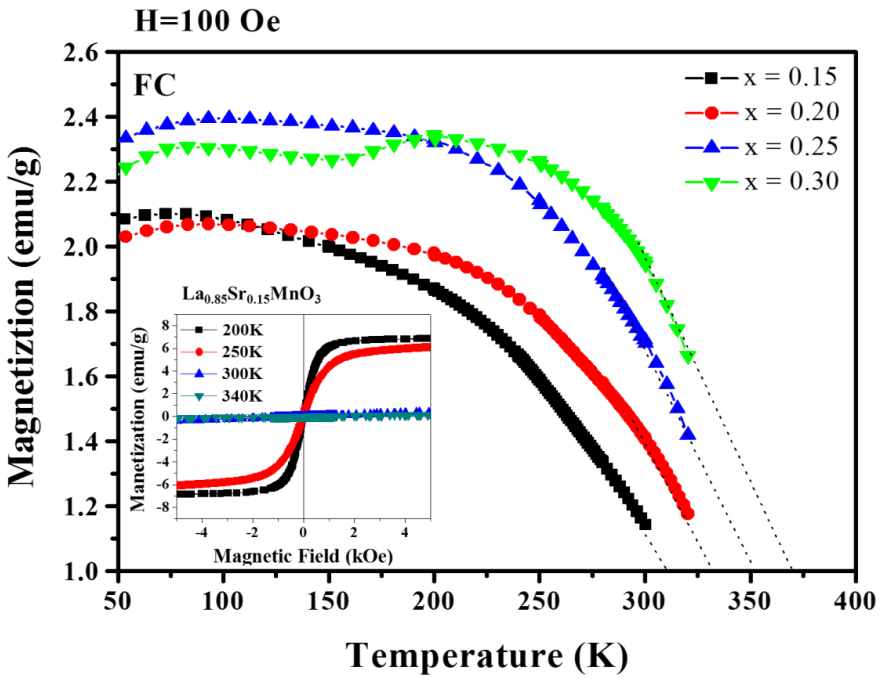

Figure 6.2. Field-cooled (FC) temperature-dependent magnetization of $La_{(1-x)}Sr_xMnO_3$ in the $0.15 \leq x \leq 0.30$ strontium content range with applied field of 100 Oe. The inset shows magnetization vs. applied magnetic field (M-H hysteresis curves) data of $La_{0.85}Sr_{0.15}MnO_3$ at various temperatures.

Figure 6.3 shows the isothermal magnetization hysteresis with variation of Sr content (x) in $La_{(1-x)}Sr_xMnO_3$ at 250 K. The value of saturation magnetization (M_s) was increased from 6 emu/g (for x =0.15) to 8.4 emu/g (for x = 0.30) with increasing Sr ratio. The increased value of M_s can be attributed to the increased exchange interaction owing to the increased Mn^{4+} ion concentration (Jonker and Santen 1950).[14] As shown in inset of Figure 4.3, all M-H curves exhibited clear hysteresis behavior at low applied magnetic fields with coercive fields (H_c) of 27.5, 29, 30 and 35 Oe and remnant magnetization (M_r) values of 0.49, 0.63, 0.75 and 0.90 emu/g for $La_{(1-x)}Sr_xMnO_3$ with x = 0.15, 0.20, 0.25 and 0.30, respectively. These moderately low values of H_c and M_r are typical characteristics of a soft magnetic material. However, the M_s and M_r values of $La_{(1-x)}Sr_xMnO_3$ system were low and needed new approach to achieve the desired range for their applications in MTG.

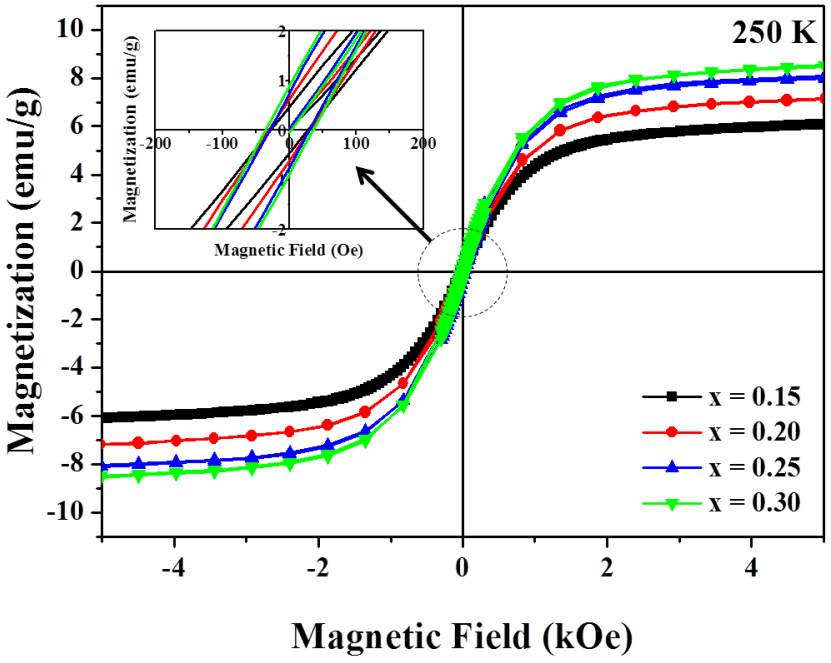

Figure 6.3. M-H hysteresis curves of $La_{(1-x)}Sr_xMnO_3$ with variation of Sr content at 250 K. The inset shows zoomed view of hysteresis curves.

The relative materials performance index (PI) for MTG can be defined by following equation,

$$\mathrm{PI} = (M_{s,\,Tc} - M_{s,\,T1}) / (T_C - T_1) \tag{6.3}$$

where T_C is Curie temperature, T_1 is applied temperature gradient for MTG, $M_{s,\,Tc}$ is saturated magnetization under constant magnetic field at T_C and $M_{s,\,T1}$ is saturated magnetization under constant magnetic field at T_1. The inset of Figure 6.2 shows the isothermal magnetization of $La_{0.85}Sr_{0.15}MnO_3$ composition at several temperatures. The PI of $La_{0.85}Sr_{0.15}MnO_3$ was found to be 0.116 emu/g·K under 5 kOe, calculated using the saturated magnetization value change from 250 K (ferromagnetic state) to 300 K (paramagnetic state). For successful operation of MTG, this value for the soft magnet should be improved significantly.

In order to achieve large M_s and M_r while maintaining soft magnetic nature, we engineered bulk composite of LSMO soft magnetic material with NCZF hard magnetic material. The LSMO composition has been chosen for the base matrix of magnetic composite due to its *Tc* close to room temperature. The NCZF powder was mechanically mixed with the LSMO powder in different weight ratios. It was found that if the compact of LSMO and NCZF mixture are sintered using normal heating schedule (1200 ^{o}C for 2 hours sintering, heating rate 5 ^{o}C/min) the most manganese element in LSMO diffused into the NCZF phase as shown in EDS mapping images of Figure 6.4. The M-T curves of the Mn element diffused LSMO and NCZF composite is shown in Figure 6.5. The Curie temperature of the LSMO-NCZF magnetic composites were gradually decreased and became increasingly blurred as increasing NCZF content. The magnetization values below Tc were also decreased from 20 wt.% NCZF, however the magnetization values above *Tc* were gradually increased as increasing NCZF content. These are because overall magnetic phases were transformed by Mn element diffusion. In order to maintain discrete phases of LSMO and NCZF in this composite system, we adopted two-step sintering approach.[19, 20] The two-step sintering suppresses the grain-boundary migration

while keeping the grain boundary diffusion active. Therefore, through the two-step sintering, the inter-granular diffusion and grain growth can be suppressed while achieving higher packing density.

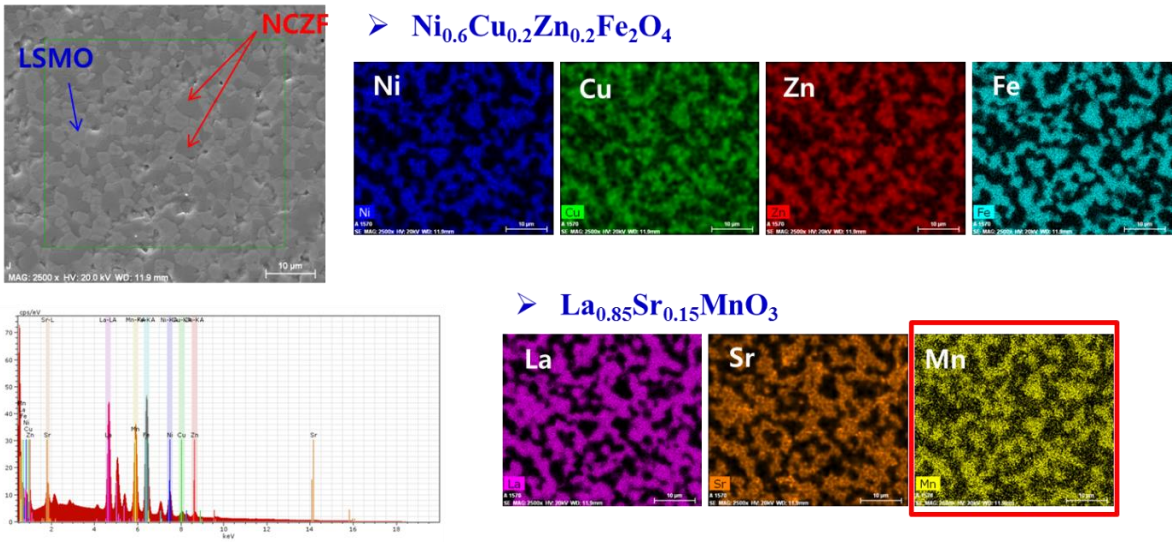

Figure 6.4. SEM and EDS mapping images of 70 wt.% LSMO – 30 wt.% NCZF magnetic Composites sintered by conventional firing schedule (1200 °C for 2hours).

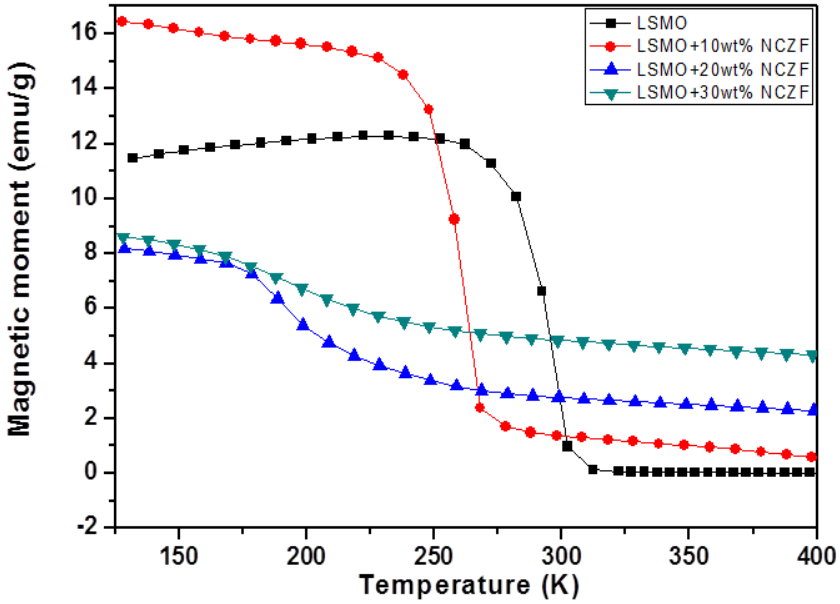

Figure 4.5. SEM Field-cooled (FC) temperature-dependent magnetization of (100-x) wt.% LSMO – x wt.% NCZF magnetic composites sintered by conventional firing schedule (1200 °C for 2hours) in the $0 \leq x \leq 30$ NCZF content range.

Figure 6.6 (a) and (b) show the X-ray diffraction (XRD) patterns of pure LSMO and NCZF ceramics sintered at 1300 °C and 950 °C for 2 hours, respectively. The data shows that the homogeneous LSMO and NCZF phases were formed without any secondary phase. Figure 6.6 (c) ~ (e) shows XRD patterns of LSMO-NCZF magnetic composites with different weight % of NCZF sintered using the two-step firing schedule, i.e., fired at 1075 °C for short duration and then sintered at 1025 °C for 8 hours. The intensity of XRD peaks was found to increase gradually with the increase of NCZF content. The peaks for LSMO and NCZF phases in composites were distinct and no impurity phases were detected, which is clear evidence that inter-diffusion of LSMO and NCZF phases did not occur and high quality two phase ceramic composites were realized.

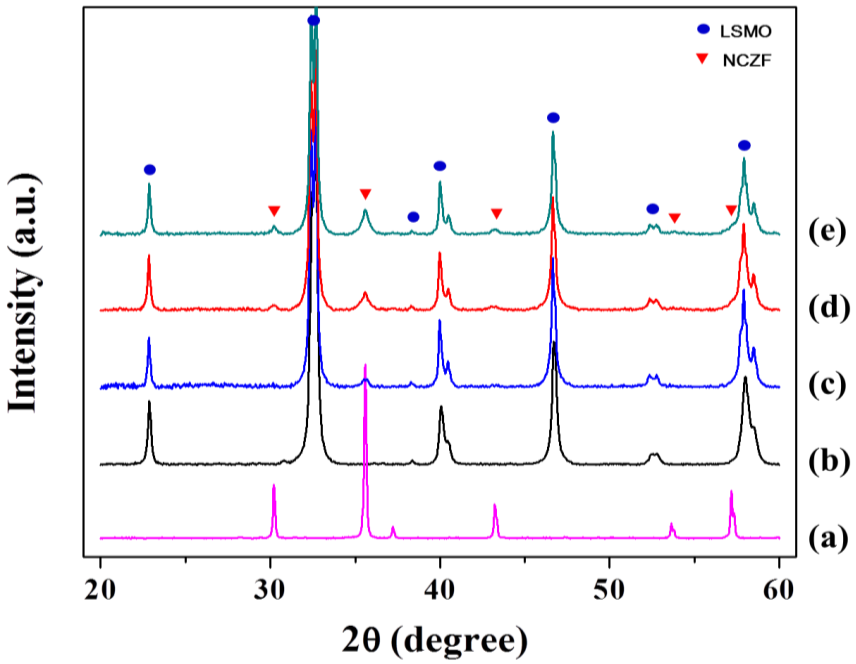

Figure 6.6. XRD patterns of (a) $Ni_{0.6}Cu_{0.2}Zn_{0.2}Fe_2O_4$, (b) $La_{0.85}Sr_{0.15}MnO_3$, (c) 90 *wt.*%LSMO-10*wt.*%NCZF, (d) 80*wt.*%LSMO-20*wt.*NCZF, and (e) 70*wt.*%LSMO-30*wt.*%NCZF magnetic composites sintered by two-step schedule (1075 °C => 1025 °C for 8 hours).

The SEM image of the surfaces of composite with 30 *wt.*% NCZF composition sintered by two-step schedule (1075 °C, 1025 °C for 8 h) is shown in Figure 6.7 (a). Figure 6.7 (b) shows an electron backscatter diffraction (EBSD) image of the morphology. A highly dense microstructure was formed by two-step sintering with the average grain size of 200 nm. The grain growth was suppressed by avoiding the grain boundary migration in the two-step sintering process. The relatively inhomogeneous size of grains might be attributed to the different size of initial powders of LSMO and NCZF. NCZF phase possessed larger grains than the LSMO as illustrated in Figure 6.7 (a) and (b). In the second step of sintering process, there is not much change in the microstructure except the reduction of porosity, because the grain boundary network is frozen. Therefore, the second step is important to achieve densification of the frozen microstructure. The normalized densification rate can be expressed as:[21]

$$\frac{d\rho}{\rho dt} = M(\rho)\frac{3s\mathrm{V}}{k_B T}\frac{\delta D}{L^4} \tag{6.4}$$

where, $s\ is$ surface energy, t is the time, k_B is the Boltzmann constant, T is the absolute temperature, V is the atomic volume, L is the mean grain size, δ is the grain boundary width, D is the grain boundary diffusivity, $M(\rho)$ is unspecified function of density. To confirm the absence of the Mn diffusion from LSMO to NCZF phase, energy-dispersive spectroscopy (EDS) mapping was conducted on the two-step sintered LSMO-NCZF (70:30 *wt.*%) composite. Figure 6.7 (c) ~ (e) shows EDS mapping images for representative elements, Mn and Fe, in each phase. Both elements were homogeneously distributed over the entire surface of the specimen, as shown in Figure 6.7 (d) and (e). However, the spatial arrangement of Mn and Fe elements was almost separated from each other as can be seen in the Figure 6.7 (c). The relatively ambiguous boundary of Mn and Fe elements in EDS mapping image could be attributed to the fact that the size of most grains (~ 200 nm) are smaller than the minimum

useful detection spot size (~ 2 μm) of EDS as shown in the electron backscatter diffraction (EBSD) image of Figure 6.7 (b). The separate distribution of Mn and Fe elements confirms that LSMO and NCZF phases were preserved during the sintering process. By employing a two-step sintering process, we achieved a dense microstructure and fine grains without inter diffusion for two phase ceramic composite system.

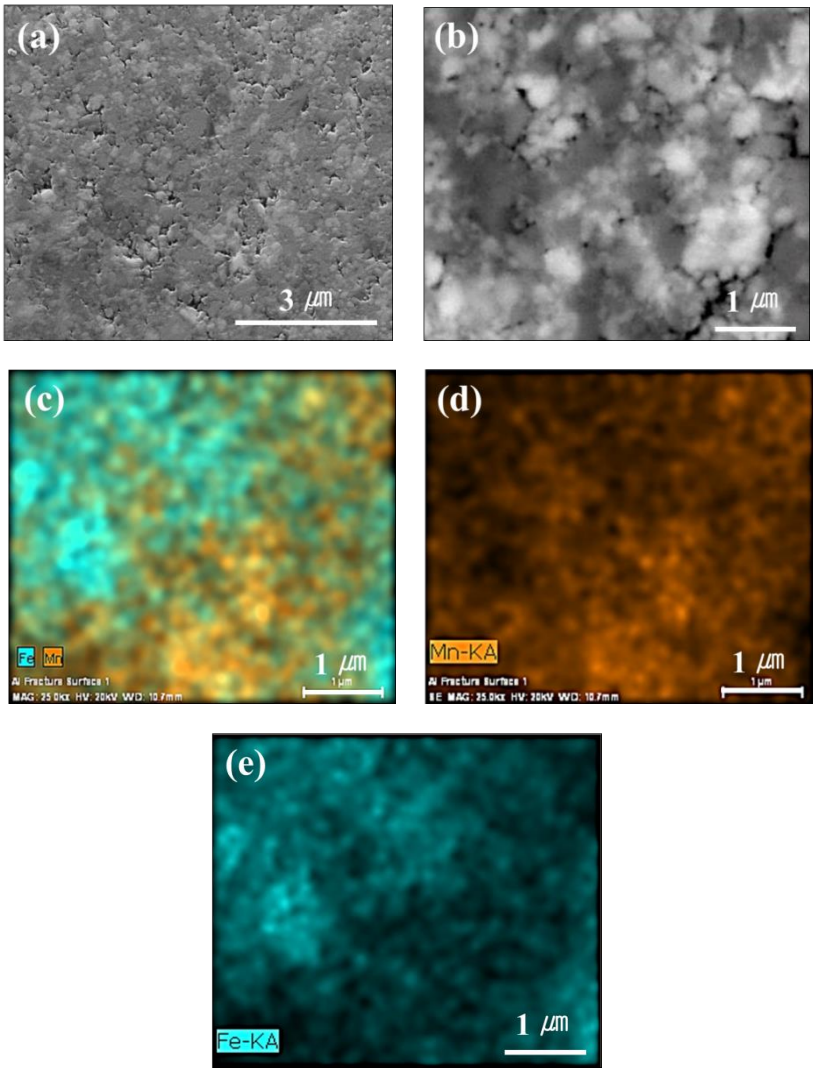

Figure 6.7. Two-step sintered LSMO-NCZF (70:30 *wt.*%) magnetic composite (a) SEM image, (b) EBSD image, (c) EDS mapping image for Fe and Mn elements, (d) EDS mapping image for Mn element and (e) EDS mapping image for Fe element.

In order to understand the magnetic domain and phase configuration of LSMO-NCZF composite, magnetic force microscopy (MFM) was conducted. MFM was performed below Curie temperature (at 290 K) of specimens to check the magnetic properties in ferromagnetic state. Figure 6.8 (a) and (b) shows the topographic and magnetic phase images of two-step sintered 30 *wt*% NCZF magnetic composite, respectively. As shown in Figure 6.8 (a) and (b), clear grain boundaries were observed and each phase had discrete and separated grains. As can be seen in Figure 6.8 (b), the magnetic grains and clusters were clearly visible, however, the magnetic domains were not resolved owing to the discontinuous magnetic grain ordering in the lattice. The NCZF grains showed quite different contrast compared with LSMO grains because the NCZF grains with hard magnetic nature have higher magnetization. It can be assumed that the NCZF grains influence the LSMO matrix with soft magnetic properties by modulating the domain structure and magnetic response of the overall composite.

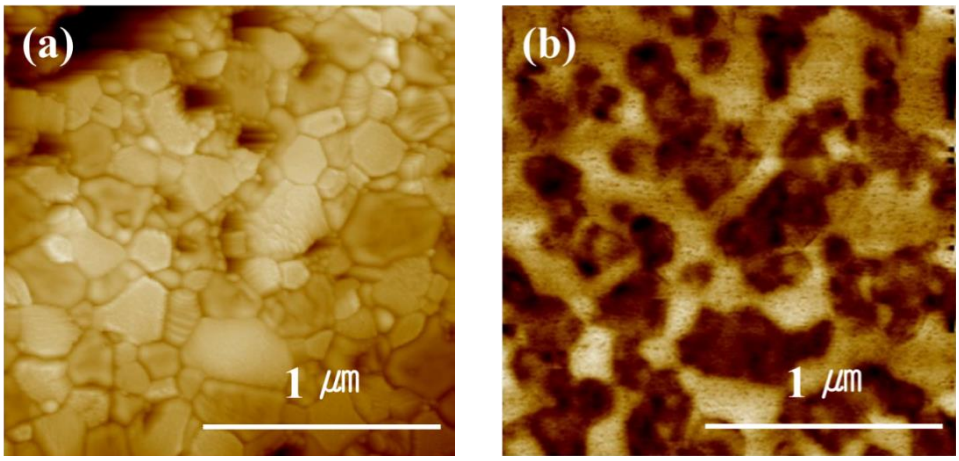

Figure 6.8. (a) Topographic and (b) MFM magnetic phase images of two-step sintered LSMO-NCZF (70:30 *wt.*%) magnetic composite

Figure 6.9 (a) shows the temperature dependence of the magnetization (M-T) curves for the mixed powder and two-step sintered magnetic composite with 30 *wt.*% NCZF composition. The zero field-cooled (ZFC) curve was measured after cooling the specimen from 350 K down

to 5 K without applying magnetic field. The field-cooled (FC) curve was obtained after initially cooling the specimen with an applied field of H = 500 Oe and then measured on heating. The ZFC and FC curves of the mixed powder and two-step sintered composite started to separate below 260 K, which indicates an irreversibility associated with the presence of magnetically disordered clusters in the lattice.[22] The phase transition from paramagnetic to ferromagnetic was observed at *Tc* of 300 K in both cases. The *Tc* was reduced by 10 K compared to the pure LSMO which might be attributed to the presence of NCZF causing changes in the defect chemistry. The similarity of the temperature dependence of magnetic response in the composite and the mixture in Figure 6.9 (a), indicates that the enhancement of magnetization comes from densification of the mixture. It is important to note that the magnetic nature of the mixture did not change after sintering and mainly densification was involved in the improvement of magnetization.

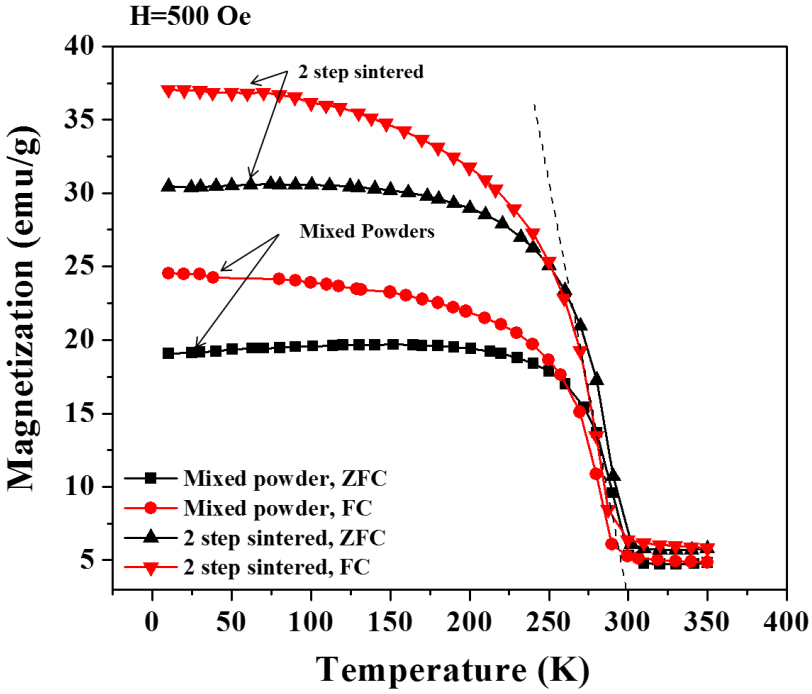

Figure 6.9. The M-T curves of mixed powder and two-step sintered magnetic composite with LSMO-NCZF (70:30 *wt.*%) composition.

Figure 6.10 (a) shows the M-H hysteresis curves for the two-step sintered 30 *wt.*% NCZF composite (with LSMO) at different temperatures. As shown in the inset of Figure 6.10 (a), all isothermal magnetization loops showed clear hysteretic characteristics with soft magnetic nature at various temperatures. In particular, it is interesting to note that the curves above the *Tc* (300 K~) had a weak hysteretic characteristic, which may be attributed to the hard magnetic nature of NCZF phase existing in the matrix even though the LSMO lattice is in the paramagnetic state. It can be seen from the M-H curve at 250 K that the M_r and M_s values of the composite significantly improved to 9.6 emu/g and 47 emu/g in comparison to that of 0.49 emu/g and 6 emu/g for pure-LSMO, respectively. On the other hand, the H_c value was only moderately increased from 27.5 Oe (for LSMO) to 178 Oe (for LSMO-30 wt% NCZF composite) owing to the hard magnetic nature of the NCZF. This can be explained by noticing that the overall magnetic response is average of the individual contributions from LSMO and NCZF phase proportional to their volume fraction.[23] The PI value estimated for the composite having 30 *wt.*% NCZF, considering M_s change in the range of 250 K - 300 K (Figure 6.10 (a)), was increased to 0.552 emu/g·K (at 5 kOe) in comparison with that of pure LSMO (0.116 emu/g·K). This value is still lower than 0.786 emu/g·K (at 5 kOe) of P.I. obtained for gadolinium (Gd) foil from M-H hysteresis curves in Figure 6.10 (b). However, the LSMO-NCZF composites have advantage of tunable Curie temperature depending on the operation temperature with relative large P.I. value. This tunability is desired and makes LSMO-NCZF composite a potential candidate for soft magnetic materials in MTG.

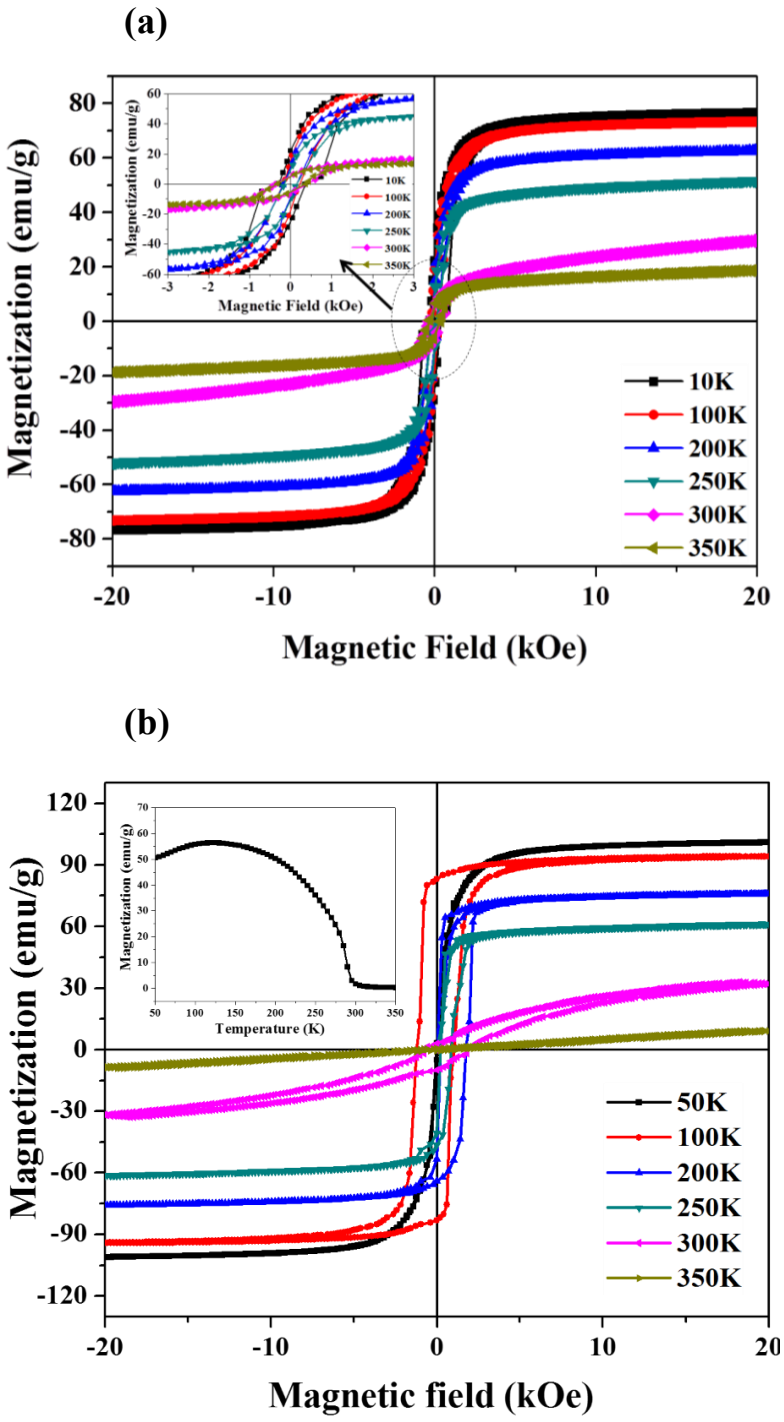

Figure 6.10. (a) The M-H hysteresis curves of two-step sintered LSMO-NCZF (70:30 *wt.*%) magnetic composites with variation of temperature. Inset is zoomed view of hysteresis curves. (b) The M-H hysteresis curve of gadolinium (Gd) foil. Inset is the M-T curves of Gd foil with variation of temperature.

6.3.2. MTG Operation Test using LSMO-NCZF Composite

Figure 6.11 (a) shows the operation test set-up for MTG with a cantilever beam structure. The hot source and heat sink were created by using thermoelectric module. A cooling fan was attached under thermoelectric module to maintain continuous cooling condition. The soft magnet was attached at the end of bimorph PVDF cantilever beam as shown in Figure 6.11 (b) and placed between hot and cold side. After applying electric field to thermoelectric module, the temperature gradient (ΔT) was induced and maintained at 80 °C (0°C / 80°C). The gap distance between cold-side and hot-side hard magnet was maintained at 6 mm. Figure 6.12 lower inset image shows the ferromagnetic state of the soft magnetic material below its Curie temperature when it is attracted to the hot-side of the permanent magnet. Figure 6.12 upper inset image shows the paramagnetic state of soft magnet when it was detached from the permanent magnet and pulled towards the heat sink after losing magnetic force of attraction. This cycle of attraction and detachment was repeated by continuous ferromagnetic and paramagnetic phase change of the soft magnet at its Curie temperature.

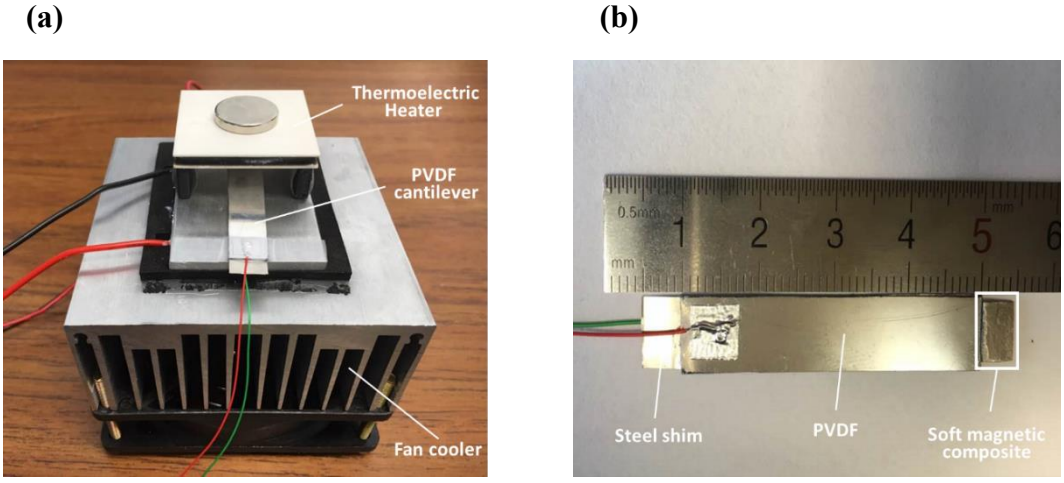

Figure 6.11 (a) MTG operation test set-up for the soft magnetic material. (b) Bimorph piezoelectric cantilever beam with LSMO–NCZF (70:30 *wt.*%) soft magnetic material developed in this study.

Figure 6.12 shows the generated output voltage at ΔT = 80 °C in MTG. The generated output voltage was approximately 2 V_{P-P} and the attraction to the magnet showed a larger output voltage than detachment. This is due to the higher attraction force by the magnet as compared to the releasing force by the cantilever. The generated maximum peak power was 17 μW at 1MΩ. The operational frequency of the soft magnetic material was around 0.2 Hz. Thermal conductivity of soft magnetic composite as a function of temperature is shown in Figure 4.13 From this data, it can be seen that thermal conductivity at Curie temperature (300K) was low, on the order of 1.75 W/(m·K). The measured thermal conductivity increased with increasing temperature but was still lower than 8.0 W/(m·K) achieved for Gd metal at 300 K. In our future studies, higher thermal conducting material such as carbon nanotube or graphene will be incorporated inside the matrix of the magnetic material to enhance the overall thermal conductivity.

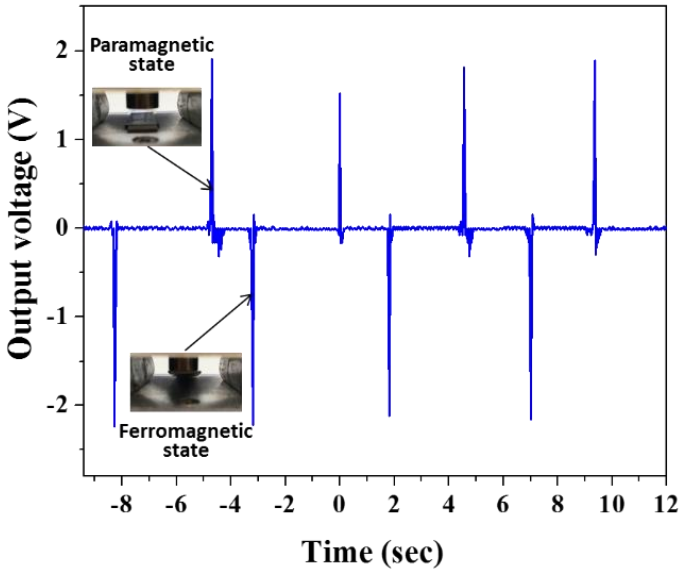

Figure 6.12. Generated output voltage by MTG using the LSMO–NCZF (70:30 *wt.*%) magnetic composite under 80°C temperature gradient (0°C/80°C)

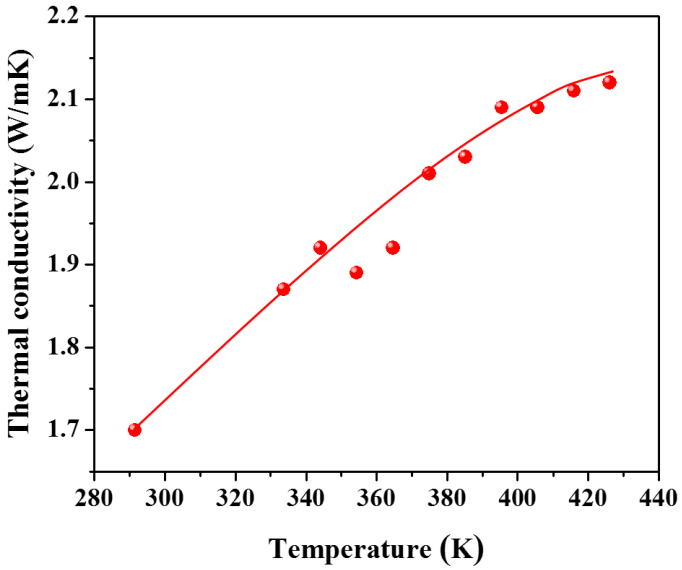

Figure 6.13. Thermal conductivity of two-step sintered LSMO-NCZF (70:30 *wt.*%) magnetic composites as function of temperature.

6.4. Summary

In summary, we have developed a soft magnetic composite that meets the requirement of magneto-thermal generator. The $La_{(1-x)}Sr_xMnO_3$ system where *Tc* can be modulated through varying Sr content (*x*) was modified with NCZF hard magnetic material for improving the M_s and M_r values while retaining its soft magnetic nature. The LSMO-NCZF ceramic composite was fabricated by two-step sintering in order to obtain full density without inter-phase diffusion. The structural, morphological, and compositional analysis indicated that the completely separated LSMO and NCZF grains with grain size below 200 nm were well developed. The LSMO-NCZF composite with 70:30 wt% ratio, exhibited significantly large variation in the saturated magnetization as a function of temperature change near its *Tc*. The fabricated MTG using this LSMO-NCZF composite showed 0.2 Hz operation frequency and generated maximum outputs of 2 V_{P-P} of output voltage and 17 μW of peak power under the thermal gradient of 80 ºC.

References

[1] G. Chen, M. Dresselhaus, G. Dresselhaus, J.-P. Fleurial, and T. Caillat, "Recent developments in thermoelectric materials," *International Materials Reviews*, 2013.

[2] M. W. Gaultois, T. D. Sparks, C. K. Borg, R. Seshadri, W. D. Bonificio, and D. R. Clarke, "Data-driven review of thermoelectric materials: performance and resource considerations," *Chemistry of Materials,* vol. 25, no. 15, pp. 2911-2920, 2013.

[3] L. Hicks, and M. Dresselhaus, "Effect of quantum-well structures on the thermoelectric figure of merit," *Physical Review B,* vol. 47, no. 19, pp. 12727, 1993.

[4] A. I. Hochbaum, R. Chen, R. D. Delgado, W. Liang, E. C. Garnett, M. Najarian, A. Majumdar, and P. Yang, "Enhanced thermoelectric performance of rough silicon nanowires," *Nature,* vol. 451, no. 7175, pp. 163-167, 2008.

[5] K. F. Hsu, S. Loo, F. Guo, W. Chen, J. S. Dyck, C. Uher, T. Hogan, E. Polychroniadis, and M. G. Kanatzidis, "Cubic AgPbmSbTe2+ m: bulk thermoelectric materials with high figure of merit," *Science,* vol. 303, no. 5659, pp. 818-821, 2004.

[6] S. Priya, and D. J. Inman, *Energy harvesting technologies*: Springer, 2009.

[7] A. Shakouri, "Recent developments in semiconductor thermoelectric physics and materials," *Materials Research,* vol. 41, no. 1, pp. 399, 2011.

[8] I. Terasaki, Y. Sasago, and K. Uchinokura, "Large thermoelectric power in NaCo 2 O 4 single crystals," *Physical Review B,* vol. 56, no. 20, pp. R12685, 1997.

[9] J.-F. Li, W.-S. Liu, L.-D. Zhao, and M. Zhou, "High-performance nanostructured thermoelectric materials," *NPG Asia Materials,* vol. 2, no. 4, pp. 152-158, 2010.

[10] R. Venkatasubramanian, E. Siivola, T. Colpitts, and B. O'quinn, "Thin-film thermoelectric devices with high room-temperature figures of merit," *Nature,* vol. 413, no. 6856, pp. 597-602, 2001.

[11] K. B. Joshi, and S. Priya, "Multi-physics model of a thermo-magnetic energy harvester," *Smart Materials and Structures,* vol. 22, no. 5, pp. 055005, 2013.

[12] P. T. McCarthy, E. E. Marinero, and T. S. Fisher, "Carbon nanotube thermal interfaces on gadolinium foil," *International Journal of Heat and Mass Transfer,* vol. 55, no. 23, pp. 6716-6722, 2012.

[13] M. Ujihara, G. Carman, and D. Lee, "Thermal energy harvesting device using ferromagnetic materials," *Applied Physics Letters,* vol. 91, no. 9, pp. 093508, 2007.

[14] G. Jonker, and J. Van Santen, "Ferromagnetic compounds of manganese with

perovskite structure," *physica,* vol. 16, no. 3, pp. 337-349, 1950.

[15] P. W. Anderson, and H. Hasegawa, "Considerations on double exchange," *Physical Review,* vol. 100, no. 2, pp. 675, 1955.

[16] P.-G. De Gennes, "Effects of double exchange in magnetic crystals," *Physical Review,* vol. 118, no. 1, pp. 141, 1960.

[17] C. Zener, "Interaction between the d shells in the transition metals," *Physical Review,* vol. 81, no. 3, pp. 440, 1951.

[18] A. Ramirez, "Colossal magnetoresistance," *Journal of Physics: Condensed Matter,* vol. 9, no. 39, pp. 8171, 1997.

[19] I.-W. Chen, and X.-H. Wang, "Sintering dense nanocrystalline ceramics without final-stage grain growth," *Nature,* vol. 404, no. 6774, pp. 168-171, 2000.

[20] X. H. Wang, X. Y. Deng, H. L. Bai, H. Zhou, W. G. Qu, L. T. Li, and I. W. Chen, "Two-Step Sintering of Ceramics with Constant Grain-Size, II: $BaTiO_3$ and Ni–Cu–Zn Ferrite," *Journal of the American Ceramic Society,* vol. 89, no. 2, pp. 438-443, 2006.

[21] X. H. Wang, P. L. Chen, and I. W. Chen, "Two-Step Sintering of Ceramics with Constant Grain-Size, I. Y2O3," *Journal of the American Ceramic Society,* vol. 89, no. 2, pp. 431-437, 2006.

[22] K. Dörr, "Ferromagnetic manganites: spin-polarized conduction versus competing interactions," *Journal of Physics D: Applied Physics,* vol. 39, no. 7, pp. R125, 2006.

[23] E. F. Kneller, and R. Hawig, "The exchange-spring magnet: a new material principle for permanent magnets," *IEEE Transactions on Magnetics,* vol. 27, no. 4, pp. 3588-3560, 1991.

7. Chapter 7: Magneto-Thermoelectric Generator Arrays for Active Heat Recovery System

7.1. Introduction

Small unmanned aerial vehicles (UAVs) (less than 1 kg) are continuously being explored for surveillance and security.[1-6] Recent focus in UAV design has been on integration of solar modules with wingspan in order to increase the endurance.[7-11] However, in order to generate sufficient power for extended flight time through solar cell modules, large surface area is required to maximize the output power and dissipate heat arising during cylcic operation.[12-15] Conventional solar modules exhibit 0.4 % decrease in output power per $1^{o}C$ rise in temperature beyond the threshold operating temperature.[16] The temperature on the back-side of module in UAV's can rise up to $70^{o}C$.[17] Similarly, there is increasing emphasis on development of the heat management system for data centers. The large packing density of transistors with increasing processing speed leads to high wasted heat, thereby, necessitating the deployment of heat dissipation system for safe operation. Rising central processing unit (CPU) temperature results in shortening of life time, malfunction, and failure.[18-20] This failure rate of CPU tends to increase exponentially with rising temperature.

The thermo-magneto-electric energy harvesting is promising methodology for high efficiency low grade heat management. The magneto-thermoelectric generator (MTG), composed of soft and hard ferromagnetic magnetic materials (here we used Gd and Nd as soft and hard magnets respectively), absorbs generated heat from the source and converts it into useful electrical energy with residual heat dissipated into the sink.[21] The driving force for MTG relies on thermally induced second order ferromagnetic to paramagnetic phase transition under thermal gradient in soft magnet.[22-27] This phase transition creates mechanical

vibration between hard magnet attached to the heat source (hot-side) that is always above the Curie temperature (294 K) and soft magnet attached on the spring in contact with the sink (cold-side). The soft magnet oscillates between the hot-side and cold-side undergoing ferromagnetic to paramagnetic phase transition (spring moving upward) and paramagnetic to ferromagnetic phase transition (spring moving downward), and this mechanical energy is converted into electrical energy through piezoelectric material. The thermal energy from the heat source is transferred and dissipated to heat sink through the soft ferromagnetic material.

Since the prediction of MTG in 2007, mostly theoretical work has been conducted in literature in optimizing the output power density and conversion efficiency.[21] Recently, carbon nanotube thermal interface has been employed for increasing the heat transfer from soft ferromagnetic material,[28] and theoretical approach to optimize the interactions between magnets and magnitude of device parameters influencing the dynamic behavior of the system has reported.[29] Here, we demonstrate feasible and practical MTG arrays, composed of flexible and lightweight piezoelectric polyvinylidene difluoride (PVDF) bimorph cantilevers. Under thermal gradient, the soft magnet (Gd) motion results in mechanical vibration of the PVDF cantilevers, thereby, generating electricity. This novel design of MTG arrays achieves vibration frequency from 1 to 3 Hz and generates 17 V and 15 μW under the thermal gradient of 80^{o}C. MTG arrays were attached to a central processing unit (CPU) inside the desktop to confirm the dual role of thermal energy harvesting and heat dissipation.

7.2. Experimental

7.2.1. Fabrication of Unimorph PVDF Cantilever for MTG

A gadolinium (Gd, 99.9% purity) foil of 127 μm thickness (Alfa Aesar Co., Inc., USA) was used to prepare soft ferromagnetic materials for the fabrication of thermo-magnetic generator,

as described previously. Briefly, prior to locating Gd foil between the hot-side and cold-side of the device, neodymium (Nd) of 1.58 mm thickness (MAGCRAFT, USA) with a sufficiently high Curie temperature than that of Gd was attached to Peltier heater using polysynthetic silver thermal paste to enhance the heat transfer from hot-side to hard magnet, and dried for 1h on hot plate at 60^{o}C. The Peltier cooler was mounted onto an aluminum heat sink with fan for past cooling up to −10^{o}C. To control distance between hard magnet and cold-side, the spacers were made from an insulating plastic film with thickness ranging between 3 mm to 7 mm by using CubePro 3D printer (3D Systems, Inc., USA). A soft ferromagnetic material was suspended on unimorph cantilever-type PVDF of 200 μm thickness with vertical Pt electrodes (KUREHA, USA), and then located adjacent to cold-side for generating restoring force like a spring.

7.2.2. Fabrication of MTG Arrays

A large Nd magnet of an area of 4 × 4 cm^2 was used for hard magnet and attached to the Peltier heater. Bimorph PVDF cantilevers were fabricated by stacking of two layers with opposite poling direction. The bimorph cantilevers were located on each edge of hard magnet. In order to increase output voltage and current of MTG, the bimorph cantilevers were connected in series and parallel.

7.2.3. Measurement of Electrical Output and Characteristics

To detect voltages generated by MTG, KEYSIGHT DSO 1014A Oscilloscope was used for electrical measurements. The resistance of the oscilloscope is 10 MΩ. The magnetic properties of the soft ferromagnetic material were characterized by an Evercool physical property measurement system (PPMS, Quantum Design).

7.3. Simulation for MTG

7.3.1. Magneto-static Modeling

In order to reduce device specific mass, thin magnetic components are necessary. Firstly, we were tried to determine optimal magnetic circuit configurations using magnetostatic modeling. Additionally, as the mechanical energy of the system is a function of the thermal modulation of the magnetic energy within the system, physical concentration of the magnetic fields is critical. Therefore, in order to overcome limitations due to shape demagnetization in thin layers, and to increase energy concentration within the system, we explored magnetic circuit configurations including simple unyoked magnetic circuit in Figure 7.1 (a), yoked magnetic circuit in Figure 7.1 (b), and simple Halbach arrays in Figure 7.1 (c). For simulation of this magnetic circuit configuration, we have employed a two-dimensional finite element analysis software package (FEMM). FEMM allows for pseudo three-dimensional analysis through z-axis symmetry simplification. Through such symmetries, two-dimensional models serve as planar or radial simplifications of three-dimensional configurations.

The configuration of the magnetic drivers in an alternately poled configuration in Figure 7.1 (a) and (b) acts to concentrate magnetic energy, while ensuring planarity in the flux lines traversing the ferromagnetic layer. These configurations provide significant improvement over single, dipole-type configurations, but result in low-flux regions at the center of the ferromagnetic layer. Furthermore, alternately poled circuits allow for significant flux leakage out the top and sides of the circuit, unless significant yoking is provided as shown Figure 7.1 (a) and (b). The Halbach configuration provide enhanced planarity in ferromagnetic flux lines, and further concentrate energy within the system with lower required yoking in Figure 7.1 (b). Whereas the magnetically-induced pressure from a single magnet system results in a 44mN/g, a Halbach configuration provides up to 185mN/g. The four times increase in magnetic energy

will result in a corresponding four-fold increase in mechanical energy, while ensuring insensitivity to shape demagnetization effects arising from thin-film form factors for deposited ferromagnetic layers.

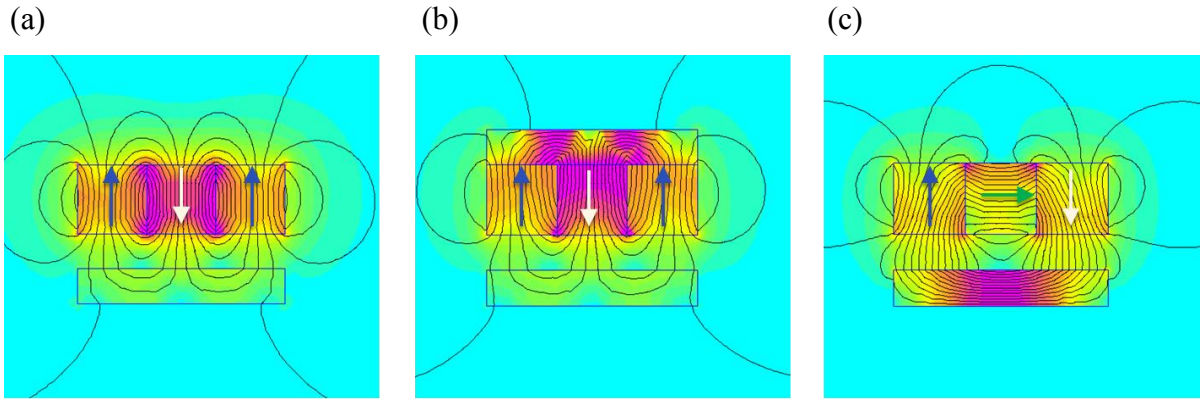

Figure 7.1. Simulated design of magnetic circuits within the device allow for concentration of magnetic energy. (a) Unyoked alternately poled magnetic circuit, (b) yoked alternately poled circuit, and (c) Halbach configuration.

7.3.2. Geometrical Tuning

The magnetic force curves with function of distance were empirically generated as shown Figure 7.2. These discretized magnetic force curves span the temperatures from 15.3 ^{o}C to 50.6 ^{o}C for the ferromagnetic materials of the harvester. The magnetic force was significantly decreased as increasing temperature. These curves are used for the geometrical tuning. In order to provide a means for tuning MTG, there are essentially three tunable parameters; hard magnet-to-gadolinium spacing (A), gadolinium-to-cold sink spacing (B), and ferromagnetic spring-to-backside magnet spacing (C). The tuning parameters are defined schematically in Figure 7.3 (b). To allow for tuning of the device to determine optimal gap spacings and backside offsets, we assumed a geometry as depicted in Figure 7.3 (a). Using the empirical force curves shown in Figure 7.2, we then calculated gap and backside offset spacings that would result in equal topside and backside magnetic forces – ensuring switching at those temperatures. An

example tuning result is presented in Figure 7.4. The 250μm thick gadolinium was used for the soft magnet and single-magnet top and backside magnets were installed. The hot and cold switching temperature were 15.3°C and 50.6°C, respectively. For this condition, the device requires a gap spacing of 1.33mm and a backside offset of 2.48mm for operation. Each cycle of the device produces about 190 μJ of energy, regardless of hot-side and cold-side temperatures. The hot source and cold sink temperatures, along with switching temperatures, only serve to influence thermal transport times, and therefore, switching frequency.

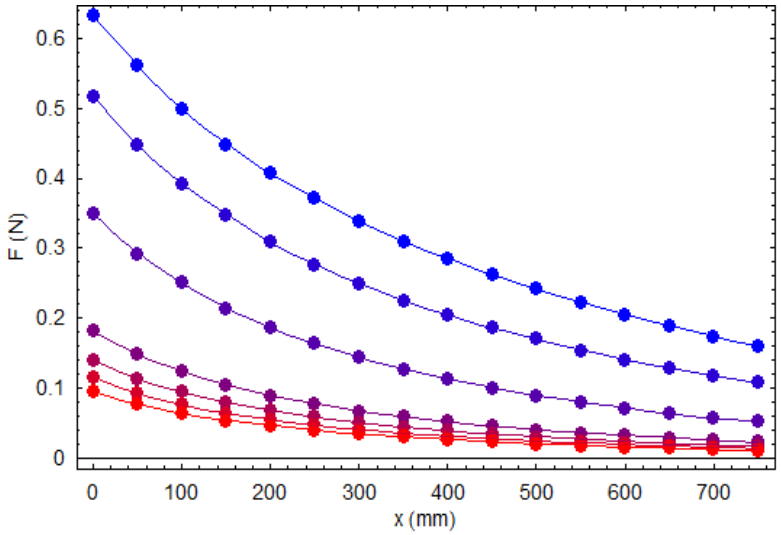

Figure 7.2. Empirically generated magnetic force curves as a function of position (relative to applied external H field) and temperature from 15.3°C to 50.6°C used in device tuning

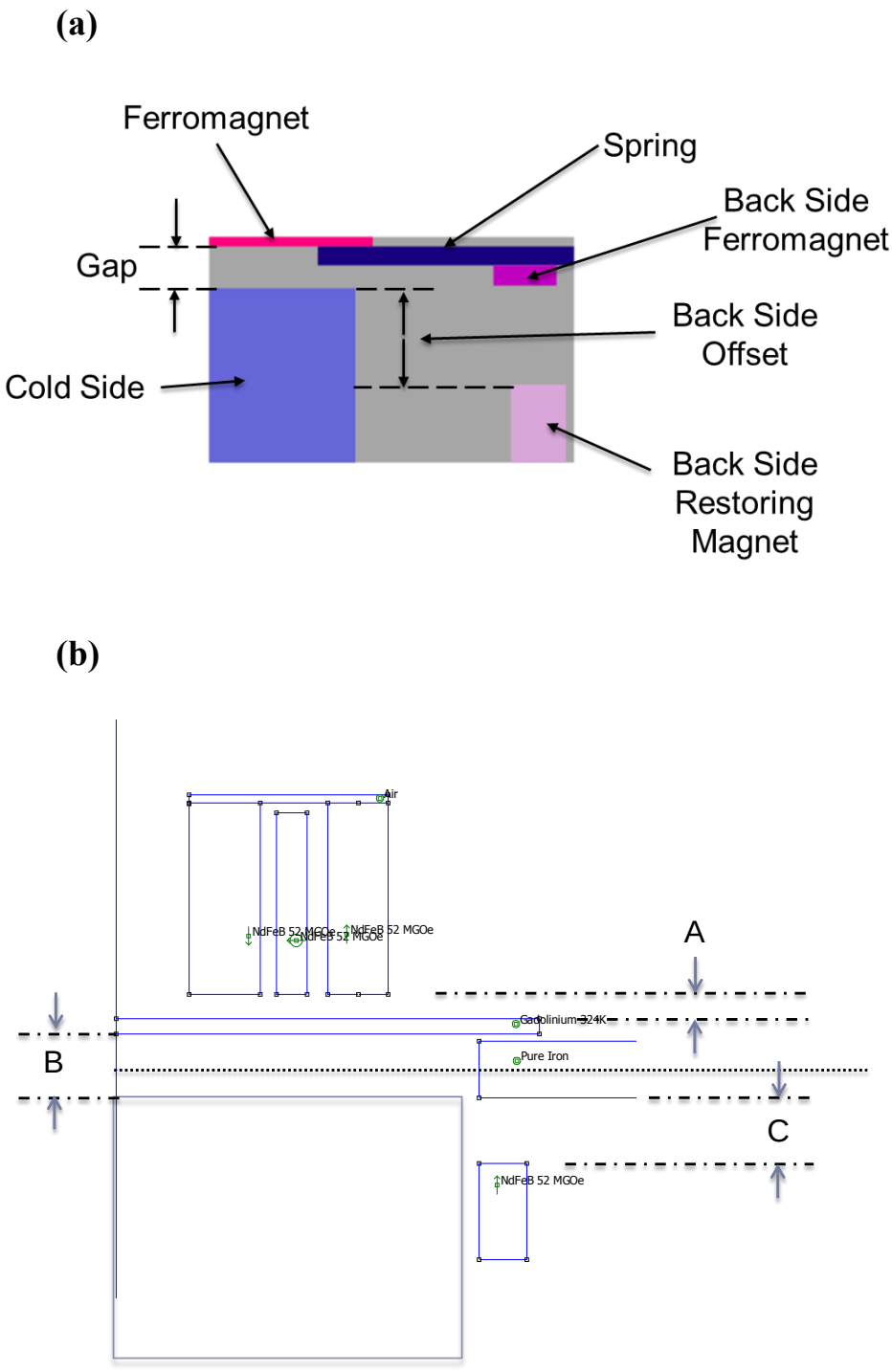

Figure 7.3. (a) Schematic representation of device geometry used in predictive tuning models. (b) The three geometrically tunable parameters for the system are; hard magnet-to-gadolinium spacing (A), gadolinium-to-cold sink spacing (B), and ferromagnetic spring-to-backside magnet spacing (C).

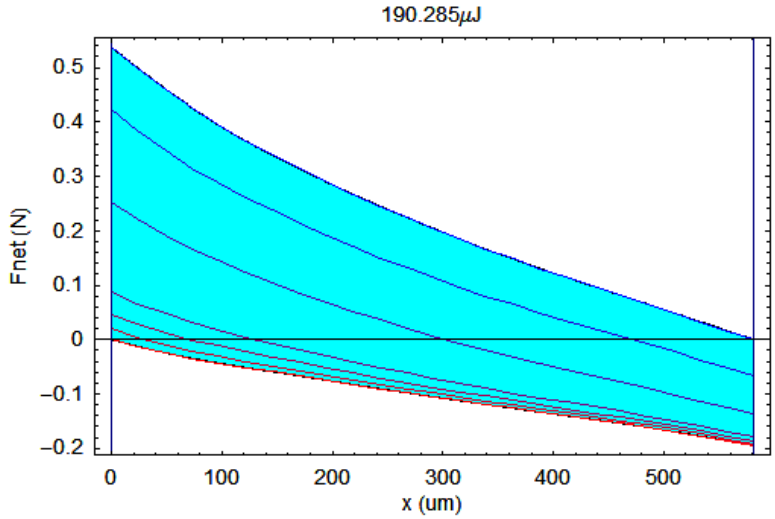

Figure 7.4. Simulation result for geometrical tuning with 250μm thick gadolinium, hot switching temperature of 15.3°C and cold switching temperature of 50.6°C.

7.3.3. Thermal Modeling

Thermal modeling was initially conducted using two different modeling packages: FEMM and a custom-designed Finite Difference Method (FDM) application in Mathematica™. Our initial static thermal model followed the same structure as the static magnetic model. The FEMM software package not only allows for magnetostatic modeling, but also allows for electrostatic and thermostatic modeling. We therefore set out to incorporate a thermal iteration step into our transient magnetic model. With plausible boundary conditions in the device walls, all heat flow can be assumed to flow in the direction of the thermal gradient. The reduced dimensionality in heat flow simplifies the requirements in terms of numerical approximation of the system. We have developed a one-dimensional, implicit finite difference method (FDM) numerical solution to the heat equation using Mathematica™. The heat equation can be express as

$$\frac{\partial T}{\partial t} = \propto \nabla^2 \mathrm{T} \qquad (7.1)$$

where T is the absolute temperature (K), t is the time (s) and α is the thermal diffusivity (m^2/s). For an adequate step size, the change in temperature with time can be approximated by

$$\frac{1}{\Delta t}(T^{t+1} - T^t) = \frac{T_{x+1}^{t+1} - 2T_x^{t+1} + T_{x-1}^{t+1}}{\Delta x^2} \tag{7.2}$$

where T_j^i is the temperature at position j and time t. Through use of the implicit approximation, the numerical model is inherently stable, albeit more computationally complex. The approximation of the heat solution can be solved for expressions of temperature at each point along within the geometry to produce a set of N simultaneous equations and N variables. Inclusion of boundary conditions provides all that is necessary to solve the equations and determine the thermal profile any time.

For the configuration depicted in Figure 7.5, a thermal gradient of 15000 °C/m generated by a hot side temperature of 400°C separated from a 0°C heat sink 8 mm distant produces a roughly linear distribution within the piston after only 60 seconds. Due to the relatively high specific heat of the working fluid (air in this example), the thermal distribution has not reached steady-state even after 12 minutes. Under actual operation conditions, it is the average temperature of the temperature dependent ferromagnet that will govern the device kinetics. The critical switching temperatures of the device will occur near the Curie temperature of the material, with specific values determined by the geometric tuning of the permanent magnetic circuits. The average temperature of the ferromagnet responds with a significantly lower time constant than does the working fluid as shown in Figure 7.5. The relative disparity in thermal kinetics supports the idea that the device will operate as a thermal transistor, rather than as a thermal sink.

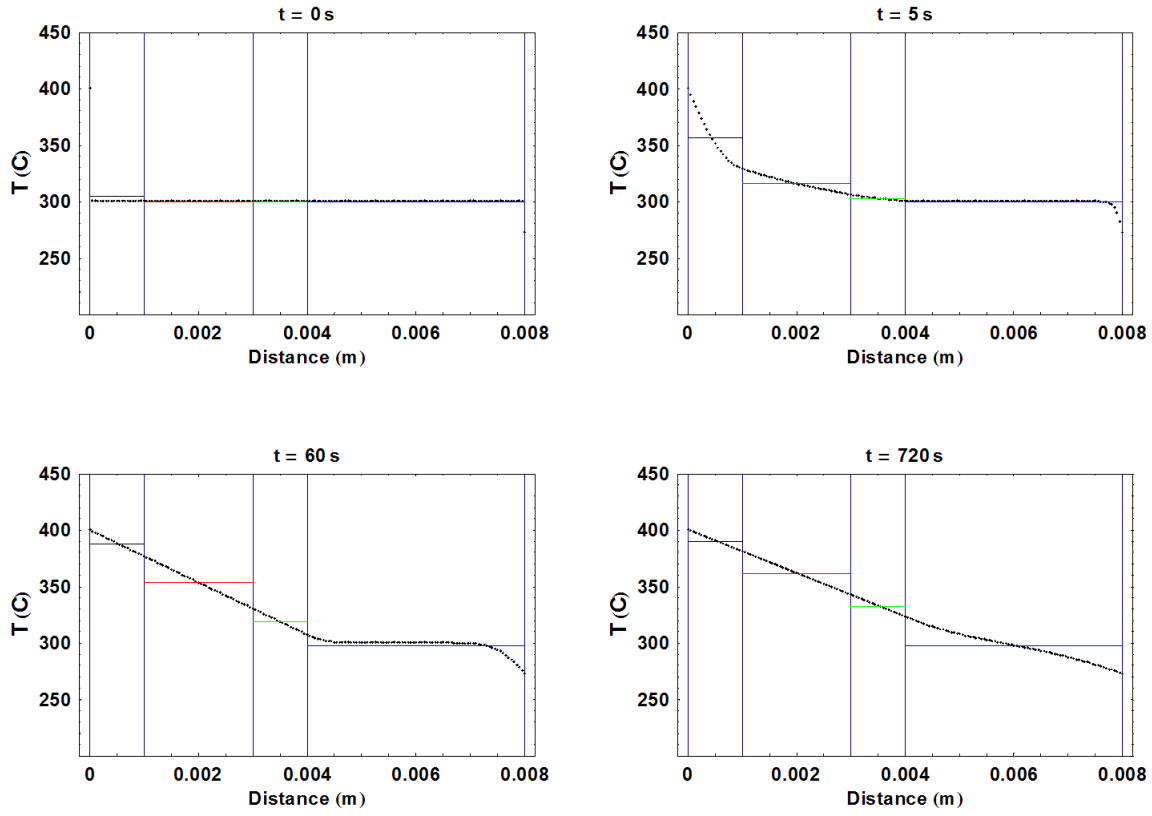

Figure 7.5. Model output graphics showing evolution of temperature for the device

Transient thermal modeling serves two purposes in optimization of device operation. First, coupled magneto-thermal analysis is critical to determine critical switching temperatures. It is the thermally-induced magnetic modulation that creates the magnetic force imbalance that leads to device state change. The second purpose of thermal modeling is to characterize and optimize switching frequency of the device. As noted by Ujihara, the net power available for harvesting in proportional to the switching frequency (Ujihara et al. 2007).[21]

Through FEA simulation, we determined that the switching frequency is critically dependent on the absolute contact resistance between the ferromagnetic material and the heat source and cold sink. As shown Figure 7.6, slight reductions of a high contact resistance to a lower value resulted in significant increases in cycle frequency. Traditionally, contact resistance is thought to be a function of several parameters, with contact pressure among the strongest influences. However, due to the relatively low forces associated with the magnetic couples, particularly in

the vicinity of the actual switching temperatures, the MTG operates in a low-pressure contact regime. While maximum pressures of the device can be increased through magnetic circuit engineering and ferromagnet face area optimization, in order for the device to operate, the net force attracting the ferromagnet to a heat source must eventually pass through zero. We are therefore required to operate within the low-pressure regime.

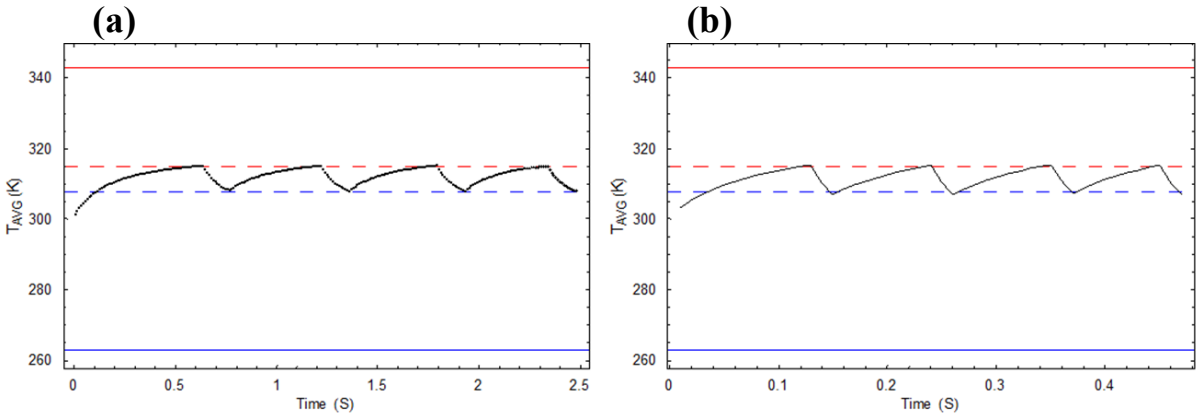

Figure 7.6. Transient thermal FEA results for a device with fixed heat source and sink temperatures and well-defined critical switching temperatures illustrates the importance of thermal contact resistance within the system.

In the low pressure regime (<1MPa), the thermal accommodation coefficient (TAC) governs the degree to which kinetic energy of a gas molecule is exchanged while in collision with a solid wall. A correlation for predicting the TAC for a given gas-solid combination is given as:[30]

$$TAC = Exp\left[-0.57\left(\frac{T_S - 273}{273}\right)\right]\left(\frac{M_g^*}{6.8 + M_g^*}\right) + \frac{2.4\mu}{(1+\mu)^2}\left\{1 - Exp\left[-0.57\left(\frac{T_s - 273}{273}\right)\right]\right\} \quad (7.3)$$

The TAC depends predominantly on the factor $2.4\mu/(1+\mu)^2$, which is a function of the ratio of molecular weights of the gas and the solid (μ). Therefore, the higher the μ-factor for the

combination, the higher the thermal conductance across the interface. Although typical contact resistance reduction is accomplished through gold plating, it is more desirable to coat the ferromagnetic material with a low-mass metallic layer in the low-pressure regime. For example, the μ factor for gold plating would be 0.26, whereas that for magnesium or aluminum would be 0.60.

7.4. Results and Discussion

7.4.1. Unimorph Cantilever Type MTG

The schematic representation of the fabrication process for MTG is shown in Figure 7.7 and detailed information is described in the experimental section. The generator comprises of three parts: hot-side with Peltier heater (4×4 cm^2) to which disk-type hard magnet (Nd) with 1.6 mm diameter was attached, the unimorph piezoelectric PVDF cantilever with soft ferromagnetic material (Gd, 4×8 mm^2), and cold-side with Peltier cooler. The inset shows the optical image of fabricated MTG with total size of 10×10 cm^2 and aluminum heat sink. Cooling fan is mounted underneath the cold-side for improving the heat transfer through forced convection. In the initial state, Gd attached to the PVDF cantilever, is attracted to the hard magnet on the hot-side due to magnetic force of attraction. As Gd makes contact with Nd, it loses attraction force due to phase transition and the cantilever is pulled back towards the cold side by restoring force of cantilever. After making contact with the cold-side, Gd is cooled below the Curie temperature and it again restores its ferromagnetic state which results in rise of magnetic force of attraction with the hard magnet, as shown in Figure 7.7. This periodic cycle continues to create mechanical deformation in the unimorph PVDF cantilever, and the cantilever generates electricity due to direct piezoelectric effect and moves the thermal energy from hot-side to cold-side repeatedly.

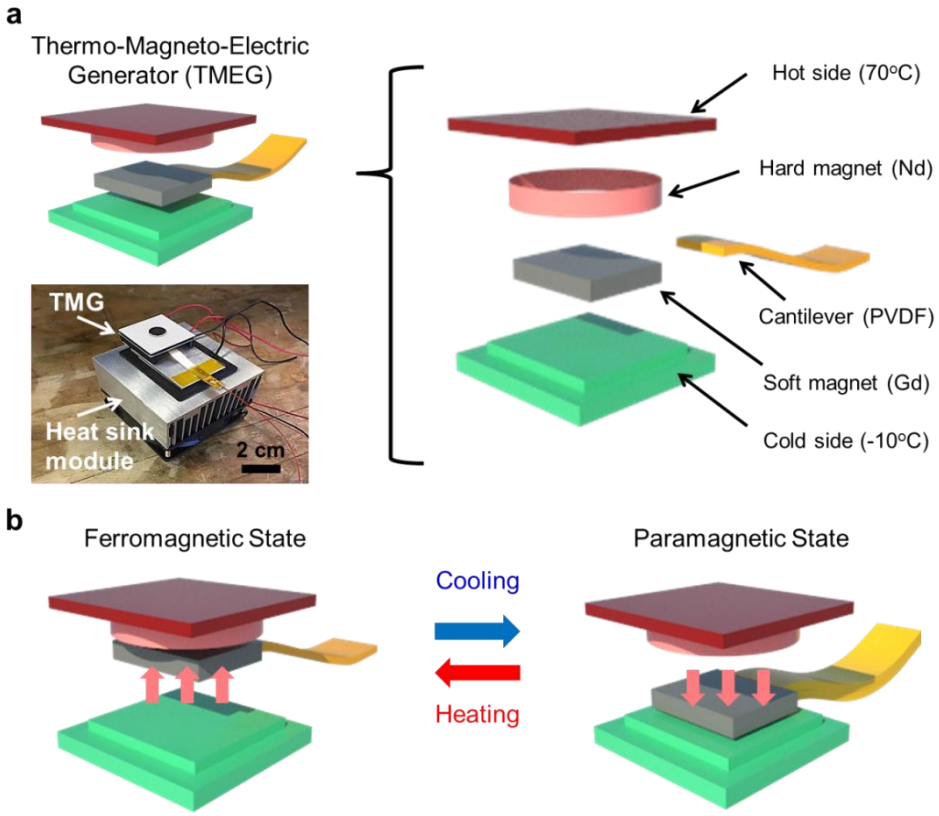

Figure 7.7. Transient Fabrication process of MTG. (a) Schematic diagram of MTG. The picture is of fabricated device image with heat sink module. (b) Schematic representation for MTG operating through second order phase transition occurring in soft magnet during periodic cooling and heating.

MTG operation was characterized under ambient condition similar to that for the UAVs at altitudes of ~60,000 ft where the outside temperature decreases up to ~–80°C.[29] Figure 7.10 (a) shows output voltage of the fabricated MTG with unimorph PVDF cantilever at a thermal gradient of 80°C. It was found to generate maximum output voltage of 2.6 V under vibration frequency of 1.56 Hz with travel distance of 3 mm between hard magnet and cold-side. The output voltage of the unimorph cantilever based MTG shows different polarity depending upon the bending direction of PVDF cantilever, as shown in the inset of Figure 7.10 (b). To confirm the polarity of generated voltage with different connection, MTG is connected with forward and reverse connection to the oscilloscope. The polarity is symmetrically changed under

different connection (see Figure 7.8). This result indicates that the measured voltage is generated from the piezoelectric PVDF through bending motion. To apply a constant thermal gradient, surface temperatures of the hard magnet and cold-side were maintained and measured for 1 h. The thermal gradient (ΔT) was saturated to 80°C (hard magnet at 70 °C and cold-side at –10 °C) after 10 min, as shown in Figure 7.10. Surface temperatures on the hard magnet and hot-side were not significantly different, which indicates that heat was effectively transferred from the Peltier heater to hard magnet as shown in Figure 7.9

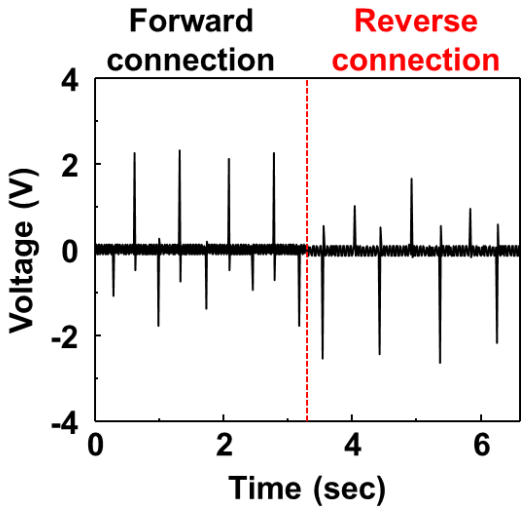

Figure 7.8. The output voltage signal from single cantilever based MTG measured in the forward and reverse connection.

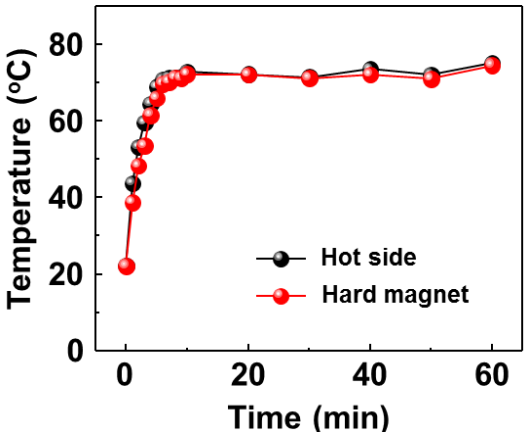

Figure 7.9. Measured temperatures on the surfaces of hot-side and hard magnet in MTG.

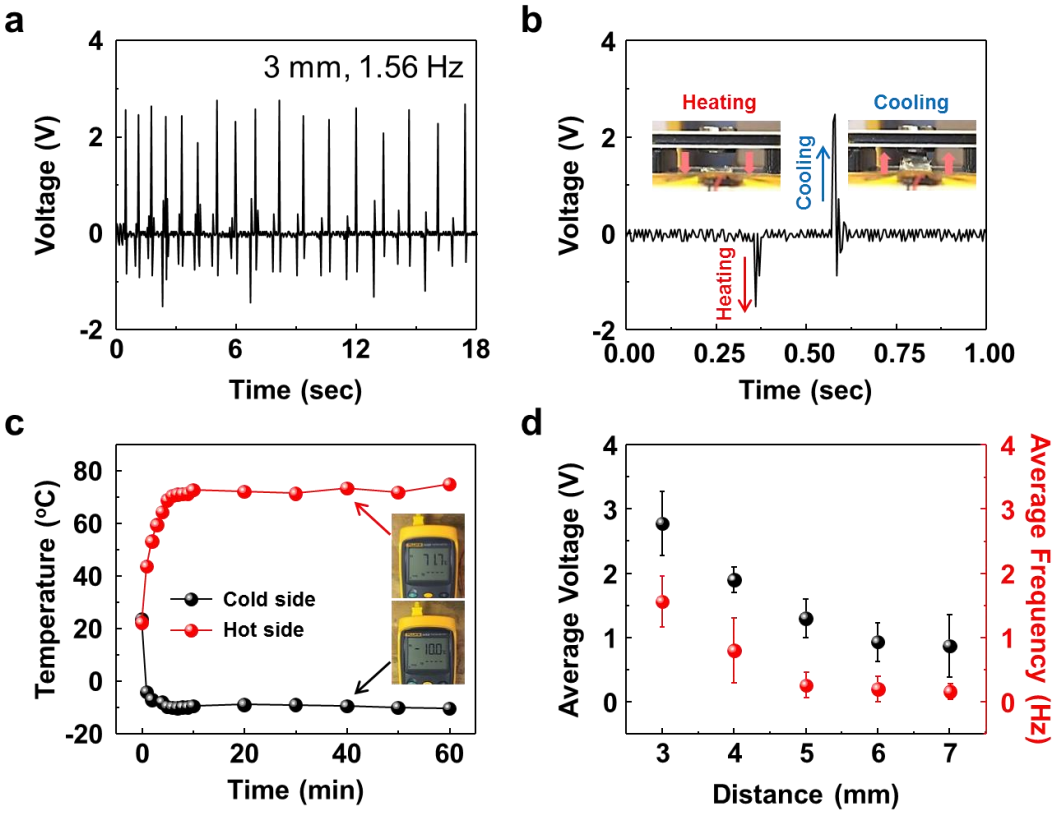

Figure 7.10. Electrical output performance of MTG (a) Output voltage of unimorph cantilever based MTG under thermal gradient of 80°C. (b) Extended output voltage during heating and cooling. The insets show snapshots of positions of soft ferromagnetic material. (c) Measured temperatures on the surfaces of cold-side and hot-side. (d) Average output voltage and vibration frequency of MTG as a function of distance between hard magnet and cold-side.

For continuous operation of MTG, specific distance between hard magnet and cold-side is required, which not only maintains the thermal gradient but also provides space for deformation of the PVDF cantilever. Figure 7.10 shows average output voltage and vibration frequency of the unimorph cantilever based MTG as function of gap distance. It can be clearly observed that small gap between hard magnet and cold-side increases output voltage and vibration frequency up to 2.6 V and 1.56 Hz, compared with large gaps. This indicates that there exists optimum separation distance between the magnets for a given thermal mass. MTGs with less than 3 mm gap distance did not provide measurable electrical response due to very small displacement of piezoelectric material. Small distance between hard magnet and cold-side results in increase of

vibration frequency due to decrease of the travel time of soft ferromagnetic material and restoring force of cantilever. The output power (P_{out}) can be defined as: $P_{out} = VI = Ef\eta$, where E is the mechanical energy applied on piezoelectric material, f is the bending frequency, and η is the energy conversion efficiency. Thus, high output voltage could be generated by increasing vibration frequency. ($V = Ef\eta/I$) The mechanical energy (E) can be defined as $E = \int F dx = \int c/(x+t)^2 dx$, where F is the magnetic force of soft ferromagnetic material, x is distance between hard magnet and cold-side, c represents material characteristics, and t is a shape related constant.[21, 31] Thus, this enhanced output power is attributed to the vibration frequency [32, 33] and magnetic force which increases the mechanical energy applied on to piezoelectric material.

Next, the coupling of thermal gradient induced phase transition and piezoelectric effect generated by vertical oscillation of soft ferromagnetic material were systematically investigated, as shown in Figure 7.7. To achieve high strain in PVDF layer, the PET elastic body was attached at bottom of PVDF according to the neutral axis theory.[33] The stress distribution significantly depends on the position of the neutral axis, which is determined from the condition that the resultant axial force acting on the cross-section is zero. Additionally, we calculated the piezopotential distributions inside the cantilever along the vertical direction by using a simple rectangular model composed of 200 μm-thickness PVDF film on the PET under the load of 640 μN. The material parameters of the PVDF, taken from the COMSOL simulation software, were used for the finite element analysis. The piezoelectric coefficient (d_{31}) of PVDF is −32.5 pC/N and PVDF was assumed to be a dielectric polymer. The piezoelectric potential of a fully coupled electro-mechanical system was calculated from the following piezoelectric coupled equations:[34, 35]

$$S = \underline{s}^E T + dE \text{ and } D = dT + \varepsilon^T E \tag{7.4}$$

where S is strain, s is compliance, T is applied stress, D is the electric charge density displacement, ε is permittivity, and E is electric field strength. In paramagnetic state, Figure 7.11 (a), there is no strain in piezoelectric, and thus no piezoelectric potential is generated. By cooling soft ferromagnetic material below Curie temperature, the phase transition from paramagnetic to ferromagnetic phase occurs. In ferromagnetic phase, soft magnetic material is attracted to hard magnet by magnetic force, and bending strain is applied to piezoelectric cantilever, resulting in piezoelectric potential. Figure 7.11 (b), maximum calculated potential difference of 38.2 V was generated as soft and hard magnets made contact. Figure 7.11 (c), after making contact with hard magnet, the temperature of soft magnet is increased above the Curie temperature. This results in second order magnetic phase transition from ferromagnetic to paramagnetic phase, resulting in cantilever movement towards the cold-side. Figure 7.11 (d), this cycle is continuously repeated under thermal gradient as shown Figure 7.11. To confirm the magnetic characteristics of soft ferromagnetic material (Gd), the temperature-dependent magnetization of Gd was measured after field-cooling at 500 Oe, which shows clear phase transitions under temperature change.

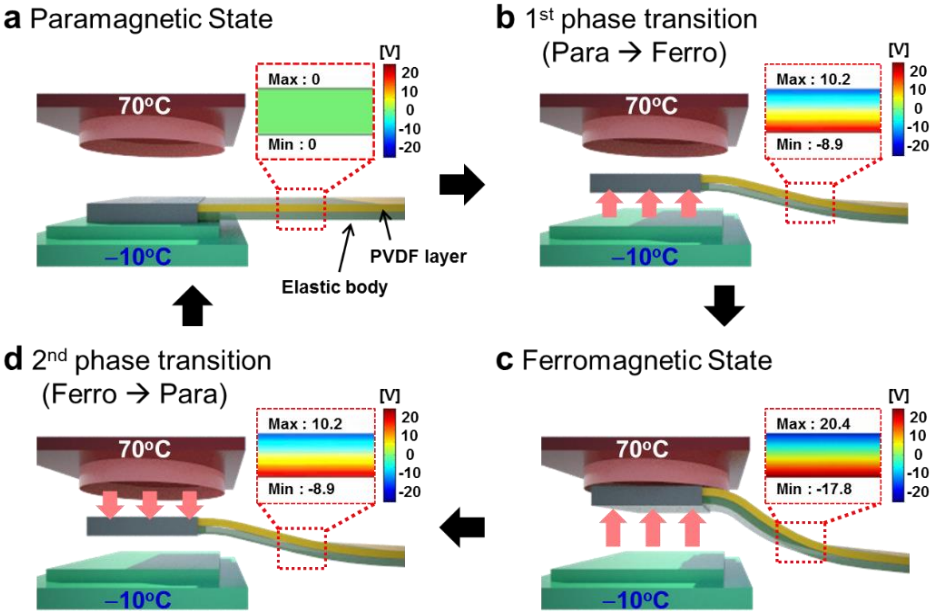

Figure 7.11. Working mechanism and numerical analysis of MTG. (a) paramagnetic state, (b) first phase transition during cooling, (c) ferromagnetic state, and (d) the second phase transition during heating. The insets show piezoelectric potential distributions of PVDF cantilever calculated by COMSOL Multiphysics software.

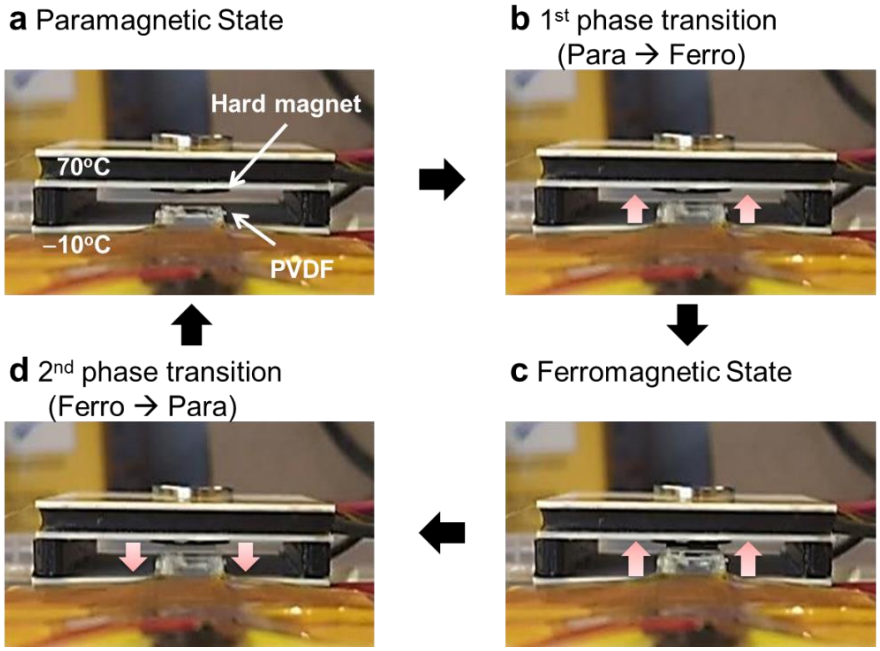

Figure 7.12. Snapshots of working mechanism of unimorph cantilever based MTG. (a) paramagnetic state, (b) the first phase transition during cooling, (c) ferromagnetic state, and (c) the second phase transition during heating.

7.4.2. Bimorph Cantilever type MTG Arrays

To obtain high output from MTG, bimorph cantilever based MTG were fabricated by stacking two PVDF with opposite poling direction and MTG arrays composed of eight bimorph cantilevers were prepared as shown in Figure 7.13 (a) and (b). Compared with unimorph cantilever based MTG, the output voltage of bimorph cantilever based MTGs is enhanced up to 4.2 V. In series connection with eight bimorph cantilevers arrays, the MTG arrays show the maximum output voltage of 17 V, which is 6 times higher than that of unimorph cantilever based MTG. This indicates that the high output voltage from the MTG can be achieved through this bimorph and arraying process. To control vibration frequency of MTG, eight bimorph cantilevers of MTG arrays are connected in parallel, resulting in an enhanced vibration frequency of 3 Hz, compared with unimorph cantilever based MTG. To optimize the output power of MTG, the output voltage of MTG was measured with external loads varying from 1 Ω to 10 MΩ, as shown in Figure 7.13 (e). The output voltage significantly increases with increasing resistance, while the output current decreases. The electrical output of unimorph, bimorph, and arrays of MTG at variable external loads were measured by oscilloscope with internal impedance of 10 M Ω, as shown in the inset of Figure 7.13 (e). Here, V_{out} is the voltage drop across resistance R, which can be measured with an oscilloscope. The generated current (I_{out}) of MTG could be calculated as V_{out}/R, (see Figure 7.14) and the output power (P_{out}) of MTG could be defined as $V_{out}I_{out}$ with various resistances. It should be noted that R is required to be less than 10 MΩ due to the resistance of oscilloscope.[36] Consequently, the instantaneous power of 15 μW across the resistance of 1 MΩ was obtained, as shown in Figure 7.13 (f), giving over 64-fold power enhancement, compared to the unimorph cantilever based MTG.

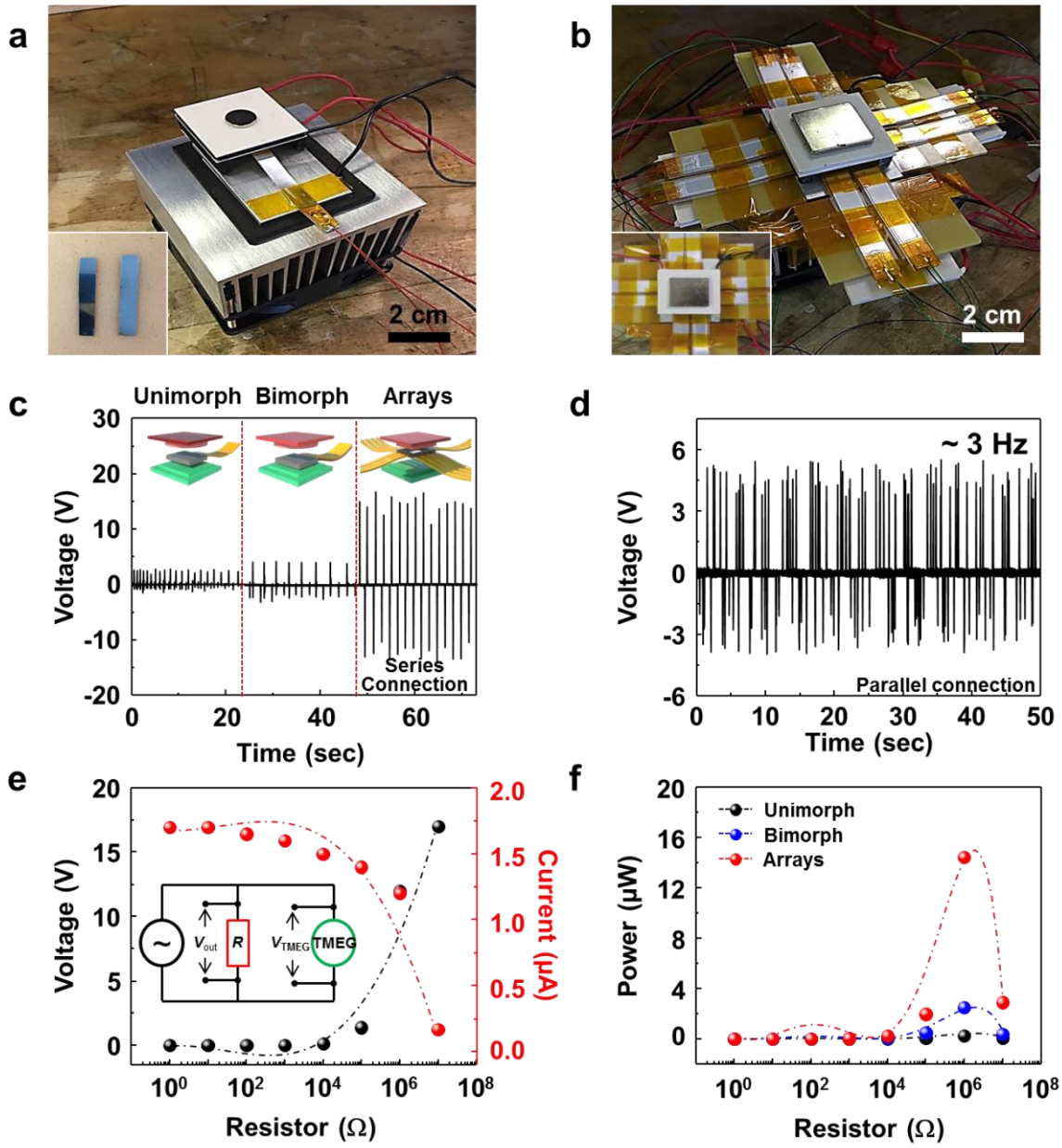

Figure 7.13. Electrical outputs and power of MTGs. Optical images of actually fabricated (a) bimorph cantilever based MTG and (b) MTG arrays composed of bimorph cantilevers. (c) Output voltages of unimorph and bimorph cantilever based MTG, and arrays in series connection. (d) Output voltage and vibration frequency of MTG arrays in parallel connection. (e) The output voltage and current density, and (f) the output power of the unimorph and bimorph cantilever based MTG, and arrays with the resistance of external loads from 1 Ω to 10 MΩ.

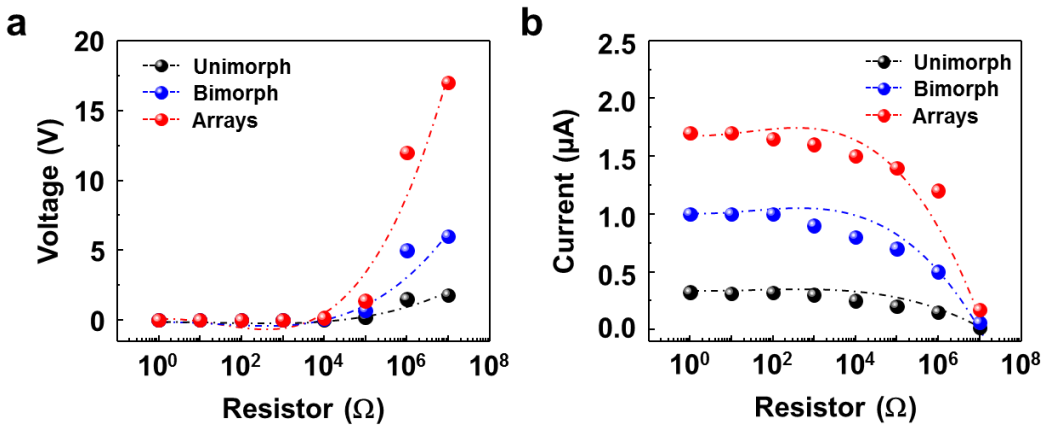

Figure 7.14. Electrical output and power of MTGs. (a) The output voltage and (b) current of the unimorph and bimorph cantilever based MTG and arrays with the resistance varying from 1 Ω to 10 MΩ.

7.4.3. MTG power generation and active heat dissipation on CPU

To demonstrate the capability of MTG in dual mode, power source and heat dissipation, we implemented two sets of practical applications. First, MTG was directly connected to three green commercial LEDs with rectifier unit. All of series connected LEDs were simultaneously powered by MTG arrays, as shown in Figure 7.15 (a) and (b). Second, the bimorph cantilever based MTG without Peltier heater was mounted onto a central processing unit (CPU) inside the desktop (Figure 7.15 (c) and (d)). Cooling system for the CPU is required to dissipate heat raised during operating. When operating desktop, the measured temperature on the surface of the CPU was ~84.5°C. It can be clearly seen that MTG successfully harvests thermal energy from the desktop and generates sufficient electrical power for two commercial green LED bulbs simultaneously. For heat dissipation capability of MTG, MTG without heater attached to CPU inside desktop, as shown in Figure 7.15 (e) and surface temperatures on CPU after power of heater and cooler turned off. It is clearly seen that low surface temperature (>3°C) on CPU during MTG operating (75s) based on residual thermal gradient, as shown in Figure 7.15 (f). Using the same measurement method, surface temperatures on Peltier heater were also

measured, resulting low surface temperature (>7°C) by operation of MTG (89s) (see Figure 7.16). These results show the feasibility of MTG as a power source and as heat dissipation device.

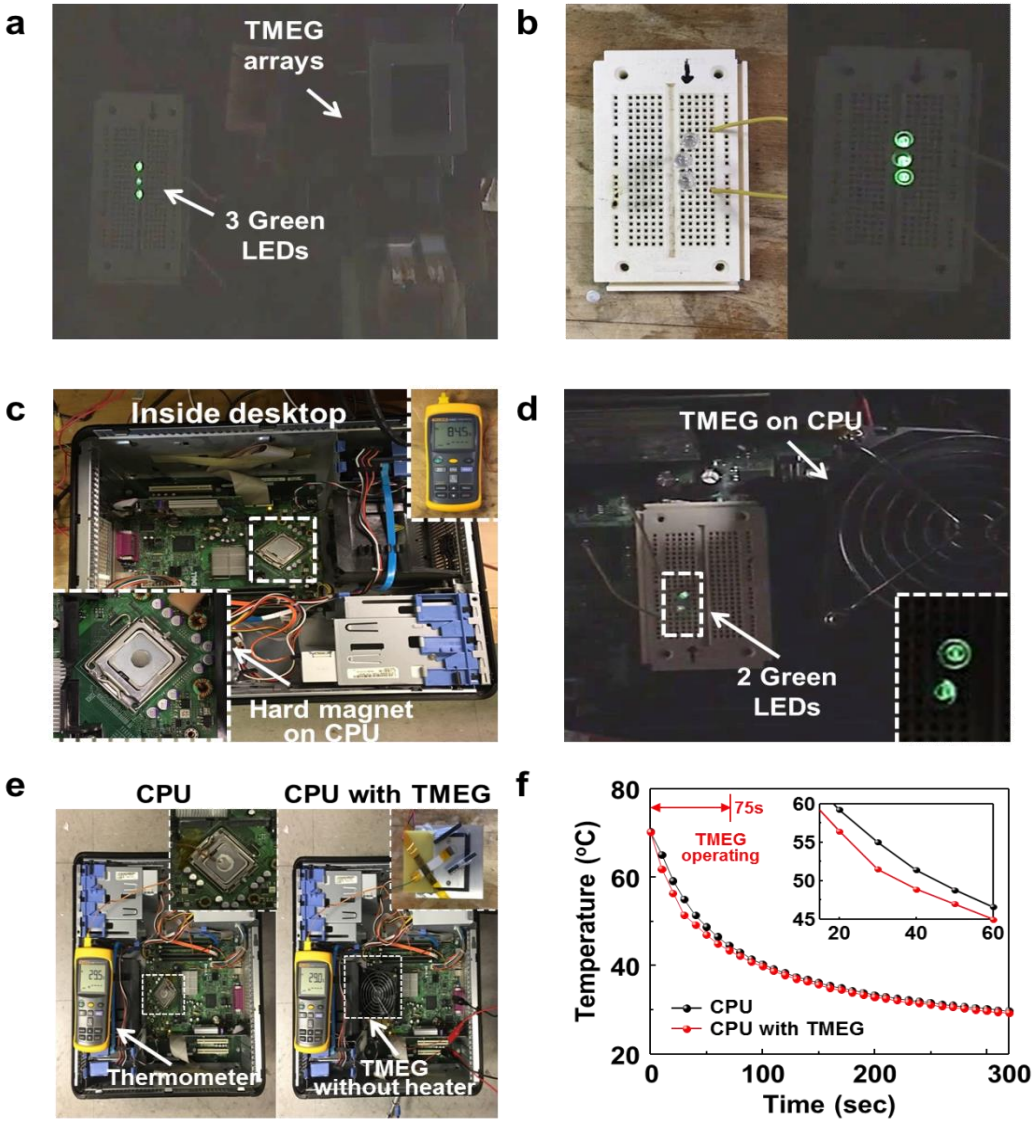

Figure 7.15. Demonstrations of the MTG as a sustainable power source and heat recovery system. (a) Photograph and (b) enlarged image of three commercial green LEDs driven by MTG arrays. (c) Photograph of a hard magnet attached to the CPU inside desktop and measured temperature on the CPU. (d) Photograph of two commercial green LEDs driven by bimorph cantilever based MTG. (e) Snapshots of MTG attached to CPU inside desktop and (f) surface temperatures on CPU with MTG and without MTG.

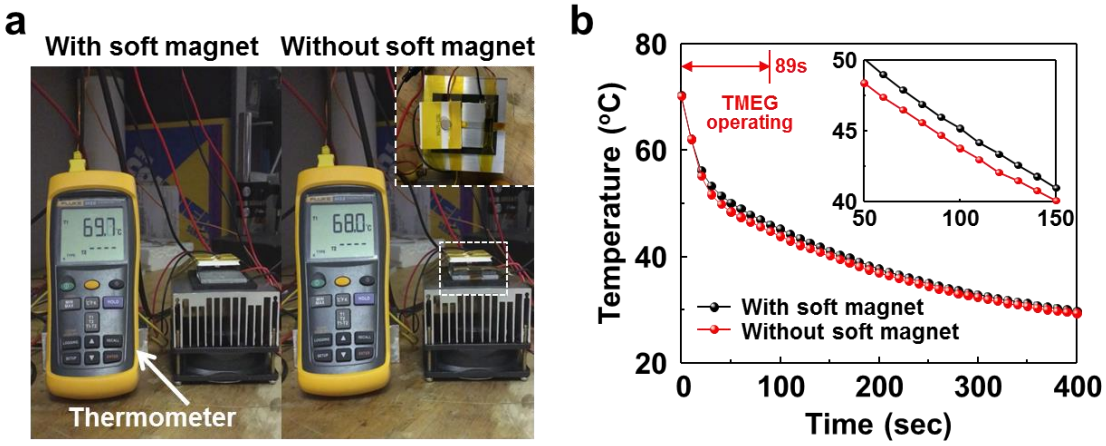

Figure 7.16. Heat dissipation of MTG. (a) Snapshots of MTG attached to Peltier heater and (b) surface temperatures on Peltier heater with MTG and without MTG.

7.5. Summary

In summary, we report novel MTG arrays, composed of flexible and lightweight polyvinylidene difluoride (PVDF) bimorph cantilevers, for active heat dissipation in electronic devices and solar modules. Under thermal gradient, the ferromagnetic phase transition of soft magnet (Gd) generates mechanical vibrations, resulting in piezoelectric output power generation. This design of MTG arrays achieved the vibration frequency from 1 to 3 Hz in parallel connection and electrical outputs of 17 V and 15 μW in series connection. Since the ambient temperature at altitudes of ~60,000 ft decreases up to ~ –80 ^{o}C, larger thermal gradient (ΔT > 80^{o}C)[29] and reliable output generation could be expected than that reported in this study. MTG arrays attached to a central processing unit (CPU) inside the desktop showed feasibility of thermal energy harvesting from wasted heat source.

References

[1] D. Floreano, and R. J. Wood, "Science, technology and the future of small autonomous drones," *Nature,* vol. 521, no. 7553, pp. 460-466, 2015.

[2] G. Gabrielli, "What price speed? Specific power required for propulsion of vehicles," *Mechanical Engineering-CIME,* vol. 133, no. 10, pp. 4-5, 2011.

[3] V. Kumar, and N. Michael, "Opportunities and challenges with autonomous micro aerial vehicles," *The International Journal of Robotics Research,* vol. 31, no. 11, pp. 1279-1291, 2012.

[4] K. Y. Ma, P. Chirarattananon, S. B. Fuller, and R. J. Wood, "Controlled flight of a biologically inspired, insect-scale robot," *Science,* vol. 340, no. 6132, pp. 603-607, 2013.

[5] D. Mellinger, N. Michael, and V. Kumar, "Trajectory generation and control for precise aggressive maneuvers with quadrotors," *The International Journal of Robotics Research*, pp. 0278364911434236, 2012.

[6] R. J. Wood, B. Finio, M. Karpelson, K. Ma, N. O. Pérez-Arancibia, P. S. Sreetharan, H. Tanaka, and J. P. Whitney, "Progress on 'pico'air vehicles," *The International Journal of Robotics Research,* vol. 31, no. 11, pp. 1292-1302, 2012.

[7] A. T. Klesh, and P. T. Kabamba, "Solar-powered aircraft: Energy-optimal path planning and perpetual endurance," *Journal of guidance, control, and dynamics,* vol. 32, no. 4, pp. 1320-1329, 2009.

[8] J.-K. Shiau, D.-M. Ma, P.-Y. Yang, G.-F. Wang, and J. H. Gong, "Design of a solar power management system for an experimental UAV," *IEEE transactions on aerospace and electronic systems,* vol. 45, no. 4, pp. 1350-1360, 2009.

[9] S. C. Spangelo, and E. G. Gilbert, "Power optimization of solar-powered aircraft with specified closed ground tracks," *Journal of Aircraft,* vol. 50, no. 1, pp. 232-238, 2012.

[10] X.-M. Tang, P. Chen, and B. Li, "Optimal air route flight conflict resolution based on receding horizon control," *Aerospace Science and Technology,* vol. 50, pp. 77-87, 2016.

[11] W. Harasani, M. Khalid, N. Arai, K. Fukuda, and K. Hiraoka, "Initial conceptual design and wing aerodynamic analysis of a solar power-based UAV," *The Aeronautical Journal,* vol. 118, no. 1203, pp. 540-554, 2014.

[12] Y. Tripanagnostopoulos, T. Nousia, M. Souliotis, and P. Yianoulis, "Hybrid photovoltaic/thermal solar systems," *Solar energy,* vol. 72, no. 3, pp. 217-234, 2002.

[13] H. Zondag, D. De Vries, W. Van Helden, R. Van Zolingen, and A. Van Steenhoven, "The yield of different combined PV-thermal collector designs," *Solar energy,* vol. 74, no. 3, pp. 253-269, 2003.

[14] T. Chow, "Performance analysis of photovoltaic-thermal collector by explicit dynamic model," *Solar Energy,* vol. 75, no. 2, pp. 143-152, 2003.

[15] L. Barra, and D. Cotante, "Annual energy production and room temperature effect in siting flat plate photovoltaic systems," *Solar energy,* vol. 51, no. 5, pp. 383-389, 1993.

[16] E. Radziemska, "The effect of temperature on the power drop in crystalline silicon solar cells," *Renewable Energy,* vol. 28, no. 1, pp. 1-12, 2003.

[17] K. Sun, M. Zhu, L. Wang, and H. Liu, "Analysis of the Hybrid Power System for High-Altitude Unmanned Aircraft," *Advances in Materials Science and Engineering,* vol. 2015, 2015.

[18] Y. Zhou, and J. Yu, "Design optimization of thermoelectric cooling systems for applications in electronic devices," *International journal of refrigeration,* vol. 35, no. 4, pp. 1139-1144, 2012.

[19] H. Hu, T. Ge, Y. Dai, and R. Wang, "Experimental study on water-cooled thermoelectric cooler for CPU under severe environment," *International Journal of Refrigeration,* vol. 62, pp. 30-38, 2016.

[20] A. Carbó, E. Oró, J. Salom, M. Canuto, M. Macías, and J. Guitart, "Experimental and numerical analysis for potential heat reuse in liquid cooled data centres," *Energy Conversion and Management,* vol. 112, pp. 135-145, 2016.

[21] M. Ujihara, G. Carman, and D. Lee, "Thermal energy harvesting device using ferromagnetic materials," *Applied Physics Letters,* vol. 91, no. 9, pp. 093508, 2007.

[22] H. E. Nigh, S. Legvold, and F. Spedding, "Magnetization and electrical resistivity of gadolinium single crystals," *Physical Review,* vol. 132, no. 3, pp. 1092, 1963.

[23] J. Coey, V. Skumryev, and K. Gallagher, "Rare-earth metals: Is gadolinium really ferromagnetic?," *Nature,* vol. 401, no. 6748, pp. 35-36, 1999.

[24] J. Cable, and E. Wollan, "Neutron diffraction study of the magnetic behavior of gadolinium," *Physical Review,* vol. 165, no. 2, pp. 733, 1968.

[25] S. Y. Dan'Kov, A. Tishin, V. Pecharsky, and K. Gschneidner, "Magnetic phase transitions and the magnetothermal properties of gadolinium," *Physical Review B,* vol. 57, no. 6, pp. 3478, 1998.

[26] D. X. Chen, and A. Sanchez, "Theoretical critical-state susceptibility spectra and their

application to high-Tc superconductors," *Journal of applied physics,* vol. 70, no. 10, pp. 5463-5477, 1991.

[27] D. Geldart, P. Hargraves, N. Fujiki, and R. Dunlap, "Anisotropy of the critical magnetic susceptibility of gadolinium," *Physical review letters,* vol. 62, no. 23, pp. 2728, 1989.

[28] P. T. McCarthy, E. E. Marinero, and T. S. Fisher, "Carbon nanotube thermal interfaces on gadolinium foil," *International Journal of Heat and Mass Transfer,* vol. 55, no. 23, pp. 6716-6722, 2012.

[29] K. B. Joshi, and S. Priya, "Multi-physics model of a thermo-magnetic energy harvester," *Smart Materials and Structures,* vol. 22, no. 5, pp. 055005, 2013.

[30] P. Misra, and J. Nagaraju, "Thermal gap conductance at low contact pressures (< 1MPa): Effect of gold plating and plating thickness," *International Journal of Heat and Mass Transfer,* vol. 53, no. 23, pp. 5373-5379, 2010.

[31] G. Akoun, and J.-P. Yonnet, "3D analytical calculation of the forces exerted between two cuboidal magnets," *IEEE Transactions on magnetics,* vol. 20, no. 5, pp. 1962-1964, 1984.

[32] S. R. Hunter, N. V. Lavrik, S. Mostafa, S. Rajic, and P. G. Datskos, "Review of pyroelectric thermal energy harvesting and new MEMs-based resonant energy conversion techniques." pp. 83770D-83770D-14.

[33] S. Ravindran, T. Huesgen, M. Kroener, and P. Woias, "A self-sustaining micro thermomechanic-pyroelectric generator," *Applied Physics Letters,* vol. 99, no. 10, pp. 104102, 2011.

[34] S. Cha, S. M. Kim, H. Kim, J. Ku, J. I. Sohn, Y. J. Park, B. G. Song, M. H. Jung, E. K. Lee, and B. L. Choi, "Porous PVDF as effective sonic wave driven nanogenerators," *Nano letters,* vol. 11, no. 12, pp. 5142-5147, 2011.

[35] K. Lefki, and G. Dormans, "Measurement of piezoelectric coefficients of ferroelectric thin films," *Journal of applied physics,* vol. 76, no. 3, pp. 1764-1767, 1994.

[36] G. Cheng, Z.-H. Lin, L. Lin, Z.-l. Du, and Z. L. Wang, "Pulsed nanogenerator with huge instantaneous output power density," *Acs Nano,* vol. 7, no. 8, pp. 7383-7391, 2013.

8. Chapter 8: Summary and Future works

8.1. Summary

8.1.1. Piezoelectric $PbTiO_3$ Nanostructures

The piezoelectric nanostructures including nanorods, nanofibers, nanobelts, nanotubes and hierarchical three-dimensional nanostructures have been attractive due to their unique physical and chemical properties such as a large surface area, excellent charge transport, high electro-mechanical coupling and superior ferroelectric properties and their possible application in nanogenerators, sensors, nanoactuator, nonvolatile memory and water splitting. Among various piezoelectric materials, $PbTiO_3$ (PTO) has some appealing characteristics such as a low aging rate of the dielectric constant, a high voltage constant (g), and a high Curie temperature of 490 ^oC. Also, the PTO has high tetragonality (c:a ratio of 1.063) which can provide a low ratio for the planar-to-thickness coupling factor. Additionally, photocatalytic characteristics of PTO for production of O_2 and H_2 by splitting water are recently received attentions.

Firstly, the vertically aligned PTO nanofiber arrays were demonstrate on a metal Ti substrate via rutile TiO_2 seeding. The growth mechanism of PTO nanofibers investigated experimentally and theoretically. From crystal surface matching simulation, the rutile TiO_2 (110) and the PTO (001) surfaces are the best fitting interface. The experimental results confirmed that only the rutile (110) TiO_2 seed layer can give a condition to grow the epitaxial PTO nanofibers with (100) orientation.

The novel 3-dimensional (3-D) PTO nanostructures with the cross-hatch pattern like aligned nanosheet arrays were also denmostrated on (100) $SrTiO_3$ (STO) substrate by a hydrothermal synthesis. According to orientation of STO subrate, different configurations of PTO nanostructures were formed, which was closely related to Ti atom configuration on the surface of the STO subrate. With use of the polycrystalline TiO_2 thin film coated STO subsrate, the 3-

D PTO nanostructure with the randomly aligned 2-D nanosheets arrays was formed, which results confirm that Ti atoms on substrate can play an importance role as guidance of the directional growth of the PTO nanostructures.

8.1.2. Piezoelectric Energy Harvester

The MEMS energy harvesting system using environmental vibrations will replace batteries and power wiring for small electronic devices including autonomous sensors systems, MEMS devices and internet of things (IoT) in near future if sufficient power can be extracted from the ambient environment continuously, robustly and at low cost. Among various harvesting system, piezoelectric MEMS energy harvesters are one of the most promising candidate for replacing battery due to their small size and availability of integration with systems. To realize the MEMS energy harvester, the three biggest challenges of higher power density, low resonance frequency and wider bandwidth currently lay on the technology. To solve these problems, two kinds of piezoelectric energy harvesters of the spiral MEMS harvester and the magnetically coupled harvester arrays were demonstrated in this work.

The spiral MEMS piezoelectric energy harvesters exhibited an ultra-low resonance frequency and high power density at low acceleration condition within small dimension. The experimental results demonstrate the ultra-low natural frequency of 48 Hz for the MEMS harvester. This is one of the lowest resonance frequency in reported piezoelectric MEMS energy harvesters. Further, the position of the natural frequency was controlled by modulating number of turns and weight of proof mass. The vibration mode shape and stress distribution were validated through the finite element analysis. The maximum output power of 23.3 nW was obtained from the 5 turns spiral MEMS energy harvester excited at 0.25g acceleration and 68Hz. The normalized volumetric energy density was calculated to be 4.92×10^{-2}

$\mu W/mm^3 \cdot g^2 \cdot Hz$. We achieved one of the highest volumetric power density in reported MEMS harvesters with useable resonance frequency range (< 200Hz).

The magnetically coupled piezoelectric energy harvester arrays (MaCoPEHA) with improved power density and broadband operation frequency was demonstrated in order to apply for continuously varying frequency condition. Using magnetic proof mass, the arrayed piezoelectric energy harvesters with different resonance frequency were magnetically coupled. They were interconnected and affected to each other by the magnetic repulsive force. All energy harvesters can take part in operation and generating power not only in their own resonance but also in the other's resonance. Thus, overall generated output power can be improved. The experimental results showed that the bandwidth of resonance frequency was significantly increased and output power was also considerably improved in comparison with the typical energy harvester arrays. The MaCoPEHA was also tested for the stray magnetic field energy harvester through the magnetic proof masses interacting with the magnetic field. The MaCoPEHA harvested electric energy from real applications including the stray magnetic fields surrounding the power cord of an electric kettle, fixed frequency vibrations of a rotary pump, and continuous varying frequency vibrations of a car engine.

8.1.3. Magneto-thermoelectric Generators

Researches for thermal generators have been focused on converting thermal energy into electrical energy. Thermoelectric devices commonly employed to generate electric power from thermal gradient. However, the thermoelectric devices have serious drawbacks of the low figure of merit ZT value around room temperature and the difficulty of maintaining large temperature gradient within thin thermoelectric materials. Thus, it is very difficult to generate high power using the thermoelectric generators around room temperature. To overcome these problems of the thermoelectric generators, the magneto-thermoelectric generator (MTG)

concept has been proposed which exploits the thermally induced second order phase transition of a soft magnetic material at their Curie temperature. The MTG can generate the electric energy via the strain of the piezoelectric cantilever induced from oscillation of the soft magnetic material between the hot and cold sources.

One of the most important issue in MTG is developing the suitable soft magnetic materials. To operate MTG near room temperature, the T_C of the soft magnetic material should be close to the room temperature while maximizing the saturated (M_s) and remnant (M_r) magnetization with small coercive field (H_c). So we engineered the composite material architecture based upon $La_{0.85}Sr_{0.15}MnO_3$ (LSMO) and $Ni_{0.6}Cu_{0.2}Zn_{0.2}Fe_2O_4$ (NCZF) that is able to meet the above mentioned requirements. The developed magnetic composite materials can successfully operate MTG.

The MTG with the Gadolinium (Gd) soft magnetic material and PVDF canilever energy harvester was also demonstrated. The design of arrayed MTG achieved the vibration frequency from 1 to 3 Hz in parallel connection and electrical outputs of 17 V and 15 μW in series connection. The MTG arrays attached to a central processing unit (CPU) inside the desktop showed feasibility of thermal energy harvesting from wasted heat source.

8.2. Future works

8.2.1. Piezoelectric $PbTiO_3$ Nanostructures

The piezoelectric $PbTiO_3$ (PTO) nanostructures including the PTO nanofiber and the 3-D PTO nanostructue were successfully synthesized using a hydrothermal synthesis. However, actul devices such as nanogenerators and accostic sensorss using these nanostructures had not been demonstrated due to the difficulty of the formation of electrodes on porous surfaces of the nano structures. As decribed in Figure 8.1., if we fill up the space between the

nanostructures by polymers such as PDMS and fabricate piezoelectric nanocomposites, and then we can easily deposite the electrodes by DC spputtering or evaporation. The nanocomposites could be seperated from the substrates mechanically and chemically. These piezoelectric nanocomposites can be good candidates for nanogenerator and utra sensitive nano accostic sensor due to thier high piezoelectric properties and flexibility.

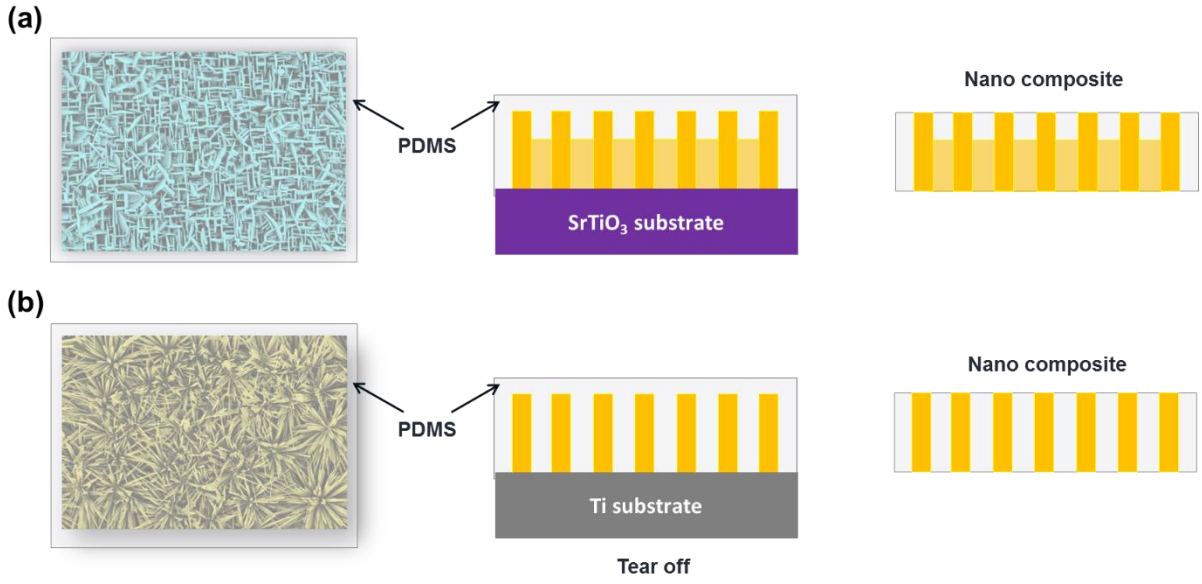

Figure 8.1. Schematic illustration for fabrication of piezoelectric nanocomposites using (a) $PbTiO_3$ 3-D nanostructures and (b) $PbTiO_3$ nanofibers.

8.2.2. Piezoelectric Energy Harvester

The magnetically coupled piezoelectric energy harvester arrays (MaCoPEHA) successfully achieved the broadband natural frequency by the magnetically induced nonlinearity. However, as presented in Figure 8.2., the arrayed cantilever energy harvesters in the MaCoPEHA were alternately shifted up and down in order to provide a magnetic force equilibrium. And also the longer beams deflected more than the shorter beams because of their lower stiffness. Because of these deflections of the cantilevers, the magnetic coupling between arrayed harvesters and the nonlinearity were reduced. For improving the magnetic coupling and avoiding these

deflection, the stiffness of the cantilevers and the magnetic force between the magnetic proof masses should be optimized through computational simulation.

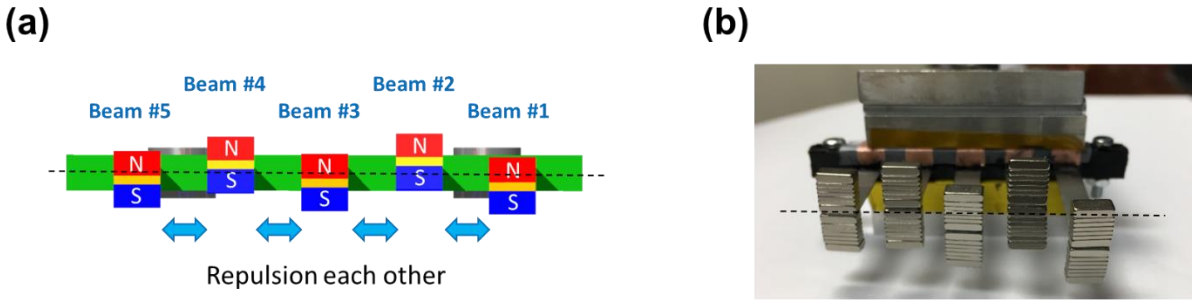

Figure 8.2. (a) Schematic description and (b) snapshot of the deflection of cantilever beam energy harvesters in MaCoPEHA by the magnetic repulsion force.

8.2.3. Magneto-thermoelectric Generators

In this work, the soft magnetic materials of LSMO-NCZF composite with the high performance index (P.I.) were synthesized for the magneto-thermoelectric generator (MTG). The MTG was successfully operated using this LSMO-NCZF composite and generated output voltage 4 V_{p-p} from 80^{o}C temperature gradient. In spite of the high P.I. value of the LSMO-NCZF composite, the operation frequency of the MTG was relatively low because of the low thermal conductivity of the LSMO-NCZF ceramic composite. To increase the operation frequency of MTG, it is neccessary to include high thermal conductivity materials such CNT or graphene to the soft magnetic materials.